3-26-2015

Tension-Compression Fatigue of an Oxide/Oxide Ceramic Matrix Composite at Elevated Temperature in Air and Steam Environments

Richard L. Lanser

TENSION-COMPRESSION FATIGUE OF AN OXIDE/OXIDE CERAMIC MATRIX COMPOSITE AT ELEVATED TEMPERATURE IN AIR AND STEAM ENVIRONMENTS

THESIS
MARCH 2015

Richard L. Lanser, Captain, USAF

AFIT-ENY-MS-15-M-222

DEPARTMENT OF THE AIR FORCE
AIR UNIVERSITY

AIR FORCE INSTITUTE OF TECHNOLOGY

Wright-Patterson Air Force Base, Ohio

AFIT-ENY-MS-15-M-222

TENSION-COMPRESSION FATIGUE OF AN OXIDE/OXIDE CERAMIC MATRIX COMPOSITE AT ELEVATED TEMPERATURE IN AIR AND STEAM ENVIRONMENTS

THESIS

Presented to the Faculty

Department of Aeronautics and Astronautics

Graduate School of Engineering and Management

Air Force Institute of Technology

Air University

Air Education and Training Command

In Partial Fulfillment of the Requirements for the

Degree of Master of Science in Aeronautical Engineering

Richard L. Lanser, BS

Captain, USAF

March 2015

AFIT-ENY-MS-15-M-222

TENSION-COMPRESSION FATIGUE OF AN OXIDE/OXIDE CERAMIC MATRIX COMPOSITE AT ELEVATED TEMPERATURE IN AIR AND STEAM ENVIRONMENTS

Richard L. Lanser, BS
Captain, USAF

Committee Membership:

Marina B. Ruggles-Wrenn, PhD
Chair

Lt Col Chad E. Ryther, PhD
Member

Thomas G. Eason, PhD
Member

Abstract

Tension-compression fatigue behavior of an oxide-oxide ceramic matrix composite was investigated at 1200°C in air and steam environments. The composite is comprised of an alumina matrix reinforced with Nextel 720 alumina-mullite fibers woven in an eight harness satin weave. The composite relies on a porous matrix for damage tolerance and crack deflection rather than on a fiber coating or fugitive interphase. Compression and tension tests to failure were conducted to characterize the basic mechanical properties of the material. Tension-compression fatigue tests were performed under load control with a sinusoidal waveform at 1 Hz frequency with a ratio of minimum to maximum stress of -1. Maximum stresses ranged from 60 to 120 MPa. Fatigue run-out was defined as 10^5 cycles and was achieved in air at 80 MPa and in steam at 70 MPa. Retained tensile properties were measured for all specimens that achieved run-out. Specimens subjected to prior fatigue in air retained 100% of their tensile strength. The steam environment degraded material properties severely. Steam reduced fatigue lives by one order of magnitude and lowered tensile strength by 17 to 38%. Tension-compression fatigue lives were lower than published tension-tension fatigue lives by at least three orders of magnitude. In air, tension-compression fatigue was also shown to be more damaging than tensile or compression creep.

The post-test composites microstructure was examined. Failure mechanisms were identified and fracture surface morphologies were characterized. The dominant failure mode under tension-compression fatigue was fiber micro-buckling with characteristic compression curl morphologies found on fiber fracture surfaces. Shortened composite lives were associated with planar fracture surfaces and coordinated fiber failure due to loss of matrix porosity and increased fiber-matrix bonding.

Acknowledgments

First, I would like to sincerely thank my research advisor Dr. Marina Ruggles-Wrenn. The success of this endeavor was made possible due to her wealth of knowledge and her dedication to student learning and research excellence. I would also like to thank Mr. Larry Zawada (AFRL/RXCCP) for sponsoring this research and his continued AFIT support. I am very appreciative of Lt Col Chad Ryther, PhD (AFRL/ RXCCP) and Dr. Thomas Eason (AFRL/RQHF) for their contributions as thesis committee members. I owe a debt of gratitude to the AFIT machine shop for their prompt and professional service. Messrs. Chris Zickefoose, Matt Thomas, Jay Anderson, Barry Page, Wilber Lacy, and John Hixenbaugh are much appreciated for their management of and assistance with the AFIT lab equipment. As always, I want to thank my wife for her encouragement, love and support throughout this research effort.

Richard L. Lanser

Table of Contents

List of Figures

Page

List of Tables

Page

TENSION-COMPRESSION FATIGUE OF AN OXIDE/OXIDE CERAMIC MATRIX COMPOSITE AT ELEVATED TEMPERATURE IN AIR AND STEAM ENVIRONMENTS

I. Introduction

1.1 Motivation

Since the introduction of powered flight at the turn of the 20th century, there has been an ever present demand for improved flight performance. Today those demands include increased engine thrust, reduced weight, reduced fuel consumption, increased payload capacity, and lower emissions. In both military and civilian applications, the primary objectives can be summarized as increased performance and lower operating costs.

In the early 20th century many aircraft structures were made of wood and fabric. In later years, the wood and fabric were replaced with aluminum alloys as well as some steel and titanium alloys [1]. Incremental improvements in the properties of these alloys were achieved over several decades. These improvements included increased strength, fracture toughness, corrosion resistance, and damage tolerance [2]. These improvements in material properties allowed for drastic improvements in aircraft speed and maneuverability. Throughout this time, researchers continued to seek new materials for continued aircraft advancement. The material family which proved to become the next stepping stone was composites [1-2].

A composite material consists of at least two distinctly different phases (or constituents) and is designed such that the composite performance exceeds

those of its individual constituents. A typical composite consists of a relatively stiff and strong component called the reinforcement held together with a relatively soft and weak matrix. The reinforcement can take the form of small particles, discontinuous fibers, or continuous fibers [3]. To some extent, the material properties can be tailored to the application, making composites a very attractive choice for designers. Although composites have only recently become advanced enough for aircraft use, they have been around for centuries in various forms such as straw-reinforced clay brick or naturally occurring bone and wood [4]. Modern composites were seen as early as 1942 in the first fiberglass boat. At that time, composites made their debut into aircraft in the form of reinforced plastics for non-structural parts such as electrical components [3].

In the 1970's, composites were used in minor structural components such as radomes and fairings. Since then, composites have been used in aircraft primary structure in order to increase aircraft performance [5]. Relatively high strength, high stiffness, and low density of the composite materials result in structural improvements [2]. At present, rising fuel costs, increased pressure to reduce emissions, and continuing demand for increased performance has led to composites being used for nearly 80% of structure volume (or 50% by weight) in aircraft such as the Boeing 787 [5,6]. The insertion of composites into aircraft structure has recently seen exponential growth; in just the last 15 years, composite content in aircraft has increased by 25-35% [7].

In addition to the aircraft structural components, aircraft engines also can benefit from improved materials. The engine thrust can be increased and fuel consumption reduced by increasing turbine engine combustion temperatures [8]. However, maximum combustion temperatures are limited by the materials used in engine components. Higher combustion temperatures can be achieved through the use of improved materials and/or the introduction of cooling. Substantial gains in allowable combustion temperature have been made through the use of film-cooling and thermal barrier coatings (TBCs). Improvements in high-temperature performance of nickel and cobalt-based superalloys have provided for some combustion temperature increases. Recently, ceramic matrix composites (CMCs), capable of maintaining excellent strength and fracture toughness at elevated temperatures emerged as candidate materials for aerospace engine applications. The lower densities and higher use temperatures of the CMCs promise improved high-temperature performance when compared to conventional superalloys [8-10].

1.2 Problem Statement

The introduction of CMC materials into high-temperature aerospace applications offers performance improvements such as extended component life and reduced operating costs. Although composites have been used successfully in aircraft structures in low temperature environments, high temperature environments pose additional requirements on material properties and performance. For example, such basic mechanical properties as ultimate tensile

strength and fracture toughness can become significantly degraded at higher temperatures. Further, oxidation and other forms of material degradation such as phase changes or grain growth can become important factors at higher temperatures [11-13].

Research into these phenomena must be conducted in order to characterize the behavior of a material at the intended use temperatures. The testing should be performed in an environment which is characteristic of the intended operating environment. For example, turbine engine components can be simultaneously exposed to high temperatures and high concentrations of water vapor. Degrading effects of this severe operating environment on mechanical properties and performance of the material must be studied. Thorough understanding of the environmental durability of structural materials is critical to developing design guidance and life prediction methodologies, as well as to assuring structural integrity and long service life of components.

1.3 Research Objectives

An oxide/oxide CMC consisting of Nextel720 fibers in an alumina matrix is currently being considered for use in combustor liners of turbine engines. In this application, the CMC is likely to be subjected to fatigue spectra that include significant tensile and compressive loads. This research evaluates the tension-compression fatigue performance of the Nextel 720/alumina (N720/A) composite at 1200°C in air and in steam.

The performance of this composite system is particularly sensitive to the fiber-matrix interface which can be affected by the intended service environment. Of particular importance in this study are the failure mechanisms operating at elevated temperature in steam. Therefore, the tension-compression fatigue of N720/A is investigated at 1200 °C in laboratory air and in steam. Post-test examination of composite microstructure lends insight into the failure and damage mechanisms and their dependence on test environment.

Results of this study provide an experimental foundation for developing design envelopes for this material along with establishing its suitability for aerospace applications. Furthermore, developing a catalog of failure mechanisms and causes corresponding to specific fracture surface morphologies and microstructural changes is important for evaluating future in-service failures and recommending corrective actions. This research effort represents a major stepping stone towards significant advances in aerospace vehicle performance.

1.4 Methodology

a. Perform monotonic compression and monotonic tension tests at 1200°C in air to determine the ultimate tensile strength (UTS) and the ultimate compressive strength (UCS) of the test material.
b. Characterize the composite microstructure and fracture surfaces produced in monotonic tension and in monotonic compression tests using an optical microscope and a scanning electron microscope (SEM).

c. Perform tension-compression fatigue tests at 1200 °C in laboratory air and in steam. All fatigue tests are performed in load control at a frequency 1.0 Hz with an R ratio (ratio of minimum stress to maximum stress) of -1.
d. Characterize the composite microstructure and fracture surfaces produced in the tension-compression fatigue tests using an optical microscope and SEM.
e. Compare the results of the tension-compression fatigue tests to the tension-tension fatigue and compression creep results previously obtained at AFIT for N720/A at 1200°C in air and in steam.
f. Identify damage mechanisms and determine failure causes under tension-compression fatigue in the characteristic environmental service conditions.

II. Background

2.1 Ceramics

Ceramic materials are defined as inorganic and typically non-metallic materials which are generally processed at high temperatures [12]. Ceramics are mainly crystalline with amorphous glass being considered a subset of ceramics [12, 14]. These materials have been manufactured and used by humans since as early as 24,000 BC with traditional uses including bricks, pottery, tiles, and art pieces [14]. Today, advanced modern ceramics are usually compounds formed between metallic and non-metallic elements [14]. These advanced ceramics include oxides, nitrides and carbides of silicon, aluminum, titanium, and zirconium [12].

One of the most important properties of ceramics is their ability to sustain high temperatures. As shown in Figure 1 below, maximum use temperatures for ceramics are significantly higher than those for polymers or metals [12]. Because of this, ceramics have long been used as thermal barriers for high-temperature furnaces, troughs, and ladles used in the manufacture of metal alloys such as steel [14]. They have even been used in extreme applications such as the thermal barrier on NASA's space shuttle where temperatures as high as 1600°C can be reached during re-entry [14]. Further, ceramics offer high resistance to chemicals (corrosion), abrasion, and wear [12]. They also have relatively high strength, hardness, and stiffness combined with low density [12]. As shown in Figure 2, at operational temperatures at or above 900°C, ceramic materials have

significantly higher strength to weight ratios than several other advanced aerospace materials [15]. It is these qualities that make ceramics candidate materials for advanced aerospace applications operating in high temperature environments.

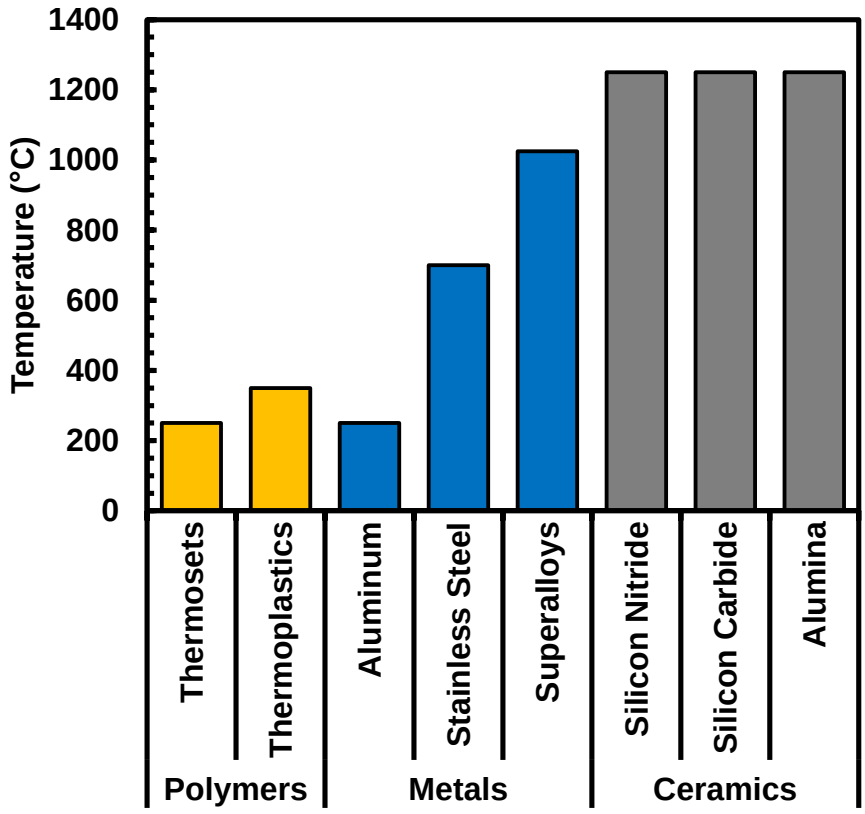

Figure 1: Comparison of maximum use temperatures for polymers, metals and ceramics. After Chawla [12].

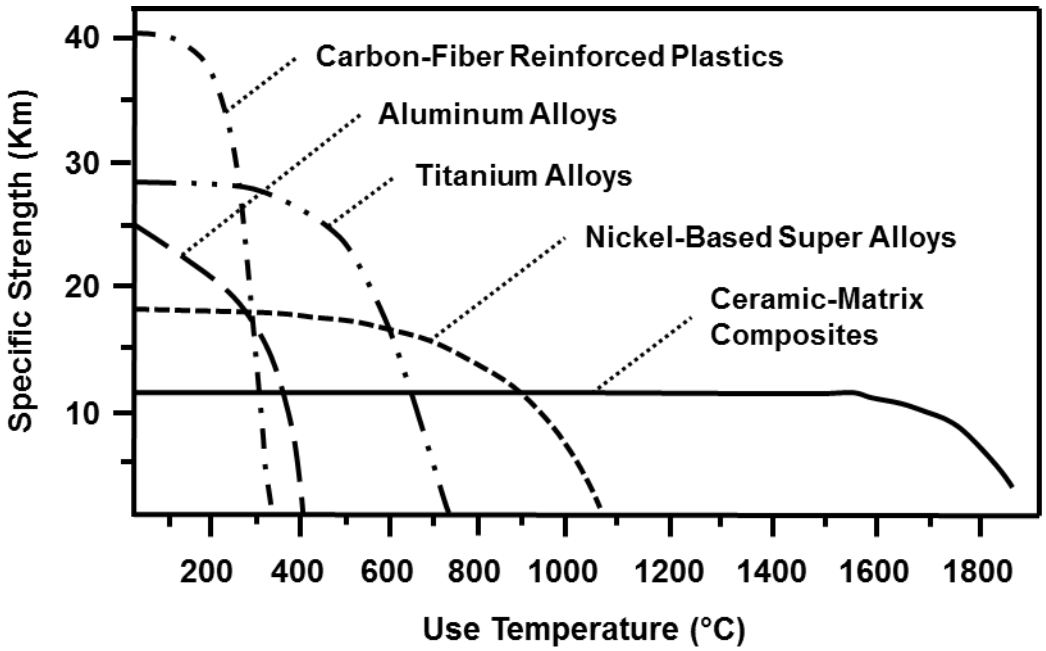

Figure 2: Comparison of strength to weight ratios of several materials at various use temperatures. After Schmidt [15].

However, monolithic ceramics are exceptionally brittle having low fracture toughness and almost no inelastic strain (ductility) [11, 12]. This quality yields poor performance under tensile, impact, and thermal shock loading [12]. Even worse, low fracture toughness and the lack of ductility or plasticity results in catastrophic failure without warning [12].

In the 1960's, a monolithic ceramic was developed to exhibit some 'ductile' behavior by inducing plasticity. However, the material still failed to achieve increased fracture toughness resulting in overall poor performance as a structural material [11]. Later research efforts in this area shifted towards increasing fracture toughness of monolithic ceramics [11]. Although some advancement was made, the materials remained macroscopically linear-elastic, meaning strain

concentrations remained and loads would not redistribute [11]. Therefore, the resulting material would still fail catastrophically without warning. A new path was needed for development of an improved high temperature structural material.

2.2 Ceramic Matrix Composites

Typically, the goal of composites is to produce a material which is stronger than its individual constituents or to harness the high strength of the fibers. This is usually accomplished by combining high strength fibers with a relatively low modulus matrix. Thus, the high strength of the fibers can be harnessed through efficient load transfer made possible by a strong bond between the matrix and fibers [12]. The matrix also provides lateral support to the fibers creating compression stability which the fibers lack on their own. The typical ratio of fiber modulus to matrix modulus in polymer matrix composites (PMC) and metal matrix composites (MMC) can vary from 10 to 100 [12].

However, these norms change with high temperature ceramics. Ceramics generally have high strength and compression stability to begin with. What they lack is fracture toughness, damage tolerance, and what is sometimes referred to as a graceful failure where the material exhibits some macro deformation allowing for load redistribution [12]. The goal behind CMC materials is to overcome these shortcomings of monolithic ceramics.

To achieve this end, ceramic materials are made into fine fibers and combined with a ceramic matrix material to form a CMC. However, the key to

producing a CMC with the superior high temperature properties of ceramics while achieving damage tolerance, fracture toughness, and graceful failure lies in the interface between the matrix and fiber [11-13]. If the interface or bond between the fibers and matrix is allowed to be too strong, the result would be a CMC with poor fracture toughness and damage tolerance similar to that of a monolithic ceramic material. This is because unlike PMC and MMC materials, CMC materials typically have ratios of fiber modulus to matrix modulus of around 1 so cracks would tend to initiate in the matrix and propagate straight through the fibers thus producing macroscopic brittle behavior similar to that of monolithic ceramics. Such crack growth behavior is schematically depicted in Figure 3 [12]. On the other hand, if the interface is too weak, there will be insufficient load transfer between the matrix and fibers [11].

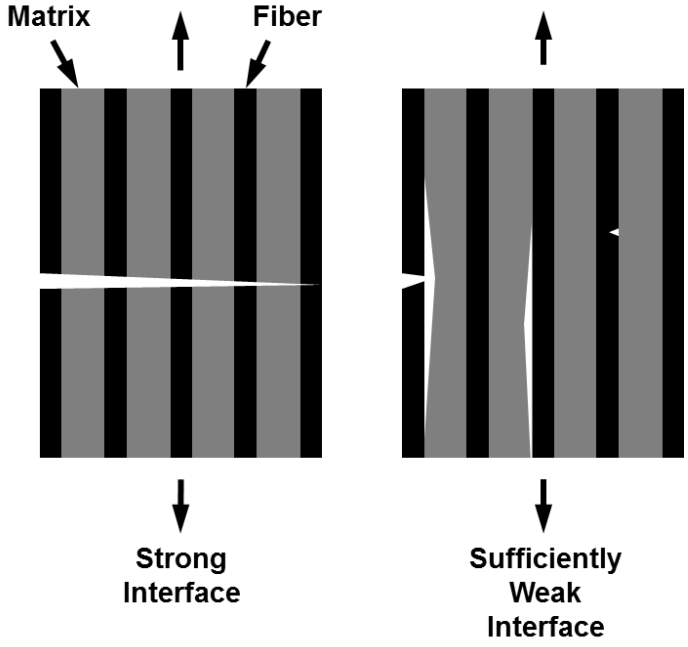

Figure 3: Representative crack growth behavior of CMC with strong interface (left) and sufficiently weak interface (right). After Chawla [12].

Controlling the bond strength of the interface achieves fracture toughness and damage tolerance primarily by means of increasing the energy required for fracture or energy dissipation [12-13]. This increase is the result of several factors. As a crack is propagating through the matrix, it will deflect around the fibers due to the relatively weak interface as depicted in Figure 3. Interface control also serves to decouple the fibers allowing fiber failures to become uncorrelated [12]. Also, with fibers fracturing along several various planes within the material (uncorrelated fracture), the matrix-fiber interface can begin to debond in the region of the matrix cracking. This leads to fibers bridging the matrix crack as strains increase followed by fiber pull-out. Each of these events dissipate additional energy resulting in a CMC which fails gracefully and exhibits increased fracture toughness and damage tolerance compared to monolithic ceramics [11-13].

Researchers and developers of CMC materials have achieved improved damage tolerance in two primary ways. The first CMC design philosophy relies on a weak fiber/matrix interface which is achieved either through the use of fiber coatings to directly control the interface properties or through the use of a fugitive interphase that is eliminated during processing. The fiber coating method has been successfully used with several materials such as silicon carbide fiber - silicon carbide matrix (SiC/SiC) CMCs with carbon and boron nitride fiber coatings [12].

The second method relies on a matrix with a controlled level of porosity. This microstructural design philosophy accepts the strong fiber/matrix interface, while encouraging crack deflection around fibers and into the exceptionally weak porous matrix [12-13]. The porous-matrix method of CMC toughening is generally used in oxide fiber – oxide matrix (oxide/oxide) CMC materials such as the Nextel 720/A studied in this research effort. This method of CMC toughening reduces manufacturing costs considerably as compared to fiber coatings typical of dense-matrix CMCs such as SiC/SiC materials [16]. Figure 4 illustrates the crack propagation mechanisms for the weak fiber/matrix interface concept and for the porous matrix concept [16].

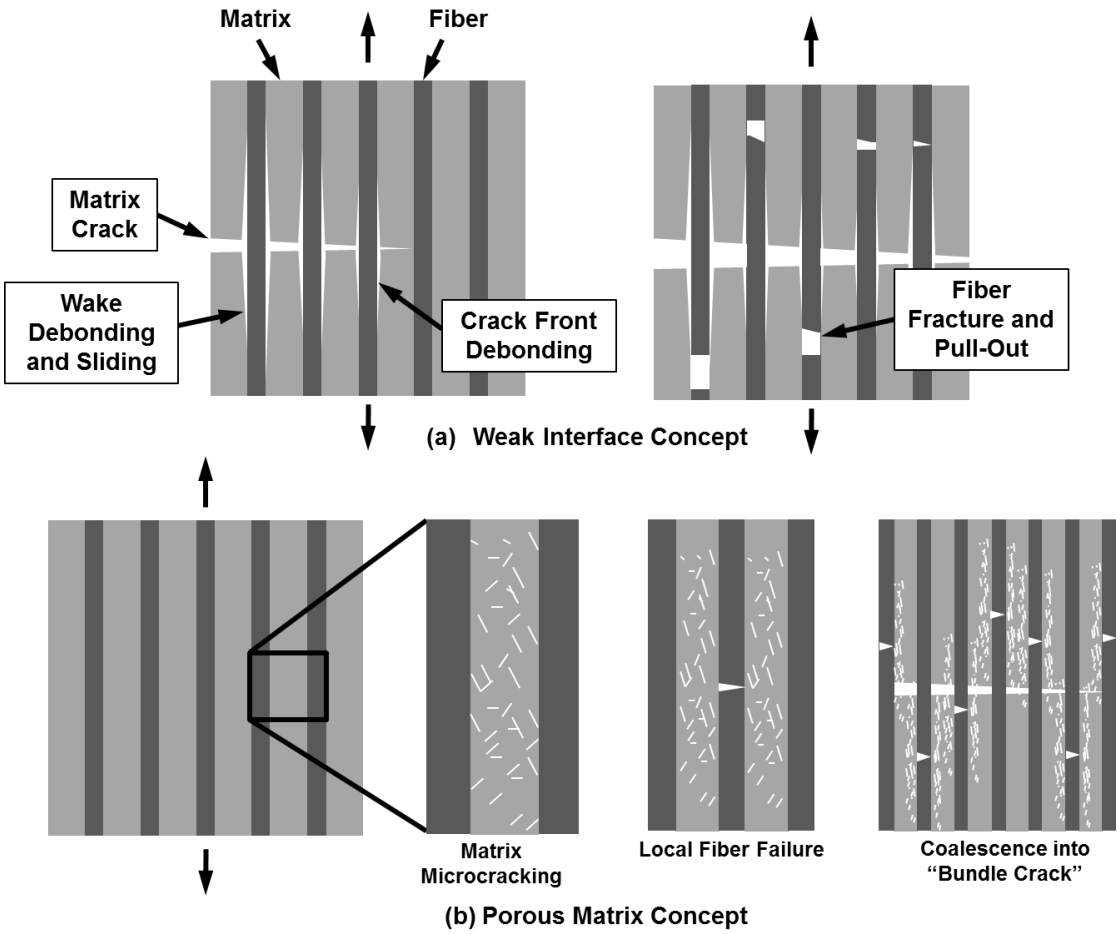

Figure 4: Illustration of two primary concepts used to achieve damage tolerance in CMCs. After Zok [16].

Controlled matrix porosity in oxide/oxide CMCs is typically achieved in one of two ways. Either a fine particulate ceramic powder is partially sintered or pyrolysis of a ceramic precursor creates the necessary porous matrix. Because neither of these processes is particularly practical with non-oxide CMC matrix materials, the porous matrix method is mainly used for oxide/oxide CMC materials [16]. In fact, the porous matrix concept was created through necessity rather than in an attempt to improve upon the weak fiber/matrix interface method.

The driver behind the porous matrix concept was the lack of fiber coatings suitable for use with oxide fibers [16].

The intended applications of CMC material systems generally include high temperatures and elevated levels of moisture such as in turbine engines. This results in a highly oxidizing environment. For this reason, thermodynamically stable constituents are desirable in CMCs. Considerable interest has been shown in oxide/oxide CMCs such as Nextel 720/A despite its lower strength and temperature capabilities compared to SiC/SiC CMCs [12]. This interest is due to the inherently increased thermo-oxidative stability of oxides over silicon carbide and other non-oxide materials. In fact, it is the inherent stability of oxides in oxidizing environments which originally motivated the development of oxide/oxide CMCs in order to meet the service longevity demands for current and future aerospace applications [16].

2.3 Previous Research

The chemical composition of the Nextel 720 fiber is 85% Al_2O_3 and 15% SiO_2 by weight. The crystalline phases of the Nextel 720 fiber are α-Al_2O_3 and mullite. An extensive review of the mechanical properties of Nextel 720 and other Nextel ceramic oxide fibers is given by Wilson and Visser [17]. The following properties were reported for the Nextel 720 fibers: density of 3.4 g/cc, thermal expansion coefficient of 6.0 ppm/°C for a temperature range of 100-1100°C, room temperature tensile strength of 2.1 GPa, and room temperature tensile modulus of 260 GPa. A Nextel 720 multi-filament strand was shown to retain 85% of its

tensile strength with a displacement rate of 12.5 mm/min with a 250 mm gauge length at 1400°C and over 95% at 1200°C. Nextel 720 is the most creep resistant among the commercially available oxide fibers. At 1100°C and 100 MPa the Nextel 720 fiber produced a low creep rate of $1x10^{-10}$/s.

Ruggles-Wrenn et al [18] studied the effect of loading rate on Nextel 720/A CMC at 1200°C in air. At a low loading rate (0.0025 MPa/s), initial strain rates were negative due to matrix densification (reduction in matrix porosity). The loss of matrix porosity combined with diffusion creep at elevated temperatures resulted in higher failure strains, and lower ultimate tensile strengths (UTS) compared to those obtained with loading rate of 25 MPa/s. Samples loaded at 25 MPa/s had UTS values of 181 MPa and failure strains of 0.36%, while the samples loaded at 0.0025 MPa/s had average UTS values of 154 MPa with failure strains ranging from 0.73% to 1.06%.

Ruggles-Wrenn and co-workers [19-21] investigated the tension-tension fatigue behavior of Nextel 720/A CMC at elevated temperatures in air and in steam. The following basic properties were obtained in tensile tests performed at 1200°C with displacement rate of 0.05 mm/s: UTS of 190 MPa, elastic modulus of 76 GPa, and failure strain of 0.38%. At 1200°C in air, the fatigue limit of 170 MPa (88% UTS) based on the fatigue run-out condition of 10^5 cycles was obtained at both 0.1 and 1 Hz. The presence of steam caused a significant reduction in the fatigue performance. In steam at 1200°C, the fatigue limit was 125 MPa (65% UTS) at the frequency of 1 Hz. In steam, the fatigue performance

degraded dramatically when the frequency was decreased to 0.1 Hz; the fatigue run-out was not achieved even at a low fatigue stress of 75 MPa (39% UTS). Increasing the fatigue frequency to 10 Hz in steam at 1200°C resulted in a fatigue limit of 150 MPa (79% UTS) with a run-out of 10^6 cycles. The resulting conclusion was that time at temperature in steam was significantly more damaging than the separate effects of fatigue loading and steam environment. Severe degradation of fatigue performance at a low frequency in steam was attributed to several factors including silicon species migration from the fiber to the matrix (fiber property degradation), matrix densification (loss of damage tolerance), and creep damage to the fibers. The improved fatigue performance at increased frequencies was attributed to the progressive breaking up of the matrix during cyclic loading which counteracted matrix densification and served to maintain the necessary level of matrix porosity. In order to keep up with the densification rate, the fatigue frequency had to be sufficiently high. This conclusion was supported by examination of fracture surfaces under scanning electron microscope (SEM). Imaging revealed coordinated fiber failures associated with fatigue at lower frequencies or longer hold times at maximum stress. These findings have been supported by additional investigation of creep performance of the Nextel 720 CMC [22-29].

Prior research at AFIT also investigated the mechanical behavior of SiC/SiC CMCs at elevated temperatures in air and in steam [30-33]. Unlike the oxide/oxide CMC, SiC/SiC composite exhibited reduced tension-tension fatigue

performance with increasing fatigue frequency at 1200°C. As in the case of the oxide/oxide CMC, the presence of steam significantly degraded the fatigue performance of SiC/SiC composite. In the case of the SiC/SiC composite, the primary damage mechanism operating in tension-tension fatigue was oxidation embrittlement of the fibers. Matrix cracks formed during initial cycles allowed the ingress of oxygen into the composite interior where it attacked the boron nitride fiber coating and the oxidation-prone fibers. The degraded fibers were fused together, then failed in a coordinated fashion in the regions of oxidation embrittlement. To combat oxidation, a multilayered self-healing matrix is typically used in SiC/SiC CMCs. This self-healing matrix fills matrix cracks through the formation of glass phases at high temperatures preventing further degradation of the composite. As a result, the composite exhibits relatively good creep performance at high temperatures in oxidizing environments. However, high frequency fatigue loading causes extensive matrix cracking at high rates beyond the self-healing matrix capabilities resulting in environment infiltration and oxidation embrittlement.

At 1200°C in steam, fatigue performance of a SiC/SiC composite with a self-healing matrix was further reduced when compression was introduced into the fatigue cycle. As under tension-tension fatigue loading, matrix cracking occurred along planes normal to the loading. However, under tension-compression fatigue loading, additional cracking also occurred along planes parallel to the loading direction. Additional rapid crack initiation and growth permitted significant

additional environmental attack on the composite interior, which overwhelmed the self-healing capability of the matrix and led to oxidation embrittlement of the composite. As a result, tension-compression fatigue performance was considerably reduced compared to that under tension-tension fatigue.

III. Material and Test Specimen

3.1 Material

The material tested in this research effort was Nextel^{TM} 720/Alumina (N720/A), an oxide-oxide ceramic composite consisting of a porous alumina matrix reinforced with N720 fibers. There is no fiber coating. The damage tolerance of the N720/A CMC is enabled by the porous matrix. The composite was manufactured by COI Ceramics, Inc. and supplied in a form of 5.76-mm thick panels comprised of 24 0/90 plies woven in an eight harness satin weave (8HSW). Table 1 lists the physical properties of the composite panel as reported by COI.

Table 1: Reported physical properties of N720/A composite panel.

Density (g/cm^3)	Fiber Volume (%)	Matrix Volume (%)	Open Porosity (%)
2.84	44.2	33.5	22.3

The N720 fibers consist of 85 wt.% Al_2O_3 and 15 wt.% SiO_2 with crystalline phases composed of alpha alumina and mullite. The alpha alumina phase is generally elongated grains less than 0.1 μm in size. Also present are larger crystals of mullite and alpha alumina. These can be as large as 0.5 μm [34].

Table 2 [35] summarizes some additional properties of N720 fibers and other similar oxide fibers. The N720 fibers have a relatively large (55-60%) volume of mullite. As a result, the density of N720 fiber is 13% less than that of N610 fiber. Additionally, large mullite content reduces the thermal expansion coefficient of

the N720 fiber by nearly 30% compared to those of the N610 fibers. These properties make N720 fibers particularly suitable for aerospace applications with thermal loading [35].

Table 2: Properties of N720 and similar oxide fibers [35].

Property	Nextel™ 720	Nextel™ 610	Nextel™ 650
Composition (% by weight)	85 - Al_2O_3 15 - SiO_2	>99 - Al_2O_3	89 - Al_2O_3 10 - ZrO_2 1 - Y_2O_3
Crystalline Phases	α- Al_2O_3 + mullite	α- Al_2O_3	α- Al_2O_3 + cubic ZrO_2
Filament Diameter (μm)	10-12	10-12	10-12
Tensile Strength (GPa)	2.1	3.3	2.5
Modulus (GPa)	260	373	358
Density (g/cc)	3.4	3.9	4.1
Thermal Expansion (ppm/ºC)	6.0	7.9	8.0

3.2 Test Specimen Geometry

Because compressive loading, and thus the potential for buckling failure modes, was involved in the fatigue cycle type, specimens with hourglass-shaped gage section were used in this work. The stress concentration inherent in an hourglass specimen was assessed. Finite element analysis of the specimen conducted by Oak Ridge National Laboratory shows that the axial stress at the edges in the middle of the hourglass section is about 3.5% higher than the average axial stress [36]. Note that hourglass specimens have been used successfully in tension-compression fatigue testing of polymer matrix composites [37]. The 5.76-mm thick composite panel was cut into 26 specimens according to

specifications shown in Figure 5. The 0º fibers were aligned with the specimen axis.

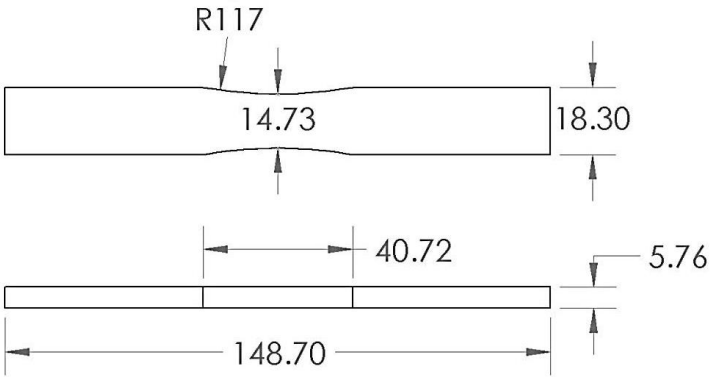

Figure 5: Test specimen drawing and dimensions (mm).

Before testing each specimen was fitted with 19 mm x 25 mm x 3.2 mm tabs of 6061-T6 aluminum alloy in order to protect the specimen surface from damage and to evenly distribute the loads from the hydraulic grips. Tabs were bonded to the gripping sections of the specimens using M-Bond 200 cyanoacrylate adhesive. Figure 6 shows a specimen with aluminum tabs attached.

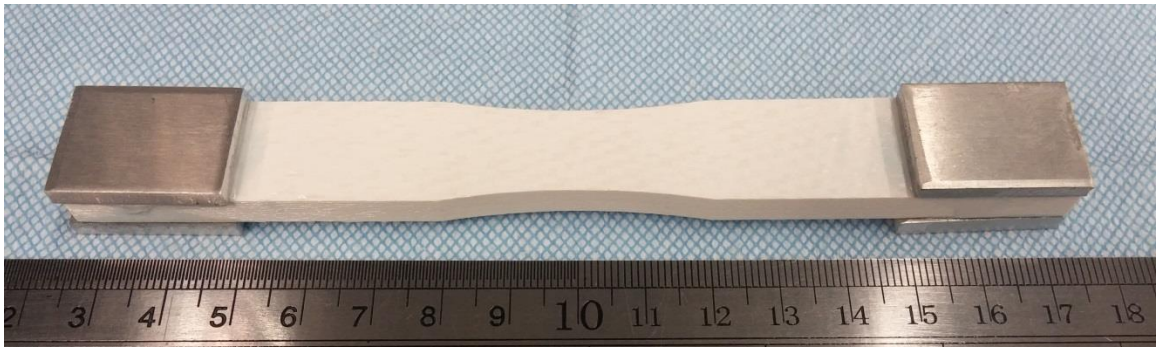

Figure 6: Specimen with aluminum alloy tabs attached (scale major units are cm).

The narrowest part of the gauge section of each specimen was measured using Mitutoyo Corporation Digital Calipers. The resulting dimensions are

reported in Table 3 along with the corresponding specimen number and specimen designation provided by COI.

Table 3: Specimen gauge section measurements.

COI Specimen Designation	Specimen Number	Thickness (mm)	Width (mm)	Area (mm^2)
14-247	1	5.70	14.70	83.8
14-248	2	5.70	14.91	85.0
14-249	3	5.72	14.70	84.1
14-250	4	5.84	14.70	85.8
14-251	5	5.75	14.72	84.6
14-252	6	5.64	14.70	82.9
14-253	7	5.75	14.69	84.5
14-254	8	5.77	14.71	84.9
14-255	9	5.79	14.71	85.2
14-256	10	5.73	14.70	84.2
14-257	11	5.73	14.70	84.2
14-258	12	5.74	14.72	84.5
14-259	13	5.80	14.83	86.0
14-260	14	5.70	14.72	83.9
14-261	15	5.80	14.72	85.4
14-262	16	5.76	14.72	84.8
14-263	17	5.73	14.71	84.3
14-264	18	5.75	14.71	84.6
14-265	19	5.78	14.74	85.2
14-266	20	5.81	14.71	85.5
14-267	21	5.74	14.70	84.4
14-268	22	5.77	14.71	84.9
14-269	23	5.80	14.72	85.4
14-270	24	5.83	14.72	85.8
14-271	25	5.74	14.74	84.6
14-272	26	5.76	14.79	85.2

IV. Experimental Procedures

4.1 Mechanical Testing and Environmental Control Equipment

An MTS Systems Corporation model 810 servo hydraulic testing system was used for mechanical testing (Figure 7). An MTS FlexTest 40 digital controller with MTS Station Manager and Multi-Purpose Testware was used for input signal generation and for data collection. Test data was stored on the desktop computer and processed using Microsoft Excel.

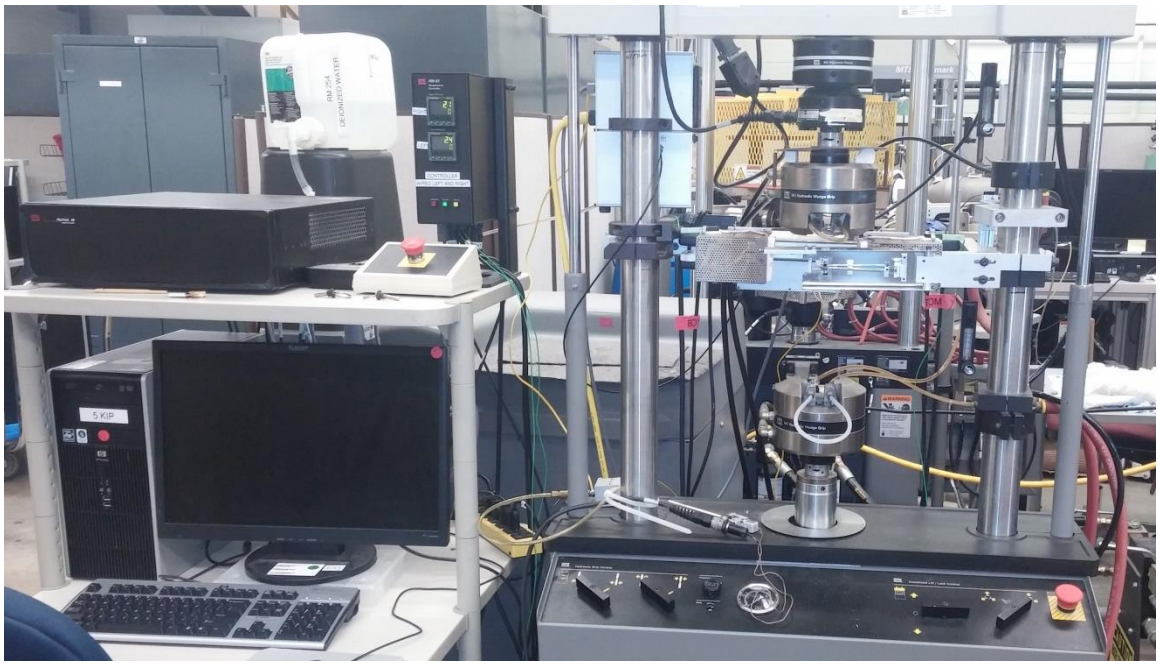

Figure 7: MTS Systems Corporation Model 810 Servo Hydraulic Testing System.

An MTS model number 661.19E-04 force transducer with a 25 kN load capacity was used for load measurement. MTS model 647.02B-03 water-cooled hydraulic wedge grips with a dynamic load capacity of 25 kN were employed in all tests. A Neslab refrigerated recirculator, model RTE-7 was used to cool the

grip wedges with recirculated 15°C deionized water. Strain measurements were taken using an MTS model 632.53E-14 high temperature low contact force extensometer with a 12.5–mm gage length (Figure 8).

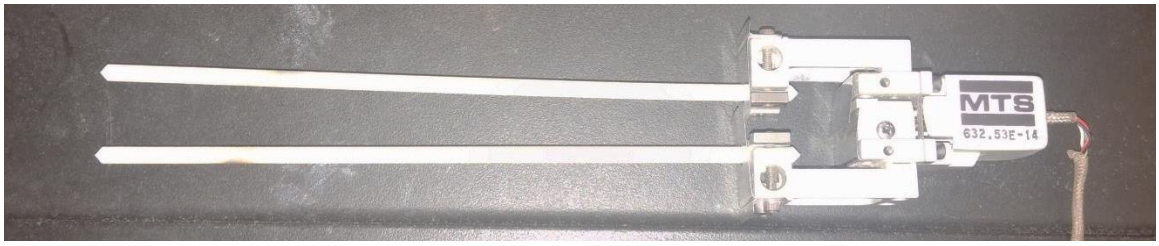

Figure 8: Extensometer.

An AMTECO Hot-Rail two-zone resistance-heated furnace and two MTS model 409.83B temperature controllers were used for high temperature testing (see Figure 9 and Figure 10). The temperature controllers use non-contacting control thermocouples exposed to the ambient oven environment near the test specimen.

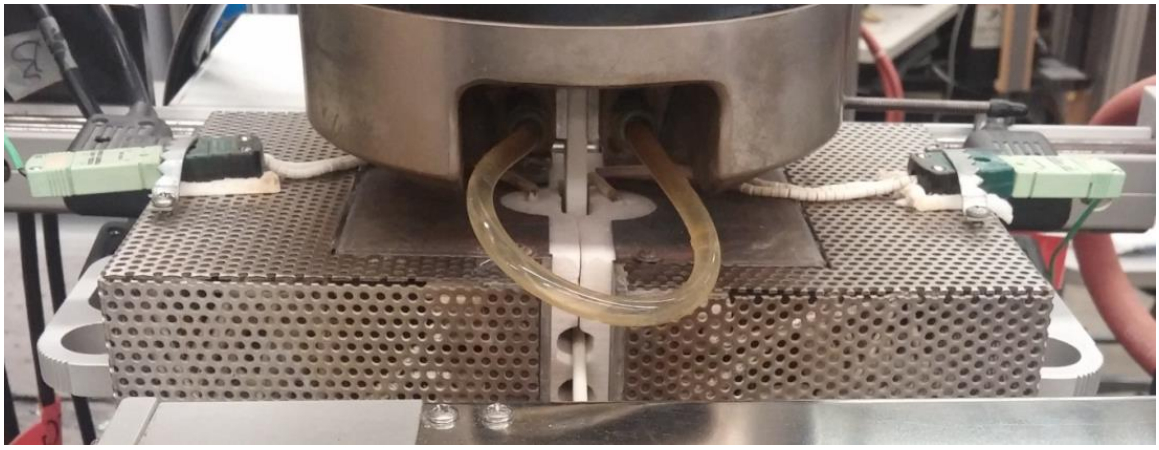

Figure 9: Furnace closed around test specimen mounted in grips.

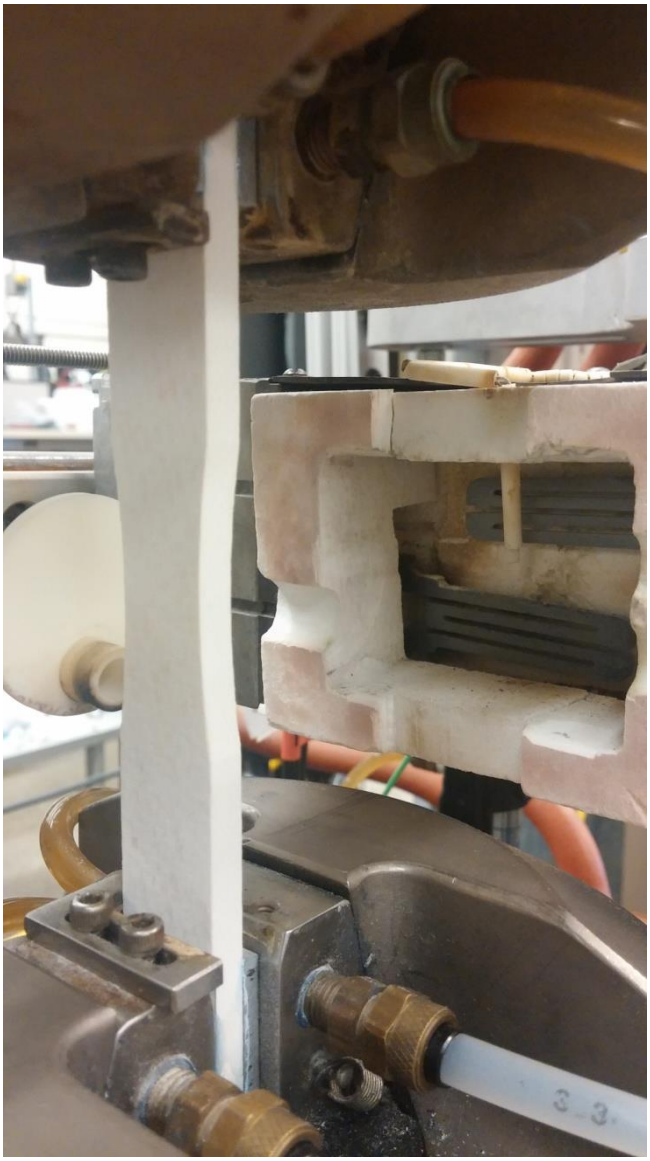

Figure 10: Right side furnace heating elements and controller thermocouple.

The furnace was calibrated on a periodic basis. To accomplish the calibration, a specimen was instrumented with R-type thermocouples connected to an Omega HH501BR hand-held digital thermometer for temperature read-out. The temperature inside the furnace was raised to 900°C at a rate of 1°C/s, then slowly increased until the specimen temperature (as monitored by the R-type

thermocouples) reached 1200°C. The furnace controllers were adjusted to determine the settings needed to achieve the desired 1200°C temperature of the test specimen. The determined settings were then used in actual tests. The power settings for testing in steam were determined by placing the specimen instrumented with thermocouples in steam environment and repeating the furnace calibration procedure.

To achieve a more uniform and repeatable temperature distribution along the specimen gage section, a cylindrical alumina susceptor was used in all tests. The susceptor fits inside the furnace, specimen gage section is located inside the susceptor, with the ends of the specimen passing through slots in the susceptor (see Figure 11). For testing in steam, steam was supplied to the susceptor through a feeding tube in a continuous stream with a slightly positive pressure, expelling the dry air and creating a near 100% steam environment inside the susceptor. An AMTECO Chromalox model HRFS-STMGEN steam generator and deionized water were used to produce steam.

Figure 11: Alumina susceptor.

4.2 Testing Procedures

4.2.1 Monotonic Tension and Monotonic Compression Tests

In all tests, a specimen was heated to 1200°C at 1°C/min, and held at temperature for 30 min prior to testing. Monotonic tension and monotonic compression tests were performed at 1200°C in laboratory air in order to determine basic tensile and compressive properties. The tension and compression tests to failure were conducted in displacement control with a

displacement rate of 0.05 mm/s. The test specimens were gripped in the testing machine using a 16 MPa grip pressure. Force, strain, displacement, displacement command, temperature, temperature command and time were recorded during the specimen heat-up as well as during the actual test.

4.2.2 Tension-Compression Fatigue Tests

In all tests, a specimen was heated to 1200°C at 1°C/min, and held at temperature for 30 min prior to testing. The same procedures were used for testing in air and in steam. Tension-compression fatigue tests were performed in load control with an R ratio (minimum to maximum stress) of -1.0 at 1.0 Hz. Fatigue run-out was defined as 10^5 cycles. This cycle count represents the number of loading cycles expected in aerospace applications at that temperature. Force, force command, strain, displacement, temperature, temperature command, cycle number and time were recorded in all tests. Peak and valley data were collected for each cycle. Full cycle data were collected for the first 25 cycles, every 10 cycles for cycles 30-100, every 100 cycles for cycles 100-1,000, every 1,000 cycles for cycles 1,000-10,000, and every 10,000 cycles for cycles 10,000-100,000. To assess the effect of steam environment on tension-compression fatigue performance all fatigue tests were performed in air and in steam. For testing in steam, the thermal soak was extended to 45 min allowing additional time to stabilize the steam environment ensuring an even temperature distribution. All specimens that achieved run-out were subjected to tensile test to

failure at 1200°C in laboratory air immediately following the fatigue test to determine the retained strength and stiffness.

4.3 Microstructural Characterization

Prior to testing all specimens were examined with an optical microscope in order to identify and document any defects. A Zeiss Discovery.V12 stereo optical microscope with a Zeiss PlanApo S 0.63x FWD 81-mm lense was used to image the specimens (Figure 12). Images were captured using a Zeiss AxioCam HRc digital camera. Image processing was carried out with AxioVision 4.8 software. Fracture surfaces of failed specimens were examined using a scanning electron microscope (FEI Quanta 450) as well as an optical microscope (Zeiss Discovery V12). The scanning electron microscope is shown in Figure 13.

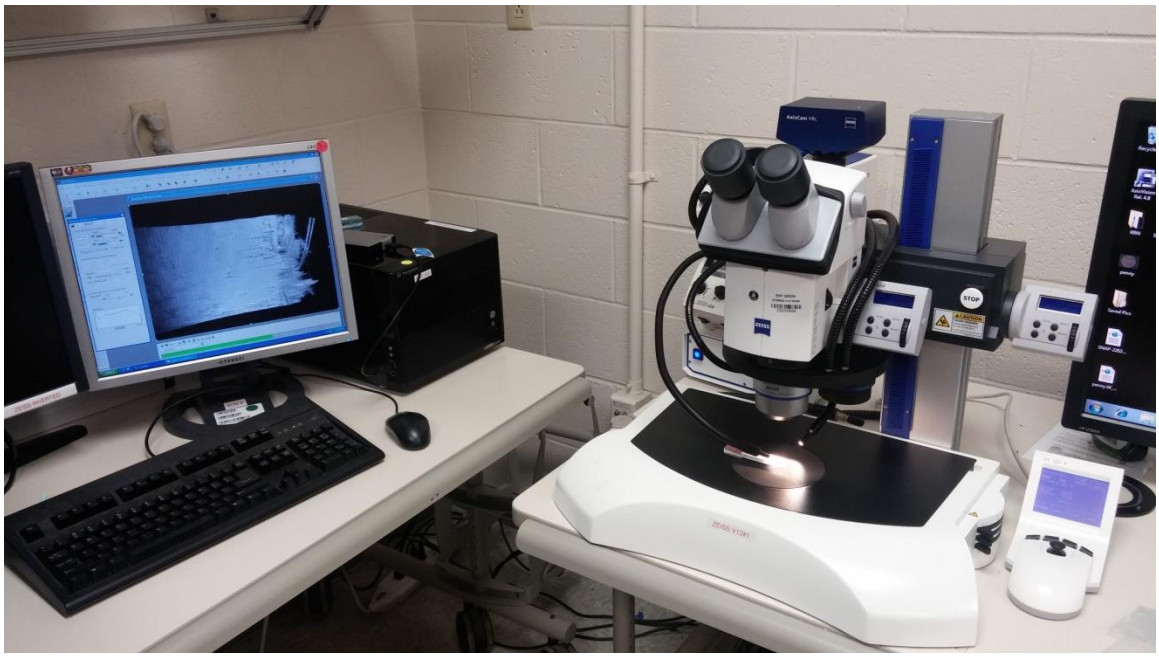

Figure 12: Zeiss Discovery.V12 stereo optical microscope.

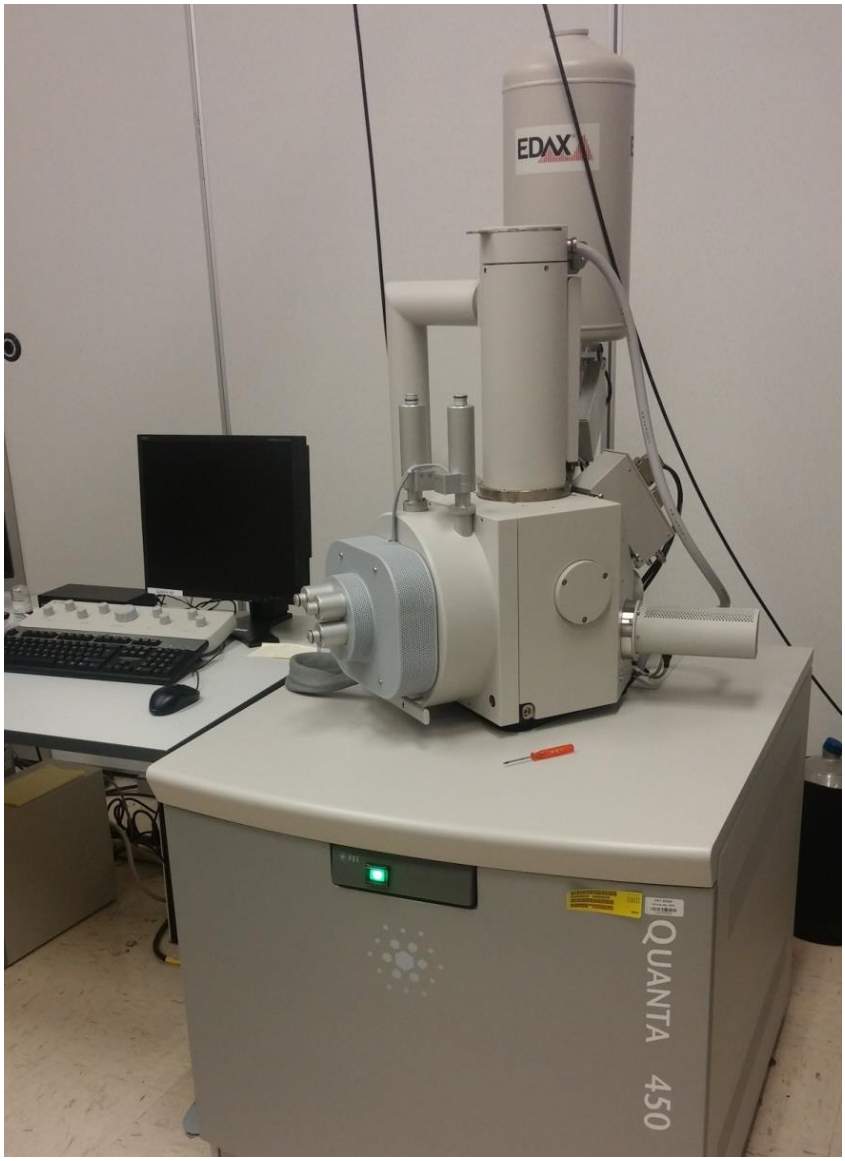

Figure 13: Quanta 450 scanning electron microscope (SEM).

For examination with an SEM the fractured portions of the specimens were cut normal to the loading direction using a Buehler IsoMet 5000 linear precision saw with a diamond abrasive cutting wheel (Figure 14). The blade speed was set to 2500 rpm with a feed rate of 10 mm/min. No cutting fluid was used in order to prevent specimen contamination.

Figure 14: Buehler IsoMet 5000 linear precision saw.

V. Results and Discussion

5.1 Thermal Expansion

All tests were conducted at 1200°C. In all tests, a specimen was heated to 1200°C at 1°C/min, and held at temperature for 30 min prior to testing (45 min for testing in steam). Strain and temperature were recorded during the specimen heat-up and the thermal soak period. These results were used to calculate the coefficient of linear thermal expansion, α, as

$$\alpha = \frac{\varepsilon}{\Delta T} \quad \textbf{(1)}$$

Here ε is the thermal strain produced during heating from T_0 = 23°C to T_1 = 1200°C and $\Delta T = T_1 - T_0$. The thermal strains and corresponding coefficients of linear thermal expansion obtained for N720/A in this study are summarized in Table 4.

Table 4: Thermal strains obtained for N720/A during temperature rise from 23°C to 1200°C and corresponding coefficients of linear thermal expansion.

Specimen Number	Thermal Strain (%)	Coefficient of Linear Thermal Expansion (ppm/°C)
1	0.84	7.1
2	0.80	6.8
3	0.83	7.0
4	0.81	6.9
5	0.83	7.0
6	0.86	7.3
7	0.85	7.3
9	0.85	7.2
10	0.83	7.0
11	0.83	7.0
12	0.79	6.7
14	0.77	6.5
16	0.83	7.0
17	0.82	7.0
21	0.76	6.4
22	0.76	6.5
23	0.77	6.6
24	0.75	6.4
25	0.76	6.4
26	0.77	6.5
Mean	0.80	6.8
Standard Deviation	0.035	0.30
Coefficient of Variation	4.4%	

Thermal expansion results obtained in this work are compared with those from prior research in Table 5. Coefficients of linear thermal expansion for N720/A composite are compared to those of the composite constituents in Table 6.

Table 5: Thermal strains obtained for N720/A during temperature rise from 23°C to 1200°C and corresponding coefficients of linear thermal expansion. Comparison of results from current work and previous research efforts [38-42].

Author	Number of Tests	Mean Thermal Strain (%)	Thermal Strain Standard Deviation (%)	Coefficient of Linear Thermal Expansion (ppm/°C)
Mehrman [38]	16	0.90	0.072	7.6
Hetrick [39]	7	0.89	0.029	7.6
Eber [40]	6	0.86	0.031	7.3
Harlan [41]	12	0.80	-	6.8
Current Research	20	0.80	0.035	6.8
Boyer [42]	10	0.73	0.014	6.2

Table 6: Thermal expansion coefficients (ppm/K) of N720/A and constituent materials [12, 43, 44].

Author	Alumina	Mullite	N720 fiber	N720/A
Chawla [12]	7-8	5.3	-	-
COI [43]	-	-	-	6.0
Bansal [44]	8.1	5.0	6.0	3.5 (room temp), 6.2 (1000°C)

Data presented in Table 5 and Table 6 demonstrate that the thermal expansion results produced in this work are consistent with the results of prior research performed at AFIT. The material manufacturer (COI) has reported a typical thermal expansion coefficient of 6.0 ppm/°C for N720/A [43]. This is somewhat lower than what was found in this research effort and reported by others [38-42]. However, Bansal [44] found that the thermal expansion coefficient of N720/A can vary significantly with temperature; specifically 3.5 ppm/°C at room temperature and 6.2 ppm/°C at 1000°C. The N720/A constituents, namely alumina and mullite, have also been known to exhibit non-linear thermal expansion coefficients with respect to varying temperatures [12].

5.2 Monotonic Tension and Monotonic Compression

To establish the baseline tension and compression properties, the N720/A specimens were tested in tension to failure and in compression to failure at 1200°C in air. The results are summarized in Table 7, where elastic modulus, strength, and failure strain are presented for both tension and compression. In all tensile tests the modulus of elasticity was calculated in accordance with the procedure in ASTM standard C 1359 as the slope of the tensile stress-strain curve within the linear region. The same method was employed to calculate the modulus of elasticity in compression tests.

Table 7: Summary of basic tensile and compressive properties for N720/A ceramic composite obtained in displacement controlled tests performed at 0.05 mm/s at 1200°C.

Specimen Designation	Ultimate Strength (MPa)	Elastic Modulus E (GPa)	Failure Strain (%)
Tensile Properties			
1	192	69	no data
2	204	67	no data
3	203	66	0.58
4	200	64	0.58
Average	200	67	0.58
Compressive Properties			
5	142	68	-0.31

Typical tensile and compressive stress-strain curves are shown in Figure 15. The decreasing modulus of the stress strain curves is attributed to continuous matrix micro-cracking during loading [43].

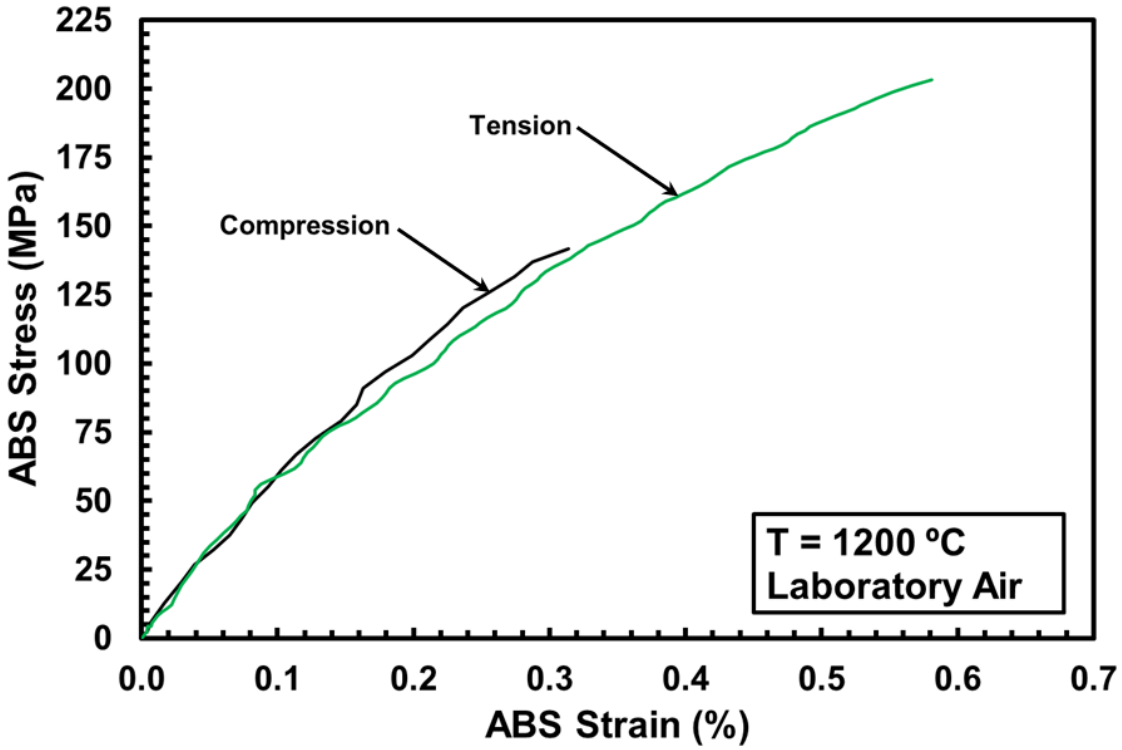

Figure 15: Monotonic tension and compression stress-strain curves obtained for N720/A composite at 1200°C in laboratory air.

Basic tension and compression properties obtained in this effort are compared with properties reported in literature in Table 8. Strength and modulus values obtained for both tension and compression in this work are in good agreement with published data. The failure strain produced in compression is in good agreement with that reported by Szymczak [45]. Conversely, the failure strains obtained in tension tests were somewhat higher than those reported in literature. This may have been due to possible changes in CMC panel manufacturing techniques.

Table 8: Summary of basic tension and compression properties for N720/A at 1200°C from literature [38, 40, 41, 43-45].

Author	Test Type	Strength (MPa)	Elastic Modulus E (GPa)	Failure Strain (%)
Szymczak [45]	Compression	122	69	0.21
Eber [38], Harlan [41]	Tension	192	75	0.38
Mehrman [38]	Tension	186	78	0.37
COI [43]	Tension	224	69	0.44
Bansal [44]	Tension	189	75	0.38
Tensile Average	Tension	198	74	0.39

5.3 Tension-Compression Fatigue at 1200°C in Air

Results of the tension-compression fatigue tests performed at 1200°C in laboratory air are summarized in Table 9. Results are also presented in Figure 16 as the maximum stress vs. cycles to failure curves. The tension-tension fatigue results obtained by Eber [40] are included in Table 9 and in Figure 16 for comparison. In Figure 16, arrow indicates that failure of specimen did not occur when the test was terminated.

Table 9: Summary of fatigue results for N720/A ceramic composite at 1 Hz at 1200°C in laboratory air. Tension-tension fatigue results from Eber [40].

Specimen Designation	Max Stress (MPa)	Cycles to Failure	Failure (or Final [a]) Strain (%)
Tension-tension fatigue, R = 0.05, Eber 2005			
6	100	120,199 [a]	0.63 [a]
7	125	146,392 [a]	1.14 [a]
8	150	167,473 [a]	1.66 [a]
9	170	109,436 [a]	2.25 [a]
Tension-compression fatigue, R = -1			
7	80	113,382	-0.96
11	80	100,000 [a]	-0.23 [a]
22	90	71,484	-0.43
10	90	28,159	-0.49
26	95	12,636	-0.32
9	100	5,264	-0.64
6	100	4,902	-0.33
23	110	3,488	-0.31
16	110	2,121	-0.44
17	120	199	-0.22

[a] Run-out, defined as 10^5 cycles. Failure of specimen did not occur when the test was terminated. See Table 13 for retained properties.

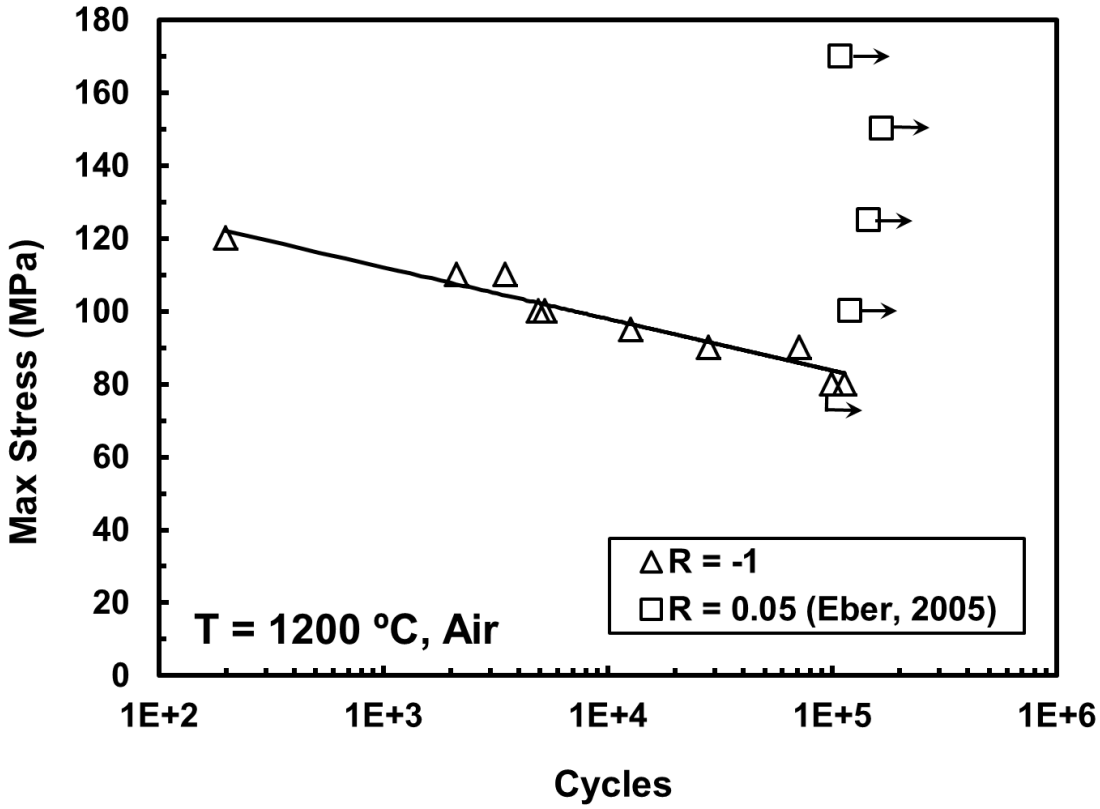

Figure 16: Stress vs. cycles to failure for N720/A ceramic composite at 1200°C in laboratory air. Arrow indicates that failure of specimen did not occur when the test was terminated. Tension-tension fatigue results from Eber [40].

At 1200°C in air, the fatigue run-out of 10^5 cycles was achieved at 80 MPa (40%UTS). It is noteworthy that all fatigue failures occurred during the compressive portion of the fatigue cycle. This result is likely due to the relatively low compressive strength of the material compared to its tensile strength.

At 1200°C in air, the tension-compression cycling is considerably more damaging than tension-tension fatigue. Including compression in the load cycle caused dramatic reductions in fatigue life of N720/A composite. For a given stress level, the cyclic lives obtained in tension-tension fatigue by Eber [40] were

at least three orders of magnitude higher than those produced under tension-compression fatigue. The run-out stress in tension-tension fatigue was a high 170 MPa, more than twice the run-out stress of 80 MPa obtained in tension-compression fatigue. Furthermore, while in tension-tension fatigue a run-out of 10^5 cycles was achieved at 125 MPa, tension-compression cyclic life at 120 MPa was a very poor 199 cycles. Including compression in the fatigue cycle reduced fatigue life by 99% for σ_{max} of 120 MPa.

The ultimate compressive strength (UCS) of the N720/A is only 71% of its ultimate tensile strength (UTS). Hence it is instructive to view maximum stress levels as %UTS and %UCS rather than in standard units of MPa. In tension-tension fatigue a run-out was achieved at 85%UTS (σ_{max} = 170 MPa). In contrast, the specimen tested in tension-compression fatigue at 85%UCS (σ_{max} = 120 MPa) survived only 199 cycles. This result indicates that the low compressive strength of the composite is not the sole reason for its poor fatigue performance in tension-compression compared to tension-tension cycling.

Note that considerably larger failure strain magnitudes were produced in tension-tension fatigue than in tension-compression fatigue. The larger failure strains are indicative of longer damage zones and more extensive fiber pullout, which is typically associated with active crack deflection and improved toughness of the CMC.

The results of this work are in stark contrast to the results reported by Jones [33] for a Hi-Nicalon/PyC/HyprSiC CMC. Jones subjected the material to fatigue loading with an R value of -1 in air at 1200°C and compared the results to those found by Delapasse [46] with an R value of 0.05. Jones found that the change in R ratio reduced fatigue life by 19% to 63% depending on the maximum stress. The relatively low loss in fatigue life with the introduction of compression into fatigue cycles might be attributed to the fairly high compressive strength of the Hi-Nicalon/PyC/HyprSiC material compared to its tensile strength. However, it should be noted that the Hi-Nicalon/PyC/HyprSiC composite studied by Jones and Delapasse has a dense matrix, a fiber coating and relies on a weak fiber/matrix interface for flaw tolerance. In contrast, the N720/A CMC studied in this work relies on an exceptionally weak porous matrix for crack deflection and flaw tolerance.

Szymczak [45] studied compressive creep behavior of N720/A at 1200 °C in air and in steam. Szymczak conducted compressive creep tests in air at creep stresses of 100, 80, and 60 MPa. Notably, a 100-h run-out was achieved in all tests performed in air. Tension-compression cyclic loading with the same maximum stress levels proved to be much more damaging than compression creep. As seen in Table 10, for a given maximum stress considerably shorter lifetimes were produced under tension-compression fatigue than under compressive creep. Reductions in lifetime were at least 68.5% for the maximum stress of 80 MPa and nearly 98.6% for the maximum stress of 100 MPa.

Table 10: Comparison of failure times for N720/A in air at 1200°C under tension-compression cyclic loading and under compressive creep. Compressive creep results from Szymczak [45].

Maximum Stress (MPa)	Failure (or Final [a, b]) Strain (%)	Cycles to Failure	Time to Failure (h)	Reduction in Lifetime (%)
Compressive Creep				
-60	-0.095 [a]	-	>100 [a]	-
-80	-0.14 [a]	-	>100 [a]	-
-100	-0.40 [a]	-	>100 [a]	-
Tension-Compression Fatigue,1 Hz, R = -1				
80	-0.96	113,382	31.50	>68.5
80	-0.23 [b]	100,000 [b]	>27.8 [b]	-
100	-0.64	5,264	1.46	>98.5
100	-0.33	4,902	1.36	>98.6

[a] Run-out, defined as 100 h. Failure of specimen did not occur when the test was terminated.

[b] Run-out, defined as 10^5 cycles. Failure of specimen did not occur when the test was terminated. See Table 13 for retained properties.

Evolution of hysteresis stress-strain response of N720/A composite with cycles at 1200°C in air is shown in Figure 17 and Figure 18 for the maximum stresses of 110 MPa and 90 MPa, respectively.

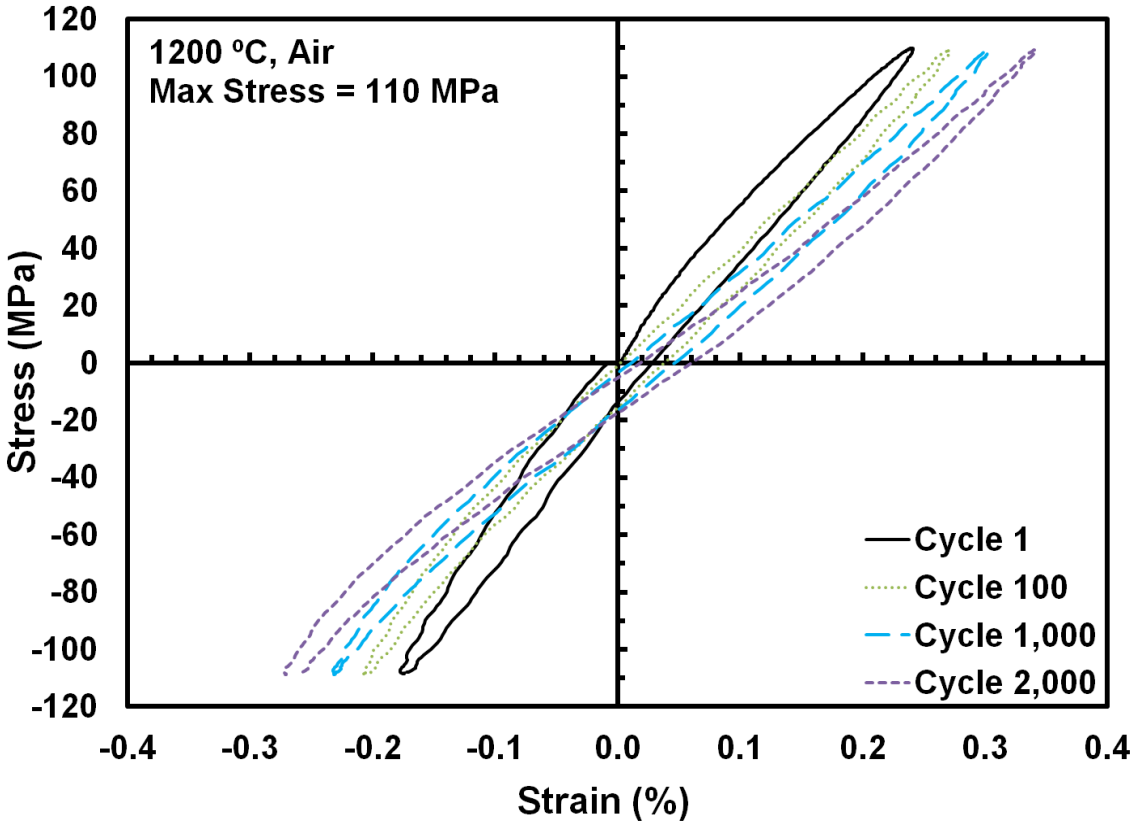

Figure 17: Evolution of stress-strain hysteresis response of N720/A composite with fatigue cycles at 1200°C in air, σ_{max} = 110 MPa, N_f = 2,121 cycles.

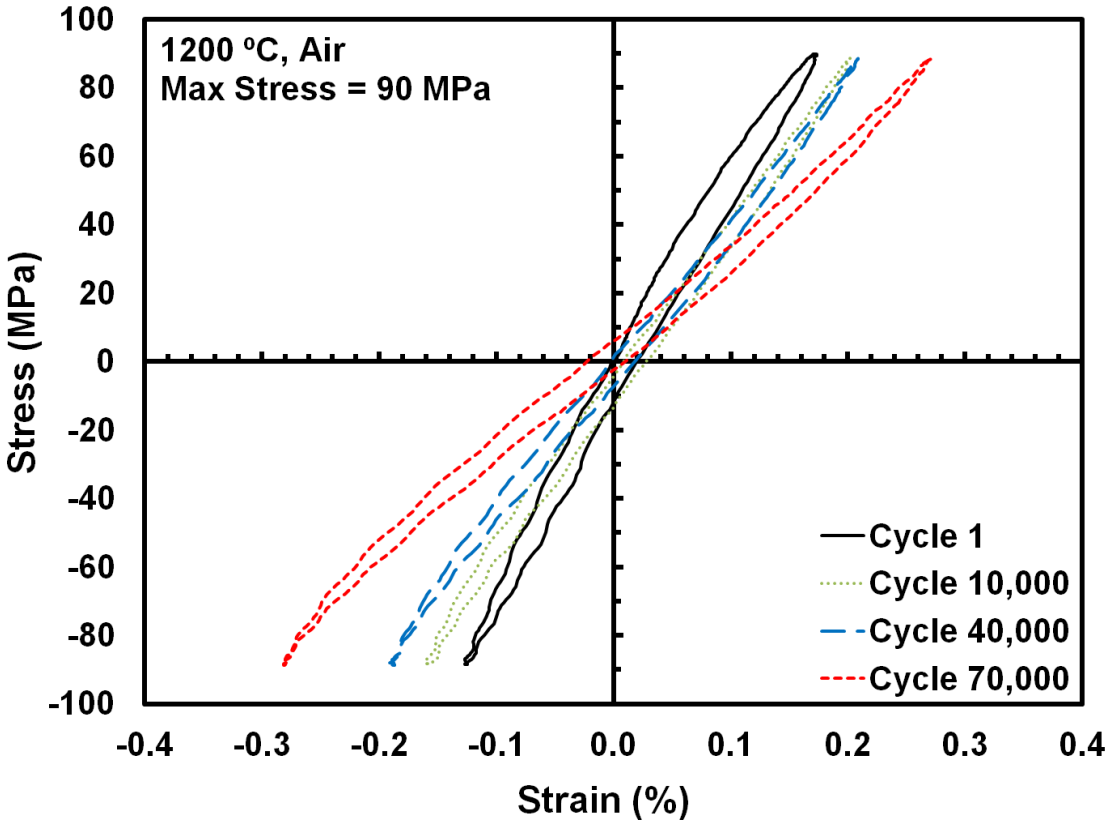

Figure 18: Evolution of stress-strain hysteresis response of N720/A composite with fatigue cycles at 1200°C in air, σ_{max} = 90 MPa, N_f = 71,484 cycles.

It is seen that the hysteresis loops produced in tension-compression tests were nearly symmetric about the origin. In all tests, the slopes of the tensile portion and of the compressive portion of the hysteresis loop were measured for the second cycle and for the last cycle. The measured tension and compression moduli were nearly the same (within 2 GPa) in all tests. In addition, the overall tensile and compressive moduli (determined as maximum stress magnitude over maximum strain magnitude) were calculated for each cycle. In all tests performed in air, the change in the overall tensile modulus with cycles was approximately the same as the change of the overall compressive modulus. This result is

evident in Figure 17 and Figure 18. Although the damage (represented by the overall modulus loss) developed in a similar manner during tensile and compression portions of the cycles, the ultimate failure always occurred on the compression side of the loading cycle.

The hysteretic stress-strain behavior of N720/A under tension-compression fatigue cycling is very different from that of Hi-Nicalon/PyC/HyperSiC composite [33]. In the case of Hi-Nicalon/PyC/HyperSiC CMC, the slope of the compressive portion of the hysteresis loops remained nearly unchanged in all tests. Contrastingly, tensile modulus decreased significantly with fatigue cycling. Not surprisingly, all failures occurred during the tensile portion of the cycle.

Maximum and minimum strains vs fatigue cycles for tests conducted with σ_{max} of 90, 95, 110, and 120 MPa at 1200°C in air are shown in Figure 19. In all tests, the evolution of minimum strain with cycles is nearly a mirror image of the change in maximum strain. In addition, higher levels of stress are generally associated with lower failure strains. Generally, lower strain accumulation with cycling indicates that less damage has occurred, and that it is mostly limited to some additional matrix cracking. However, in the case of 110 and 120 MPa tests conducted in this study, low accumulated strains are more likely due to early bundle failures leading to specimen failure. Similar observation was reported by Hetrick [39] who investigated tension-tension fatigue of N720/A at 1200°C.

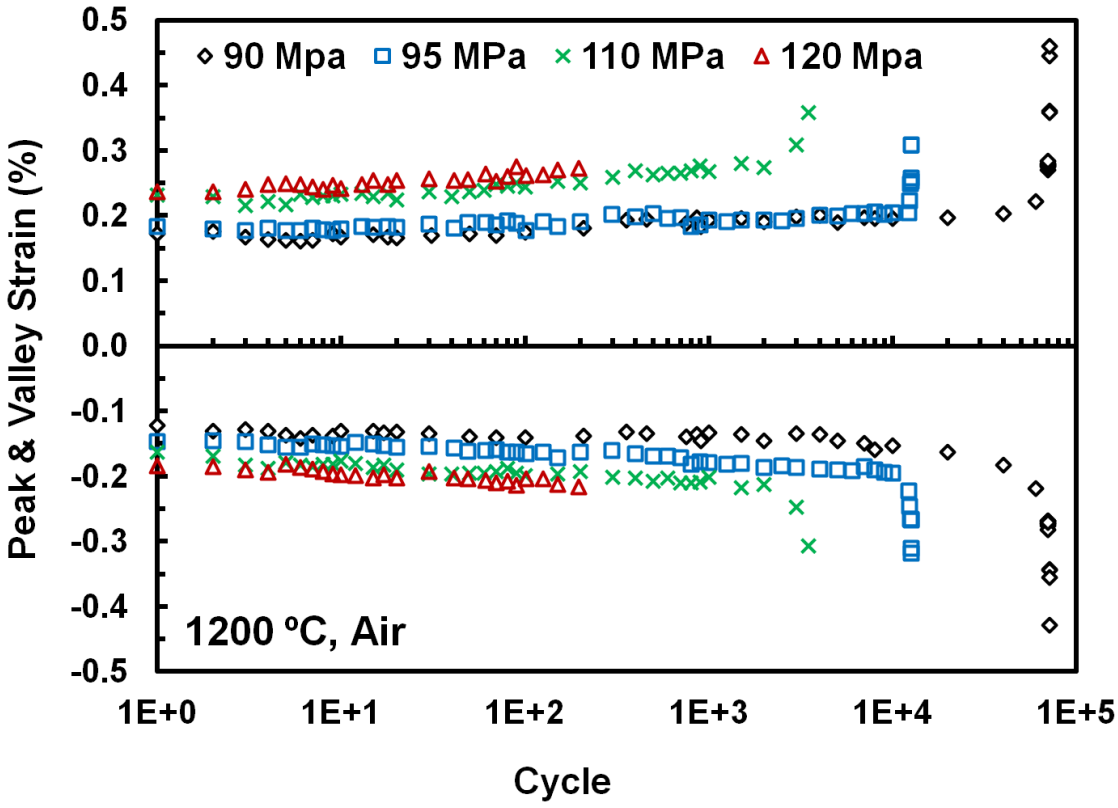

Figure 19: Peak Maximum and minimum strains vs. fatigue cycles for N720/A ceramic composite at 1200°C in air.

Of importance in cyclic fatigue is the reduction in stiffness (hysteresis modulus determined from the maximum and minimum stress-strain data points during a load cycle), reflecting the damage development during fatigue cycling. Change in modulus is shown in Figure 20, where normalized modulus (i.e. modulus normalized by the modulus obtained in the first cycle) is plotted vs. fatigue cycles.

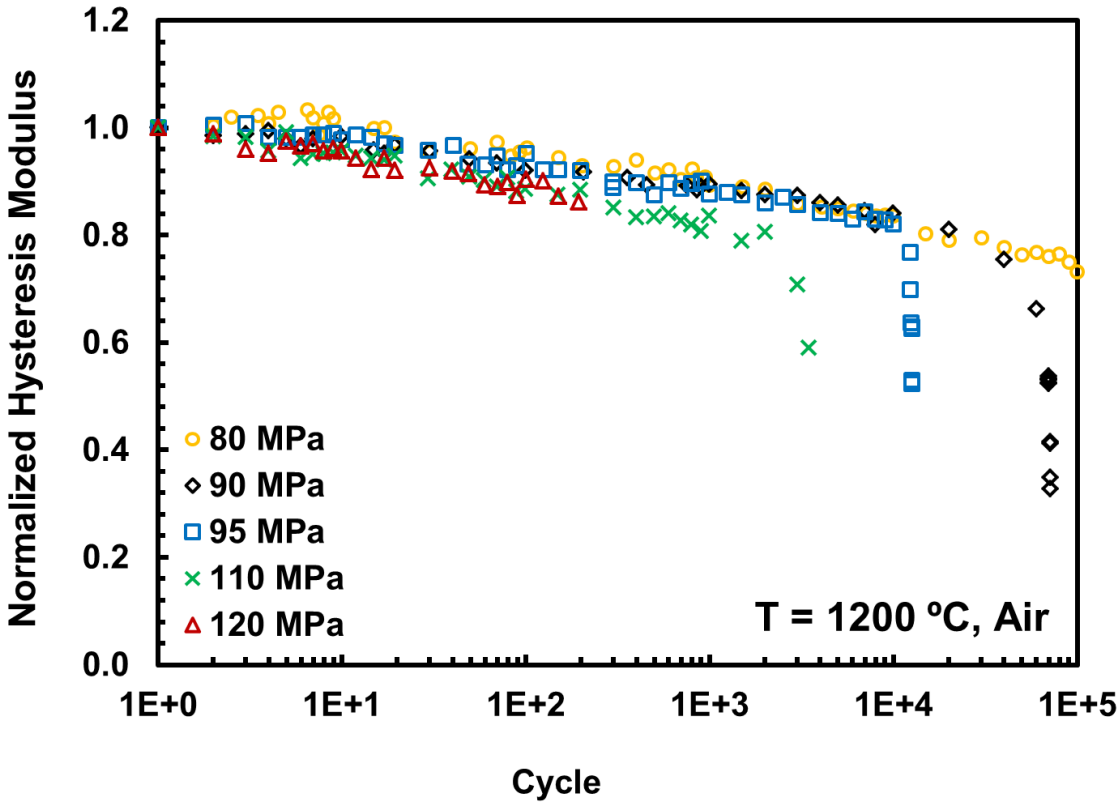

Figure 20: Normalized hysteresis modulus vs fatigue cycles for N720/A ceramic composite at 1200°C in air.

The results in Figure 20 reveal the slight increase in damage accumulation rates for higher stress levels. Cycling with higher maximum stress produces more damage during each cycle leading to earlier failures. Notably, specimens cycled with lower maximum stresses exhibit greater degree of damage as evidenced by a considerably greater modulus loss at the end of cyclic life. It is noteworthy that although some tests achieved run-out, a decrease in normalized modulus with cycling was still observed.

5.4 Tension-Compression Fatigue at 1200°C in Steam

Results of the tension-compression fatigue tests performed at 1200°C in steam are summarized in Table 11 and in Figure 21. The results of the tension-compression fatigue tests obtained at 1200°C in air as well as the results of the tension-tension fatigue tests reported by Eber [40] are also included in Table 11 and in Figure 21 for comparison. In Figure 21, arrow indicates failure of specimen did not occur when the test was terminated.

Table 11: Summary of fatigue results for N720/A ceramic composite at 1 Hz at 1200°C in laboratory air and in steam. Tension-tension fatigue results from Eber [40].

Specimen Designation	Test Environment	Maximum Stress (MPa)	Cycles to Failure	Failure (or Final [a]) Strain (%)
Tension-Tension Fatigue, R = 0.05, Eber 2005				
6	Air	100	120,199 [a]	0.63 [a]
7	Air	125	146,392 [a]	1.14 [a]
8	Air	150	167,473 [a]	1.66 [a]
9	Air	170	109,436 [a]	2.25 [a]
12	Steam	100	100,780 [a]	0.71 [a]
13	Steam	125	166,326 [a]	1.08 [a]
14	Steam	150	11,782	1.12
15	Steam	170	202	0.81
Tension-Compression Fatigue, R = -1				
7	Air	80	113,382	-0.96
11	Air	80	100,000 [a]	-0.23 [a]
22	Air	90	71,484	-0.43
10	Air	90	28,159	-0.49
26	Air	95	12,636	-0.32
9	Air	100	5,264	-0.64
6	Air	100	4,902	-0.33
23	Air	110	3,488	-0.31
16	Air	110	2,121	-0.44
17	Air	120	199	-0.22
13	Steam	60	100,000 [a]	-0.22 [a]
18	Steam	60	100,000 [a]	-0.13 [a]
21	Steam	70	100,000 [a]	-0.22 [a]
8	Steam	75	86,548	-0.40
24	Steam	80	22,426	-0.41
12	Steam	80	8,581	-0.83
20	Steam	90	9,092	-0.34
15	Steam	90	5,023	-0.79
25	Steam	95	2,316	-0.29
19	Steam	100	450	No data
14	Steam	100	247	-0.41

[a] Run-out, defined as 10^5 cycles. Failure of specimen did not occur when the test was terminated. See Table 13 for retained properties.

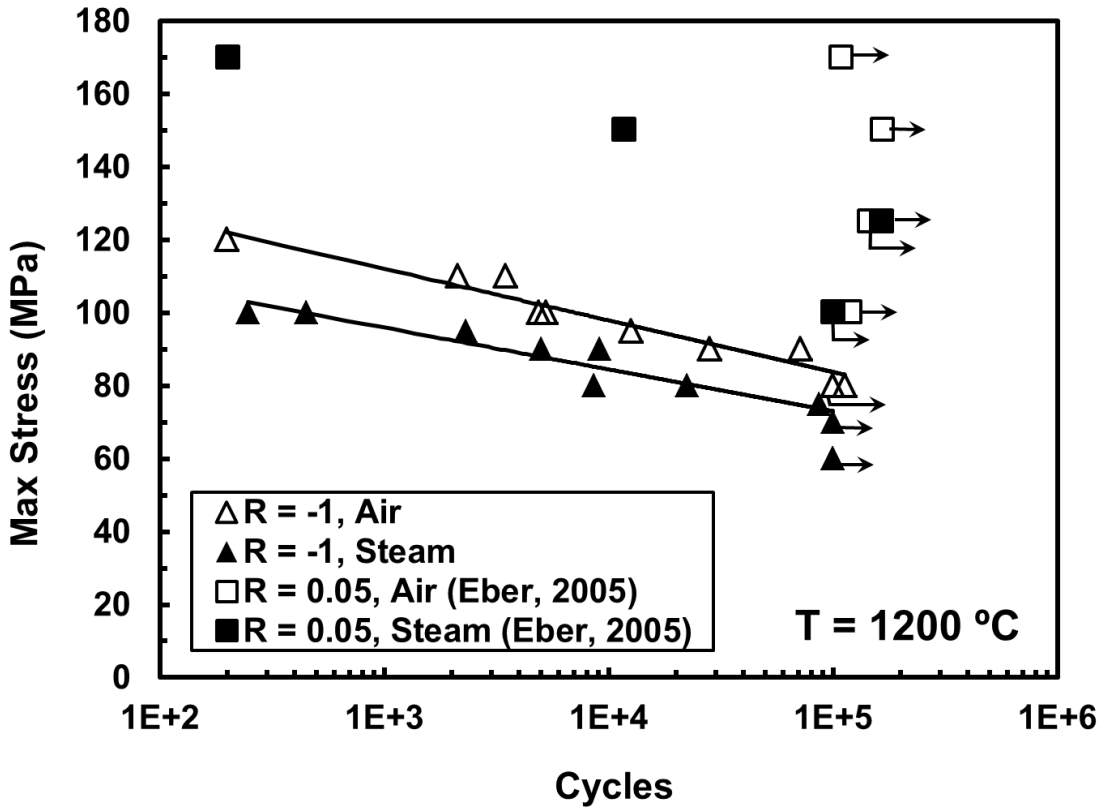

Figure 21: Stress vs. cycles to failure for N720/A ceramic composite at 1200°C in laboratory air and in steam. Arrow indicates that failure of specimen did not occur when the test was terminated. Tension-tension fatigue results from Eber [40].

Presence of steam causes significant degradation in fatigue performance of the N720/A composite. In steam the fatigue run-out was reached only at 70 MPa (35%UTS). Recall that in air the fatigue run-out of 10^5 cycles was achieved at a higher maximum stress of 80 MPa (40%UTS). The reduction in cyclic life due to steam was 80-92% for the maximum stress of 80 MPa. Similar reductions in cyclic lifetimes due to steam were observed under tension-tension fatigue [38-40]. However, detrimental effect of steam on cyclic lifetimes was considerably more pronounced in the case of tension-tension fatigue than under tension-

compression fatigue. The cyclic lifetimes produced in steam in tension-compression fatigue were nearly an order of magnitude lower than those produced in air. Conversely, in the case of tension-tension fatigue steam reduced the cyclic lifetimes by one to three orders of magnitude [38-40].

The results in Table 11 show that in steam for a maximum stress of 100 MPa, cyclic lifetimes under tension-compression fatigue were 247 and 450 cycles, while a run-out of 10^5 cycles was achieved under tension-tension fatigue. For a given maximum stress level, the introduction of compressive loading into fatigue cycle causes a nearly 1000-fold reduction in cyclic life in steam.

It is instructive to compare the lifetimes produced during tension-compression fatigue tests at 1200°C in steam in the current work with those obtained during creep tests performed at the same maximum stresses [45] (see Table 12 and Figure 22).

Table 12: Comparison of failure times for N720/A in steam at 1200°C under tension-compression cyclic loading and under compressive creep. Compressive creep results from Szymczak [45].

Max. Stress (MPa)	Failure (or Final [a]) Strain (%)	Cycles to failure	Time to failure (s)	Reduction in Lifetime (%)
Compressive Creep				
-40	-1.577	-	13,920	-
-60	-1.128	-	2,355	>97.6
-100	-0.188	-	6.5	98.1
Tension-Compression Fatigue,1 Hz, R = -1				
60	-0.22 [a]	100,000 [a]	100,000 [a]	-
60	-0.13 [a]	100,000 [a]	100,000 [a]	-
100	No strain data	450	450	-
100	-0.41	247	247	-

[a] Run-out, defined as 10^5 cycles. Failure of specimen did not occur when the test was terminated. See Table 13 for retained properties.

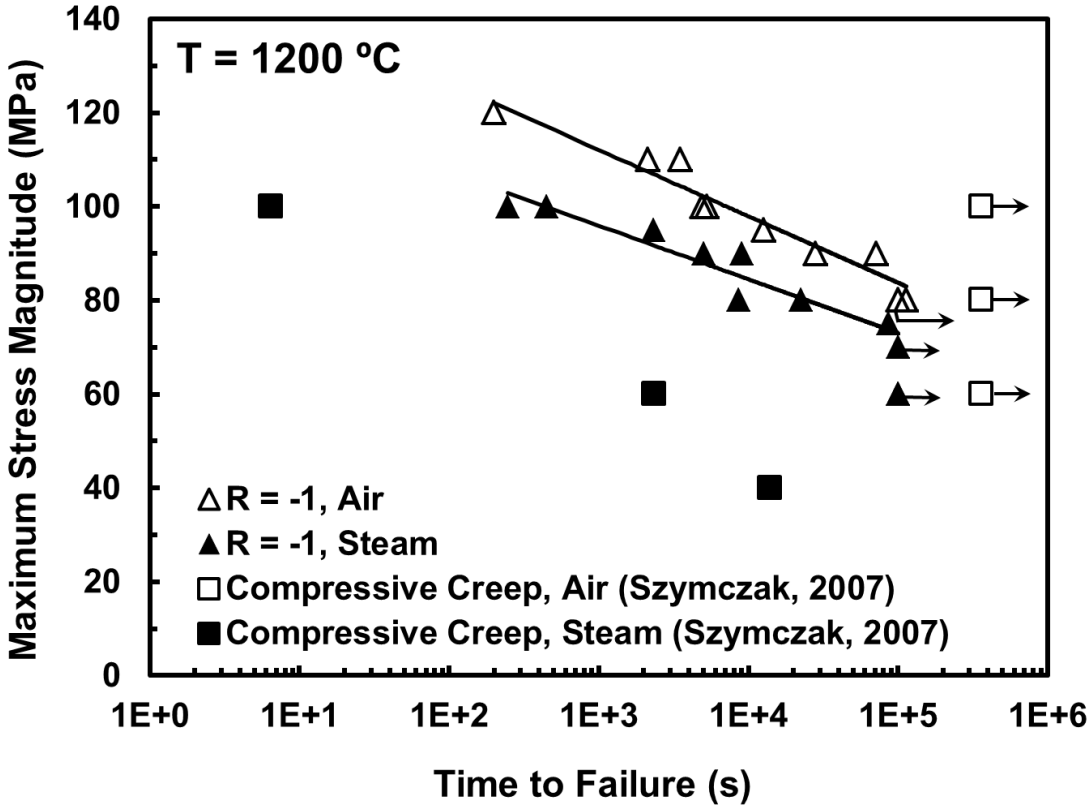

Figure 22: Stress vs. time to failure for N720/A ceramic composite at 1200°C in laboratory air and in steam. Arrow indicates that failure of specimen did not occur when the test was terminated. Compressive creep results from Szymczak [45].

Recall that at 1200°C in air, tension-compression cyclic loading with the same maximum stress levels proved to be much more damaging than compression creep. Contrastingly, in steam compression creep results in much shorter lifetimes than the tension-compression cycling. In steam, reductions in lifetime were at least 97.6% for the maximum stress of 60 MPa and nearly 98.1% for the maximum stress of 100 MPa. Apparently in steam, creep loading is the most damaging for the porous matrix oxide/oxide composite, followed by tension-compression fatigue, then tension-tension fatigue loading.

At 1200 °C in air, creep lifetimes exceed the tension-compression fatigue lifetimes in air. In contrast at 1200°C in steam, creep lifetimes are much shorter than those obtained in tension-compression cycling. Recent studies [47, 48] show that water attacks grain boundaries and degrades the strength of the polycrystalline alumina. Kronenberg et al [48] reported that alumina specimens heat treated under hydrostatic pressure in the presence of water developed two types of hydrogen defects: interstitial hydrogens in the bulk and molecular water clusters near surfaces, grain boundaries and cracks. Moreover, it was found that the presence of hydrogen defects reduced the yield stress of fine-grained alumina by a factor of 6. The weakening was attributed to a change in the predominant deformation mechanism, from dislocation glide to grain boundary sliding and cracking. It is possible that hydrogen defects that are introduced into the alumina matrix of the N720/A specimens during compressive creep tests conducted at 1200 °C in steam, also contribute to the degradation of creep performance in steam.

Additionally, it is recognized that the presence of steam promotes densification of alumina matrix and increased matrix-fiber bonding [47, 51]. Because the N720/A composite derives its damage tolerance from a porous matrix, the stability of matrix porosity against densification is a vital issue. Compressive creep loading in steam promotes additional sintering of the matrix and subsequent loss of matrix porosity [20, 24]. The densification of matrix occurring under static (creep) loading in either tension or compression

accelerates failure and reduces the lifetime of the composite. Contrastingly, cyclic loading (tension-tension as well as tension-compression) causes progressive matrix cracking and weakening of the fiber matrix interface thereby counteracting matrix densification and prolonging composite lifetime in steam. While tension-compression cycling in steam has a beneficial effect on composite durability compared to the compression creep loading, we recognize that shorter lifetimes are produced under tension-compression than under tension-tension fatigue. Once again we note that matrix densification and loss of matrix porosity is one of the major causes of the poor performance of the N720/A composite. While tension-tension cycling promotes continuous matrix cracking, tension-compression cycling likely promotes matrix densification during compression portion of the cycle.

Times to failure under tension-compression fatigue at 1200°C in air and in steam are compared to those produced under tensile creep [26] in Figure 23. Unlike the compressive creep lifetimes, tensile creep lifetimes exceed the lifetimes produced under tension-compression fatigue. Apparently, compression creep in steam is the most damaging loading/environment combination.

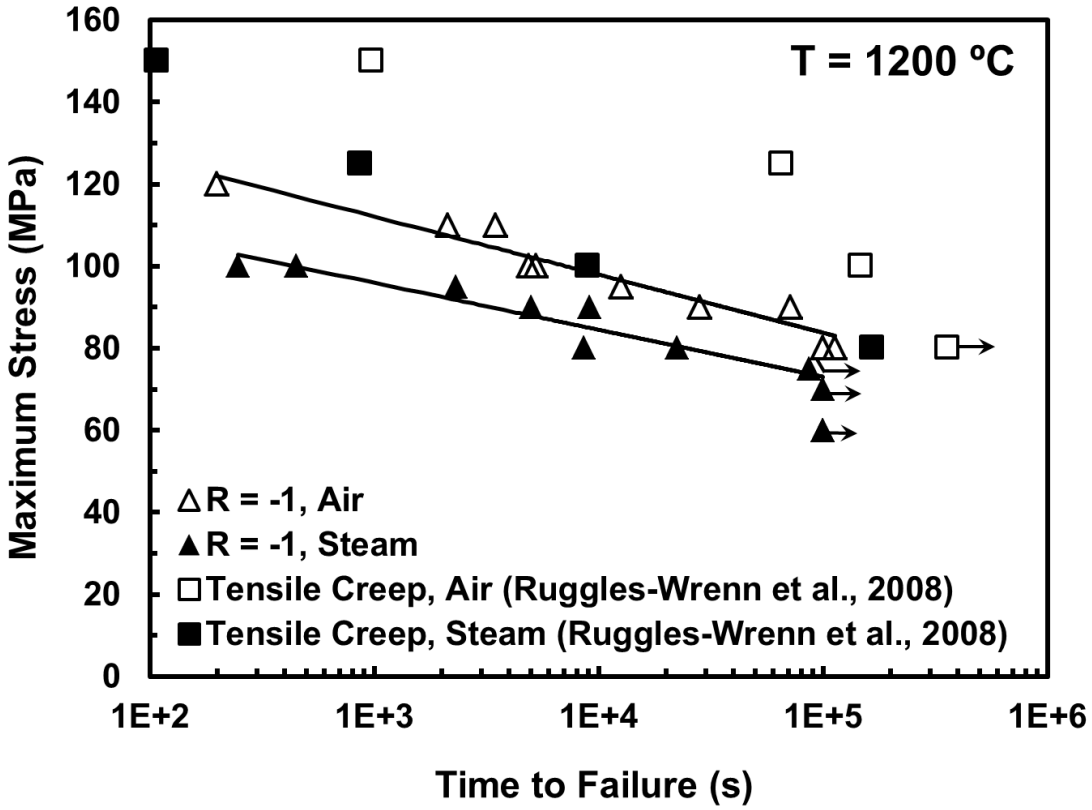

Figure 23: Stress vs. time to failure for N720/A ceramic composite at 1200°C in laboratory air and in steam. Arrow indicates that failure of specimen did not occur when the test was terminated. Tensile creep results from Ruggles-Wrenn et al. [26].

Evolution of hysteresis stress-strain response of N720/A composite with cycles at 1200°C in steam (Figure 24) appears to be qualitatively similar to that observed at 1200°C in air.

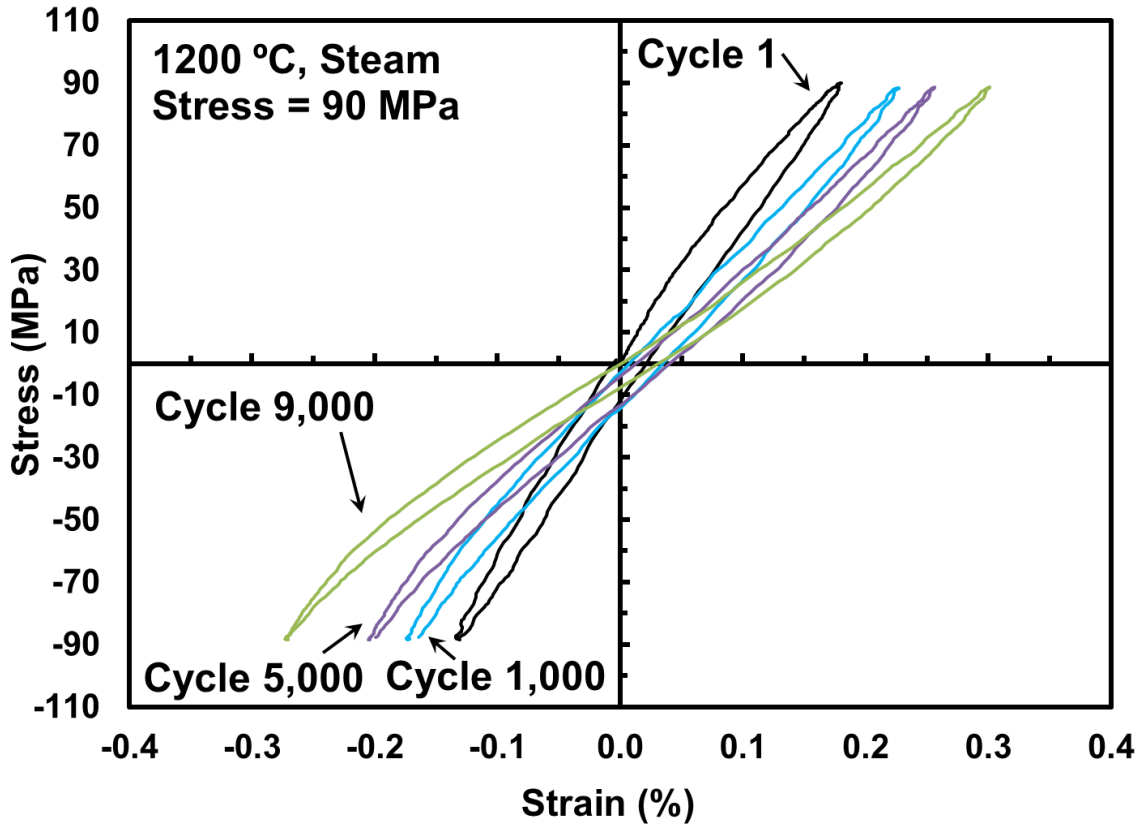

Figure 24: Evolution of stress-strain hysteresis response of N720/A composite with fatigue cycles at 1200°C in steam, σ_{max} = 90 MPa, N_f = 9,092 cycles.

Maximum and minimum strains vs fatigue cycles for tests conducted with σ_{max} of 90 MPa at 1200°C in air and in steam are shown in Figure 25. Results in Figure 25 reveal that strain accumulation is accelerated in the presence of steam.

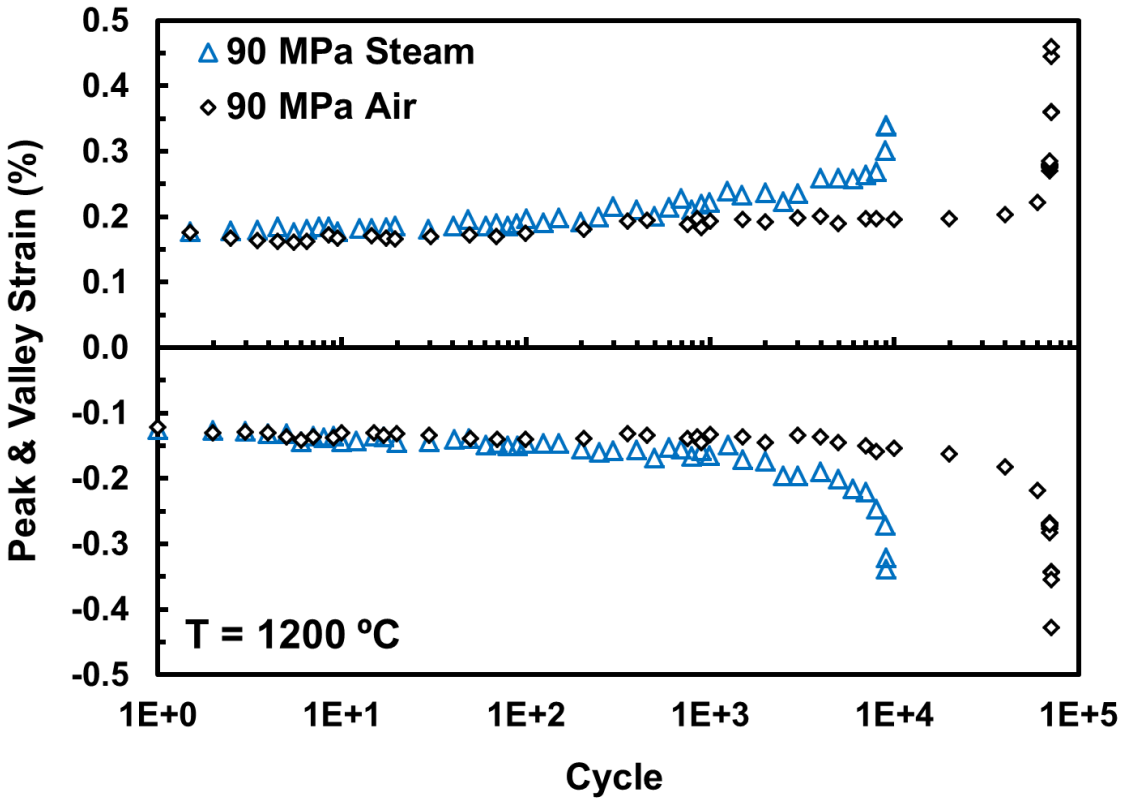

Figure 25: Maximum and minimum strains vs. fatigue cycles for N720/A ceramic composite at 1200°C in air and in steam.

Figure 26 shows the change in normalized hysteresis modulus with fatigue cycles at 1200°C in air and in steam. Significant contrast between the air and steam results is evident. Significant reductions in hysteresis modulus occur far earlier in the cyclic life in steam than in air for a given maximum stress. Moreover, the modulus loss with cycles in the 90 MPa test in steam is similar to that observed in the 110 MPa test in air.

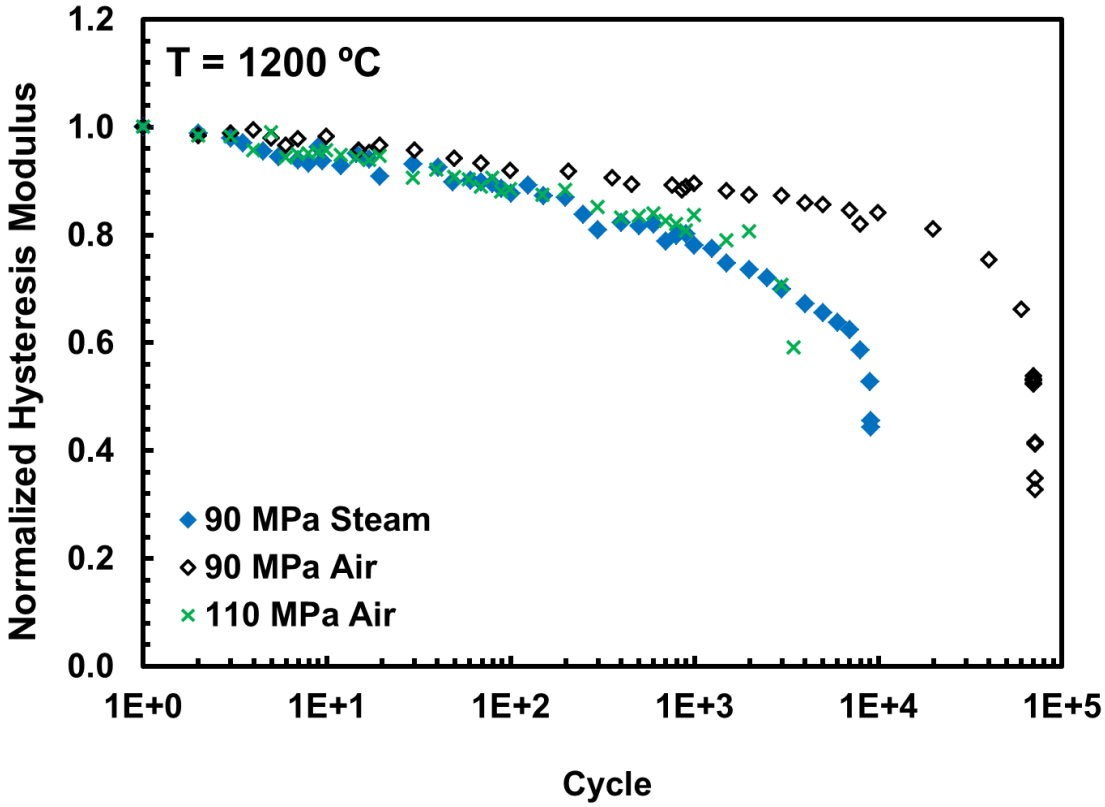

Figure 26: Normalized hysteresis modulus vs fatigue cycles for N720/A ceramic composite at 1200°C in air and in steam.

5.5 Effect of Prior Tension-Compression Fatigue at 1200°C on Tensile Properties

All specimens that achieved run-out were subjected to tensile test to failure at 1200°C in laboratory air to determine the retained strength and stiffness. Evaluation of retained properties is useful in assessing the damage state of the composite subjected to prior loading. Retained strength and stiffness of the tension-compression fatigue specimens that achieved run-out are summarized in Table 13 and in Figure 27. Table 13 also presents retained tensile properties reported by Eber [40] for the case of prior tension-tension fatigue.

Table 13: Retained tensile properties of N720/A specimens subjected to prior fatigue at 1200°C in air and in steam. Post tension-tension fatigue results from Eber [40].

Fatigue Stress (MPa)	Fatigue Environment	Retained Strength (MPa)	Strength Retention (%)	Retained Modulus (GPa)	Modulus Retention (%)	Failure Strain (%)
Prior Tension-Compression Fatigue, R = -1						
80	Air	205	103	37	55	0.71
60	Steam	165	83	33	49	0.53
60	Steam	165	83	34	51	0.44
70	Steam	123	62	31	46	0.47
Prior Tension-Tension Fatigue, R = 0.05, Eber 2005						
100	Air	194	101	53	71	0.44
125	Air	199	104	55	73	0.45
150	Air	199	104	43	57	0.53
170	Air	192	100	41	55	0.51
100	Steam	174	91	48	64	0.40
125	Steam	169	88	52	69	0.43

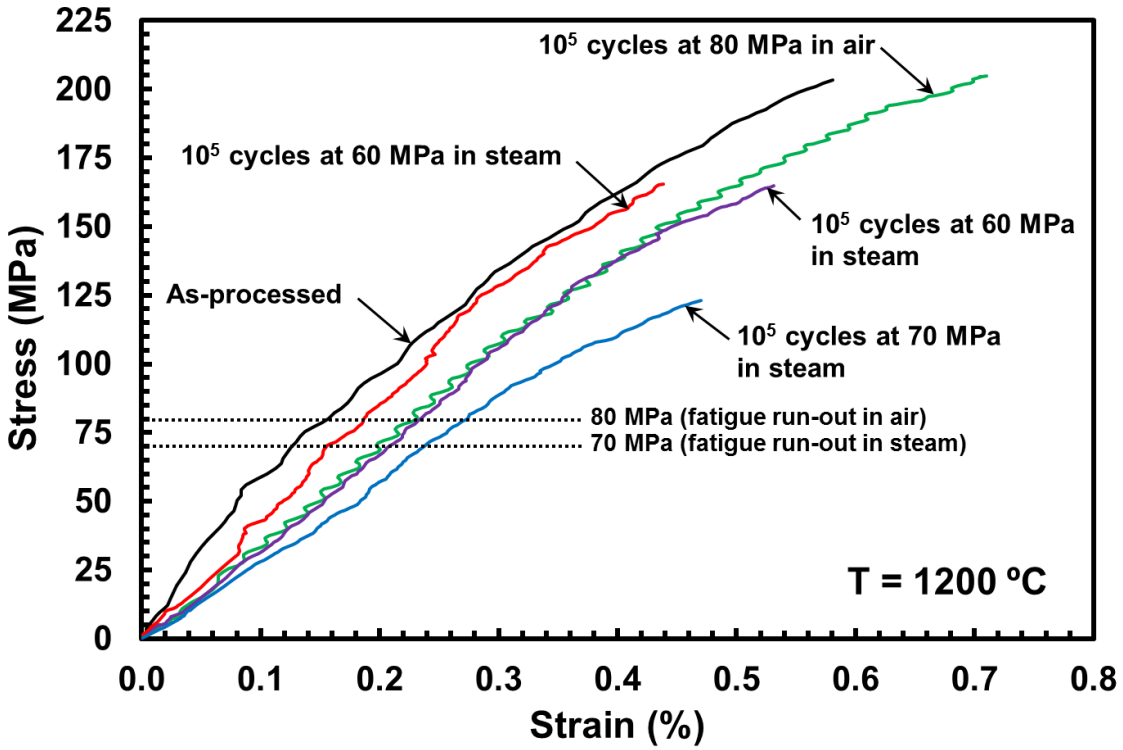

Figure 27: Effects on tensile stress-strain behavior of prior tension-compression fatigue at 1200°C in air and in steam.

Results in Table 13 reveal that prior tension-compression fatigue at 1200°C in air did not reduce the tensile strength of the composite. The specimens subjected to 10^5 fatigue cycles in air retained 103% of its tensile strength. However, a modulus loss of 45% was observed. Prior tension-compression fatigue in steam caused significant degradation of tensile strength. Specimen subjected to 10^5 fatigue cycles in steam retained only 62% - 83% of their tensile strength. The loss of tensile strength suggests that prior tension-compression fatigue in steam caused significant degradation of the N720 fibers. Prior tension-tension fatigue in steam also caused degradation of tensile strength and stiffness [40]. However, both strength loss and modulus loss were greater in the case of prior tension-compression fatigue. This result indicates that tension-compression fatigue is more damaging than tension-tension fatigue for N720/A composite.

A recent study by Wannaparhun et al. [50] concluded that at 1100°C in water-vapor environment, SiO_2 could be leached from Nextel™720 fiber. Wannaparhun et al. [50] proposed that H_2O reacted with the SiO_2 in the mullite phase of N720 fibers exposed to water-vapor. The reaction product, $Si(OH)_4$ then dispersed into the alumina matrix. Ruggles-Wrenn et al. [20] performed energy dispersive x-ray spectroscopy (EDS) of several N720/A samples exposed to tension-tension fatigue testing in air and in steam at 1200°C. As-processed specimens were examined for comparison. The results confirmed that in the presence of steam, silicon migrated from the fibers into the adjacent alumina matrix. It was proposed

that the depletion of the mullite phase from the N720 fibers could be the cause of reduced fatigue performance of the N720/A in steam [20].

These findings were supported by Armani et al. [51], who tested N720 fiber tows in creep at 1200°C in air and in steam. Armani and co-workers reported that a porous alumina layer (void of mullite) of ~2.2-µm thickness formed on the exterior of the fibers tested in steam. Conversely, fibers tested in air did not exhibit such degradation. Formation of a ~2.2-µm thick porous alumina layer that no longer contributed to the load-bearing capacity of the fiber was significant considering the 10-12 µm diameter of N720 fiber.

5.6 Microstructural Characterization

5.6.1 Optical Microscopy

The fracture surfaces and microstructure of the failed N720/A specimens were examined using optical microscopy and the SEM. Post-test microstructural characterization is useful in determining failure and damage mechanisms along with establishing baseline fracture morphologies corresponding to various loading and environmental conditions. Results of the microstructural characterization using optical microscopy are presented in this section.

The fracture surfaces obtained in monotonic compression and tension tests are shown in Figure 28 and Figure 29, respectively. The differences are quite dramatic. A long damage zone and a fairly large fracture surface are produced in the compression test. Moreover, the compression fracture surface is oriented at an angle to the loading direction and exhibits a somewhat progressive stair-step

failure across plies. On the other hand, a shorter damage zone is produced in the tension test. The tension failure surface clearly shows plies failing on alternating planes. Both tension and compression fracture surfaces have a brushy appearance, indicating fibrous fracture associated with crack deflection and damage tolerance.

Another significant difference between tension and compression failures is the presence of fiber micro-buckling in compression as evidenced by the curved and raised appearance of the surface fiber bundles indicated by the red oval in Figure 28. This feature is not seen in the tension fracture surface. These trends are consistent with those reported for N720/A at 1200 °C in compression testing [45] and in tension testing [38 - 42, 44].

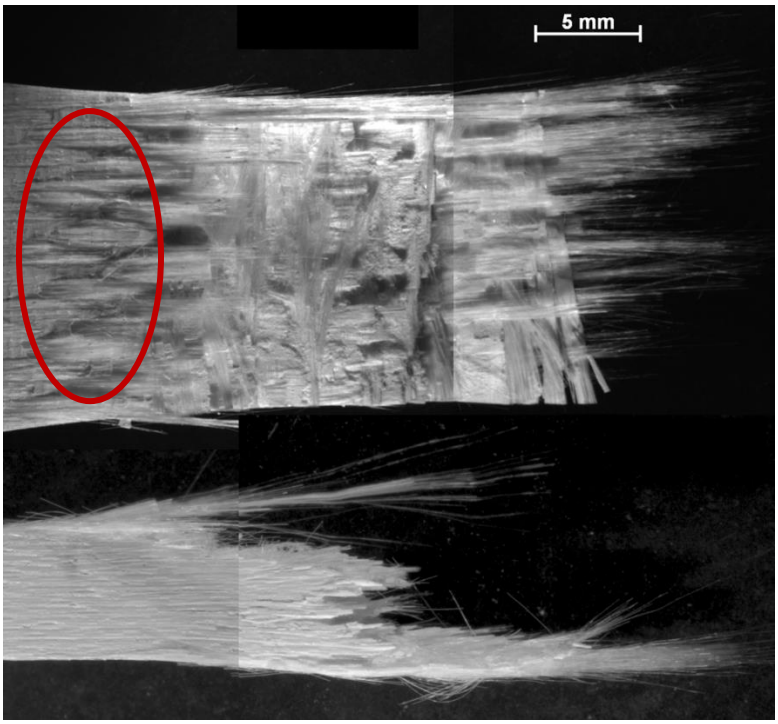

Figure 28: Fracture surface obtained in a compression to failure test at 1200°C in air.

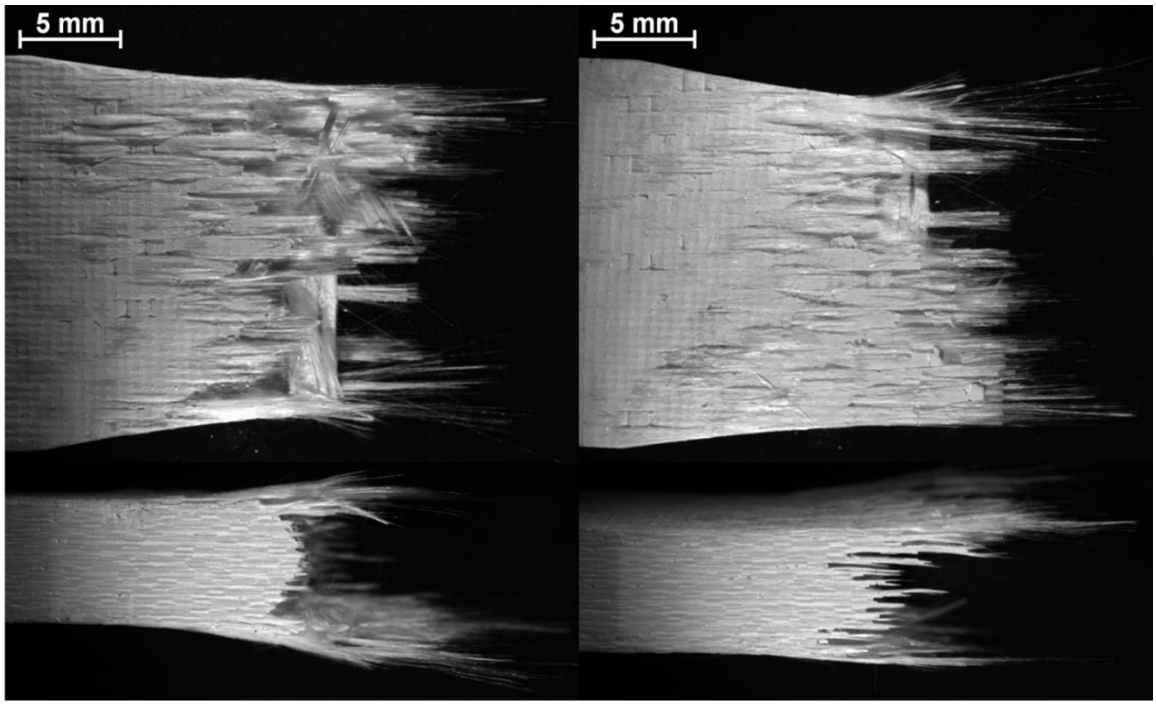

Figure 29: Fracture surface obtained in a tension to failure test at 1200°C in air.

Figure 30 and Figure 31 show the fracture surfaces obtained in tension tests of the N720/A specimens subjected to 10^5 cycles of prior tension-compression fatigue in air and in steam, respectively. Recall that the specimen pre-fatigued in air retained 100% of its tensile strength. The fracture surface in Figure 30 exhibits the same general features as the N720/A fracture surface produced in tension to failure test (Figure 29). However, note the slightly less brushy appearance and the presence of fiber bundle micro-buckling due to the prior tension-compression fatigue cycling (Figure 30). The less brushy appearance is generally attributed to matrix densification.

In contrast, the fracture surface of the N720/A specimen pre-fatigued in steam (Figure 31) has a shorter damage zone and is more planar and less brushy in appearance. The lack of a brushy appearance, small damage zone size, and relatively planar fracture indicate that the steam significantly reduced the CMC damage tolerance and inhibited crack deflection through matrix porosity. It appears that matrix porosity decreased and fiber-matrix bonding increased. Although both specimens achieved fatigue run-out, the retained properties of the two specimens were very different. While the specimen pre-fatigue in air retained 100% of its tensile strength, the specimen pre-fatigued in steam retained only 62% of its tensile strength. Such considerable loss of tensile strength suggests fiber degradation due to steam.

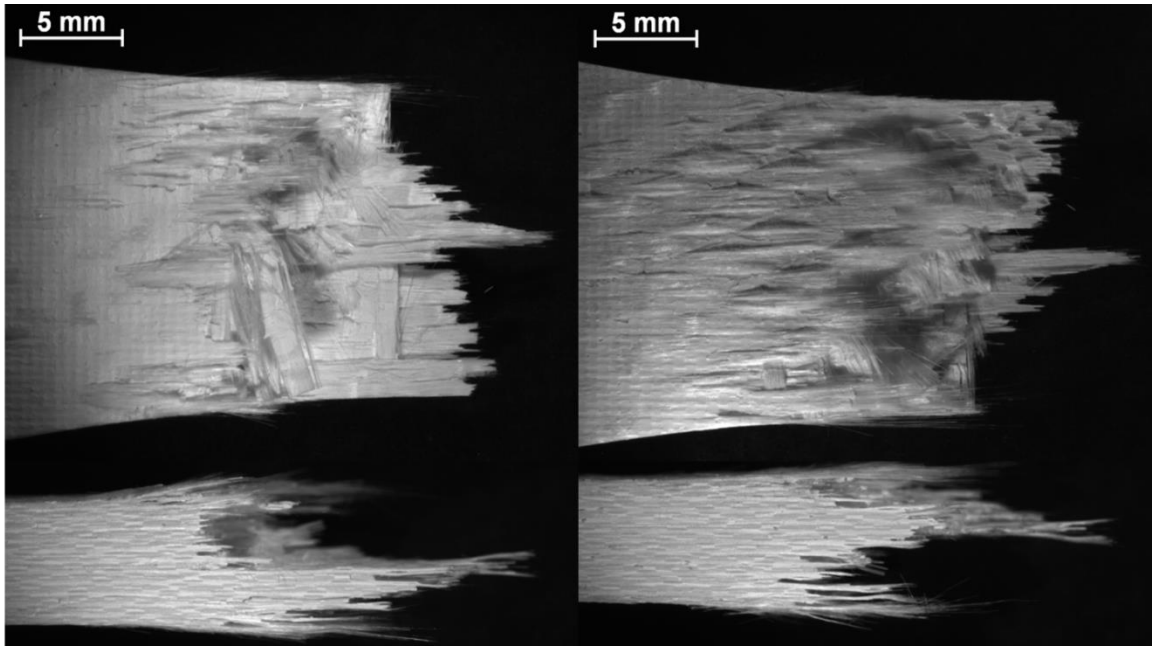

Figure 30: Fracture surface obtained in a tensile test of a N720/A specimen subjected to 10^5 cycles of prior tension-compression fatigue with σ_{max} = 80 MPa at 1200°C in air.

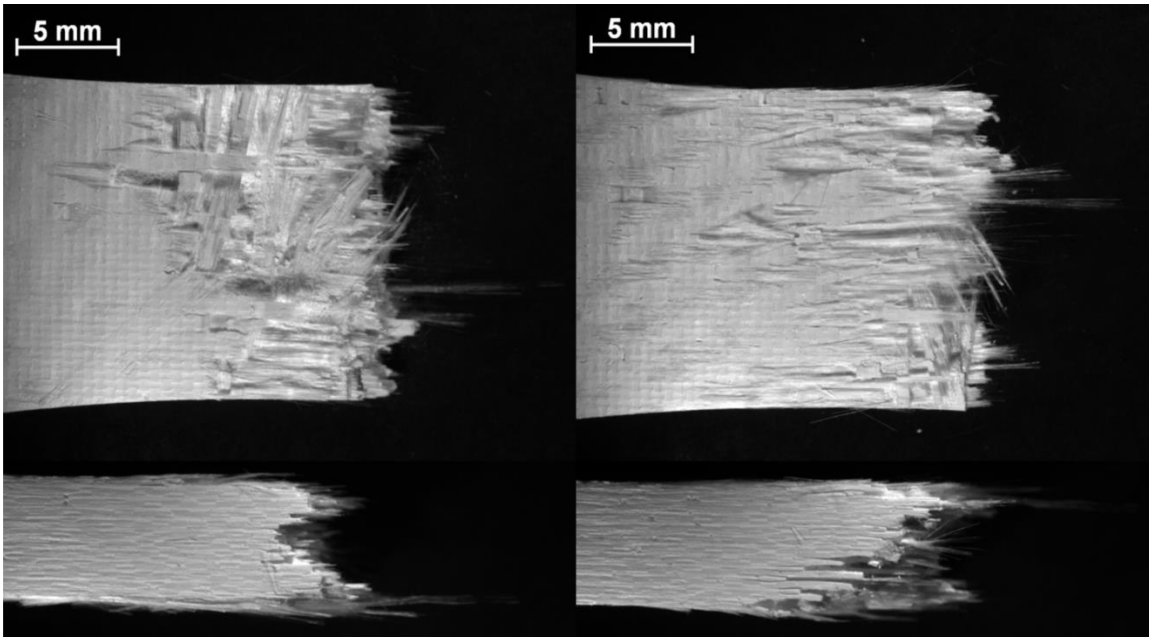

Figure 31: Fracture surface obtained in a tensile test of a N720/A specimen subjected to 10^5 cycles of prior tension-compression fatigue with σ_{max} = 70 MPa at 1200°C in steam.

Figure 32 shows a fracture surface obtained in tension-compression fatigue with a maximum stress of 80 MPa at 1200°C in air. Figure 33 shows a fracture surface obtained in tension-compression fatigue with a maximum stress of 75 MPa at 1200°C in steam. As was the case with all fatigue failures in this research effort, specimens shown in Figure 32 and Figure 33 failed in compression. Note that these specimens produced the longest cyclic lives in their respective environments culminating in fatigue failures. As in the case of fatigue run-out specimens, the fracture surfaces produced in fatigue in steam are relatively planar, while fracture surfaces produced in fatigue in air have a more brushy appearance. Both specimens exhibit significantly shorter damage zones than the as-processed specimen failed in compression test (Figure 28).

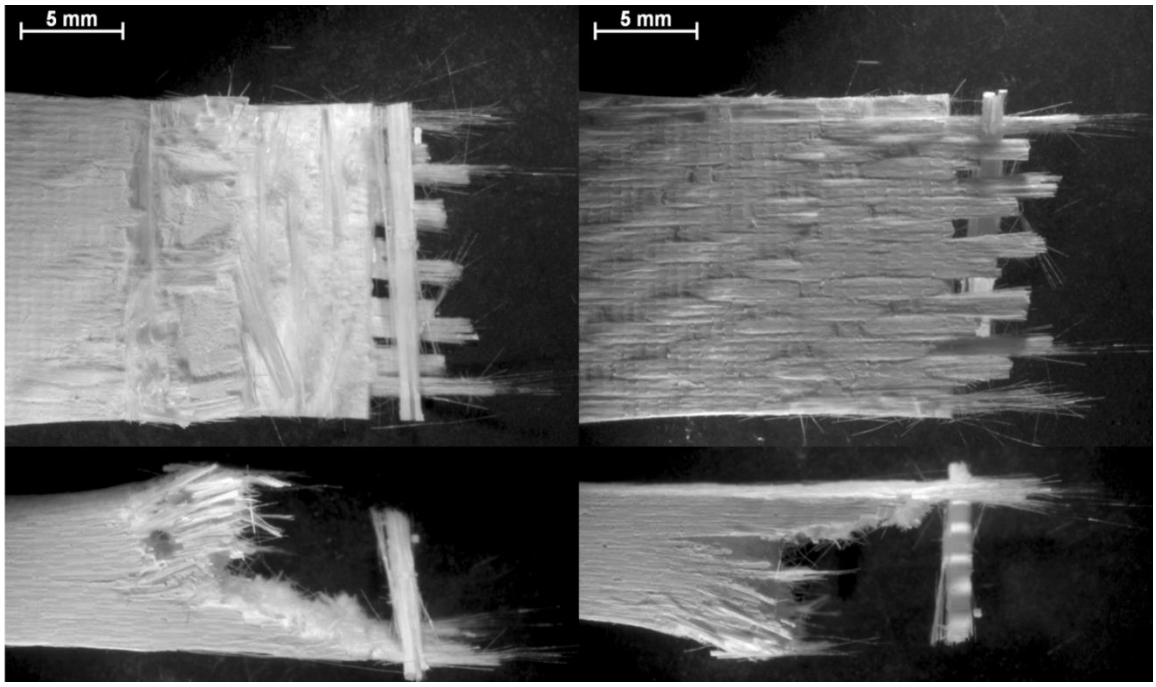

Figure 32: Fracture surface obtained in a fatigue test conducted at 1200°C in air. σ_{max} = 80 MPa, N_f = 113,382 cycles.

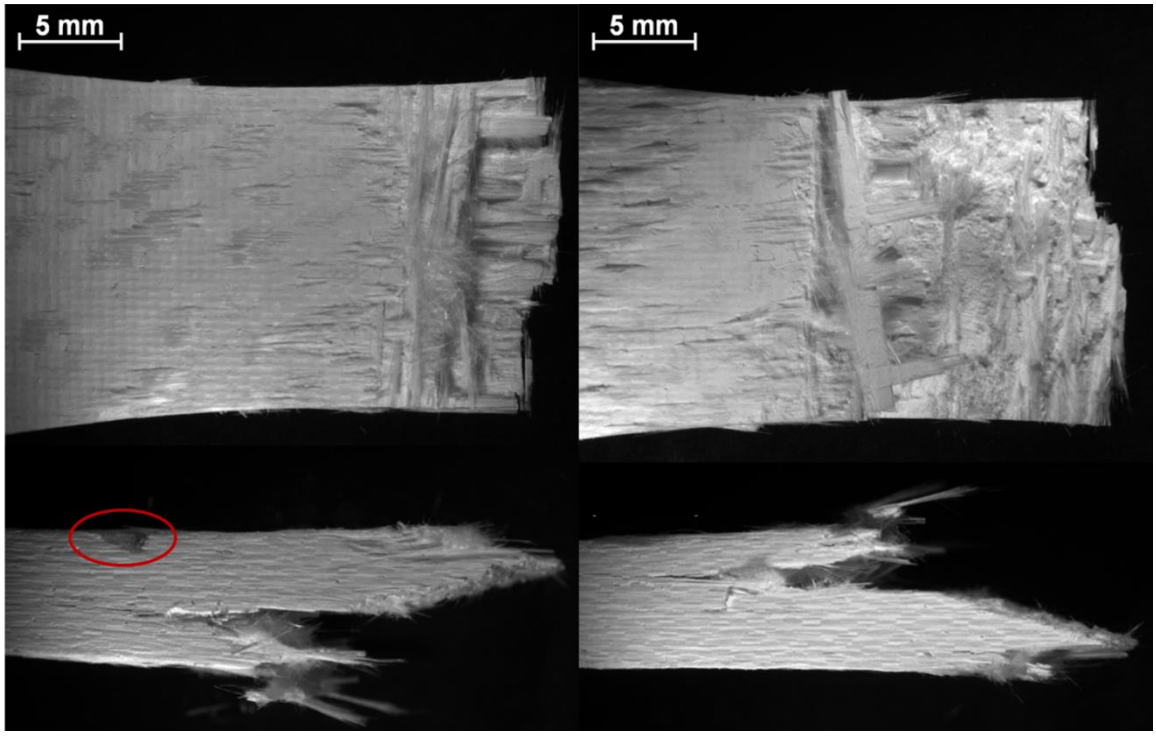

Figure 33: Fracture surface obtained in a fatigue test conducted at 1200°C in steam. σ_{max} = 75 MPa, N_f = 86,548 cycles.

Of particular importance is the damage indicated by the red oval in Figure 33. This damage was noted on the specimen in the as-received condition. The damage, located within the gauge section of the specimen had approximate dimensions of 1.1 mm x 2 mm x 0.6 mm. As seen in Figure 33, cracks did not initiate from this preexisting damage. There is no sign of cracking at this location; the fracture surface is also well removed from this pre-existing damage. This is a prime example of the good damage tolerance exhibited by this material system. The fatigue life of this specimen was consistent with those of the other specimens tested in steam during this effort. This should be expected due to the fact that no cracking initiated at the preexisting damage. In monolithic ceramics cracks initiate at defects such as this, leading to catastrophic failure.

Fracture surfaces obtained in fatigue tests performed with the maximum stress of 95 MPa in air and with the maximum stress of 90 MPa in steam are shown in Figure 34 and Figure 35, respectively. These fatigue tests were neither the longest nor the shortest, but rather of intermediate duration. While the differences between the fracture surfaces in Figure 34 and Figure 35 become more subtle, the specimen tested in air exhibits a longer damage zone and a slightly more fibrous fracture.

Fracture surfaces obtained in fatigue tests performed with the maximum stress of 120 MPa in air and with the maximum stress of 100 MPa in steam are shown in Figure 36 and Figure 37, respectively. Note that these specimens produced the shortest fatigue lives in their respective test environments. Not surprisingly, the effects of steam on fracture surface appearance are minimal. Both specimens have significantly shorter damage zones (~22 mm each) than the specimens tested in compression to failure in this research (~31 mm) and in prior work [45] (~45 mm). Note that damage lengths were measured parallel to the specimen length using dial calipers.

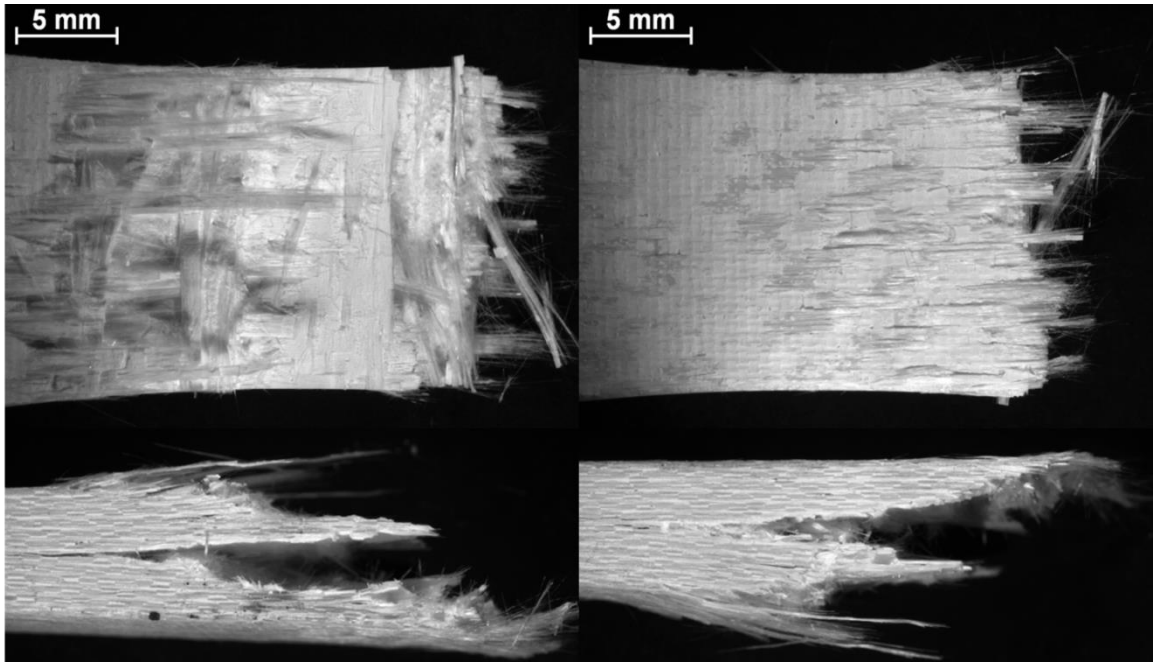

Figure 34: Fracture surface obtained in a fatigue test conducted at 1200°C in air. σ_{max} = 95 MPa, N_f = 12,636 cycles.

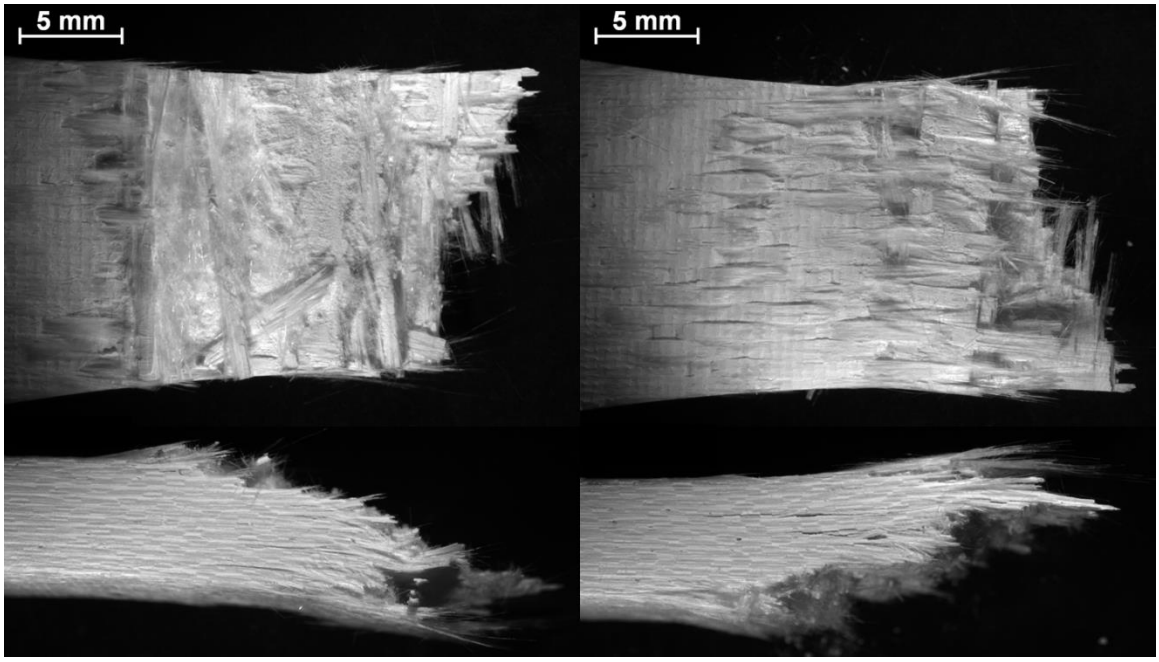

Figure 35: Fracture surface obtained in a fatigue test conducted at 1200°C in steam. σ_{max} = 90 MPa, N_f = 9,092 cycles.

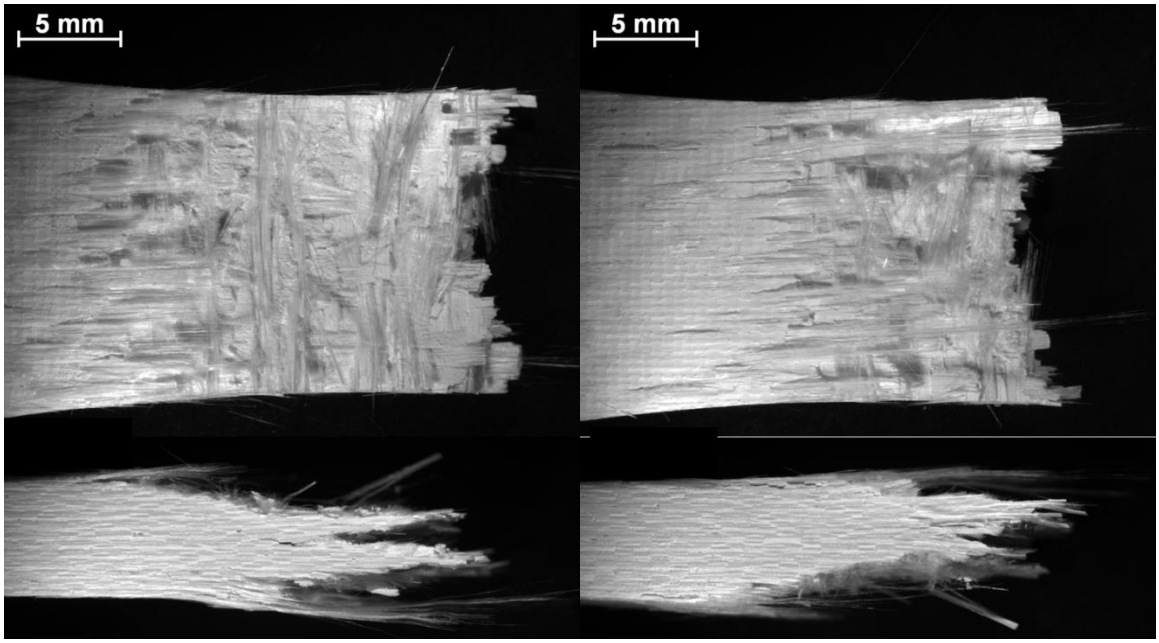

Figure 36: Fracture surface obtained in a fatigue test conducted at 1200°C in air. σ_{max} = 120 MPa, N_f = 199 cycles.

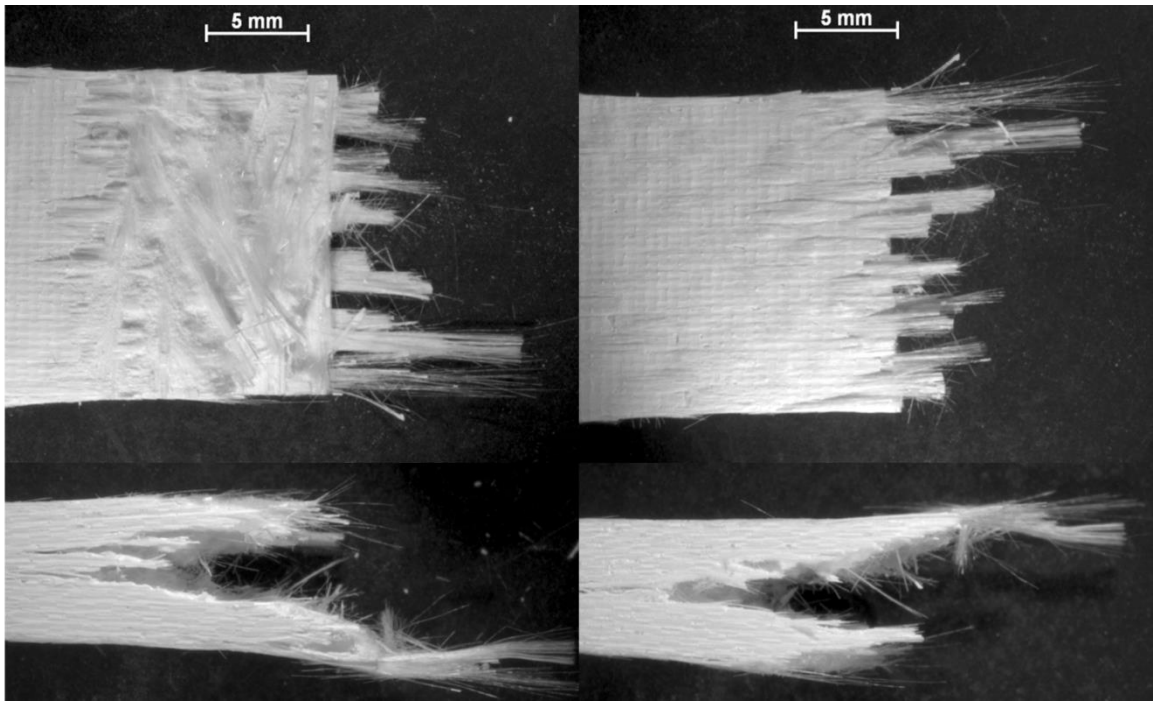

Figure 37: Fracture surface obtained in a fatigue test conducted at 1200°C in steam. σ_{max} = 100 MPa, N_f = 450 cycles.

Figure 38 shows the fracture surfaces of N720/A specimens which failed in compressive creep tests in steam at 1200°C, Szymczak [45]. The differences between the fracture surfaces obtained in tension-compression fatigue and those obtained in compressive creep are readily apparent. The fracture surfaces produced in compressive creep are much less fibrous. Again, recall that these compressive creep failures are associated with significantly shorter lifetimes than the tension-compression fatigue lifetimes in steam with similar maximum loads.

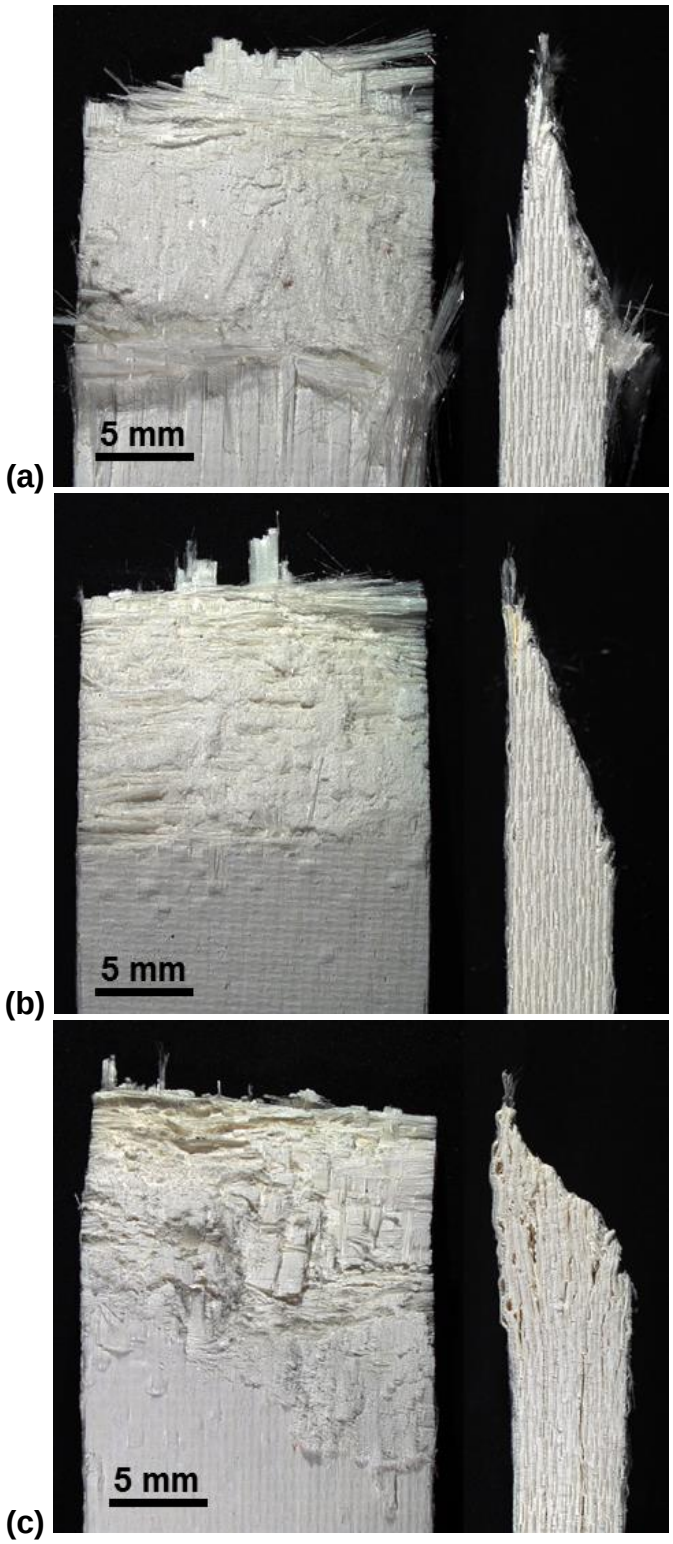

Figure 38: Fracture surfaces of N720/A specimens failed in compressive creep in steam at 1200°C: (a) -100 MPa, (b) -60 MPa, (c) -40 MPa, images from Szymczak [45].

For each specimen that failed in tension-compression fatigue the length of the damage zone was measured parallel to the specimen length using dial calipers, then plotted vs. the maximum applied stress (Figure 39) and vs. cycles to failure (Figure 40). It is seen that longer damage zones correspond to higher maximum stresses. For a given maximum stress the damage zones obtained in air are the same as or only slightly longer than those obtained in steam. Conversely, results in Figure 40 reveal that for a given fatigue lifetime much shorter damage zones are obtained in steam than in air.

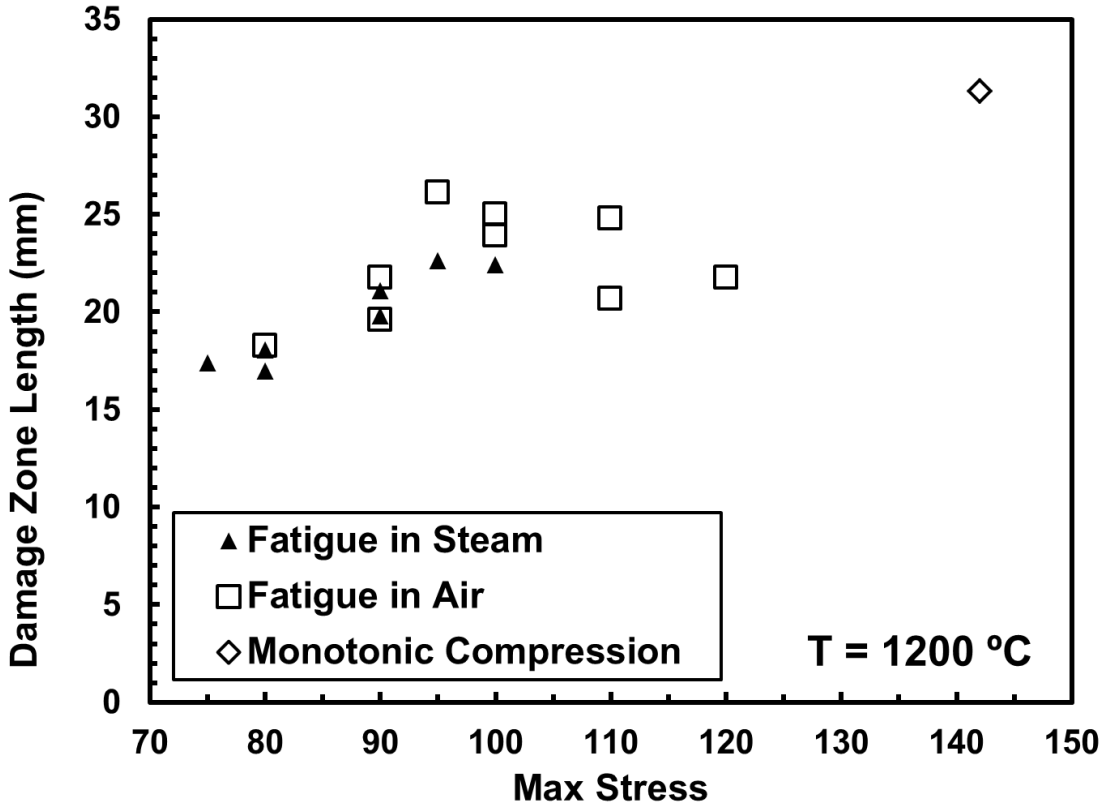

Figure 39: Length of damage zone vs. maximum stress for N720/A specimens failed in tension-compression fatigue.

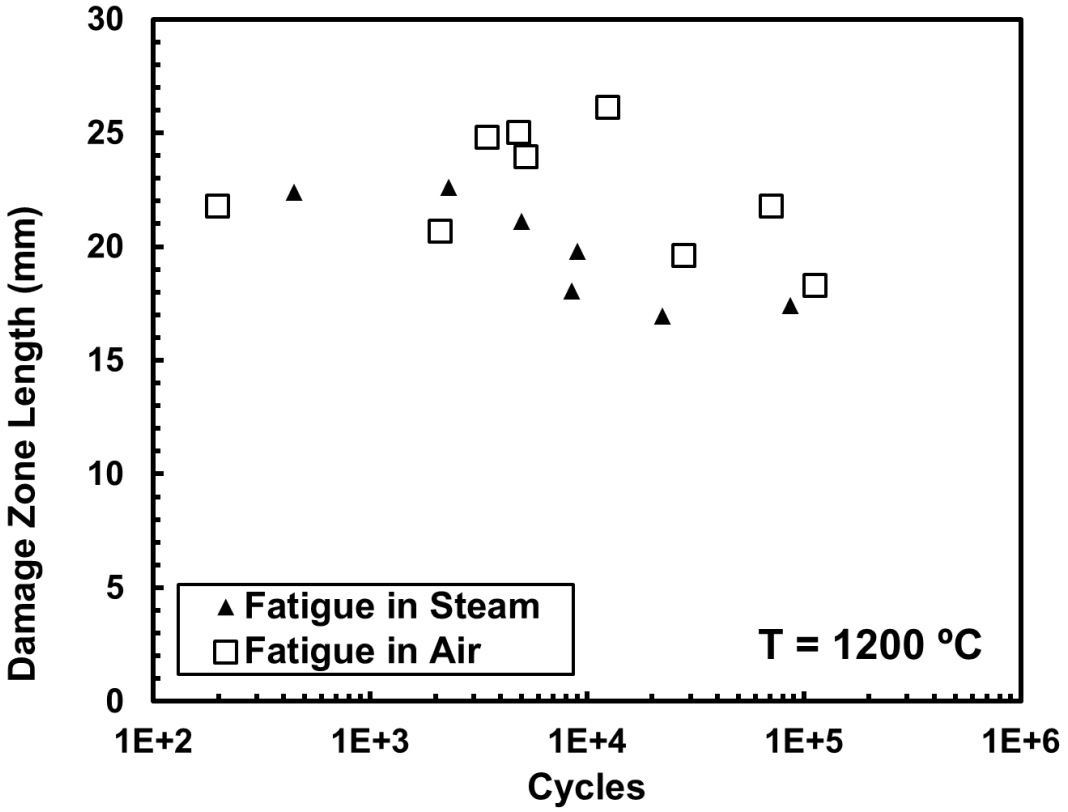

Figure 40: Length of damage zone vs. cycles to failure for N720/A specimens failed in tension-compression fatigue.

5.6.2 Scanning Electron Microscopy

A more thorough understanding of damage and failure mechanisms as well as of the influence of environment can be gained by examining the fracture surfaces with a scanning electron microscope (SEM).

Figure 41 and Figure 42 show the fracture surfaces obtained in tension tests of the N720/A specimens subjected to 10^5 cycles of prior tension-compression fatigue in air and in steam, respectively. The fracture surface of the specimen pre-fatigued in air (Figure 41 a) exhibits large areas of brushy failure and fiber pullout. In contrast the fracture surface of the specimen pre-fatigued in steam

(Figure 42 a) exhibits extensive regions of coordinated fiber fracture. This trend is further illustrated in Figure 41 b-c and Figure 42 b-c. The increased level of fiber pull-out seen in Figure 41 indicates robust crack deflection as well as relatively little bonding between fibers and matrix. Recall that the specimen pre-fatigued in air retained 100% of its tensile strength which indicates that little or no damage occurred to the fibers.

The planar fracture surface dominated by regions of coordinated fiber failure indicates that matrix densification and an increase in fiber-matrix bonding occurred in the specimen pre-fatigue in steam. The matrix cracks were able to propagate through fibers reducing the retained tensile properties. Additionally, fiber degradation due to the depletion of the mullite phase may be another factor contributing to the reduced strength and stiffness of the specimen pre-fatigued in steam.

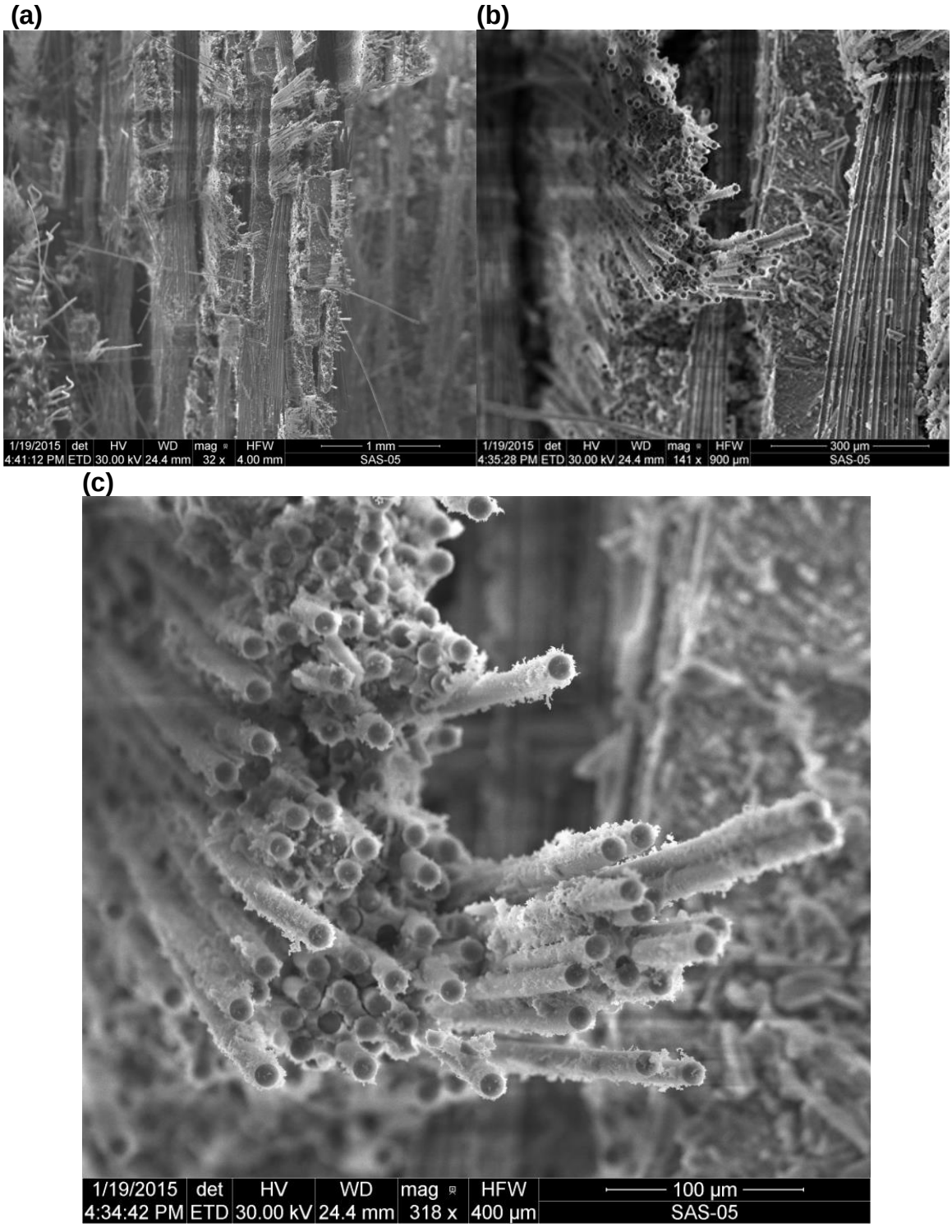

Figure 41: SEM micrographs of fracture surface obtained in tensile tests of N720/A specimens subjected to 10^5 cycles of prior tension-compression fatigue with σ_{max} = 80 MPa at 1200°C in air.

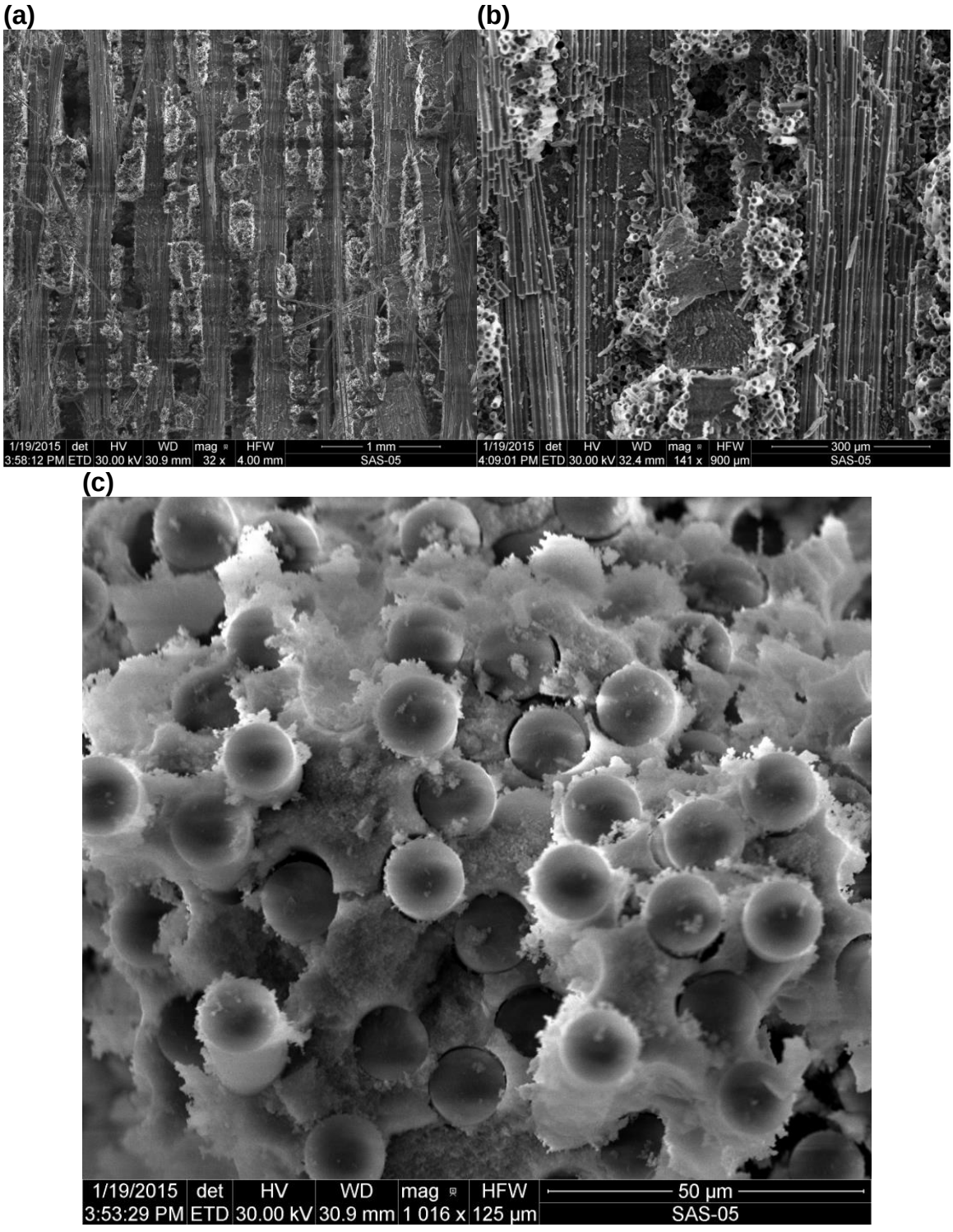

Figure 42: SEM micrographs of fracture surface obtained in tensile tests of N720/A specimens subjected to 10^5 cycles of prior tension-compression fatigue with σ_{max} = 70 MPa at 1200°C in steam.

The SEM micrographs of the fracture surfaces produced in tension-compression fatigue tests with the longest lifetimes are shown in Figure 43. The differences between the fracture surfaces obtained in air (Figure 43 a-c) and in steam (Figure 43 d-f) are evident. The fracture surface produced in air (Figure 43 a) is fibrous with considerable regions of fiber pull-out where individual fibers are clearly discernible. In contrast, the fracture surface produced in steam (Figure 43 d) is dominated by planar regions of brittle failure. Higher magnification images show the typical features of the predominantly fibrous fracture surface in air (Figure 43 b and c) and the planar fracture surface in steam (Figure 43 e and f). Notably, the fibrous fracture surface is associated with a longer damage zone and a longer fatigue life, while a planar fracture surface is accompanied by a shorter damage zone and a shorter fatigue life.

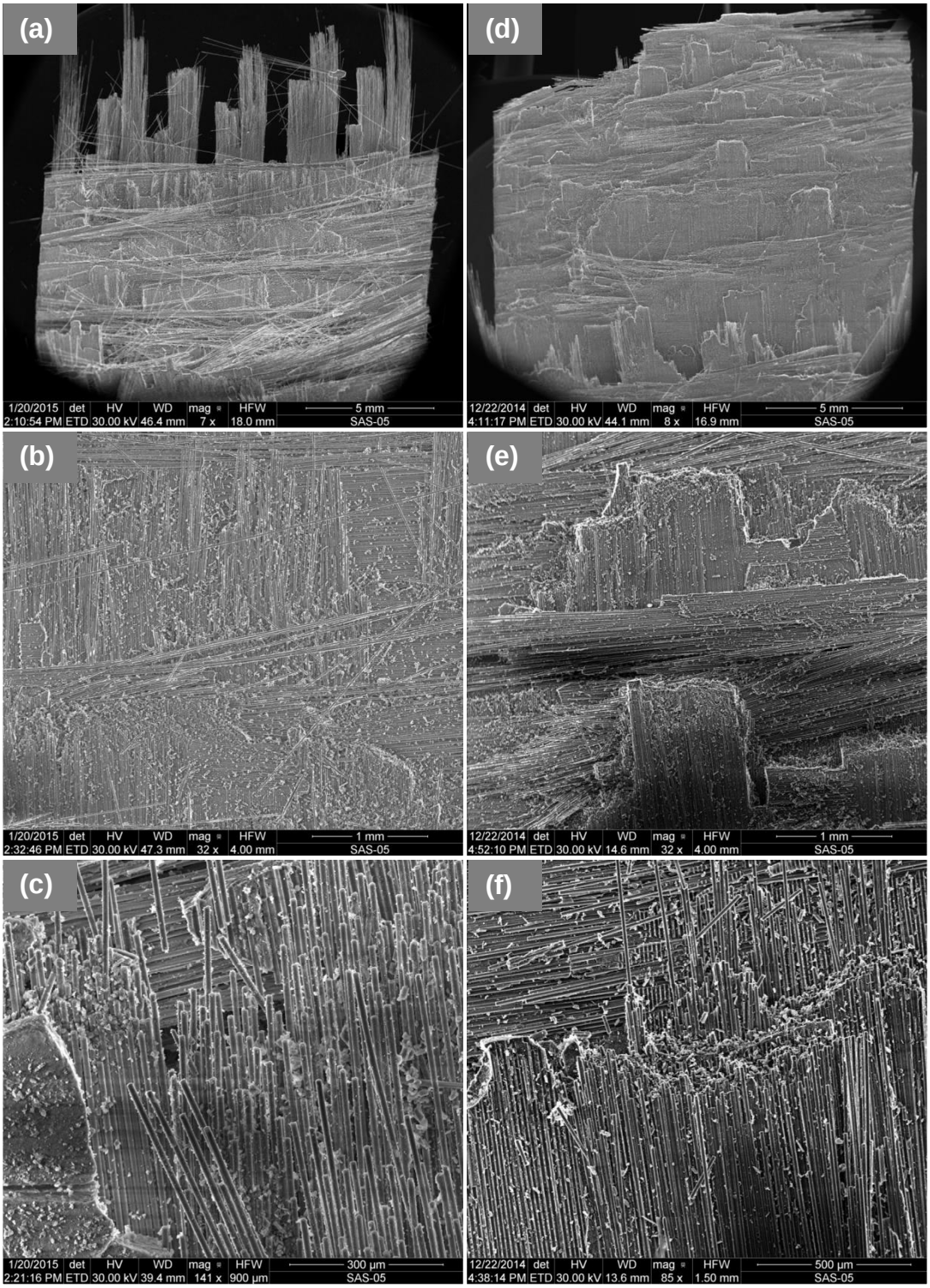

Figure 43: SEM micrographs of fracture surfaces obtained in tension-compression fatigue tests performed at 1200°C: (a)-(c) in air, σ_{max} = 80 MPa, N_f = 113,382 cycles and (d)-(f) in steam, σ_{max} = 75 MPa, N_f = 86,548 cycles.

The SEM micrographs of the fracture surfaces produced in tension-compression fatigue with the shortest cyclic lives are shown in Figure 44 and Figure 45. However, the differences between the fracture surfaces obtained in air (Figure 44 a-c) and in steam (Figure 44 d-f) are not as pronounced. The fracture surface produced in air is somewhat brushier than that produced in steam. Still, higher magnification images reveal increased fiber/matrix bonding in steam (Figure 45), indicating progressive matrix densification in steam. Note that the cyclic life in air was more than 10 times that in steam. Progressive matrix densification in steam accounts for the reduction in cyclic life.

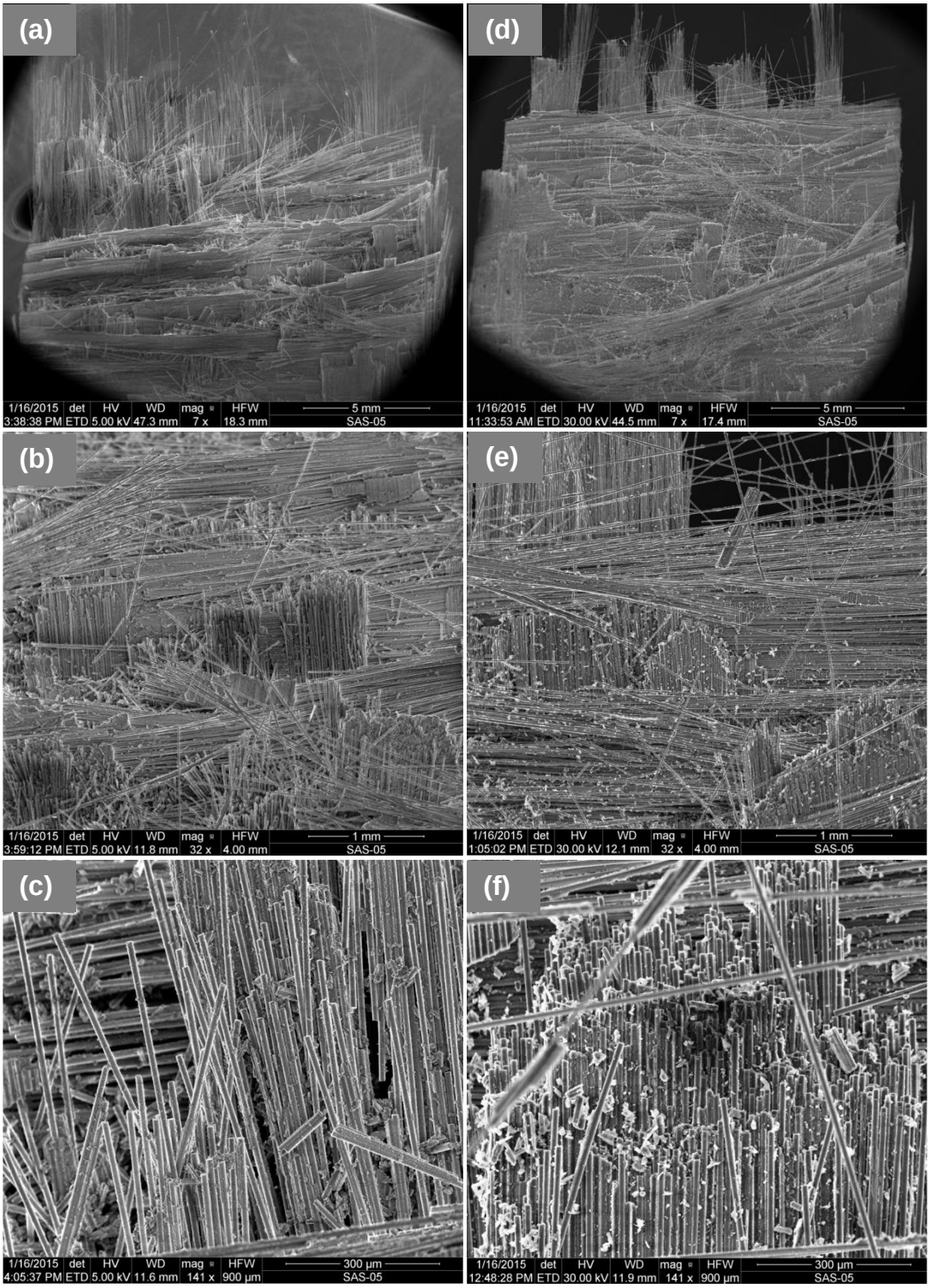

Figure 44: SEM micrographs of fracture surfaces obtained in tension-compression fatigue tests performed at 1200°C: (a)-(c) in air, σ_{max} = 100 MPa, N_f = 5,264 cycles and (d)-(f) in steam, σ_{max} = 100 MPa, N_f = 450 cycles.

(a)

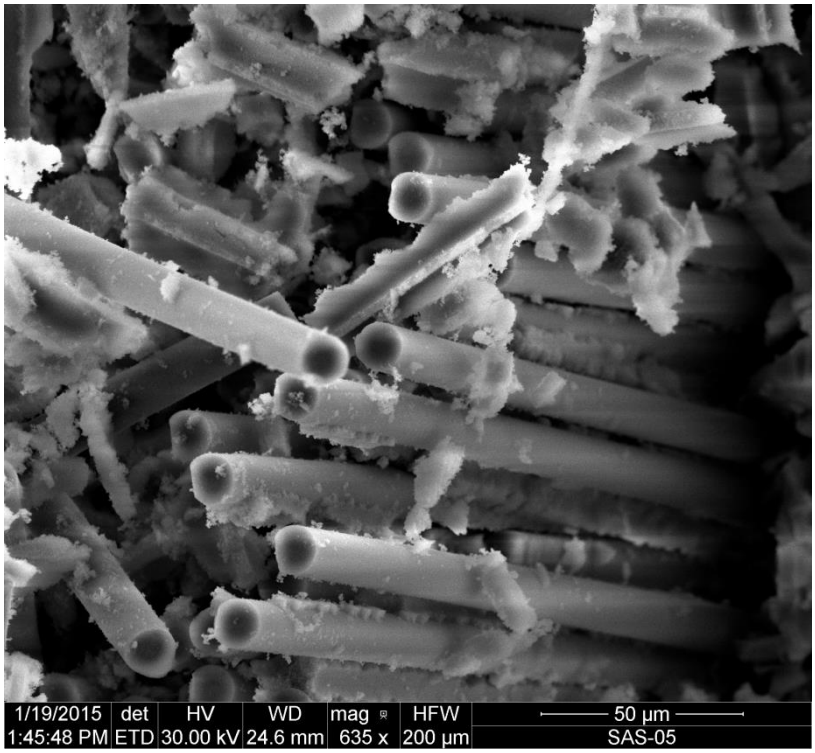

(b)

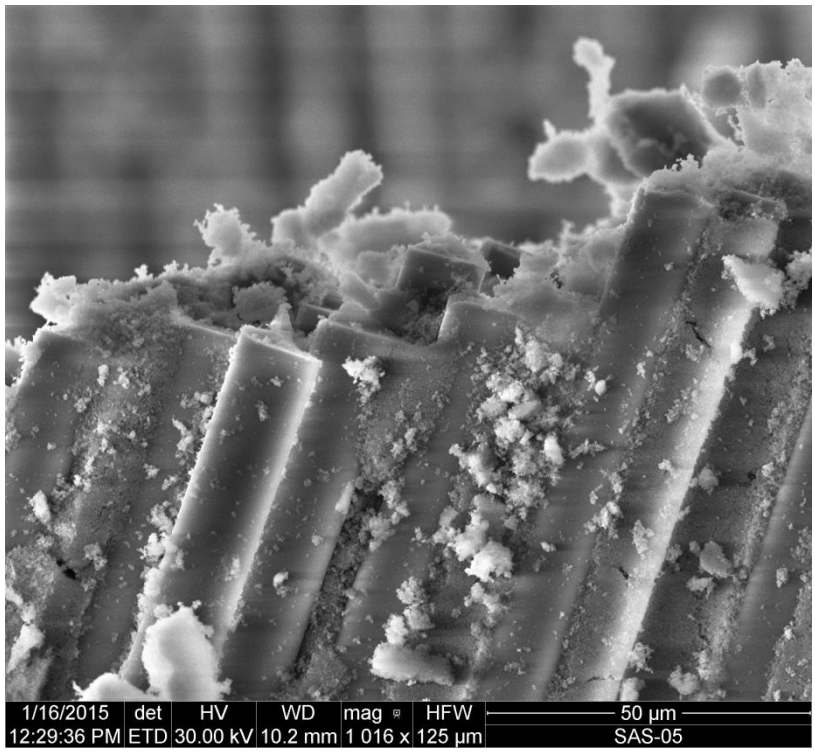

Figure 45: SEM micrographs of fracture surfaces obtained in tension-compression fatigue tests performed at 1200°C: (a) in air, σ_{max} = 100 MPa, N_f = 5,264 cycles and (b) in steam, σ_{max} = 100 MPa, N_f = 450 cycles.

It is evident that the test environment has a strong influence on composite microstructure. Brushy fracture surfaces dominated by areas of uncorrelated fiber failure and fiber pullout are produced in air. These microstructural features are indicative of damage-tolerant behavior and are generally accompanied by longer fatigue lifetimes. Contrastingly, coordinated fiber failure and planar fracture are prevalent in steam. Planar fracture surfaces typically represent brittle behavior and a shortened fatigue life of a CMC.

Mehrman [21] examined tension-tension fatigue behavior of the N720/A composite at 1200°C in air in steam. Mehrman also reported an increase in coordinated fiber fracture and a reduction in fatigue life (about one order of magnitude) due to steam. Mehrman showed that introducing hold times at the maximum load during fatigue cycling reduced fatigue lives. Hetrick [39] found that tension-tension fatigue lives decrease by about two orders of magnitude when the fatigue frequency decreased by one order of magnitude. Reducing the fatigue frequency effectively increased time at higher load in the test environment. Hetrick concluded that for longer fatigue lives the fatigue frequency must be sufficiently high to continually break apart the matrix to counteract matrix densification and fiber-matrix bonding. Results of this work demonstrate that including compression in the load cycle produced a similar reduction in fatigue life and similar changes in the fracture surface appearance. Hence it is likely that the compression portion of the tension-compression fatigue cycle promotes matrix densification and fiber-matrix bonding.

Because all fatigue failures in this study occurred during a compression portion of the cycle, the fracture surfaces produced in fatigue were considerably different from those produced under tensile loading. These differences are particularly apparent in the SEM micrographs with higher magnification. Examine the individual fibers and their fracture surfaces in Figure 46 and Figure 47. Fiber micro-buckling and resulting compression curl are readily visible.

Compressive failure in fiber-reinforced composites is generally associated with micro-buckling of the fibers [52-55]. The in-phase buckling of the fibers causes flexural stresses in the fibers. Compression curls are formed when a planar crack normal to the loading direction forms on the tension side of the fiber. The crack then changes direction due to internal shear stresses and becomes more parallel to the loading direction. Finally, the crack front curls towards the opposite edge of the fiber and the ultimate fracture of the fiber occurs. Fiber micro-buckling was prevalent throughout the fracture surfaces of the specimens that failed in compression during tension-compression fatigue, but not in the fracture surfaces produced in tension.

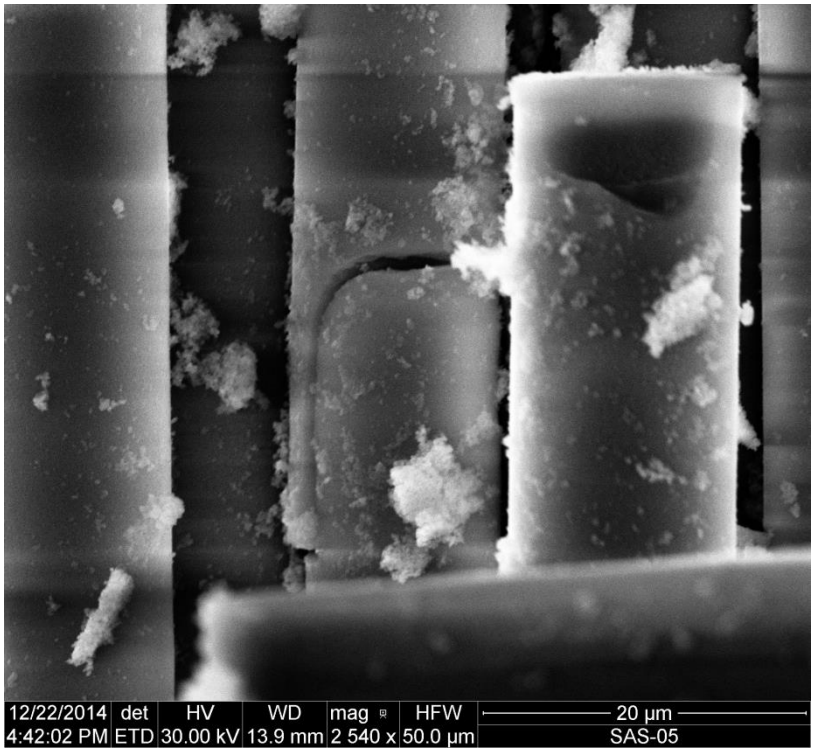

(a)

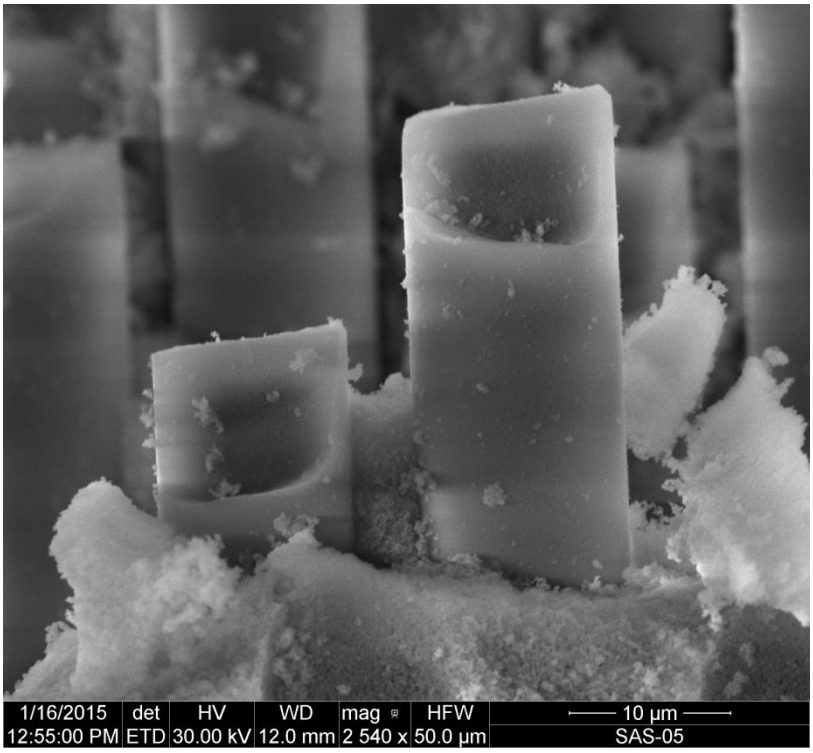

(b)

Figure 46: Fracture surface obtained in tension-compression fatigue. Failure occurred during compression portion of fatigue cycle. Note fracture surfaces of the individual fibers.

(a)

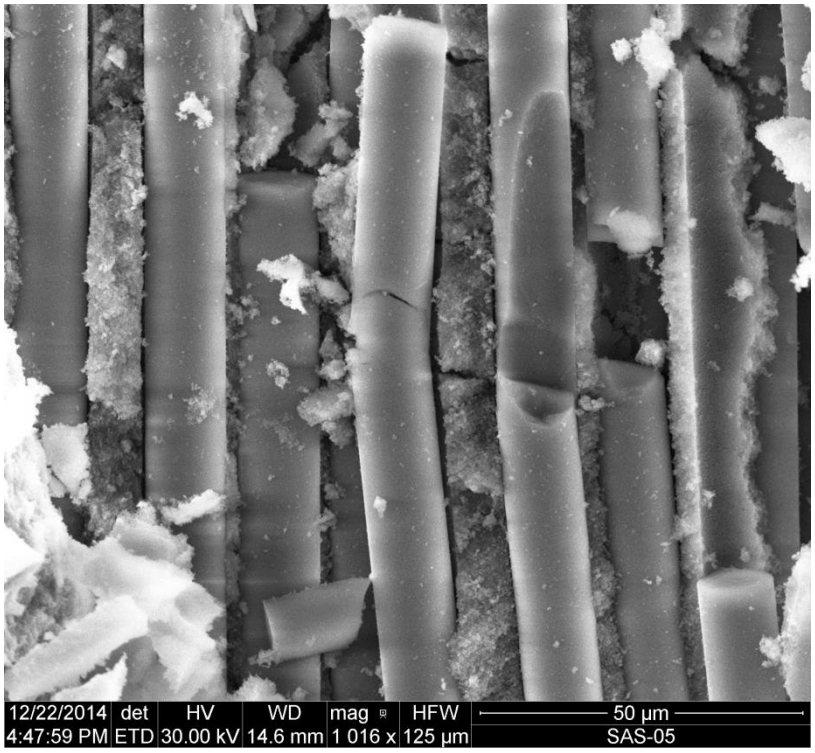

(b)

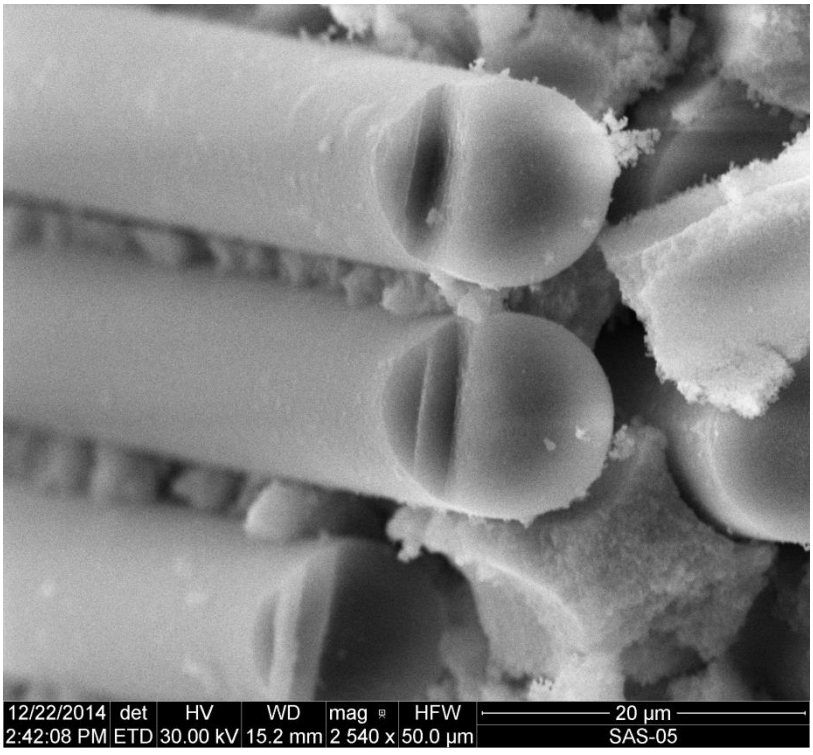

Figure 47: Fracture surface obtained in tension-compression fatigue. Failure occurred during compression portion of fatigue cycle. (a) Fiber micro-buckling. (b) Compression curl.

VI. Conclusions and Recommendations

6.1 Conclusions

Tension-compression fatigue behavior of N720/A ceramic composite was investigated at 1.0 Hz at 1200°C in air and in steam. The R (ratio of minimum to maximum stress) was -1 and the fatigue stresses ranged from 60 to 120 MPa. The fatigue run-out was achieved at 80 MPa (40%UTS) in air and at 70 MPa (35%UTS) in steam. The presence of steam noticeably degrades tension-compression fatigue performance. Fatigue lives were reduced by approximately an order of magnitude due to steam. Prior fatigue in air with the maximum stress of 80 MPa causes no reduction in tensile strength, suggesting that no damage occurred to the fibers. Prior fatigue in steam with the maximum stresses of 60 and 70 MPa reduced the tensile strength by 17-38%, indicating significant degradation of fiber performance. Notably, prior fatigue in air or in steam resulted in modulus loss of about 50%.

Tension-compression fatigue is considerably more damaging than tension-tension fatigue. Including compression in the load cycle can decrease fatigue lifetimes by nearly three orders of magnitude. At 1200°C tension-compression fatigue was also found to be more damaging than compressive creep in air. Conversely, in steam compressive creep was more damaging than tension-compression fatigue.

The damage and failure of the N720/A composite at 1200°C in both air and steam environments are due to loss of matrix porosity and increased fiber-matrix

bonding. In steam, depletion of mullite phase from the N720 fibers also contributes to the degradation of composite performance. During tension-tension fatigue in air, cyclic loading opposes matrix densification by causing progressive matrix cracking and weakening of the fiber-matrix interface. In steam, the beneficial effects of tension-tension cycling on damage tolerance of the N720/A composite compensate for the negative effects of the loss of mullite from the N720 fibers, resulting in improved durability. Compressive loading during tension-compression fatigue promotes matrix densification and strengthening of fiber/matrix bond, which serve to degrade damage tolerance of the composite and to reduce fatigue lives. In steam, matrix densification and strengthening of fiber/matrix bond under compression work together with the degradation of N720 fibers to further degrade the fatigue performance of the composite. In air and in steam the appearance of the fracture surface may be correlated with tension-compression fatigue life. A brushy fracture surface is indicative of longer cyclic life. In contrast, planar fracture surface corresponds to a short fatigue life.

6.2 Recommendations

The results presented here should be reproduced using multiple specimens for each test condition in order to show reproducibility and the magnitude of statistical variation. The microstructural investigation performed in this research effort should be expanded to include examination of the composite with a transmission electron microscope (TEM). The TEM observations would permit direct assessment of the effect of loading type and/or test environment on

changes in matrix porosity. TEM observations would also enable a more thorough evaluation of microstructural changes in the fibers under different loading conditions and/or test environments. Results of such investigation could be complemented with those reported by Armani [51] for the N720 fiber tows.

Tension-compression fatigue tests with different values of R should be performed to assess the influence of mean stress on fatigue performance of N720/A composite.

Appendix A: Additional Optical Micrographs

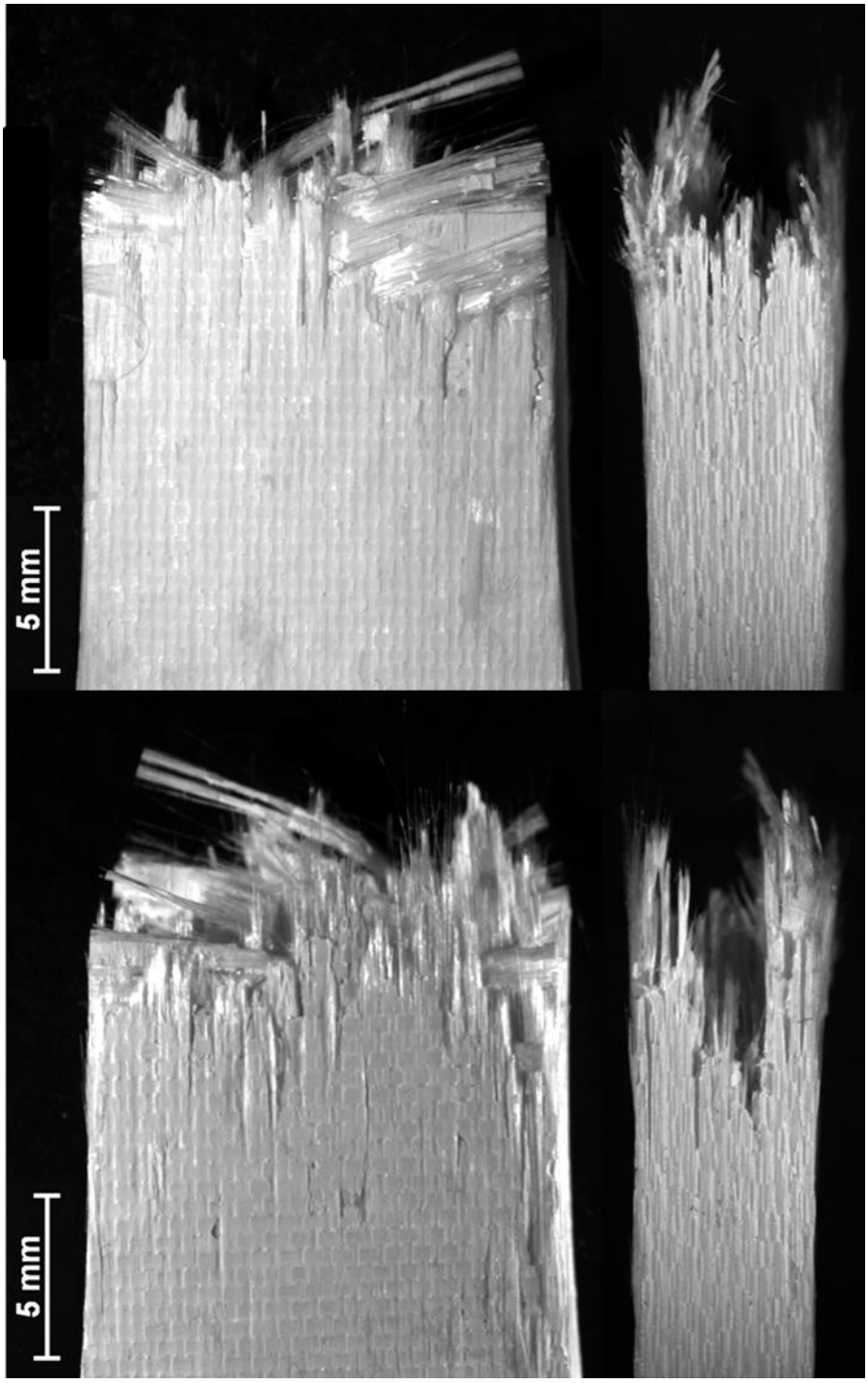

Figure 48: Optical micrographs of fracture surface obtained in a tension to failure test at 1200°C in air. Specimen number 1.

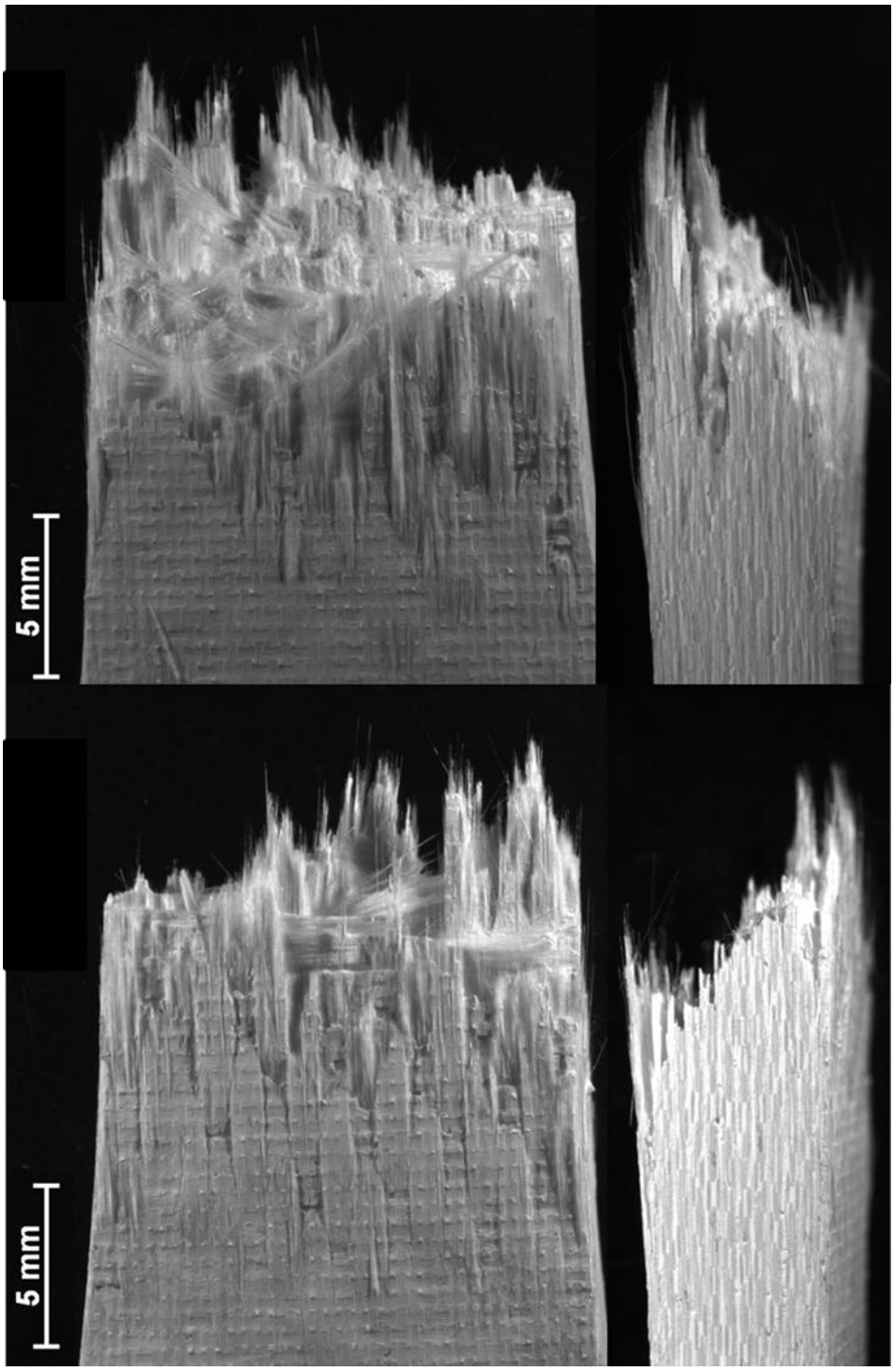

Figure 49: Optical micrographs of fracture surface obtained in a tension to failure test at 1200°C in air. Specimen number 2.

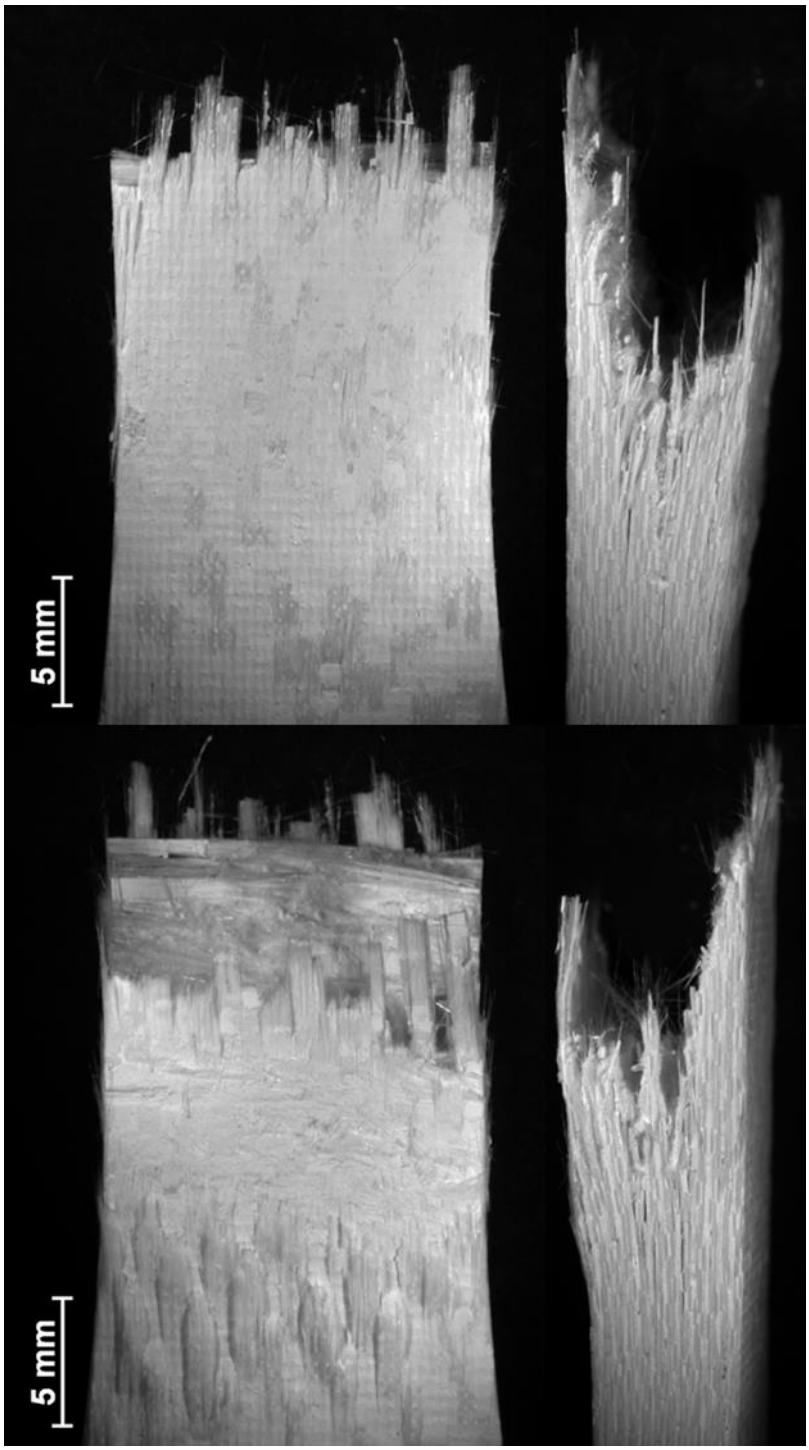

Figure 50: Fracture surface obtained in a fatigue test conducted at 1200°C in air. σ_{max} = 90 MPa, N_f = 71,484 cycles.

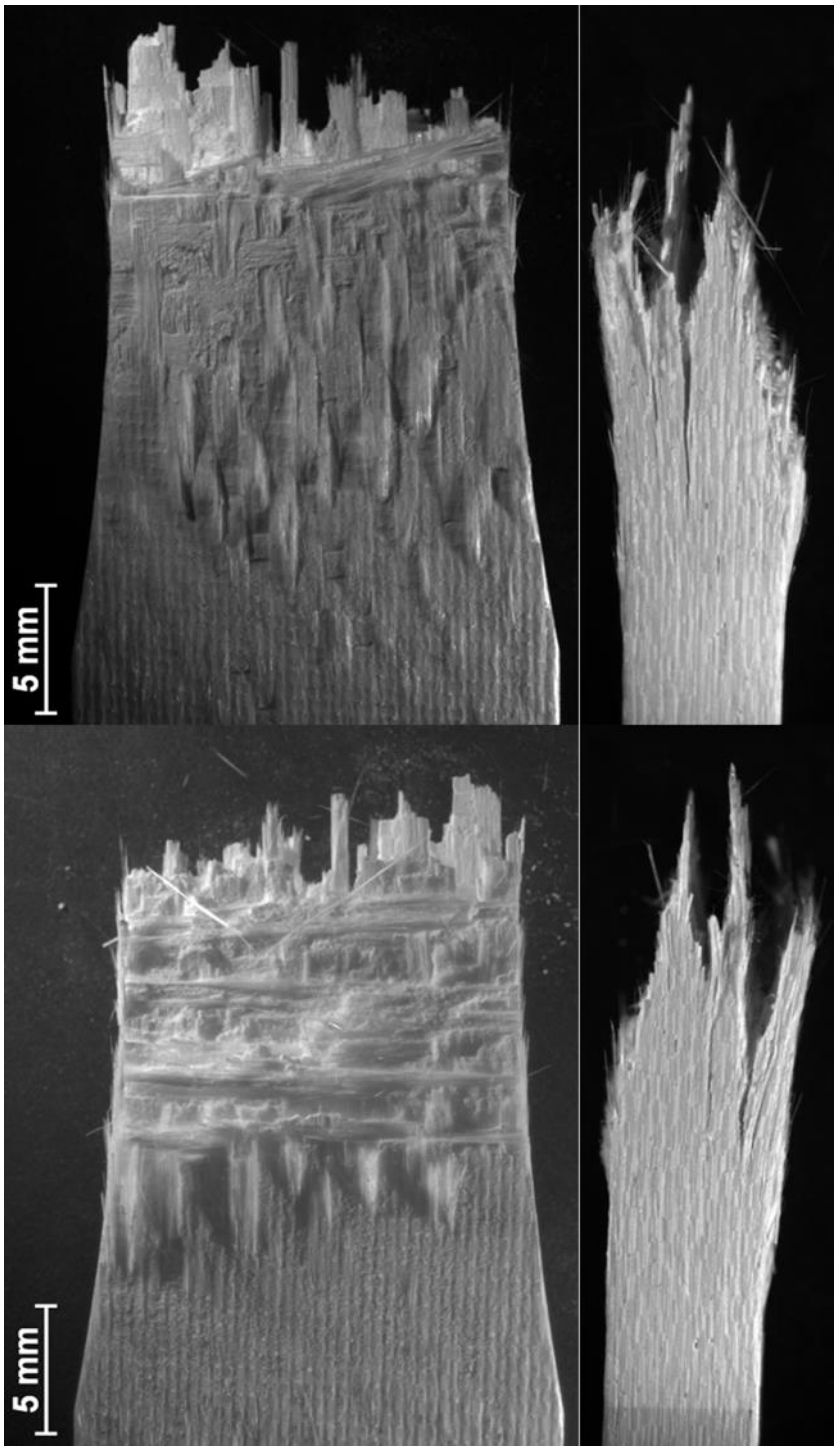

Figure 51: Fracture surface obtained in a fatigue test conducted at 1200°C in air. σ_{max} = 90 MPa, N_f = 28,159 cycles.

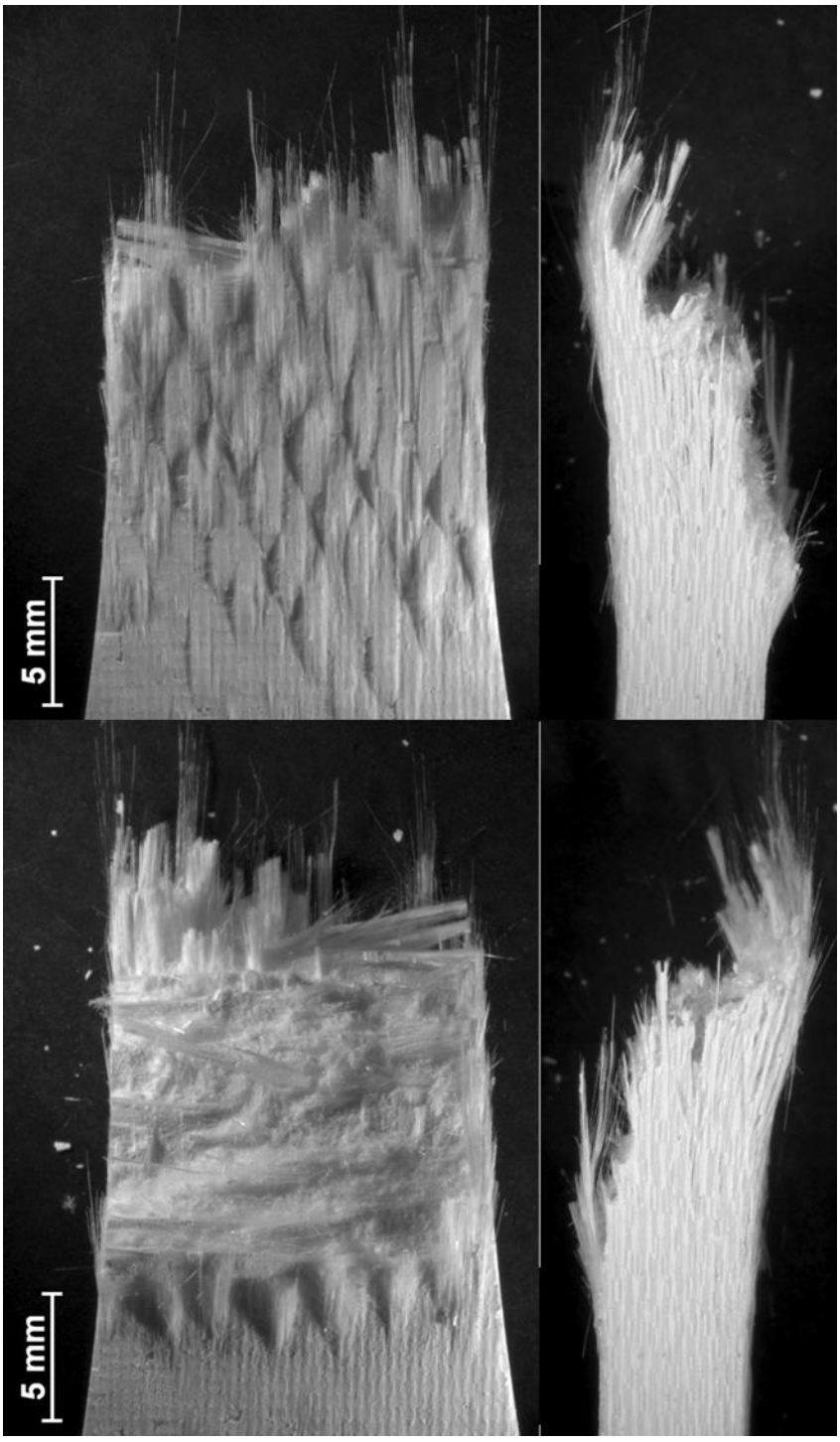

Figure 52: Fracture surface obtained in a fatigue test conducted at 1200°C in air. σ_{max} = 100 MPa, N_f = 5,264 cycles.

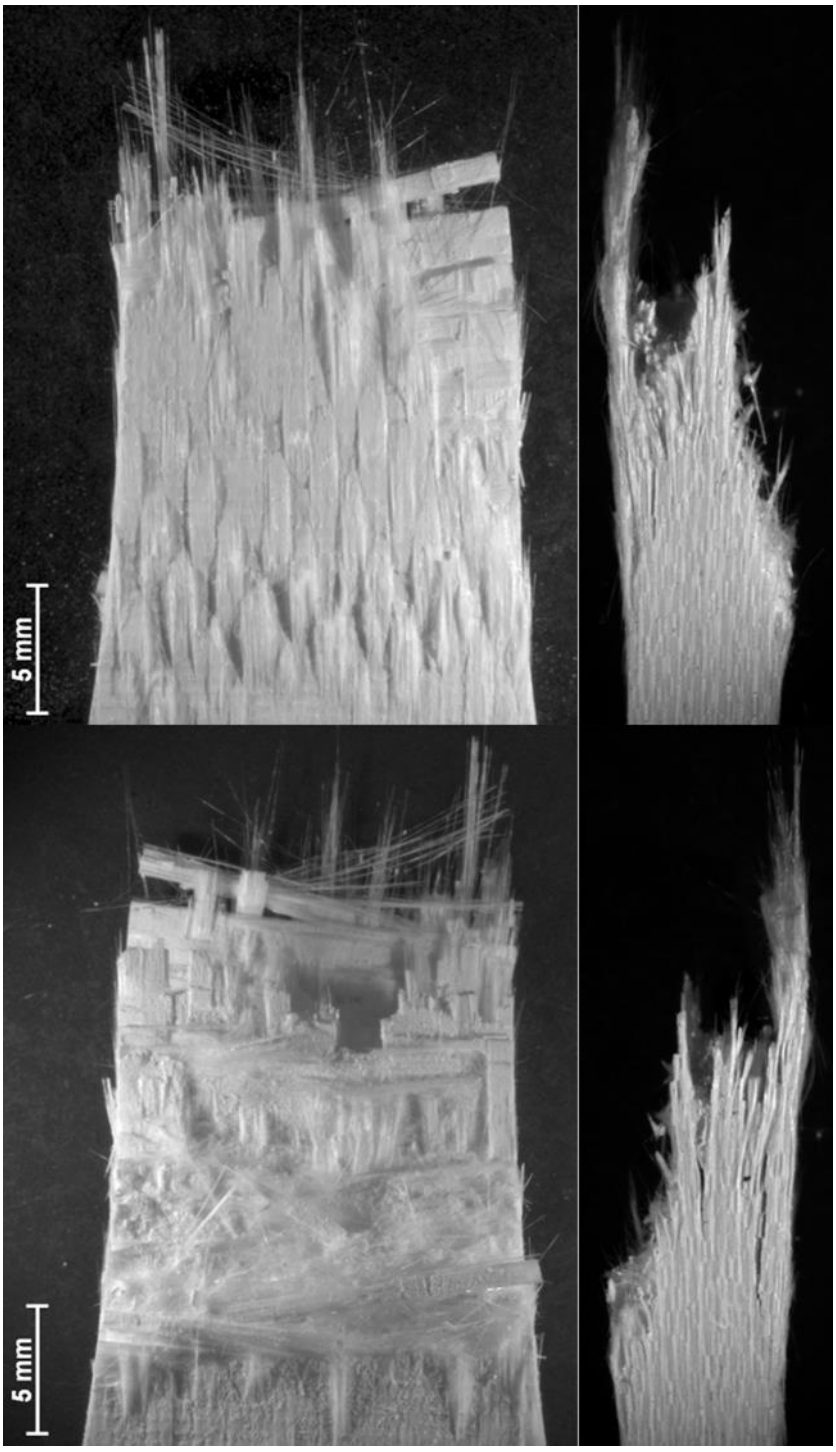

Figure 53: Fracture surface obtained in a fatigue test conducted at 1200°C in air. σ_{max} = 100 MPa, N_f = 4,902 cycles.

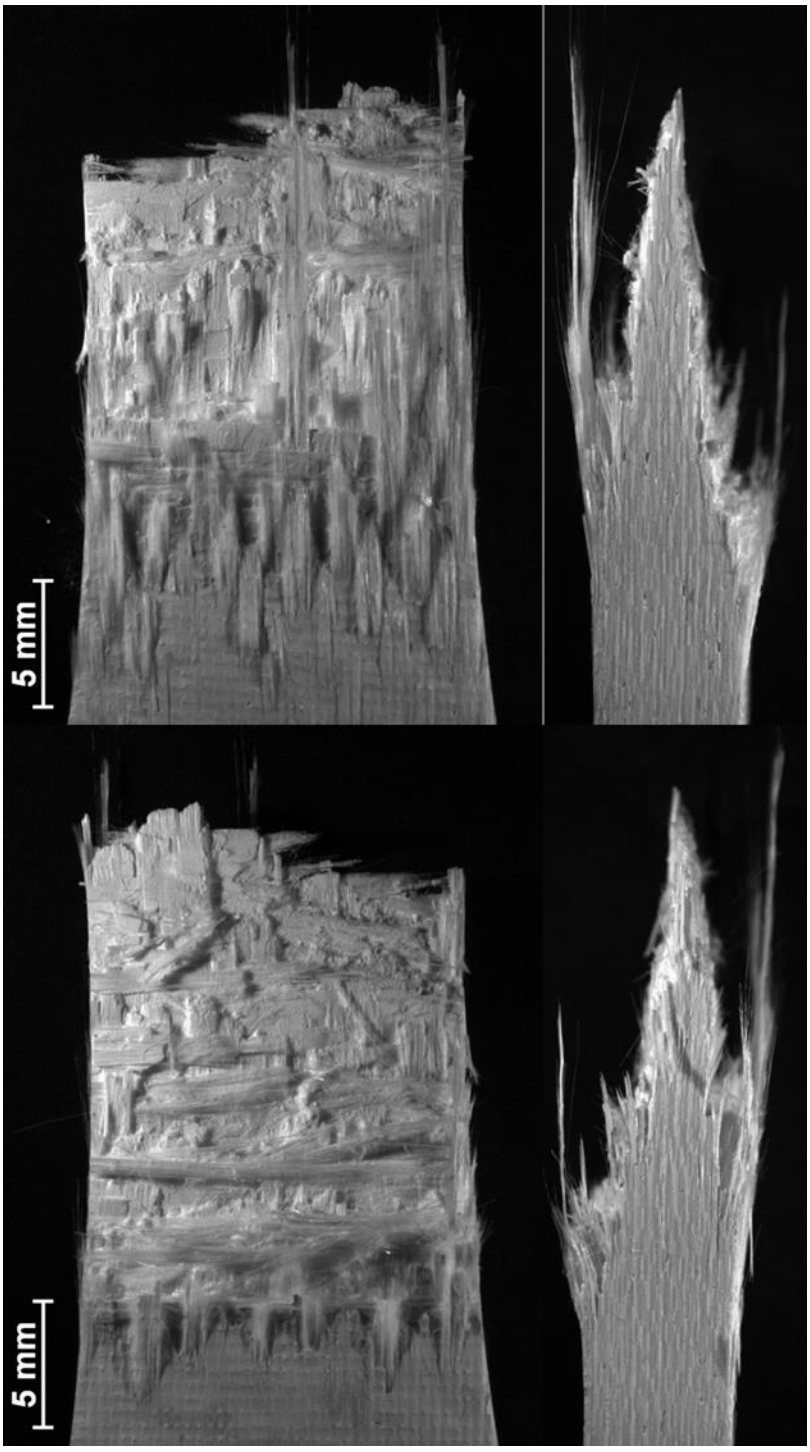

Figure 54: Fracture surface obtained in a fatigue test conducted at 1200°C in air. σ_{max} = 110 MPa, N_f = 3,488 cycles.

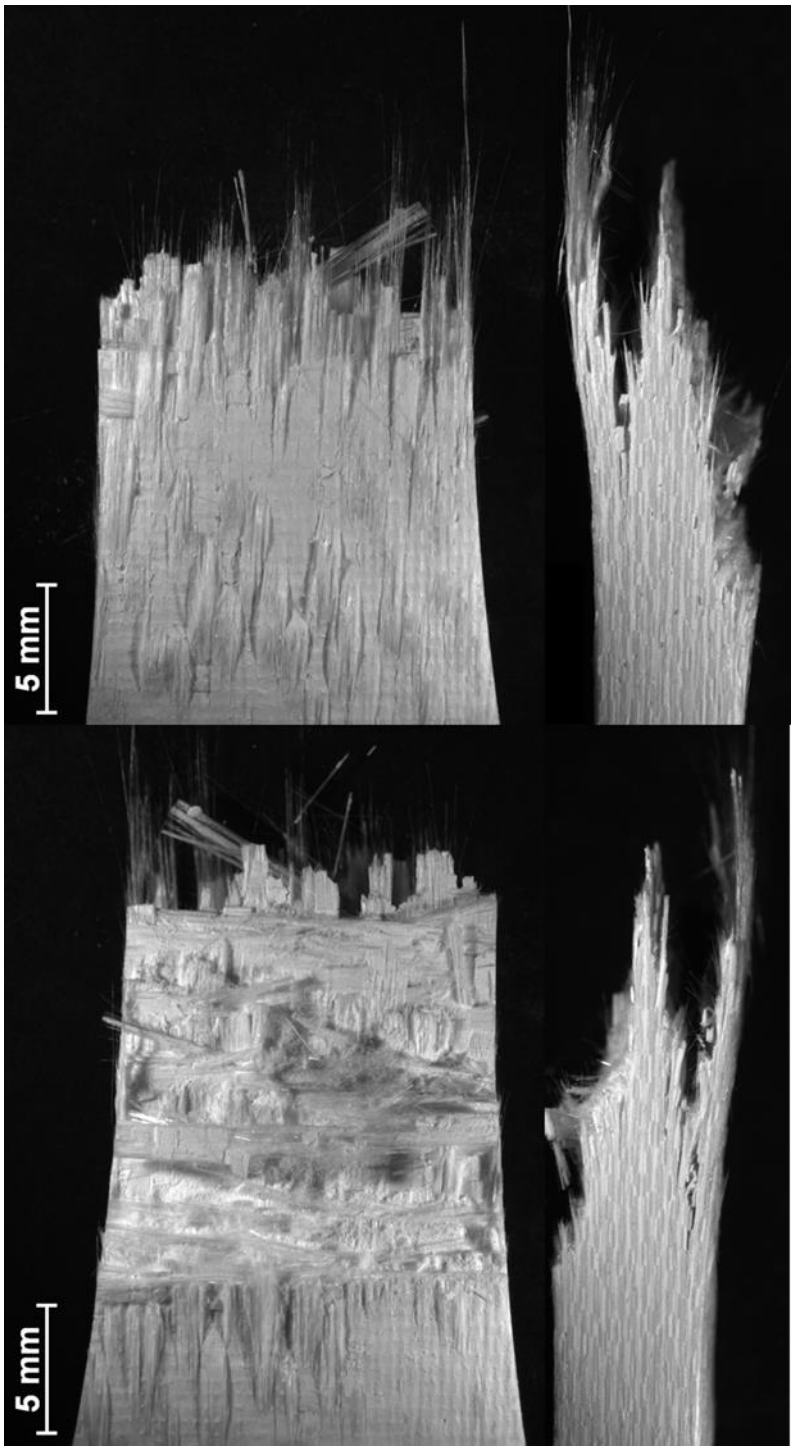

Figure 55: Fracture surface obtained in a fatigue test conducted at 1200°C in air. σ_{max} = 110 MPa, N_f = 2,121 cycles.

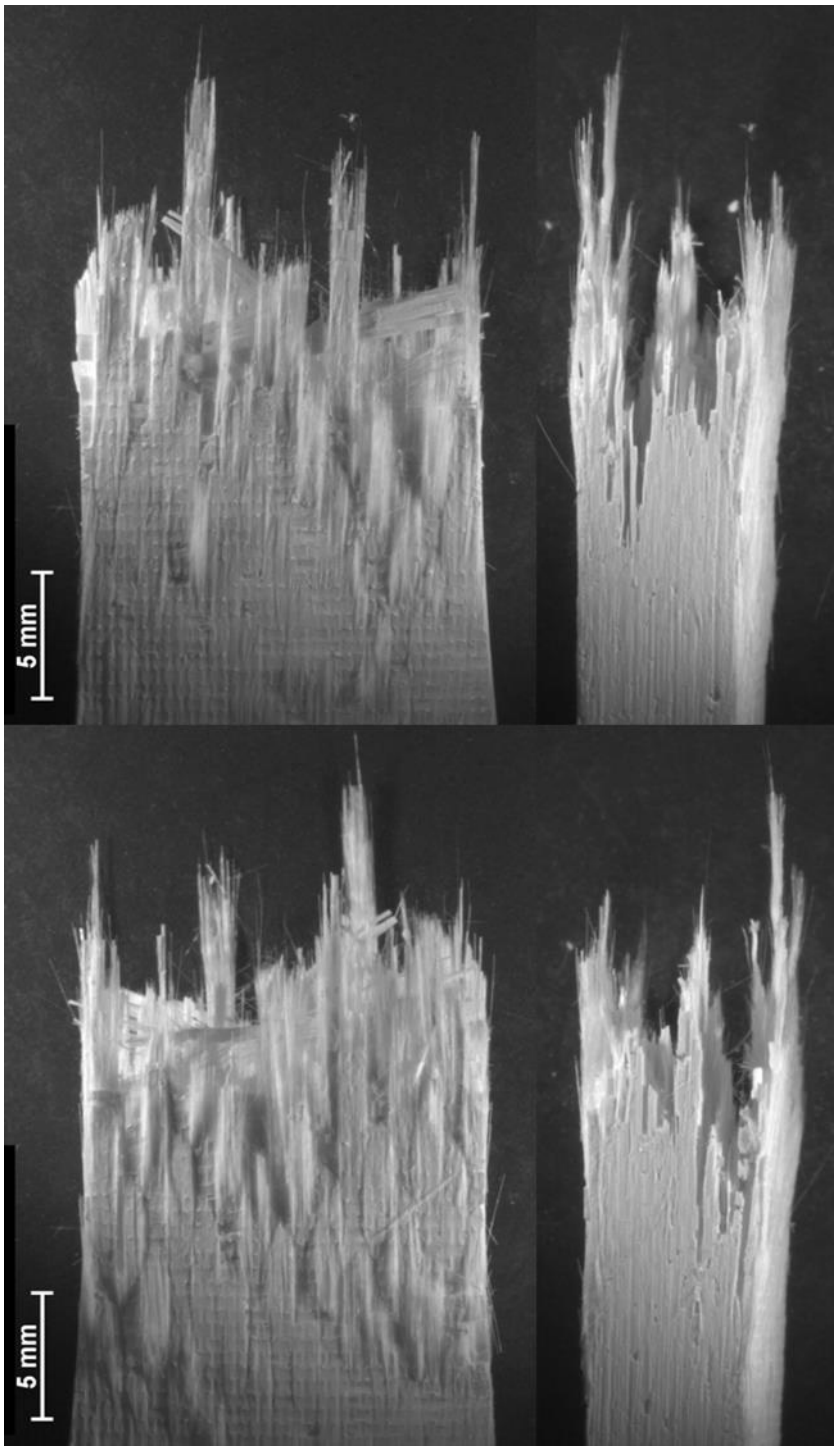

Figure 56: Optical micrographs of fracture surface obtained in a tensile test of a specimen subjected to 10^5 cycles of prior tension-compression fatigue with σ_{max} = 60 MPa at 1200°C in steam. Specimen number 13.

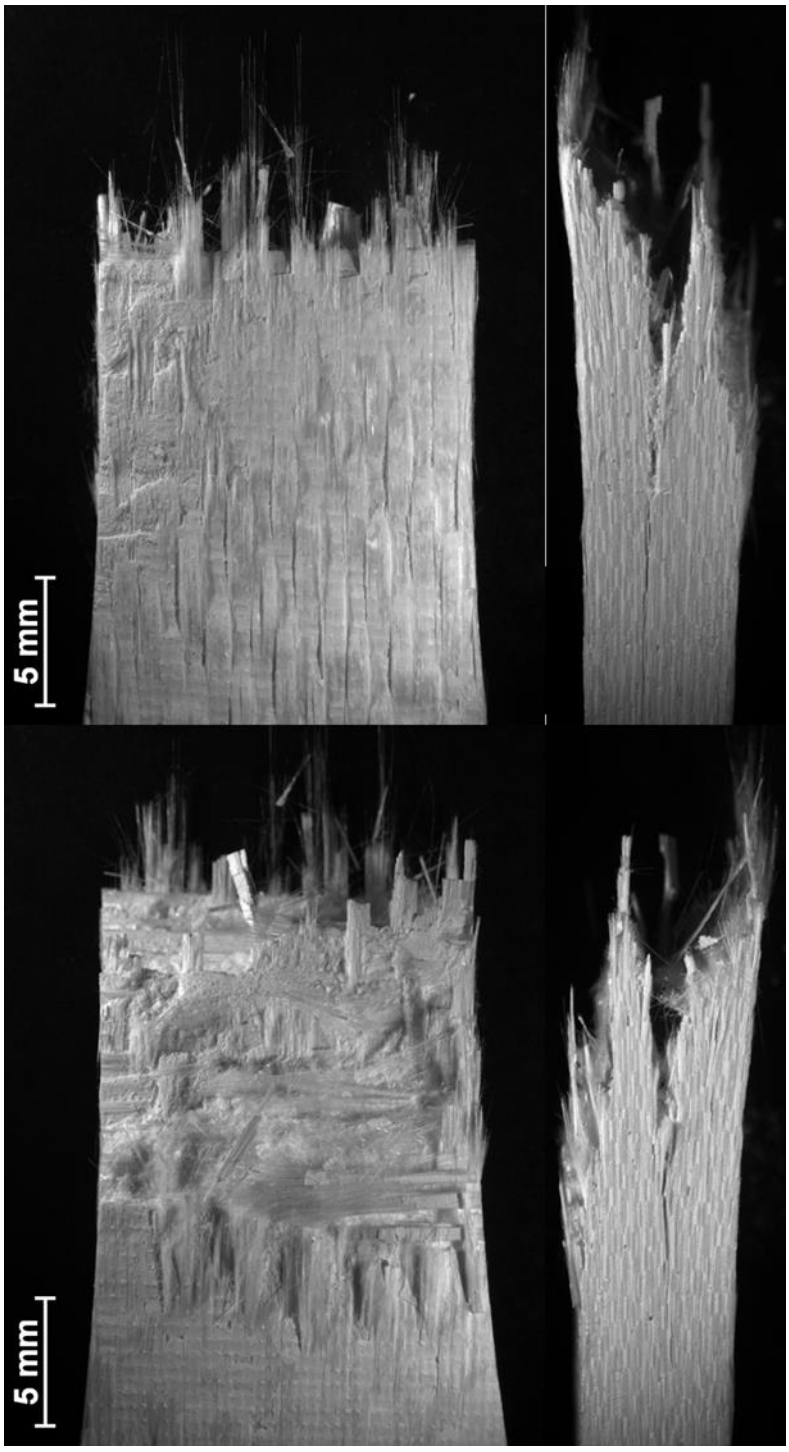

Figure 57: Fracture surface obtained in a fatigue test conducted at 1200°C in steam. σ_{max} = 80 MPa, N_f = 22,426 cycles.

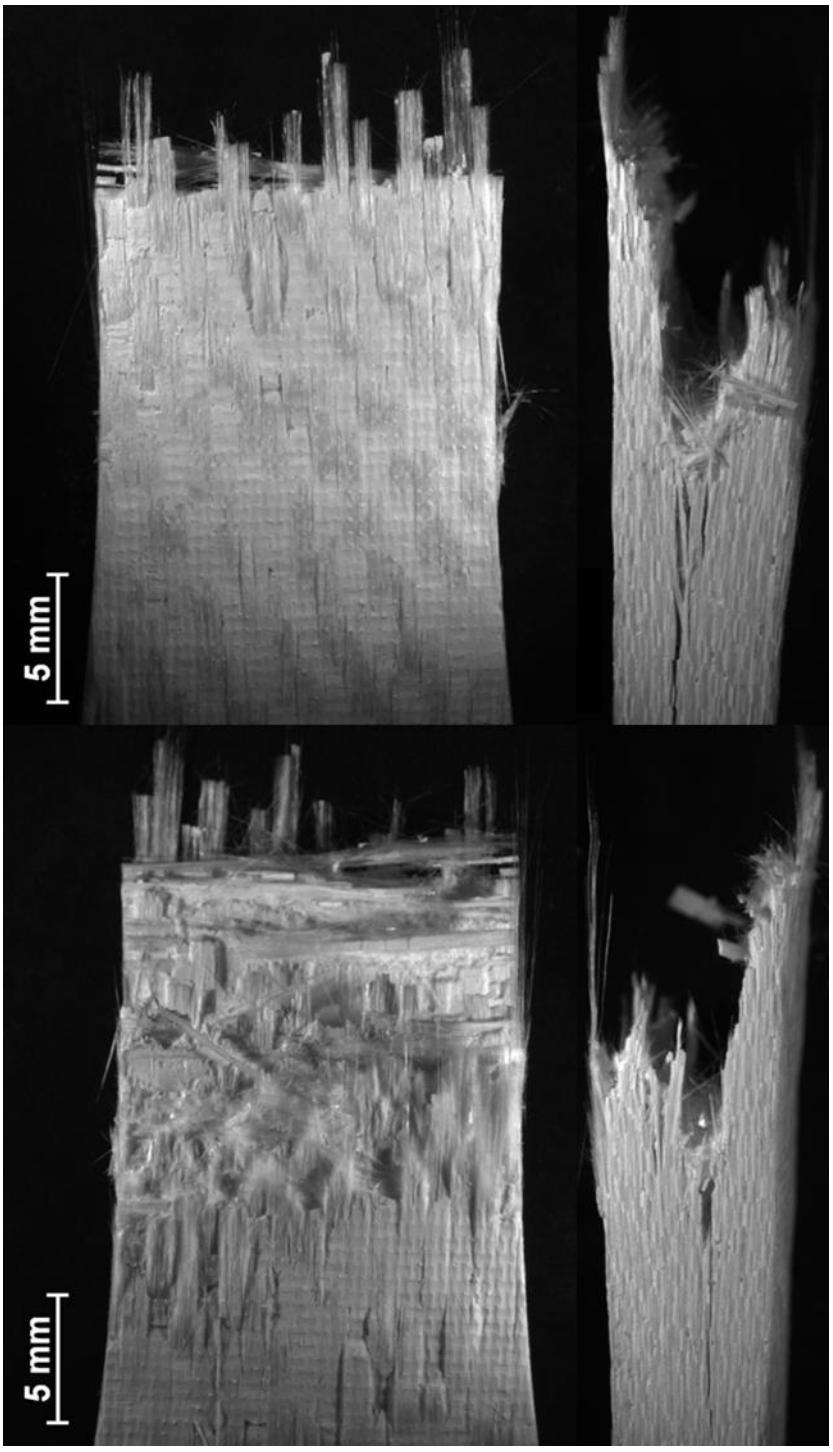

Figure 58: Fracture surface obtained in a fatigue test conducted at 1200°C in steam. σ_{max} = 80 MPa, N_f = 8,581 cycles.

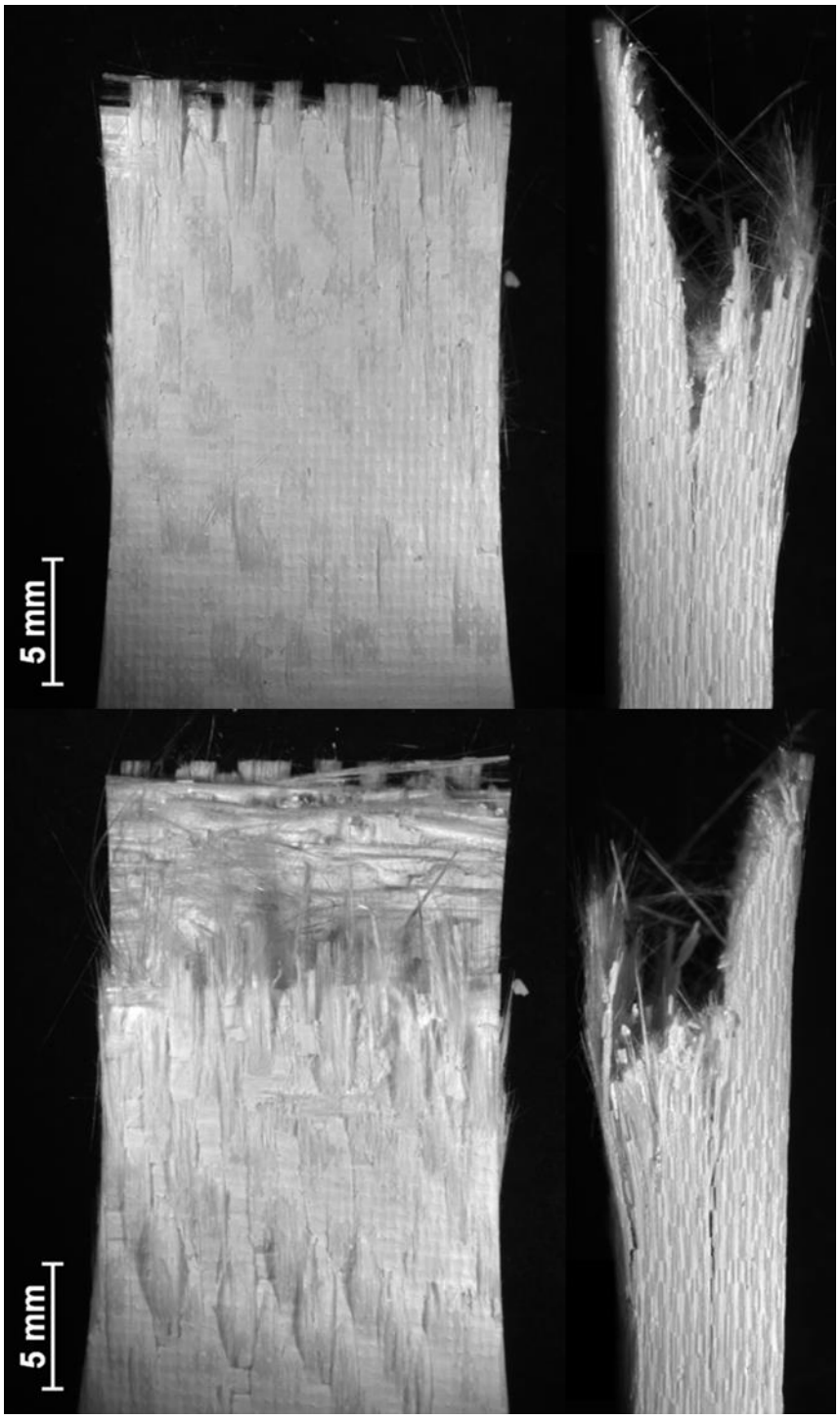

Figure 59: Fracture surface obtained in a fatigue test conducted at 1200°C in steam. σ_{max} = 90 MPa, N_f = 5,023 cycles.

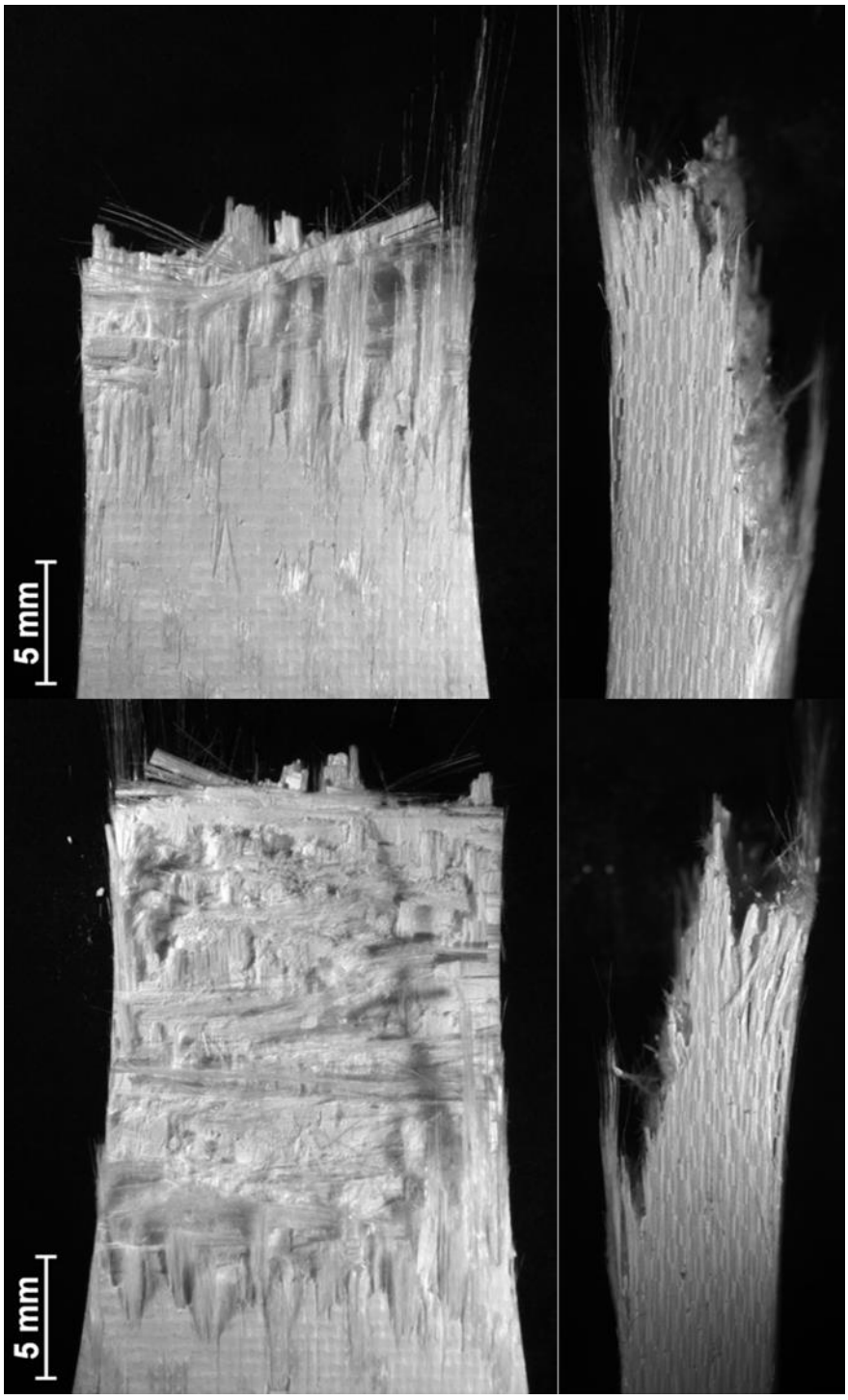

Figure 60: Fracture surface obtained in a fatigue test conducted at 1200°C in steam. σ_{max} = 95 MPa, N_f = 2,316 cycles.

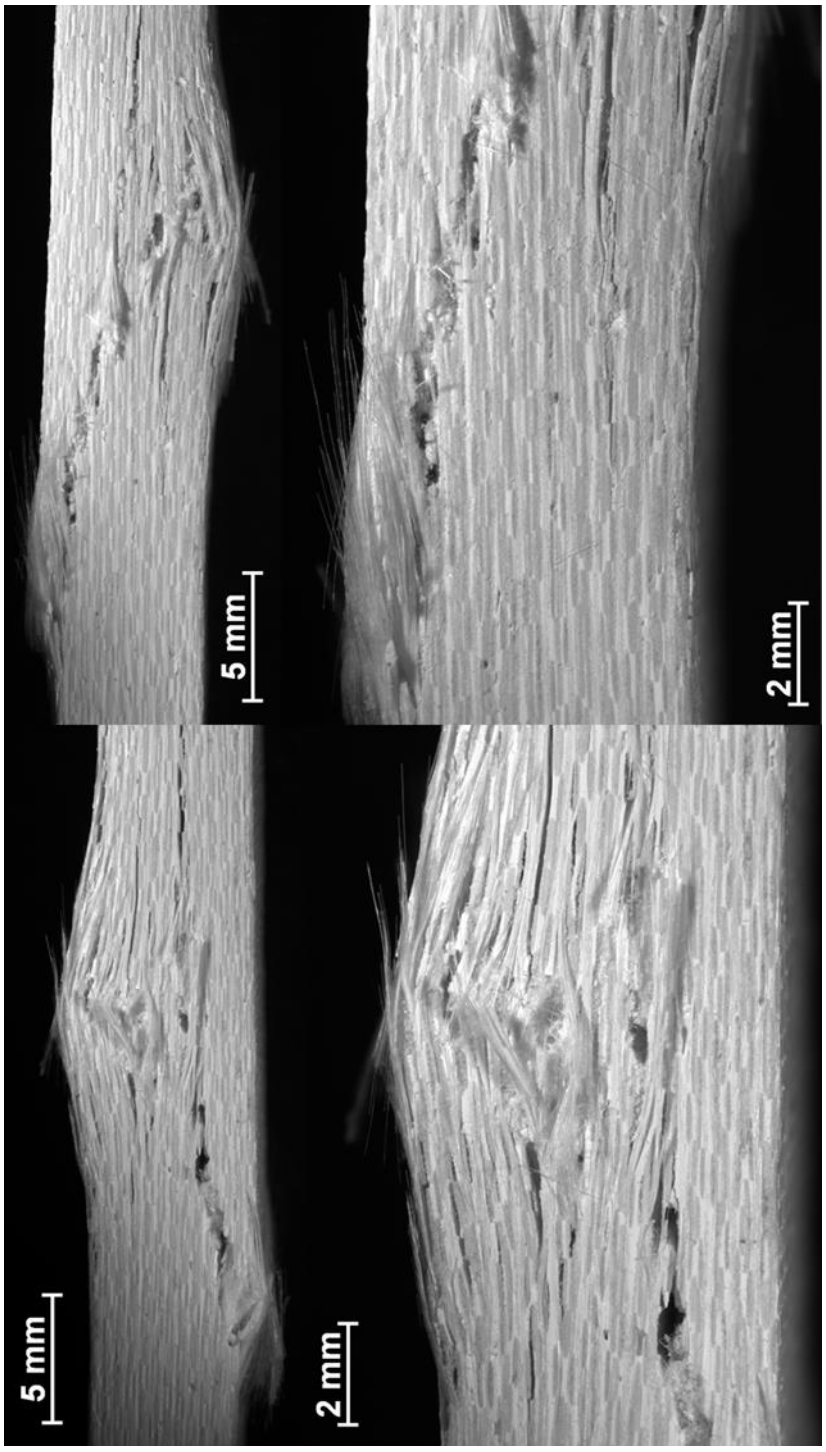

Figure 61: Fracture surface obtained in a fatigue test conducted at 1200°C in steam. σ_{max} = 100 MPa, N_f = 247 cycles.

Appendix B: Additional SEM Micrographs

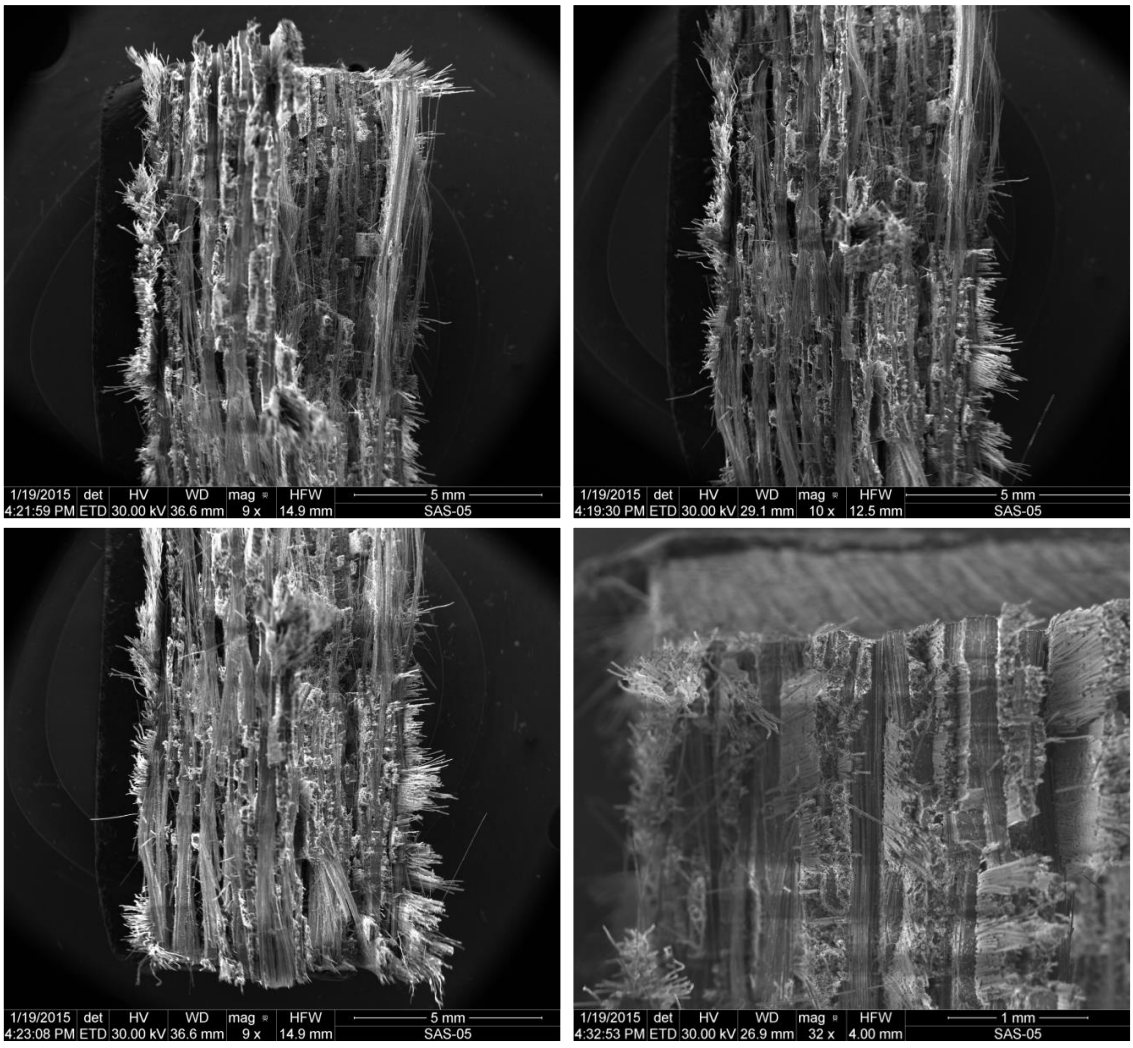

Figure 62: SEM micrographs of a fracture surface obtained in a tensile test of N720/A specimen subjected to 10^5 cycles of prior tension-compression fatigue with σ_{max} = 80 MPa at 1200°C in air.

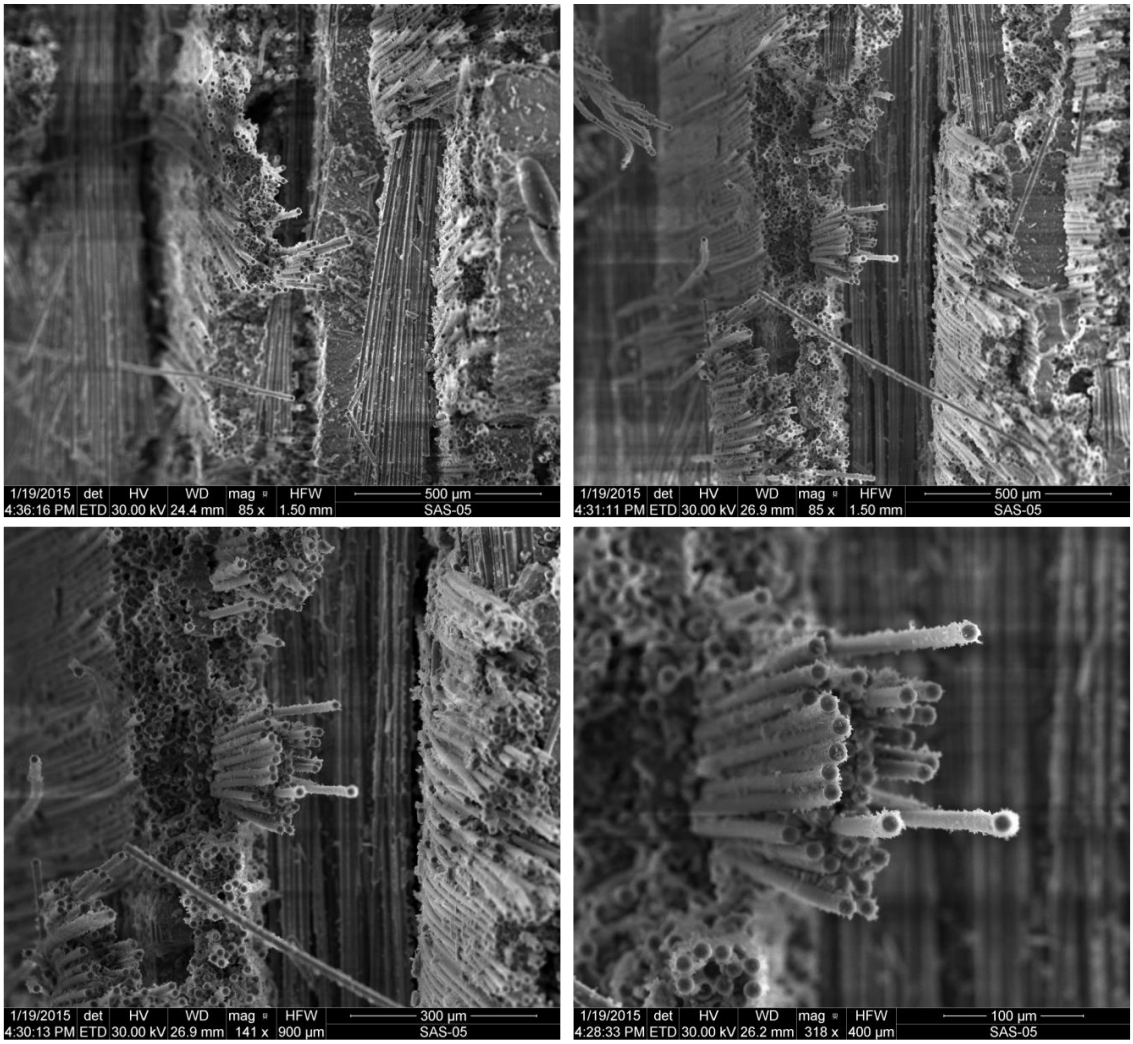

Figure 62 (continued): SEM micrographs of a fracture surface obtained in a tensile test of N720/A specimen subjected to 10^5 cycles of prior tension-compression fatigue with σ_{max} = 80 MPa at 1200°C in air.

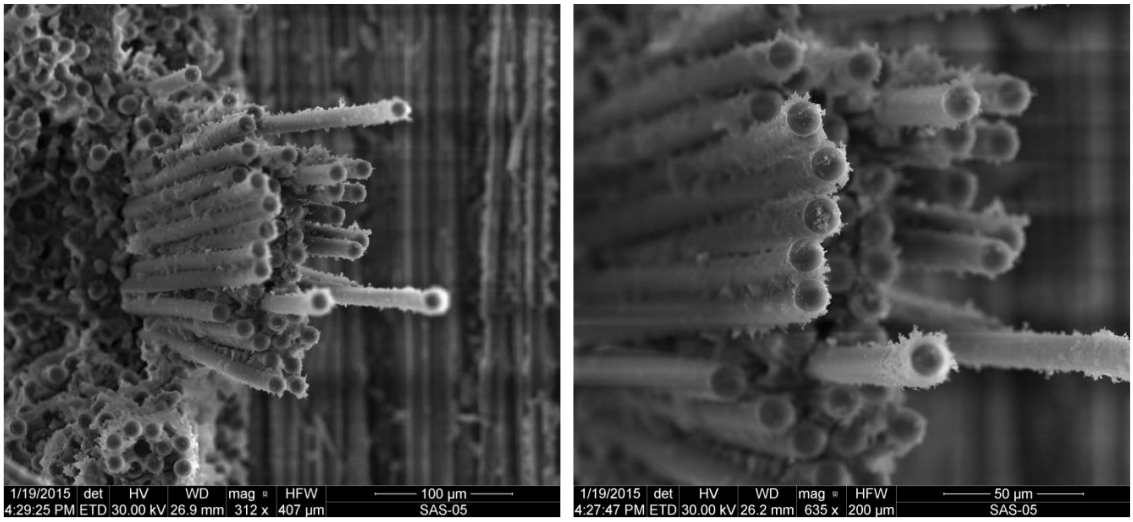

Figure 62 (continued): SEM micrographs of a fracture surface obtained in a tensile test of N720/A specimen subjected to 10^5 cycles of prior tension-compression fatigue with σ_{max} = 80 MPa at 1200°C in air.

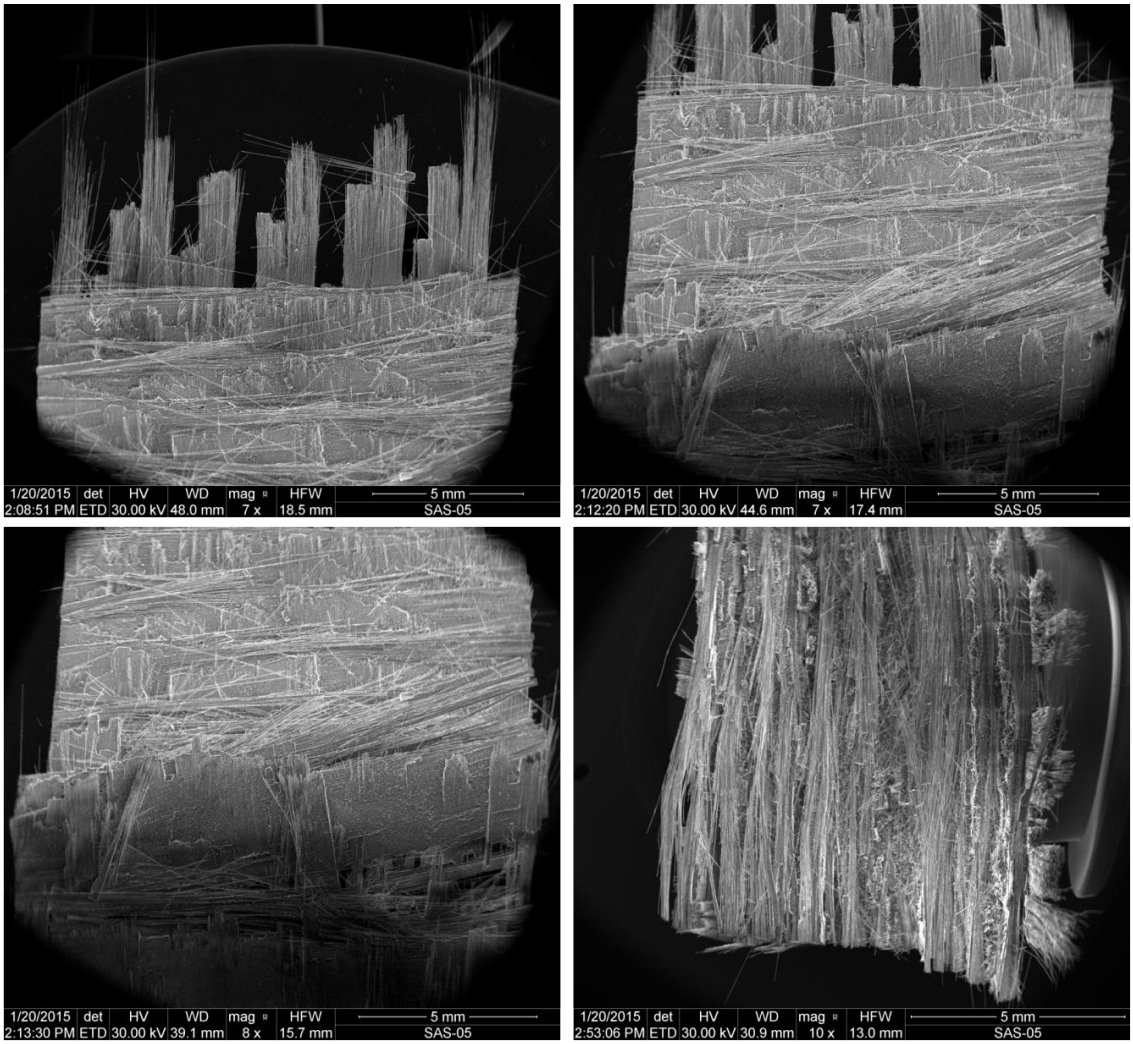

Figure 63: SEM micrographs of a fracture surface obtained in tension-compression fatigue tests performed at 1200°C in air, σ_{max} = 80 MPa, N_f = 113,382 cycles.

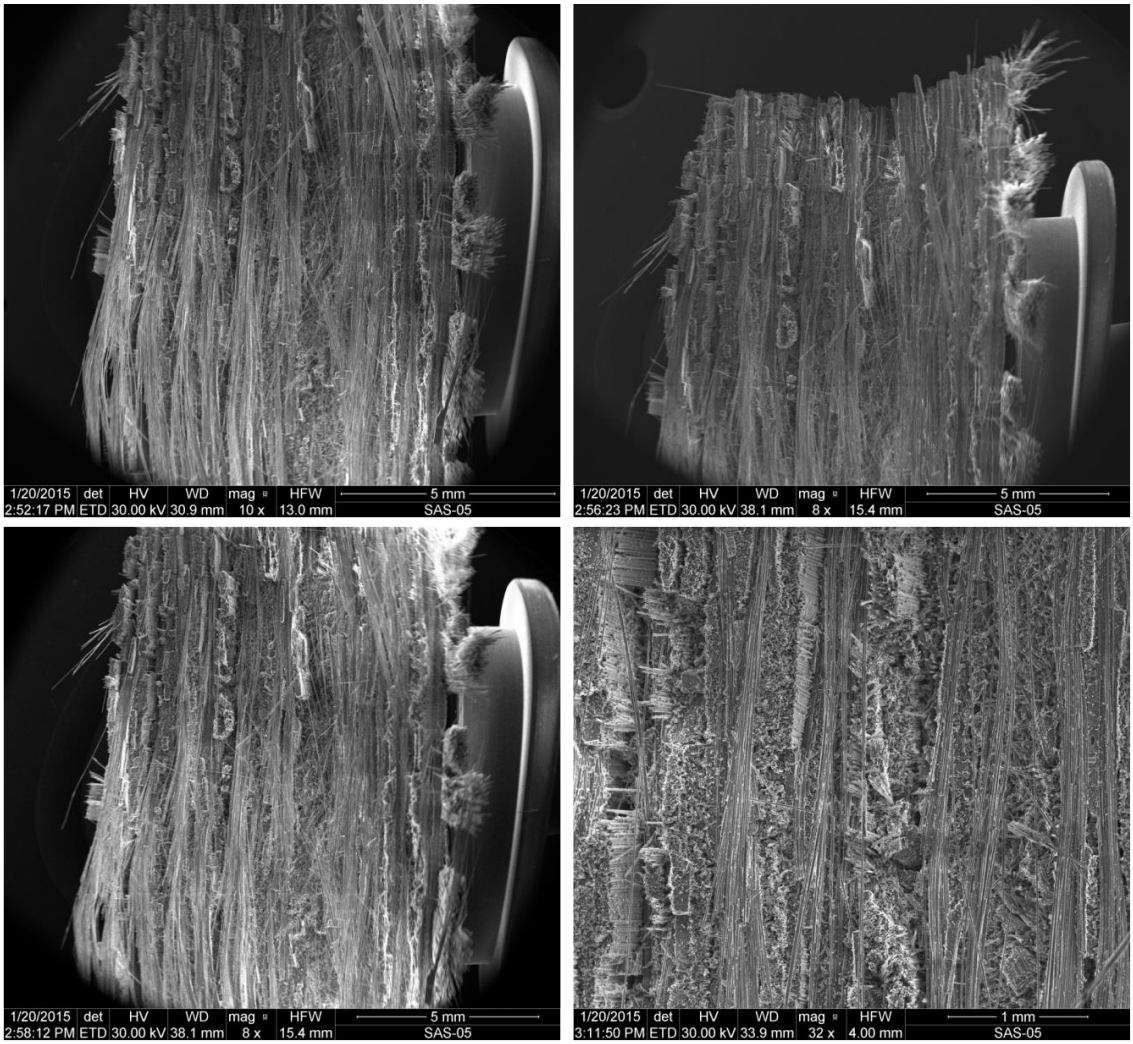

Figure 63 (continued): SEM micrographs of a fracture surface obtained in tension-compression fatigue tests performed at 1200°C in air, σ_{max} = 80 MPa, N_f = 113,382 cycles.

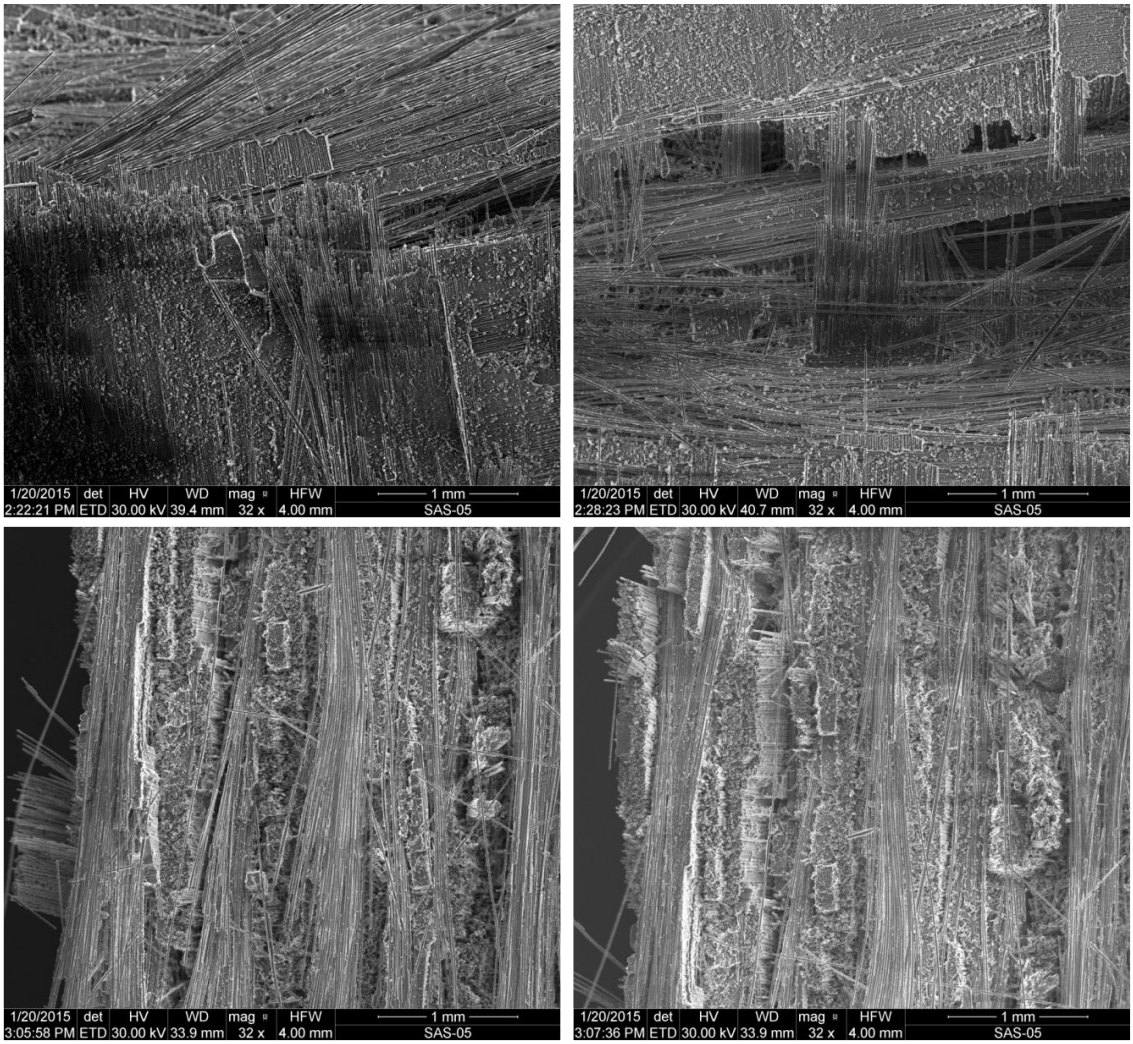

Figure 63 (continued): SEM micrographs of a fracture surface obtained in tension-compression fatigue tests performed at 1200°C in air, σ_{max} = 80 MPa, N_f = 113,382 cycles.

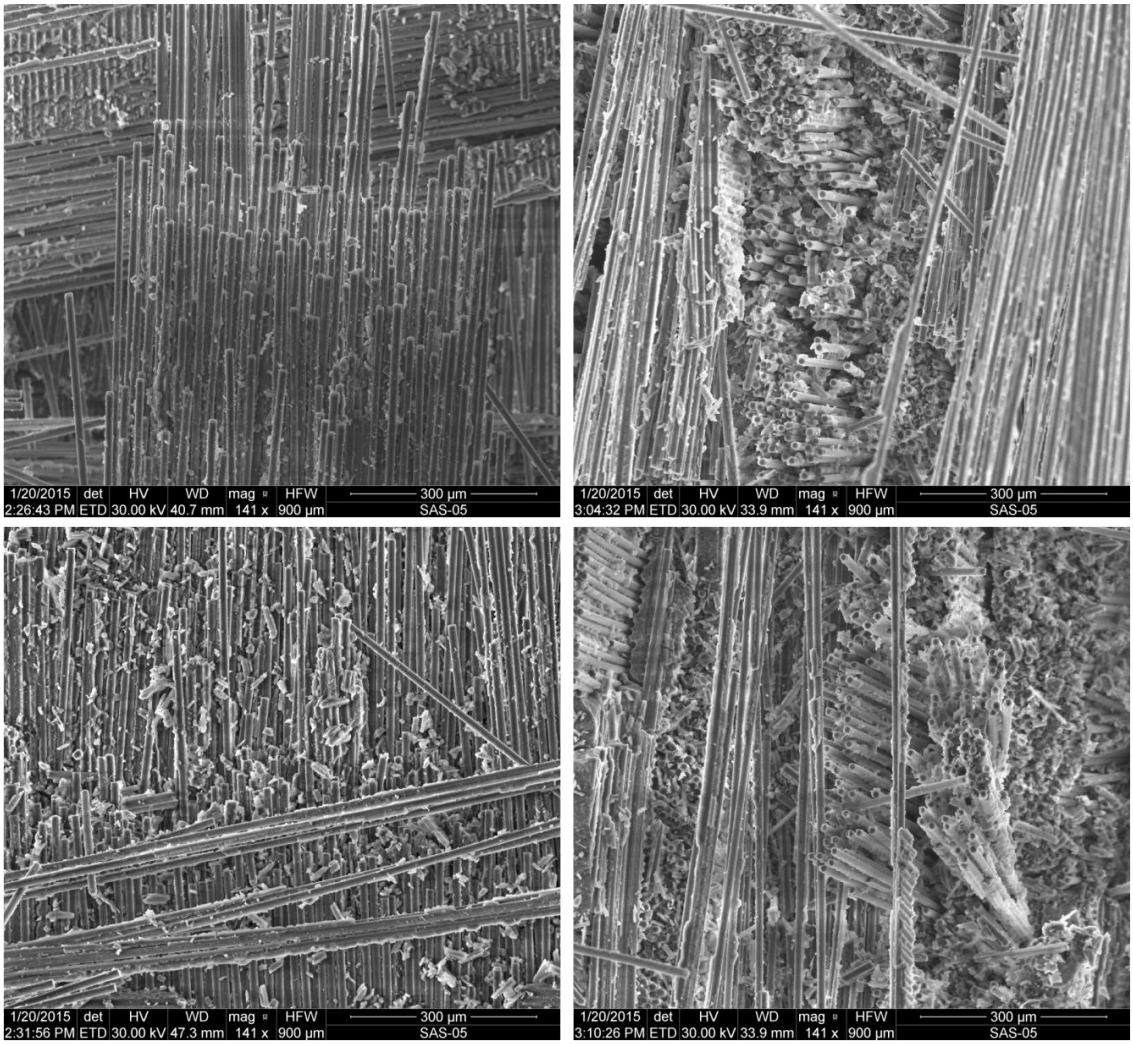

Figure 63 (continued): SEM micrographs of a fracture surface obtained in tension-compression fatigue tests performed at 1200°C in air, σ_{max} = 80 MPa, N_f = 113,382 cycles.

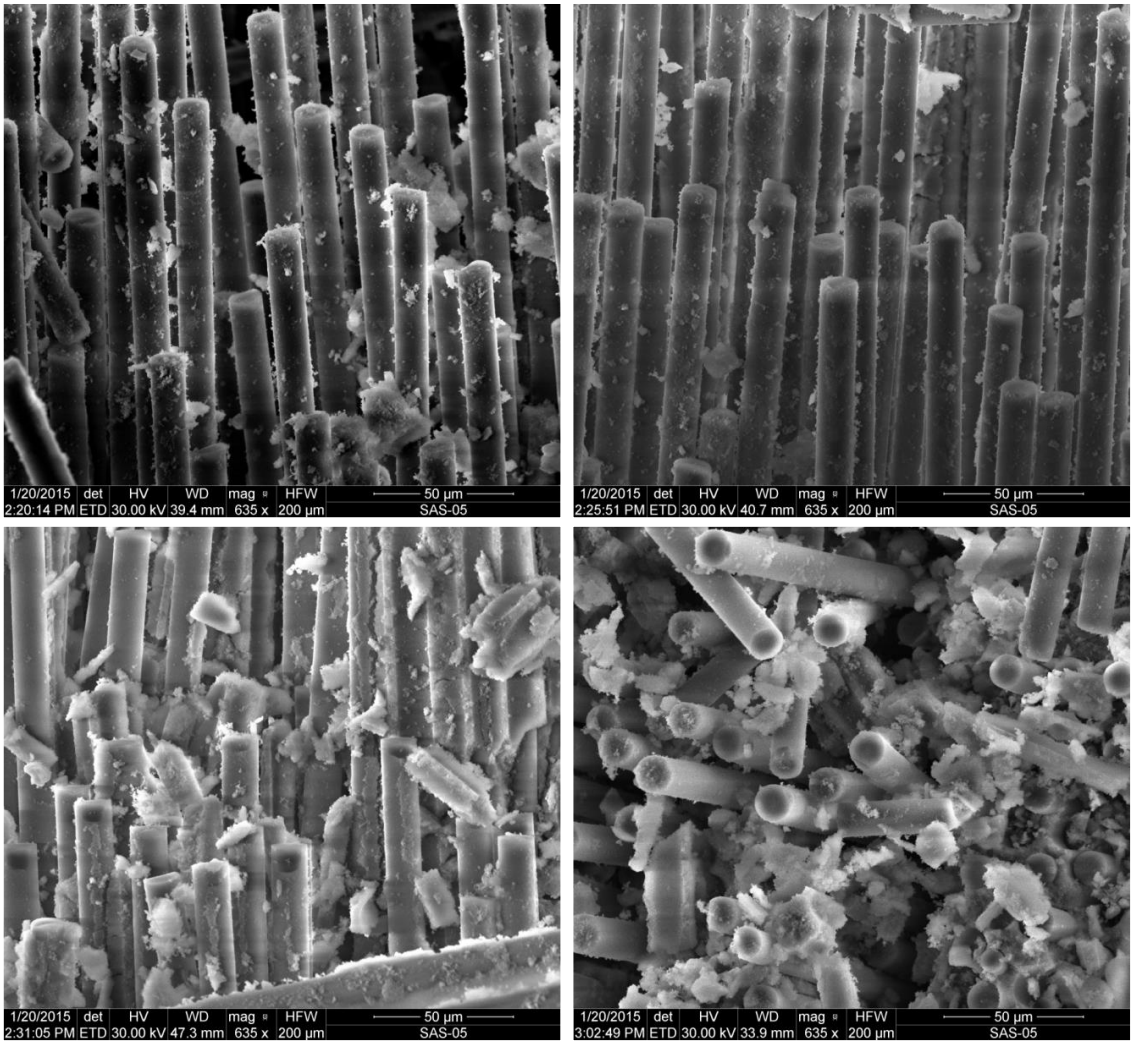

Figure 63 (continued): SEM micrographs of a fracture surface obtained in tension-compression fatigue tests performed at 1200°C in air, σ_{max} = 80 MPa, N_f = 113,382 cycles.

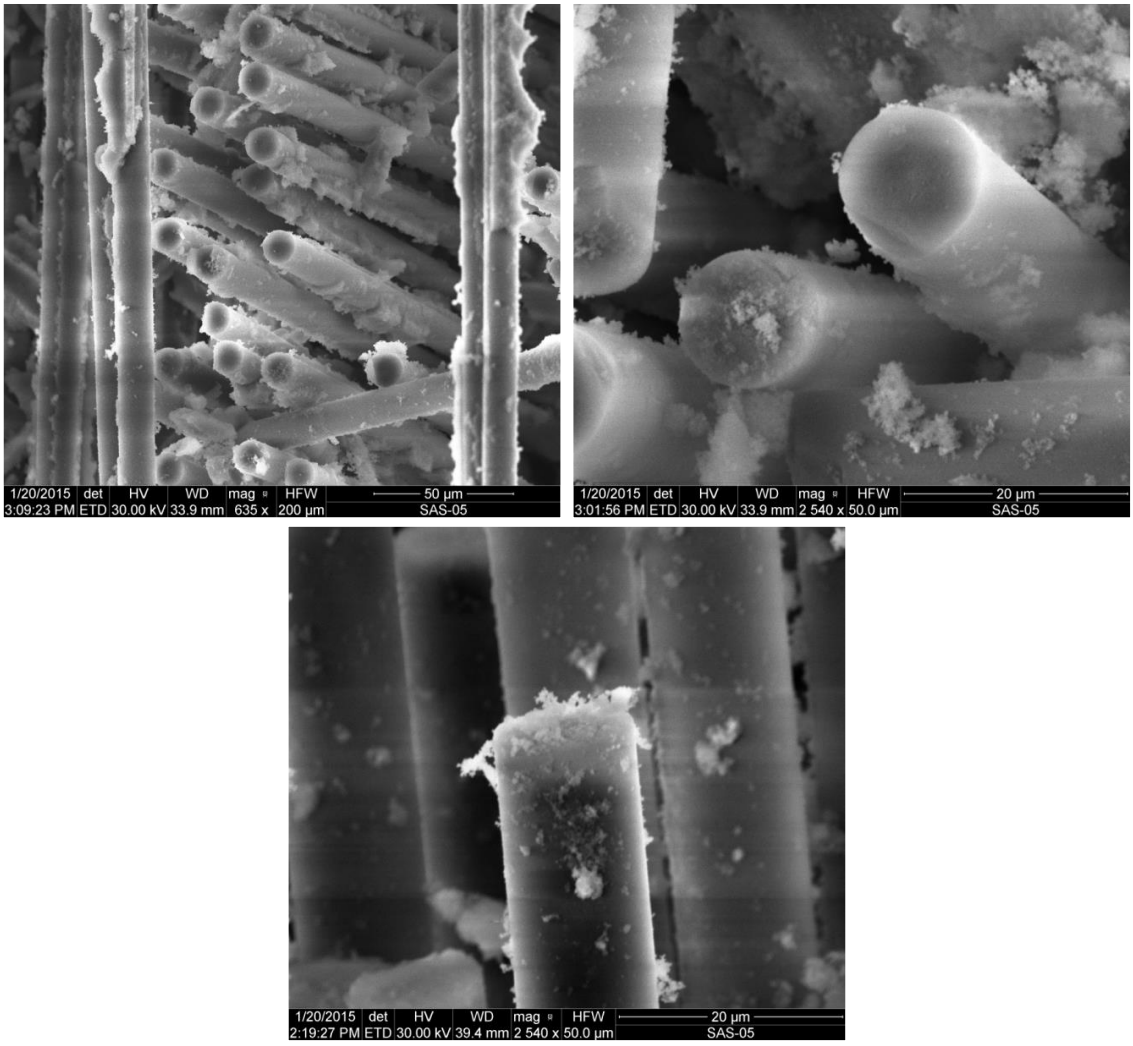

Figure 63 (continued): SEM micrographs of a fracture surface obtained in tension-compression fatigue tests performed at 1200°C in air, σ_{max} = 80 MPa, N_f = 113,382 cycles.

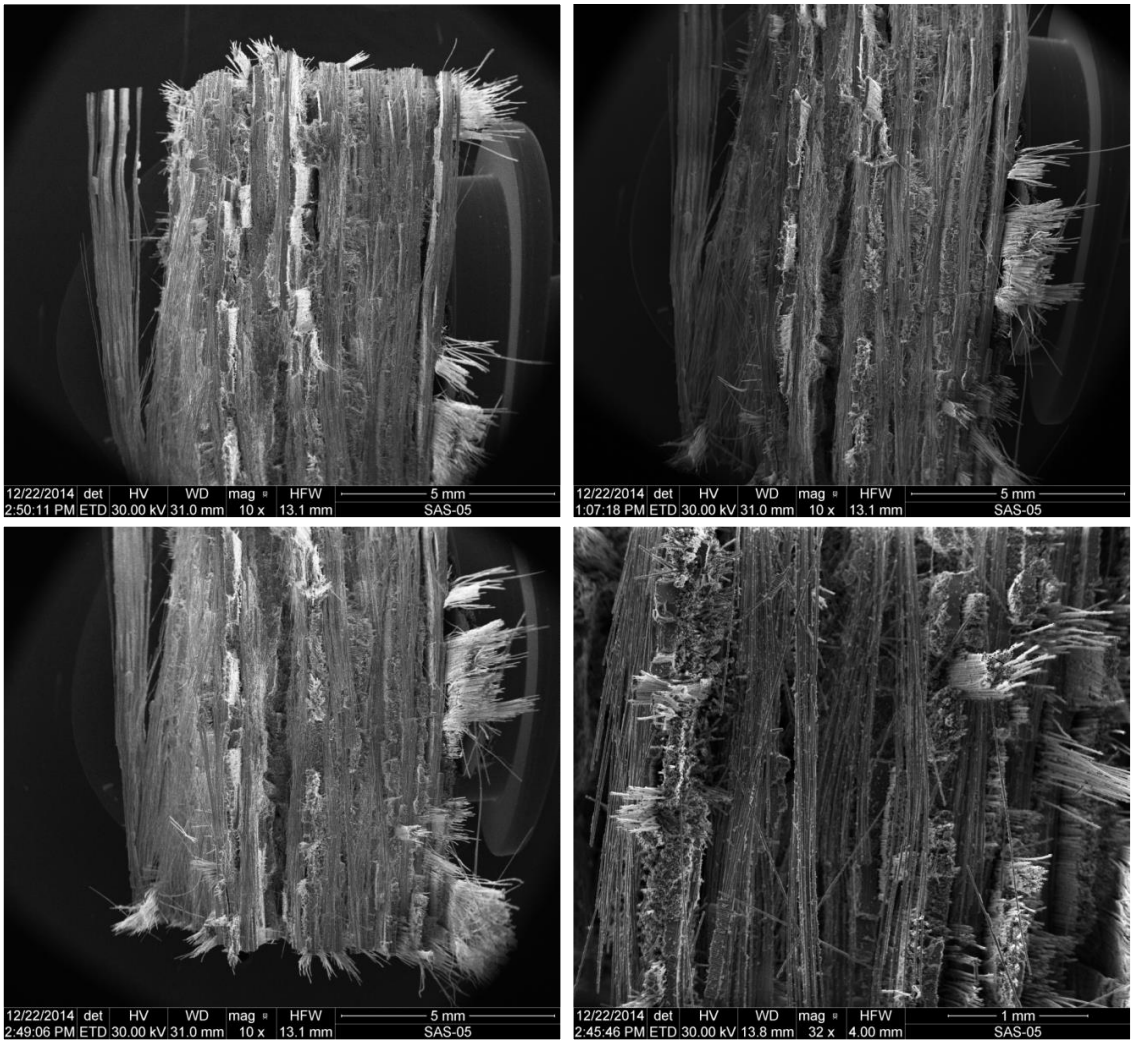

Figure 64: SEM micrographs of a fracture surface obtained in tension-compression fatigue tests performed at 1200°C in air, σ_{max} = 90 MPa, N_f = 71,484 cycles.

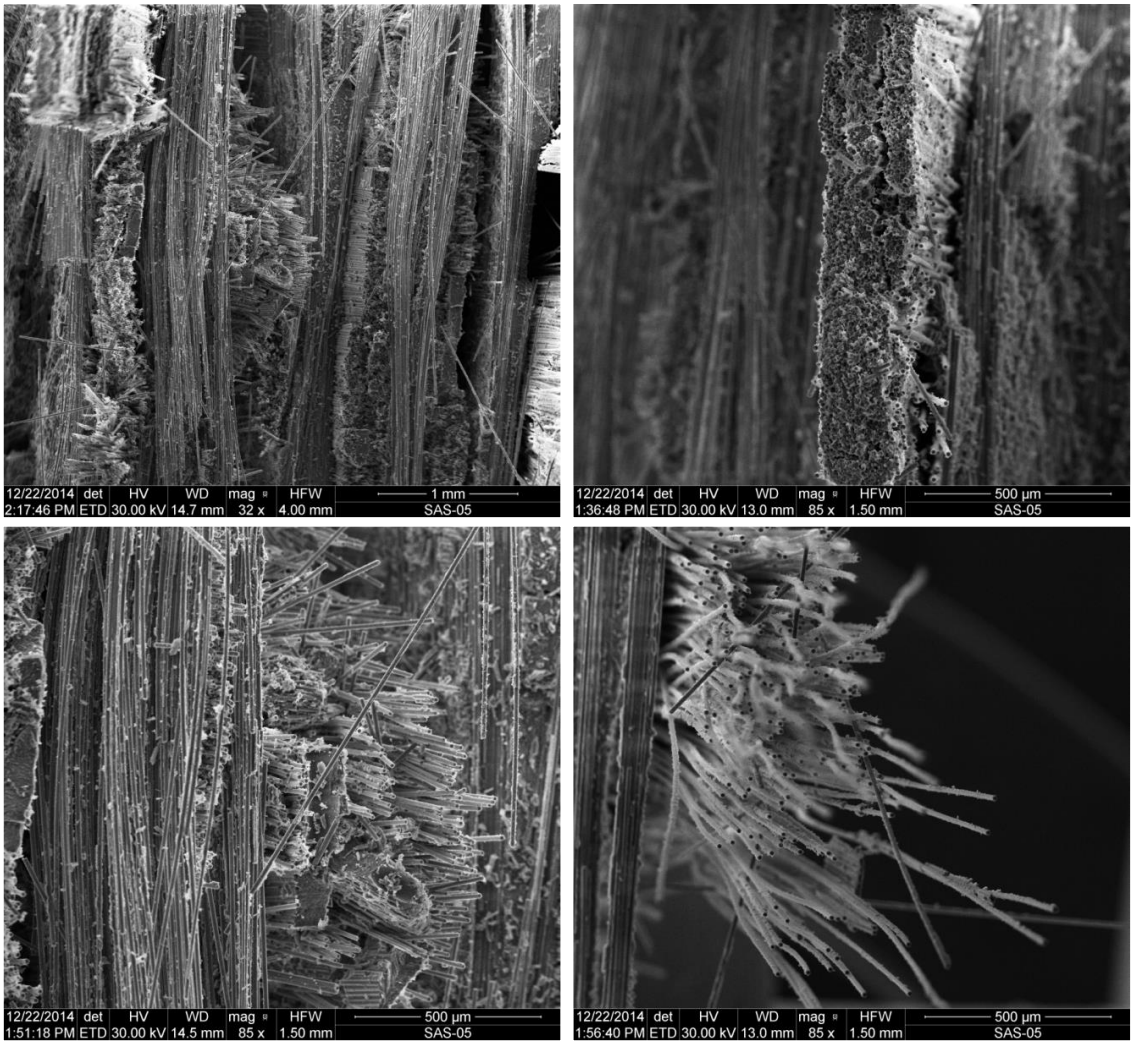

Figure 64 (continued): SEM micrographs of a fracture surface obtained in tension-compression fatigue tests performed at 1200°C in air, σ_{max} = 90 MPa, N_f = 71,484 cycles.

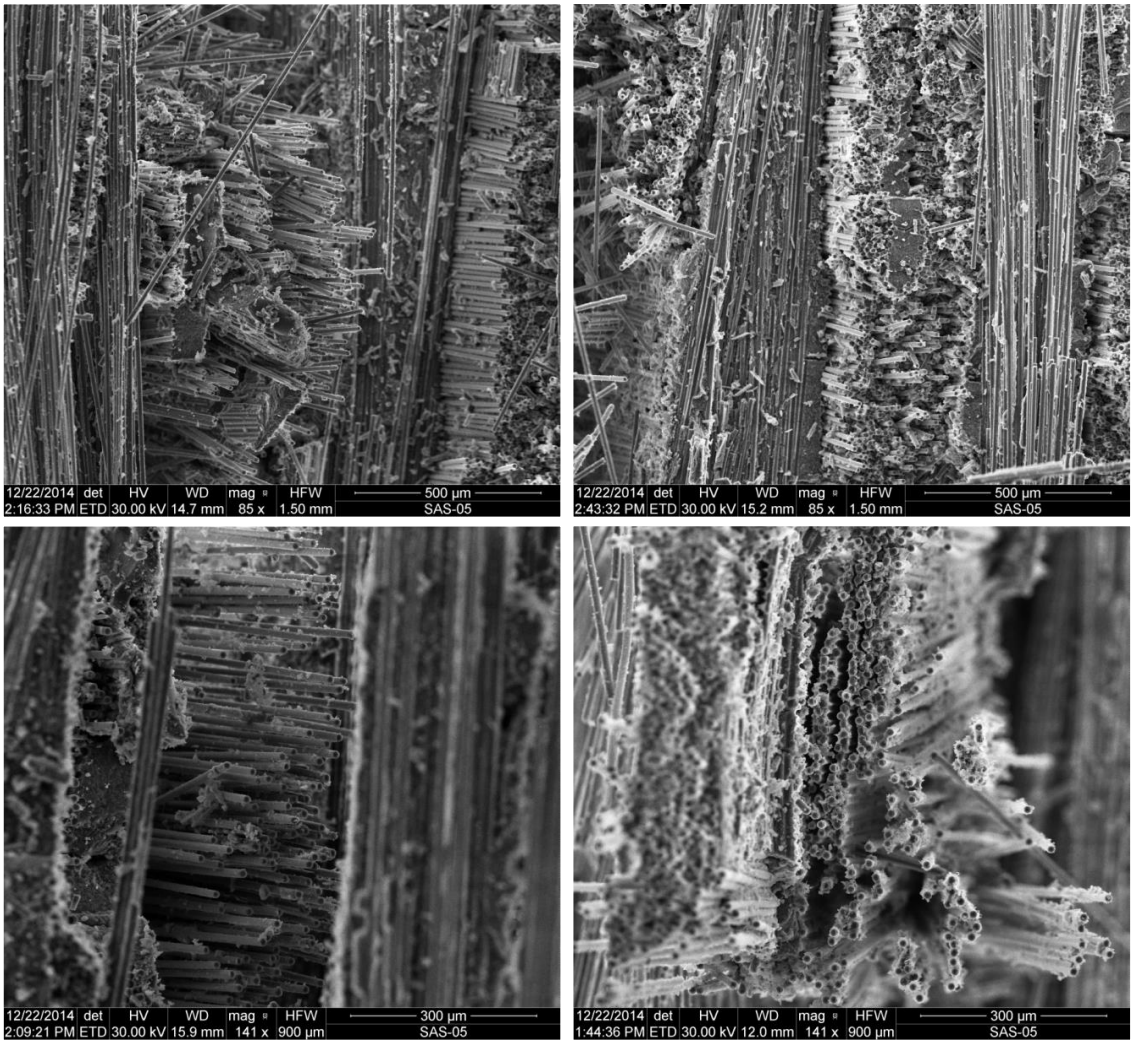

Figure 64 (continued): SEM micrographs of a fracture surface obtained in tension-compression fatigue tests performed at 1200°C in air, σ_{max} = 90 MPa, N_f = 71,484 cycles.

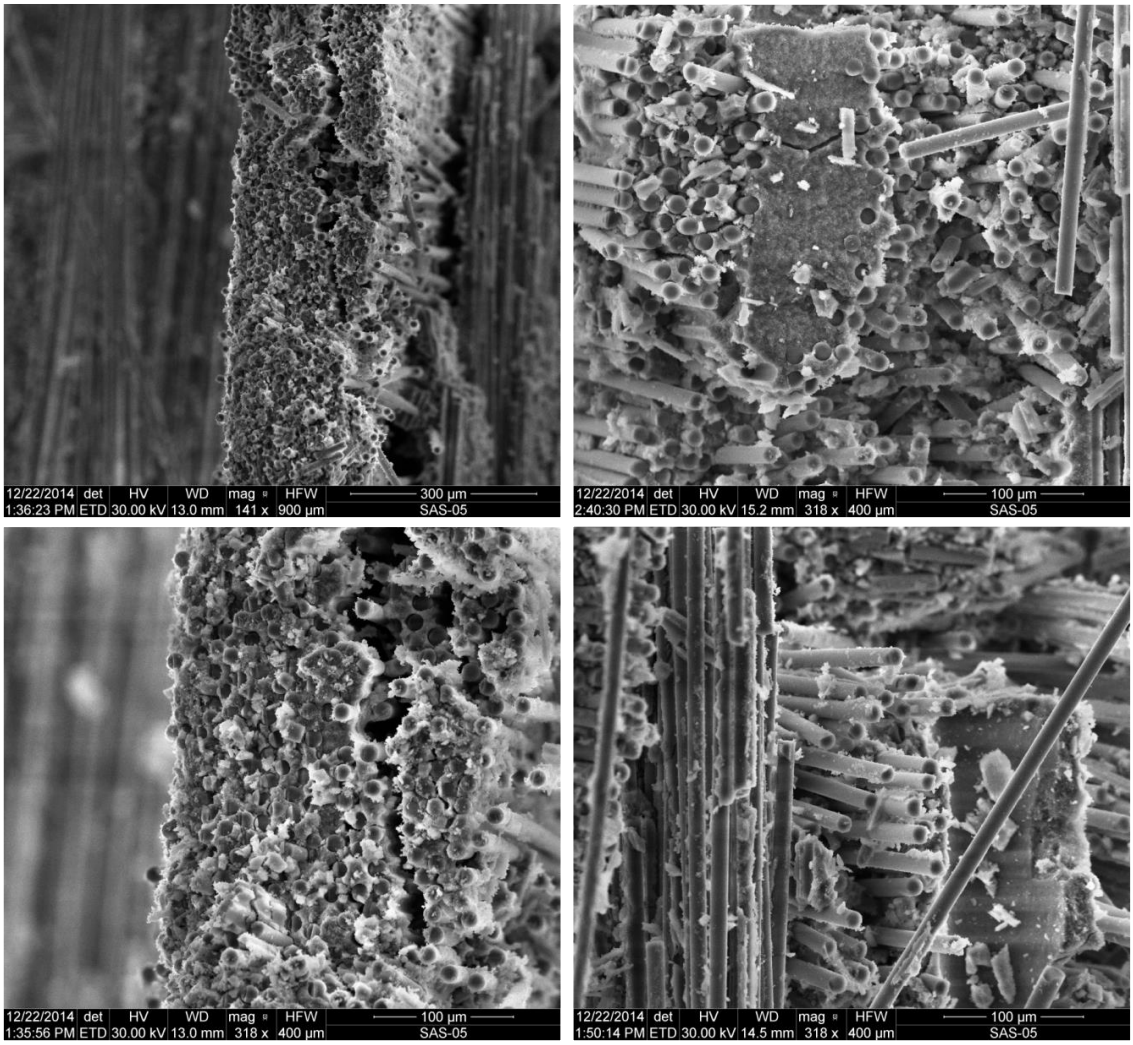

Figure 64 (continued): SEM micrographs of a fracture surface obtained in tension-compression fatigue tests performed at 1200°C in air, σ_{max} = 90 MPa, N_f = 71,484 cycles.

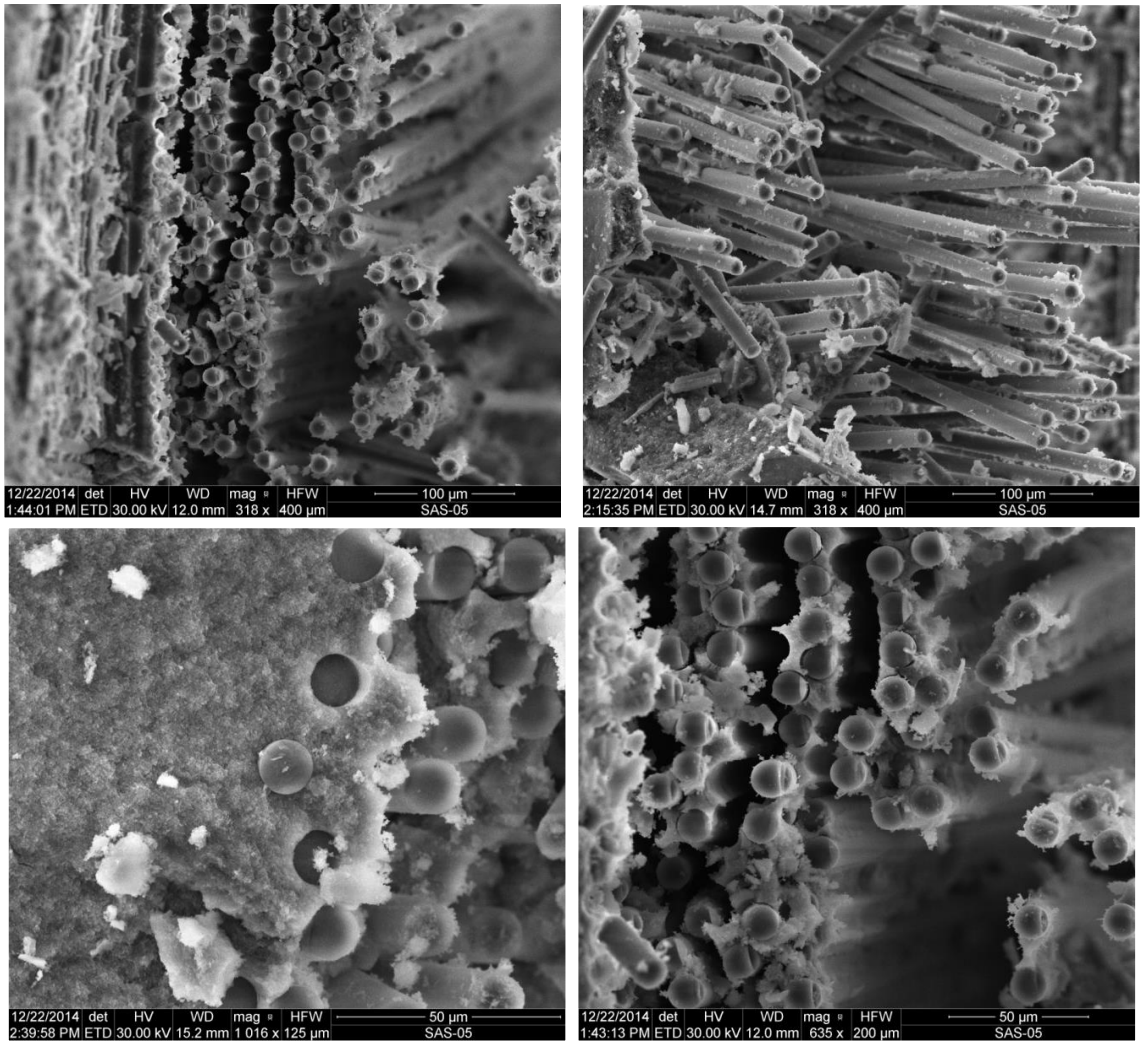

Figure 64 (continued): SEM micrographs of a fracture surface obtained in tension-compression fatigue tests performed at 1200°C in air, σ_{max} = 90 MPa, N_f = 71,484 cycles.

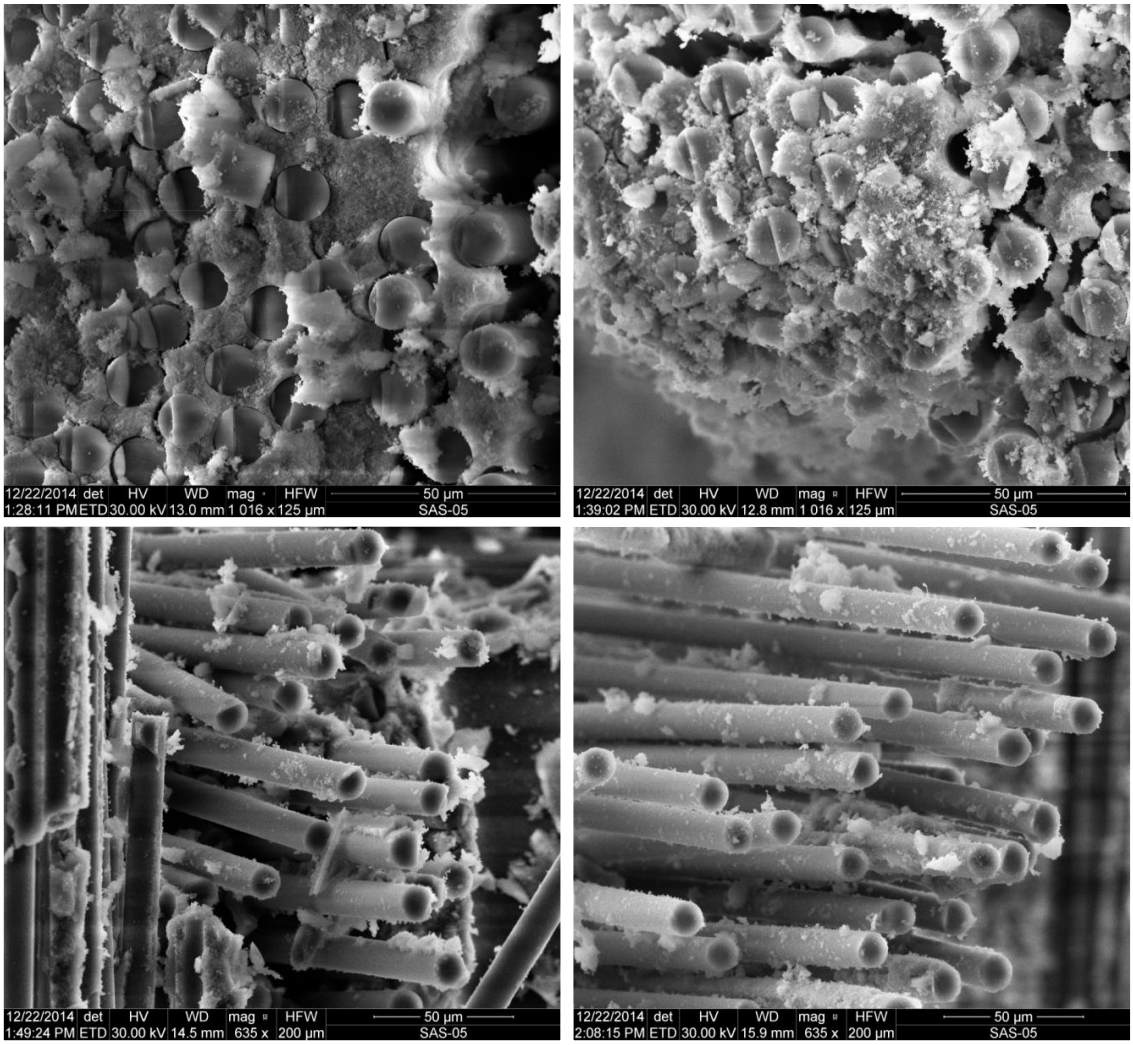

Figure 64 (continued): SEM micrographs of a fracture surface obtained in tension-compression fatigue tests performed at 1200°C in air, σ_{max} = 90 MPa, N_f = 71,484 cycles.

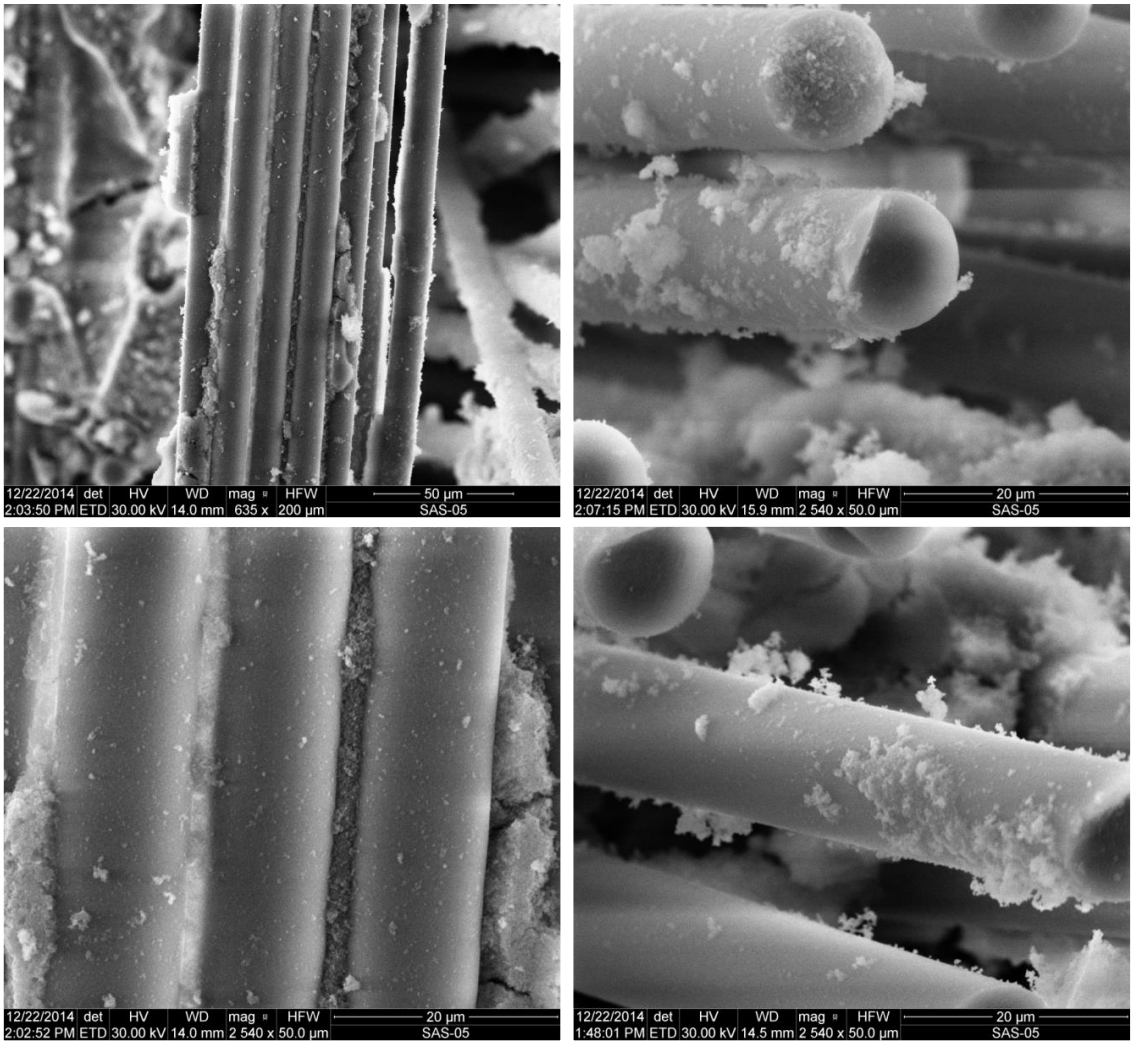

Figure 64 (continued): SEM micrographs of a fracture surface obtained in tension-compression fatigue tests performed at 1200°C in air, σ_{max} = 90 MPa, N_f = 71,484 cycles.

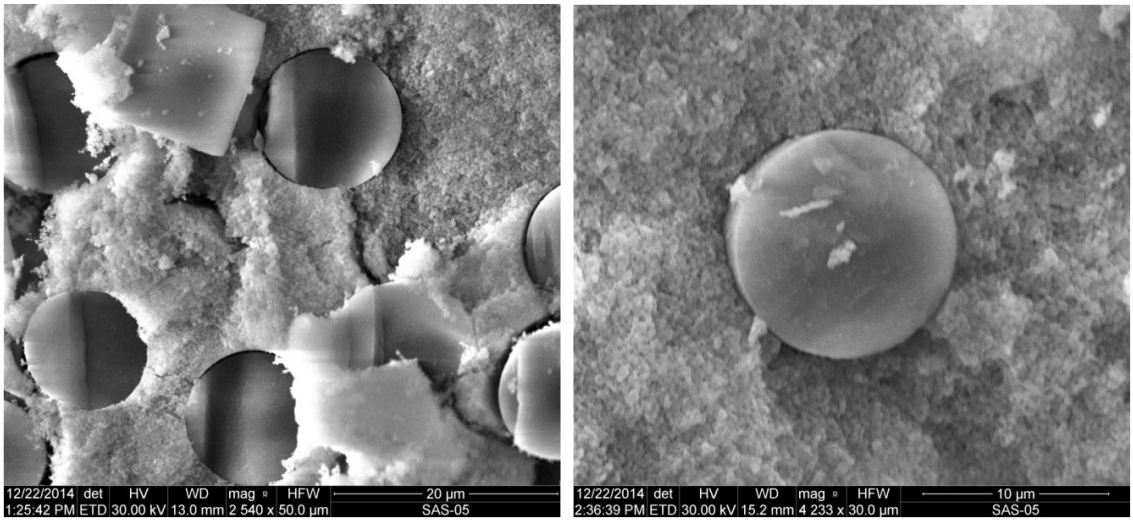

Figure 64 (continued): SEM micrographs of a fracture surface obtained in tension-compression fatigue tests performed at 1200°C in air, σ_{max} = 90 MPa, N_f = 71,484 cycles.

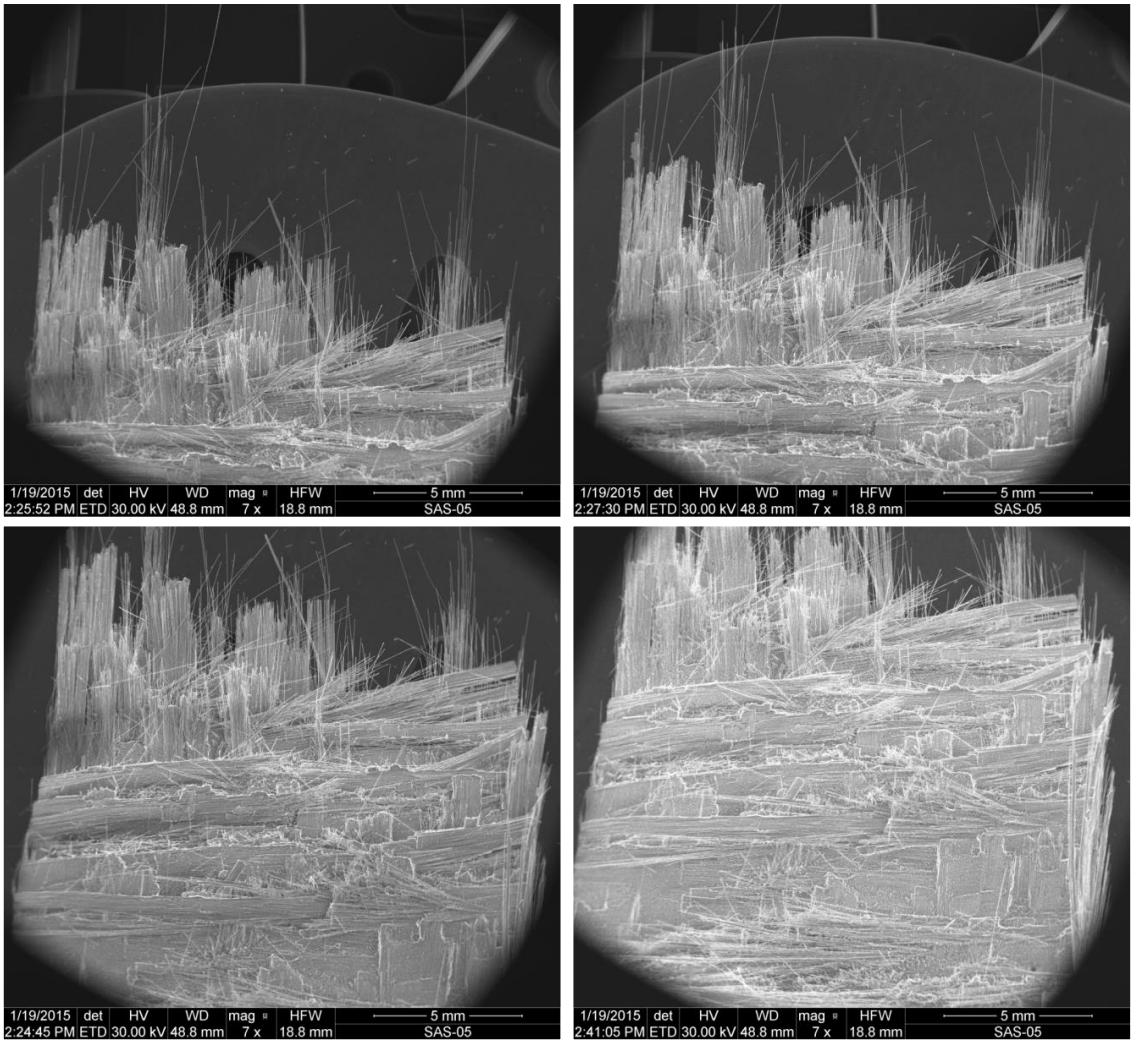

Figure 65: SEM micrographs of a fracture surface obtained in a tension-compression fatigue test performed at 1200°C in air, σ_{max} = 100 MPa, N_f = 5,264 cycles.

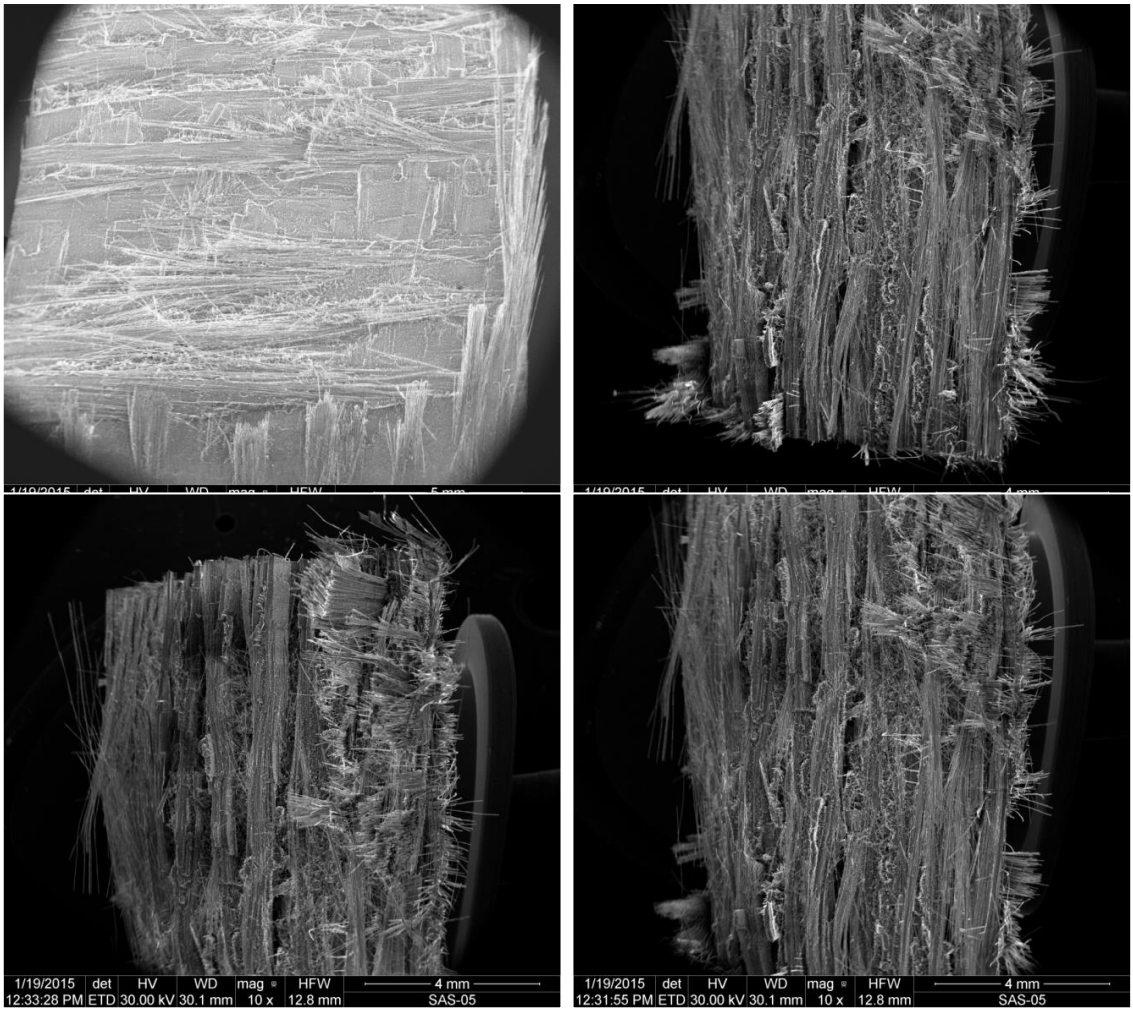

Figure 65 (continued): SEM micrographs of a fracture surface obtained in a tension-compression fatigue test performed at 1200°C in air, σ_{max} = 100 MPa, N_f = 5,264 cycles.

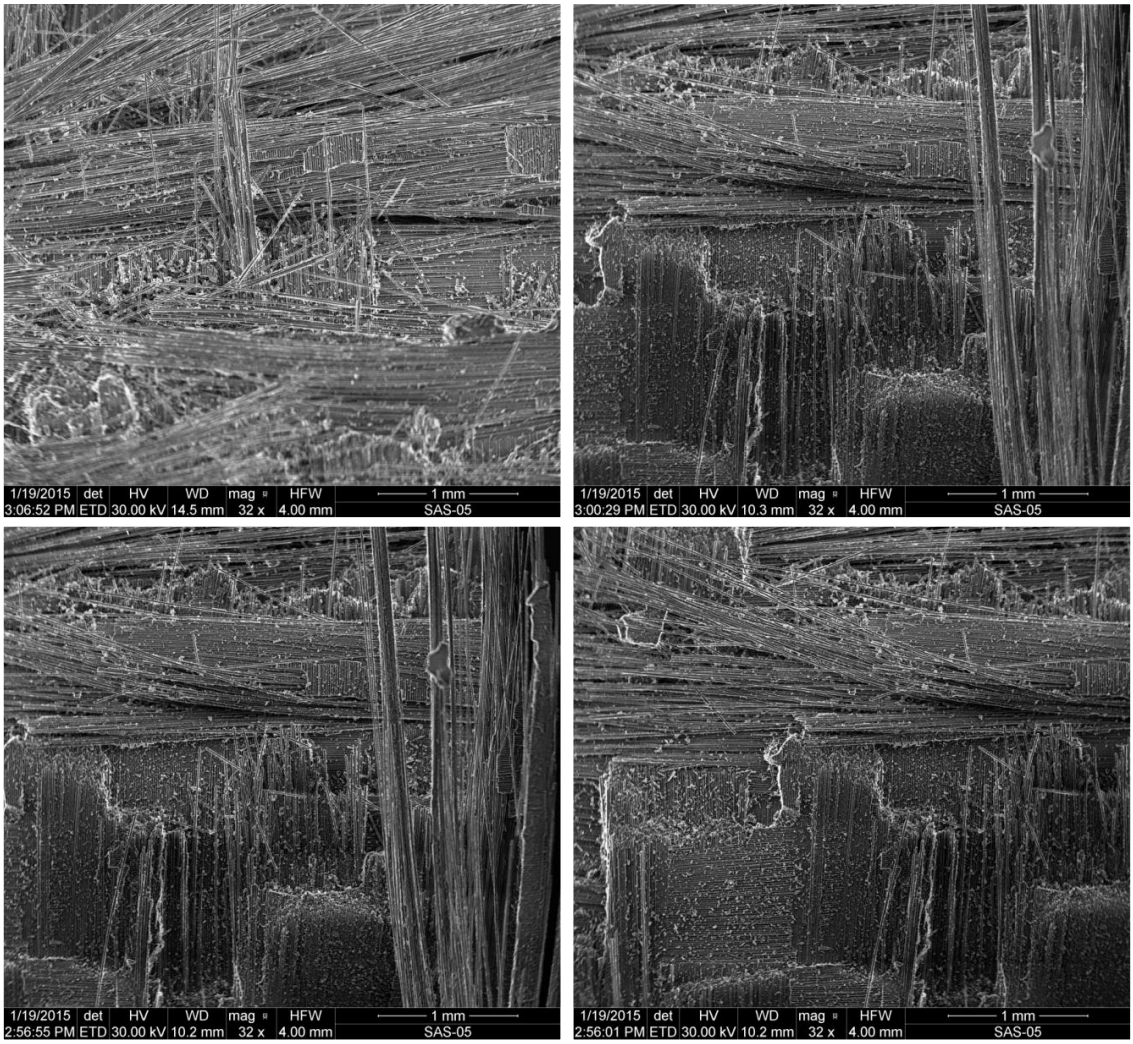

Figure 65 (continued): SEM micrographs of a fracture surface obtained in a tension-compression fatigue test performed at 1200°C in air, σ_{max} = 100 MPa, N_f = 5,264 cycles.

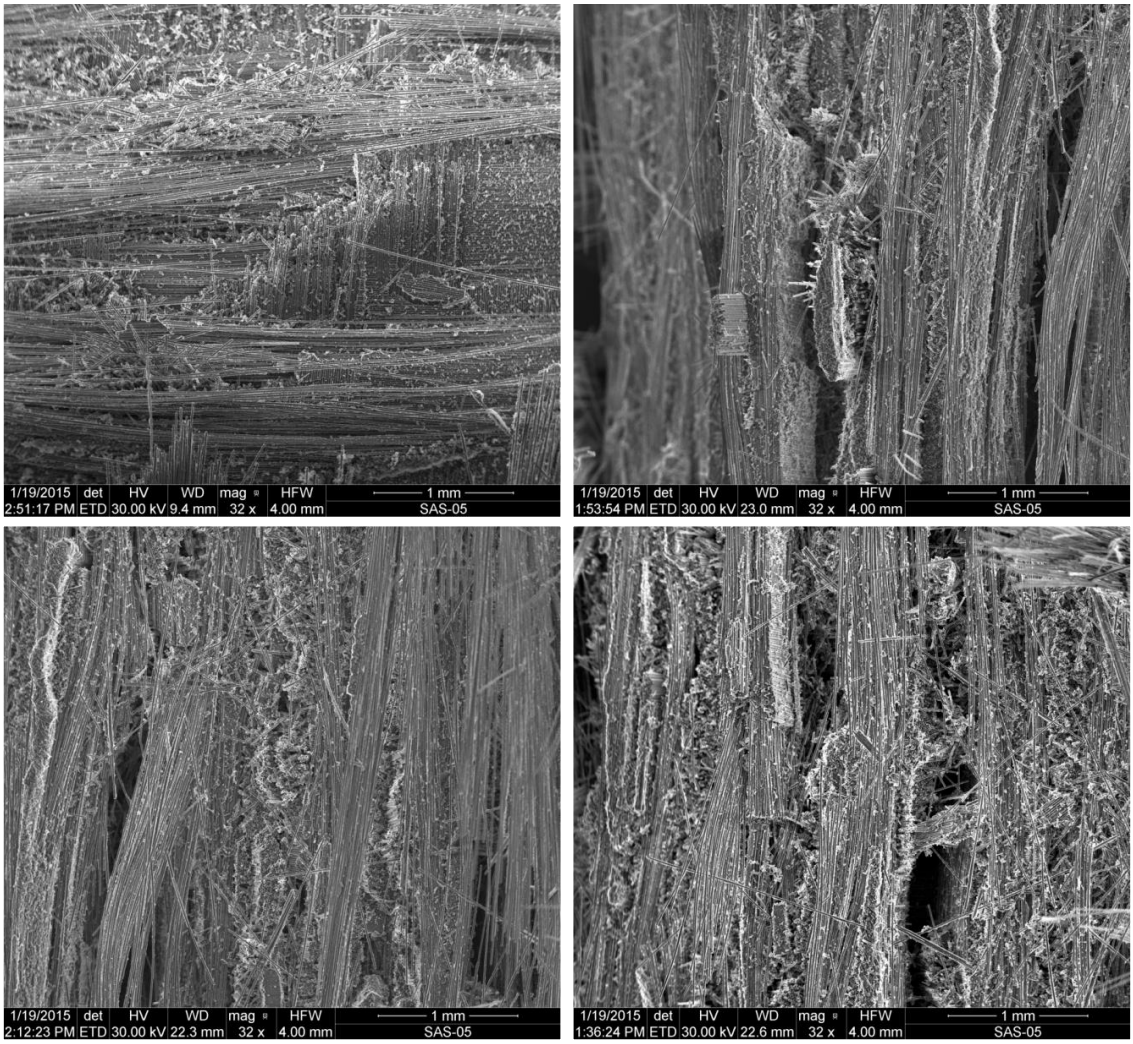

Figure 65 (continued): SEM micrographs of a fracture surface obtained in a tension-compression fatigue test performed at 1200°C in air, σ_{max} = 100 MPa, N_f = 5,264 cycles.

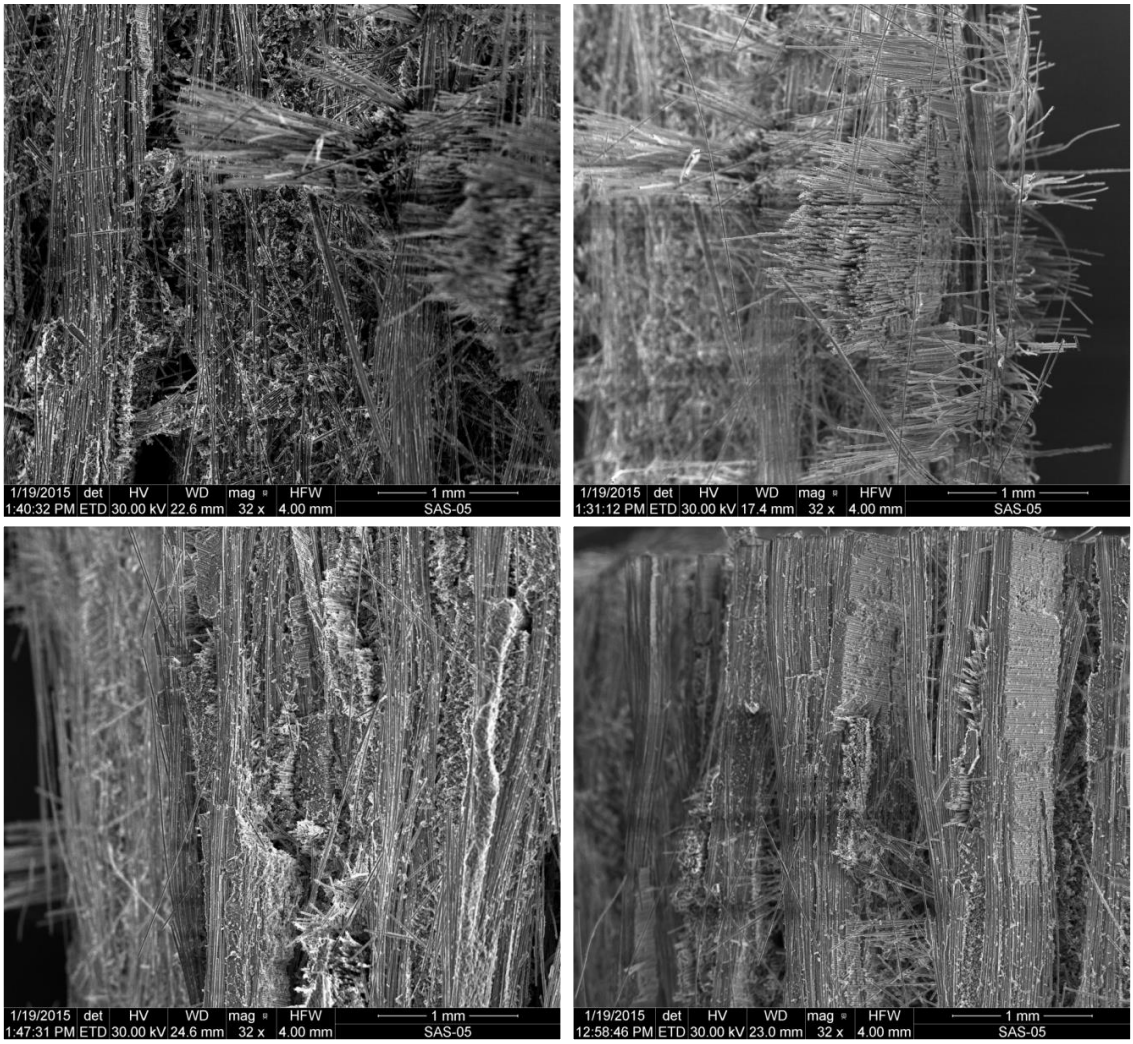

Figure 65 (continued): SEM micrographs of a fracture surface obtained in a tension-compression fatigue test performed at 1200°C in air, σ_{max} = 100 MPa, N_f = 5,264 cycles.

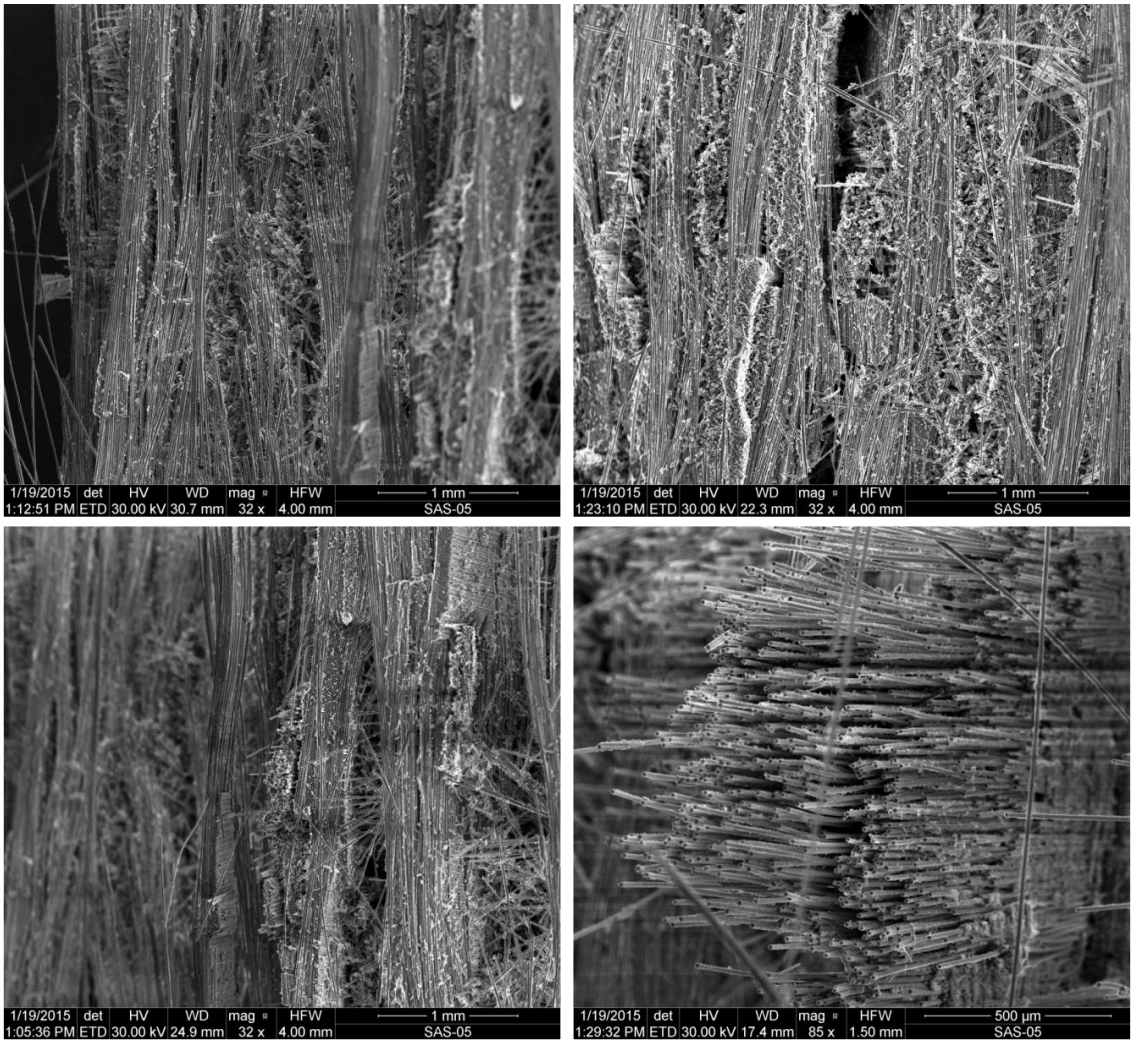

Figure 65 (continued): SEM micrographs of a fracture surface obtained in a tension-compression fatigue test performed at 1200°C in air, σ_{max} = 100 MPa, N_f = 5,264 cycles.

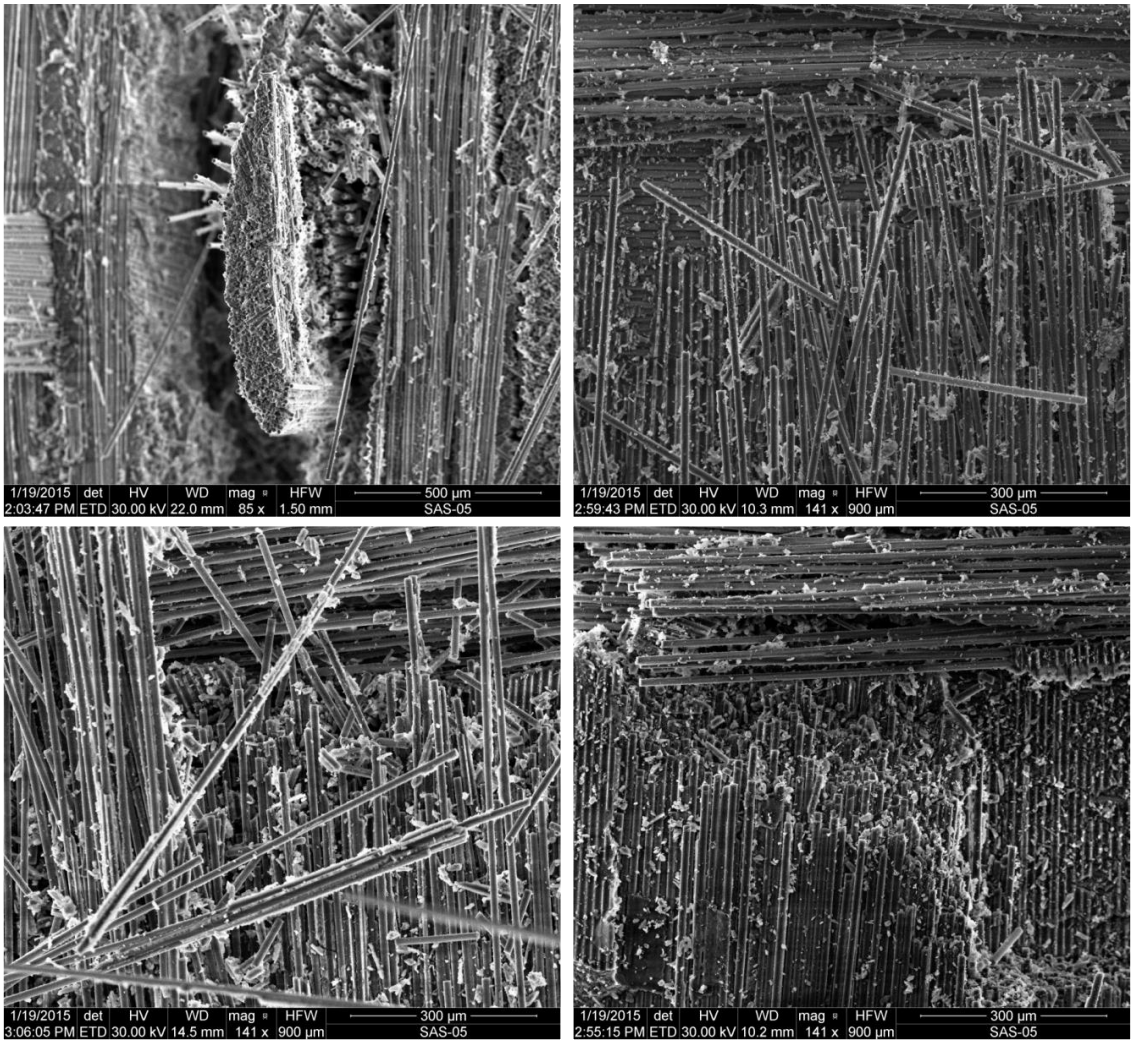

Figure 65 (continued): SEM micrographs of a fracture surface obtained in a tension-compression fatigue test performed at 1200°C in air, σ_{max} = 100 MPa, N_f = 5,264 cycles.

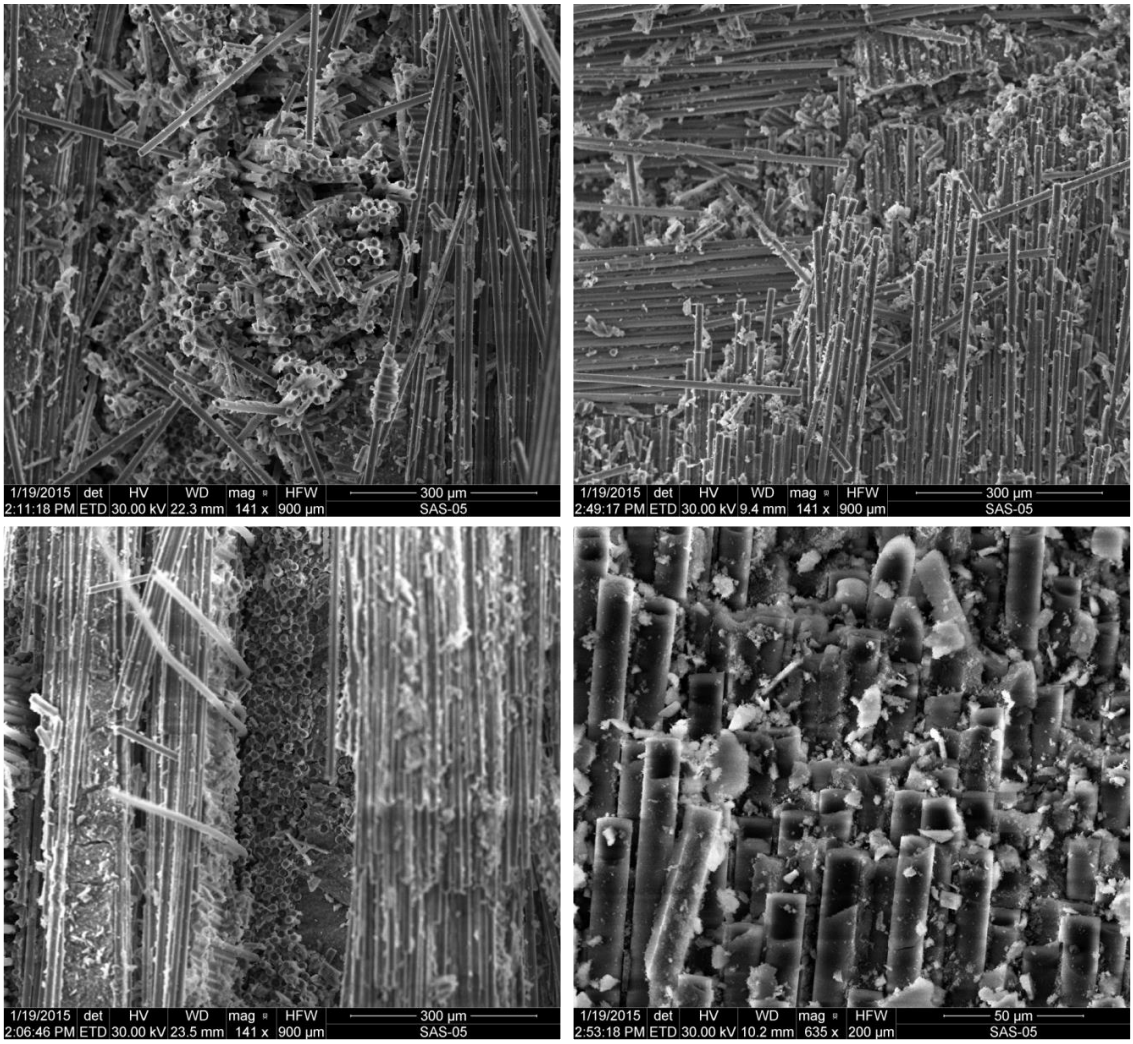

Figure 65 (continued): SEM micrographs of a fracture surface obtained in a tension-compression fatigue test performed at 1200°C in air, σ_{max} = 100 MPa, N_f = 5,264 cycles.

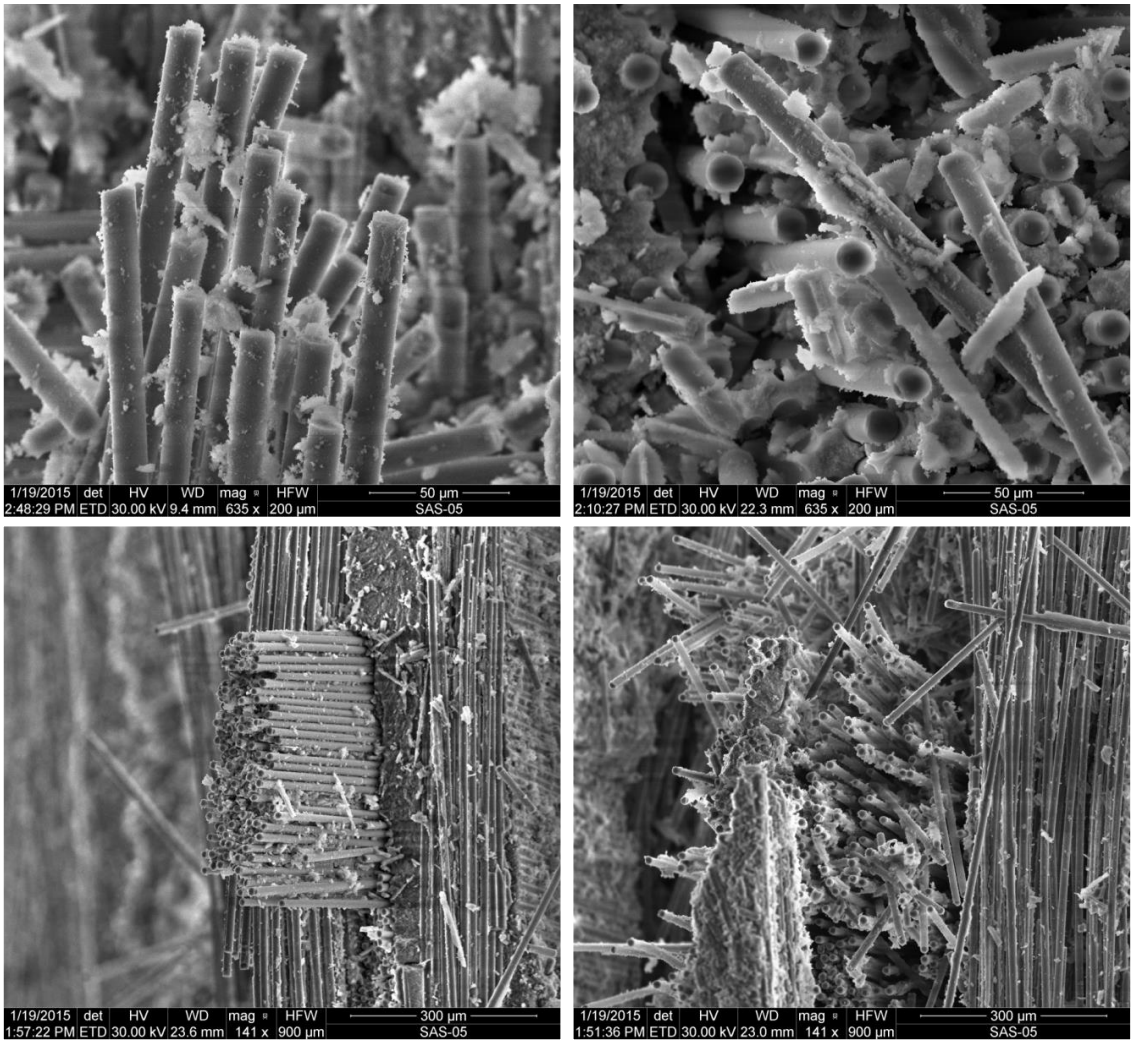

Figure 65 (continued): SEM micrographs of a fracture surface obtained in a tension-compression fatigue test performed at 1200°C in air, σ_{max} = 100 MPa, N_f = 5,264 cycles.

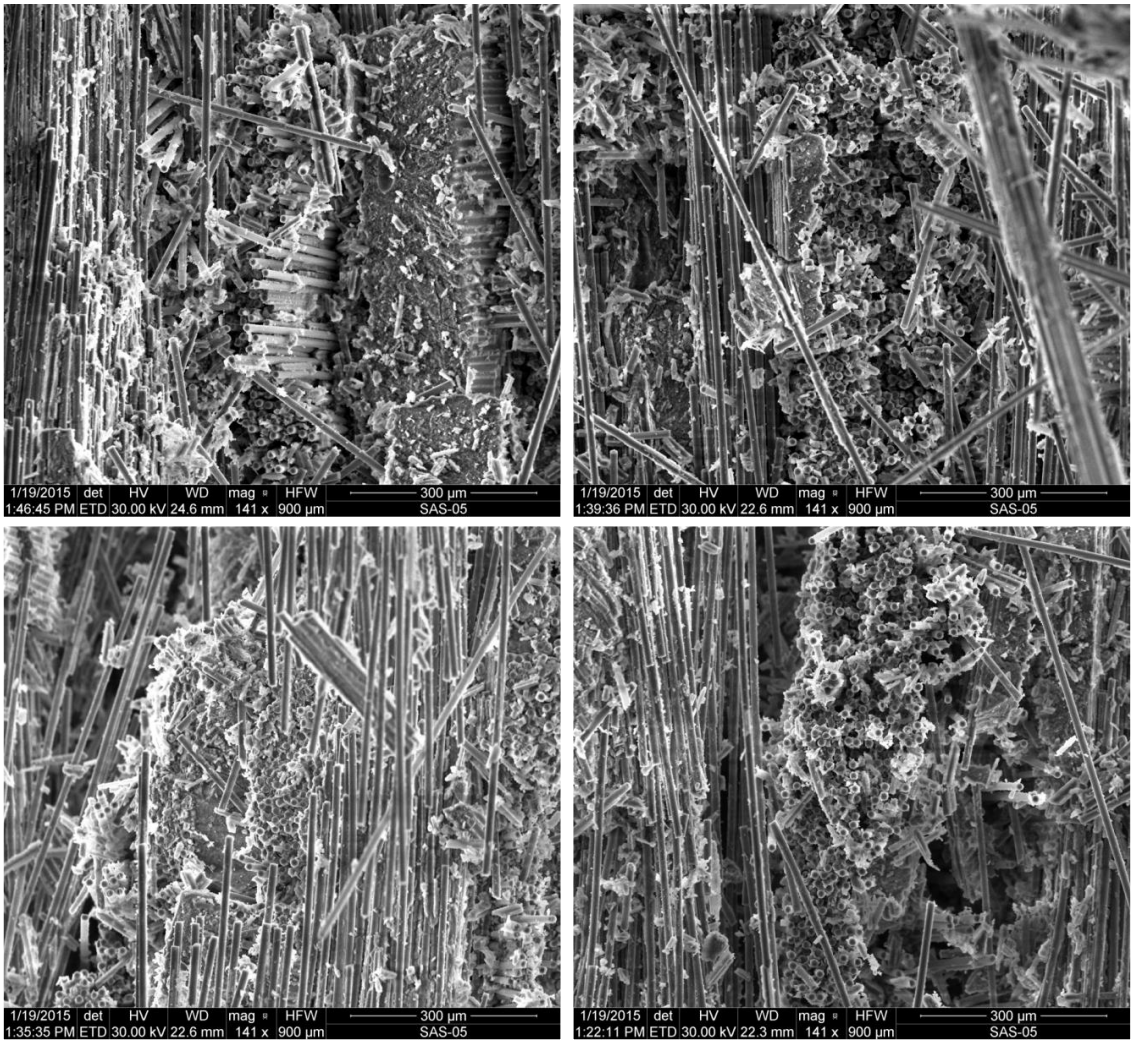

Figure 65 (continued): SEM micrographs of a fracture surface obtained in a tension-compression fatigue test performed at 1200°C in air, σ_{max} = 100 MPa, N_f = 5,264 cycles.

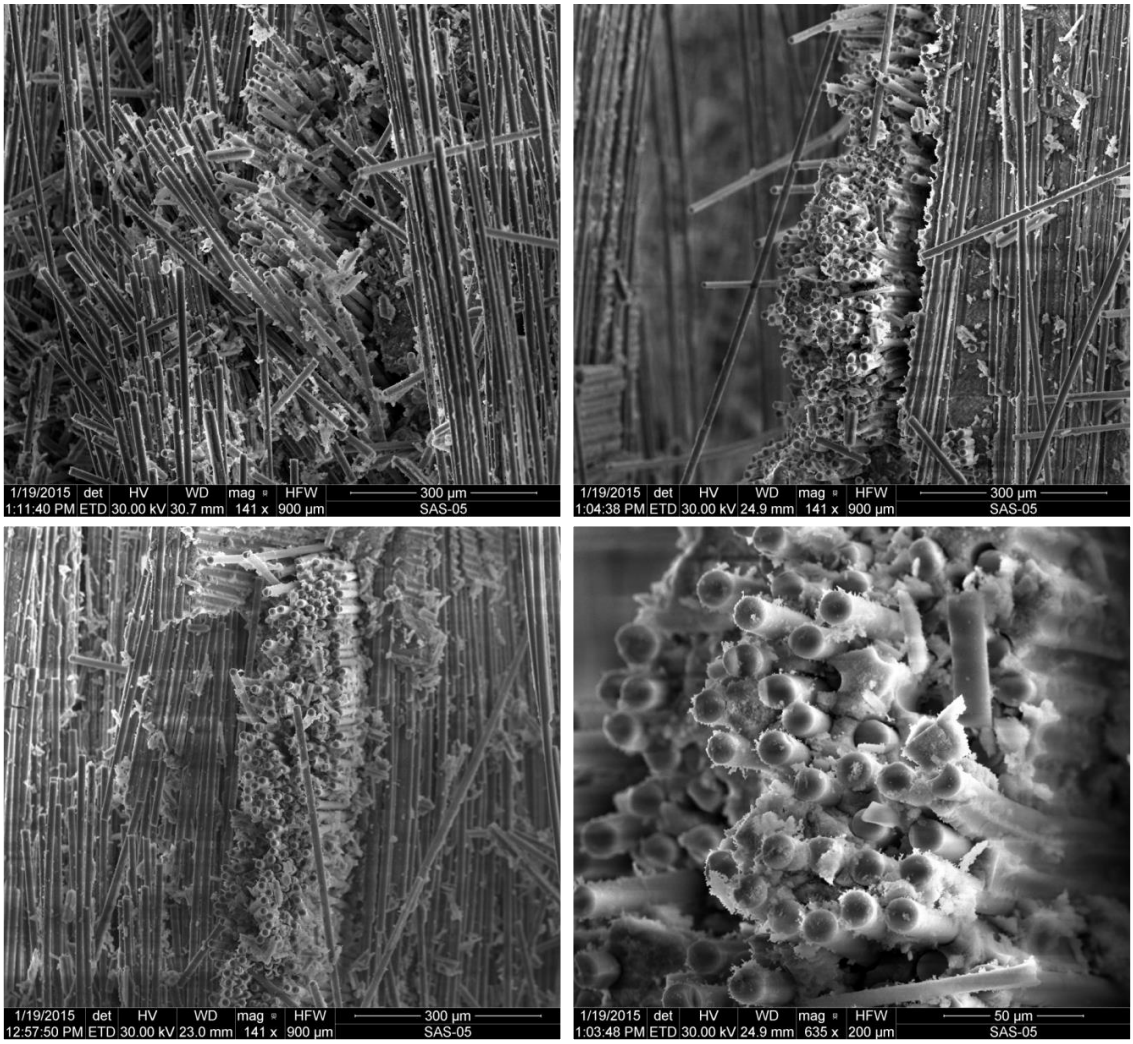

Figure 65 (continued): SEM micrographs of a fracture surface obtained in a tension-compression fatigue test performed at 1200°C in air, σ_{max} = 100 MPa, N_f = 5,264 cycles.

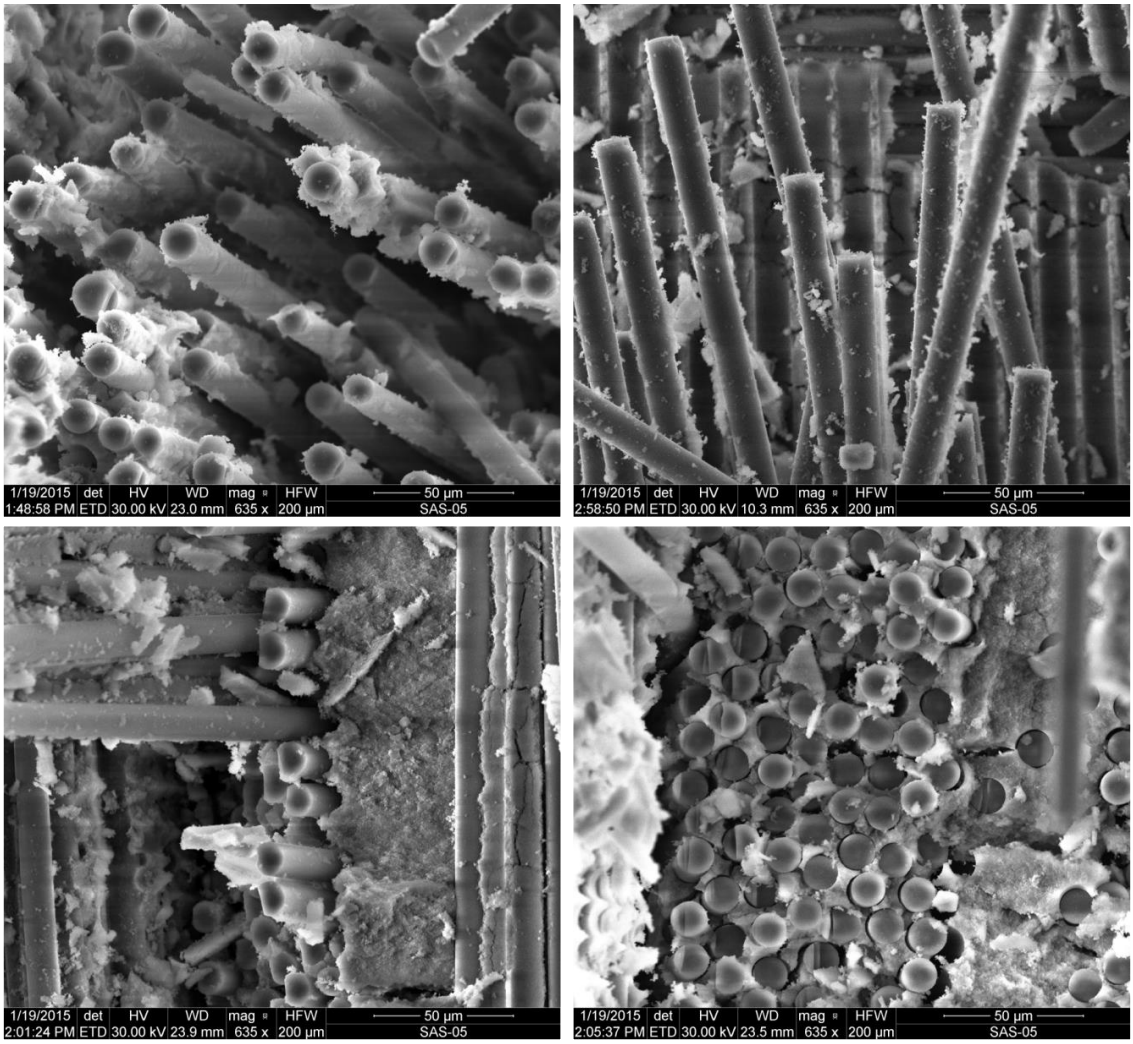

Figure 65 (continued): SEM micrographs of a fracture surface obtained in a tension-compression fatigue test performed at 1200°C in air, σ_{max} = 100 MPa, N_f = 5,264 cycles.

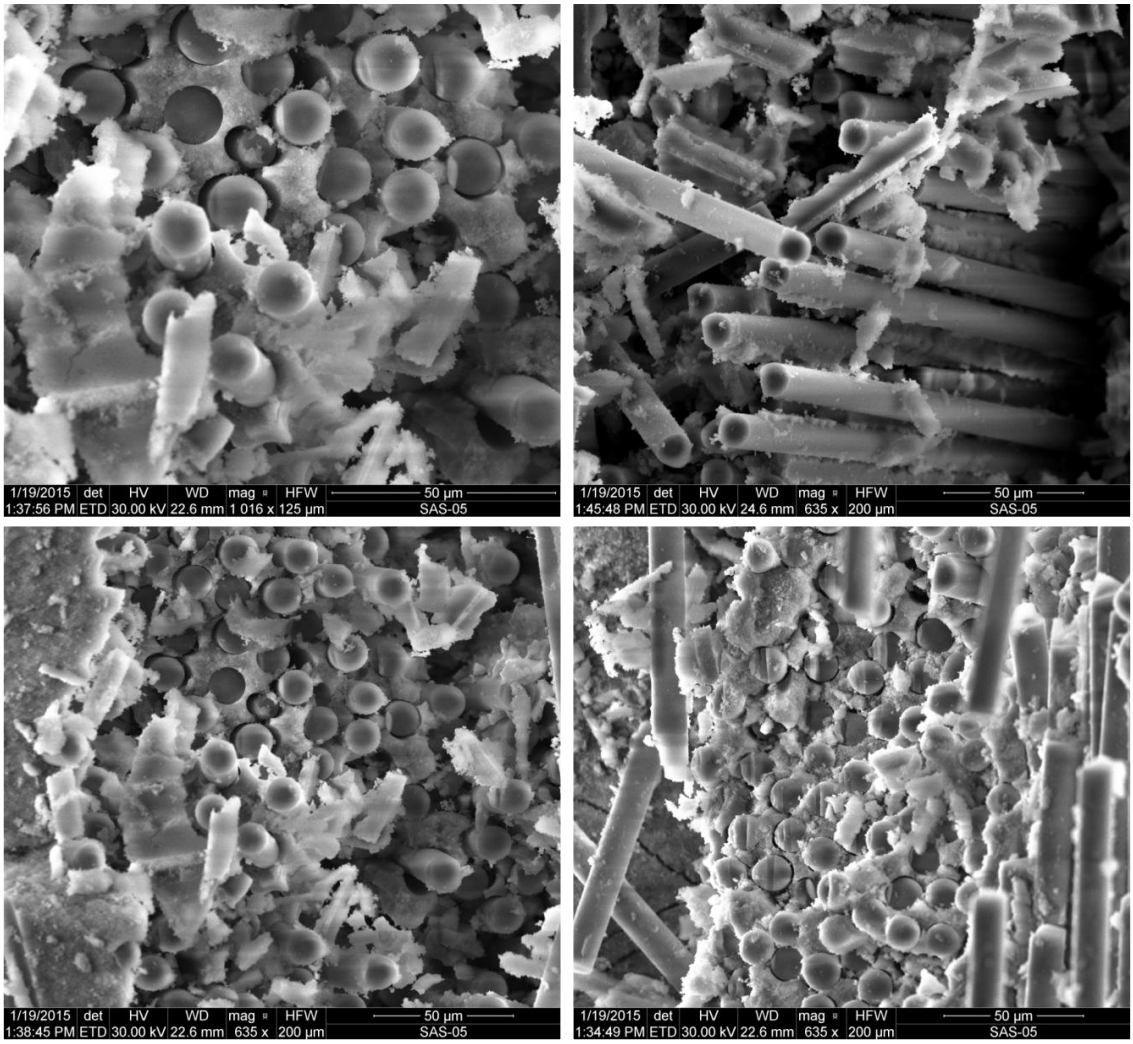

Figure 65 (continued): SEM micrographs of a fracture surface obtained in a tension-compression fatigue test performed at 1200°C in air, σ_{max} = 100 MPa, N_f = 5,264 cycles.

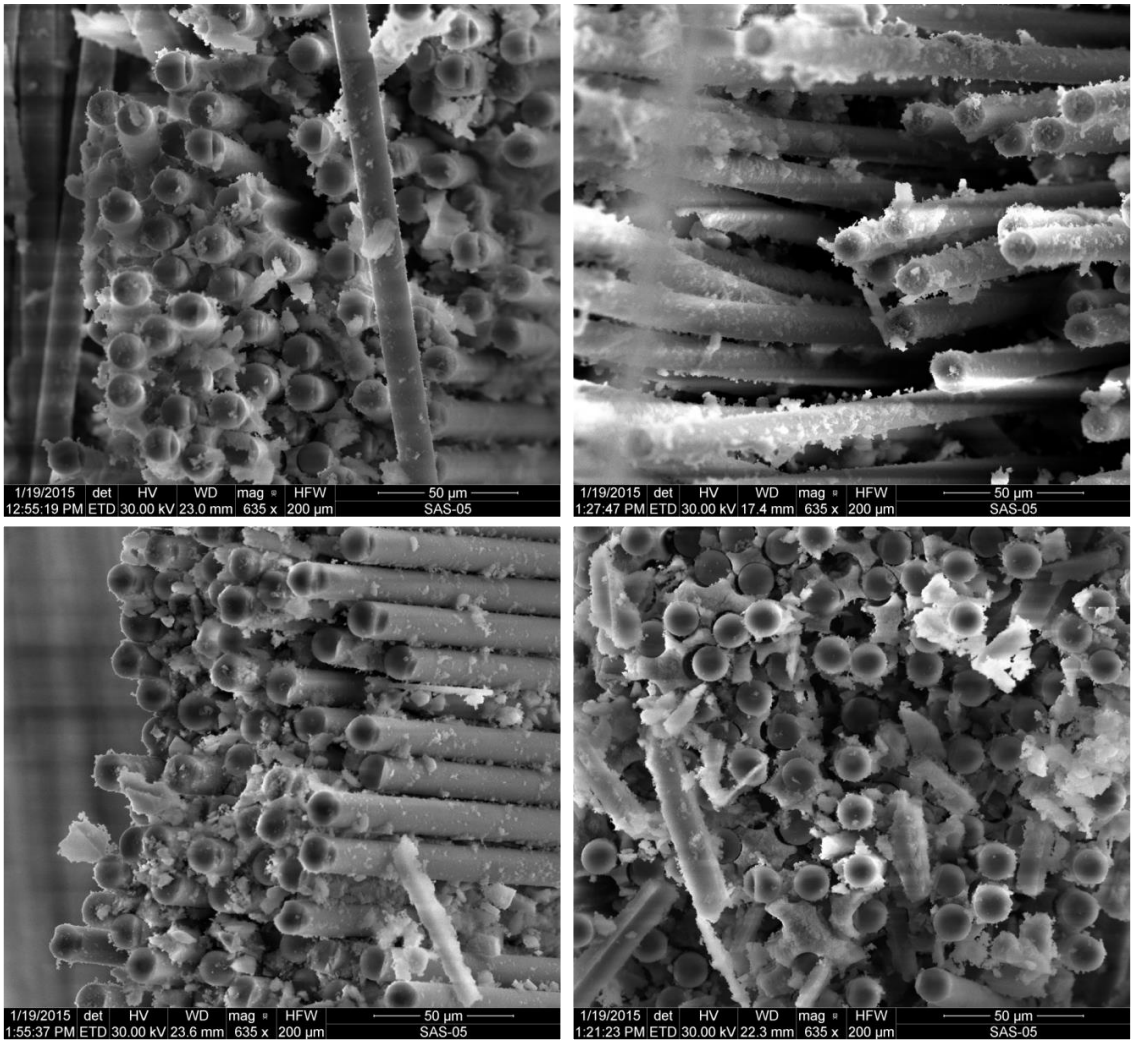

Figure 65 (continued): SEM micrographs of a fracture surface obtained in a tension-compression fatigue test performed at 1200°C in air, σ_{max} = 100 MPa, N_f = 5,264 cycles.

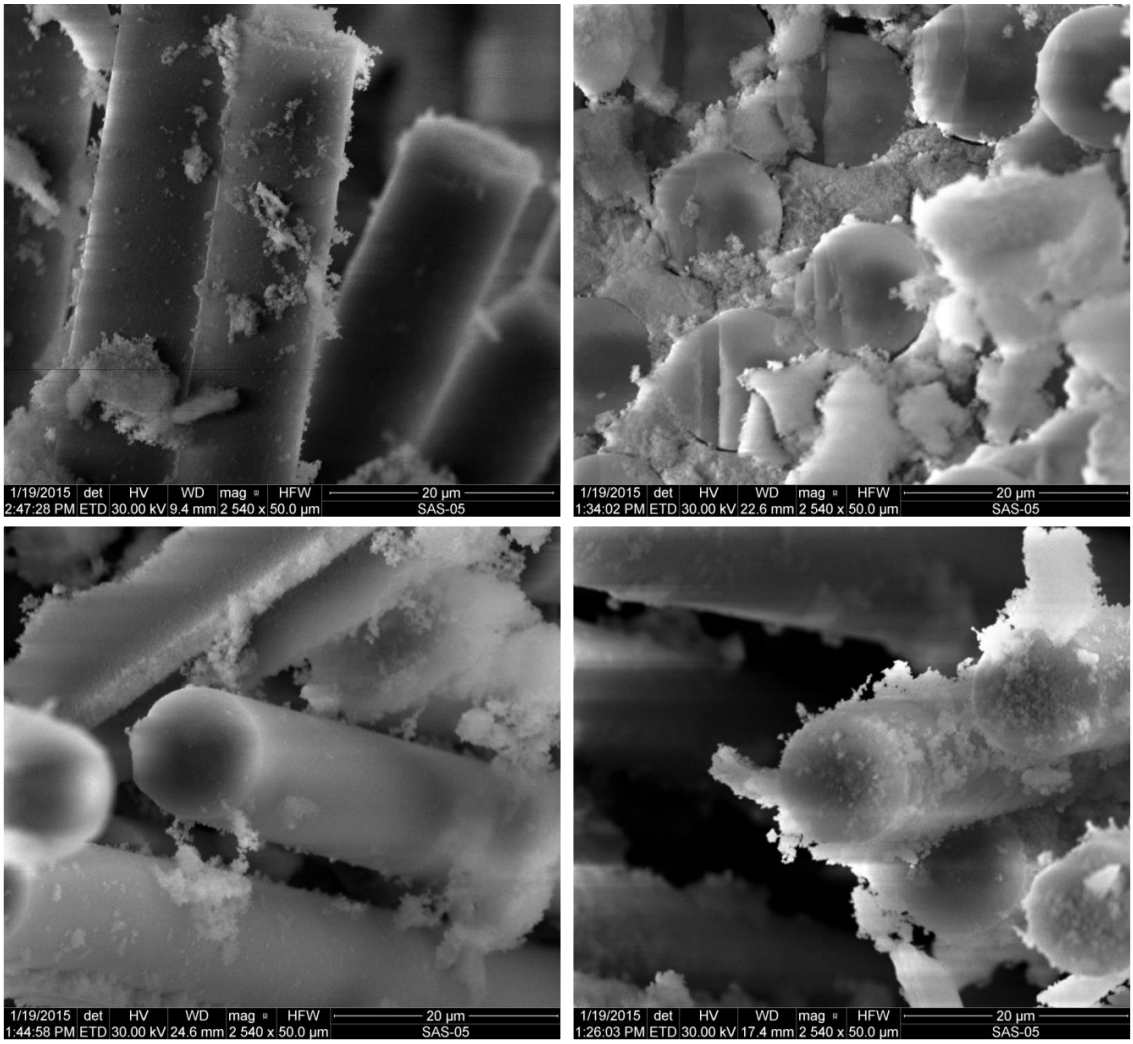

Figure 65 (continued): SEM micrographs of a fracture surface obtained in a tension-compression fatigue test performed at 1200°C in air, σ_{max} = 100 MPa, N_f = 5,264 cycles.

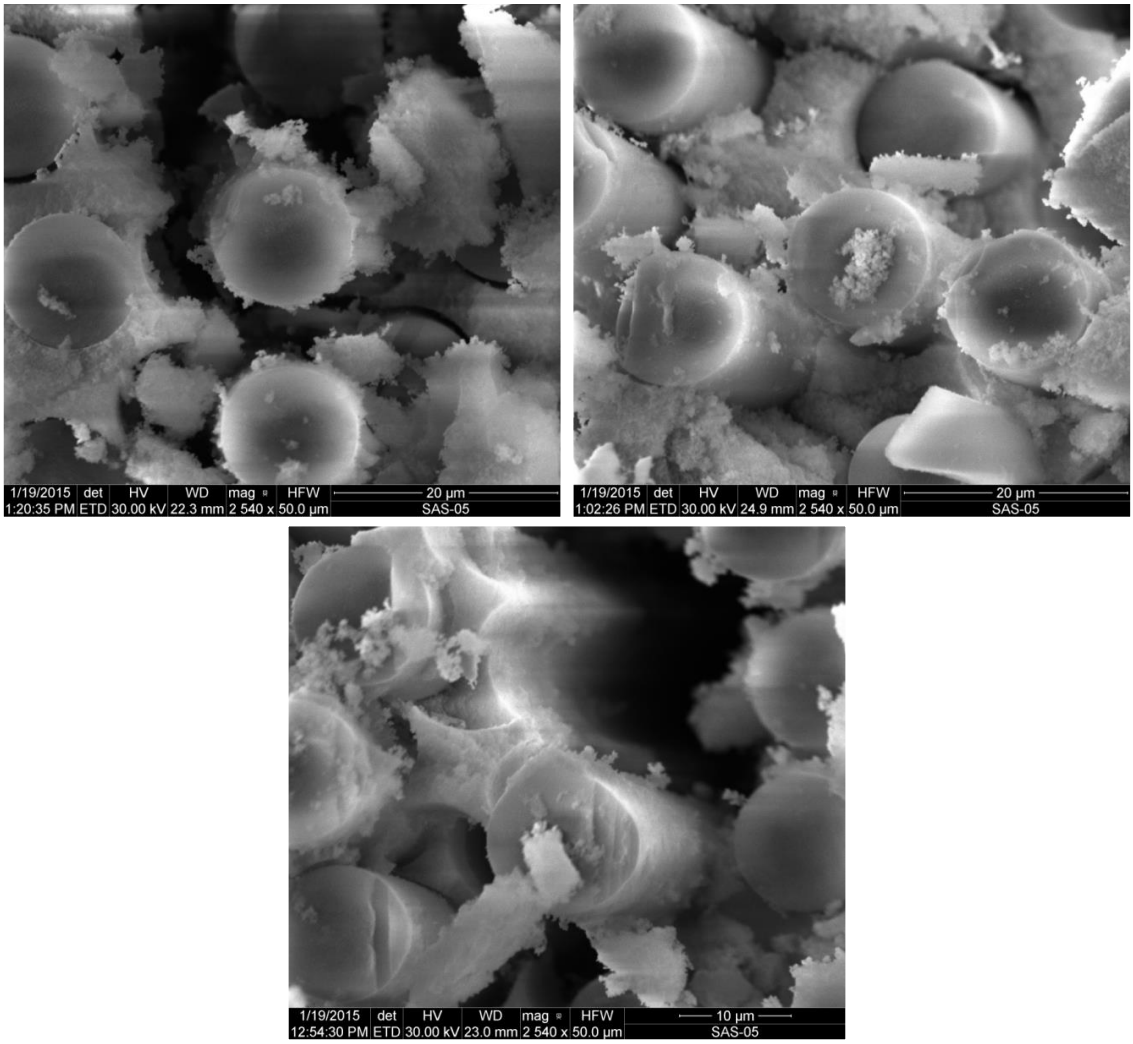

Figure 65 (continued): SEM micrographs of a fracture surface obtained in a tension-compression fatigue test performed at 1200°C in air, σ_{max} = 100 MPa, N_f = 5,264 cycles.

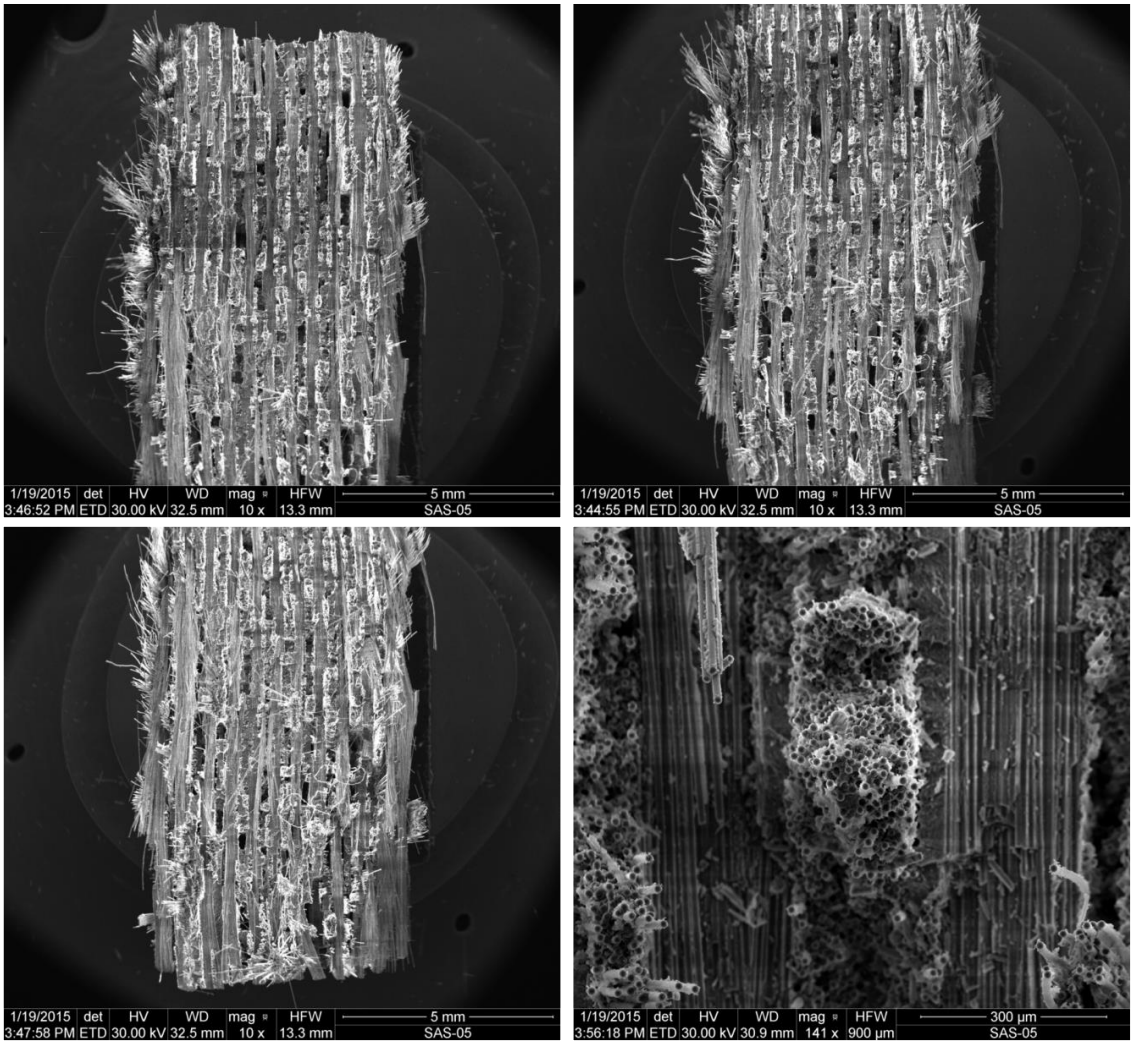

Figure 66: SEM micrographs of a fracture surface obtained in a tensile test of an N720/A specimen subjected to 10^5 cycles of prior tension-compression fatigue with σ_{max} = 70 MPa at 1200°C in steam.

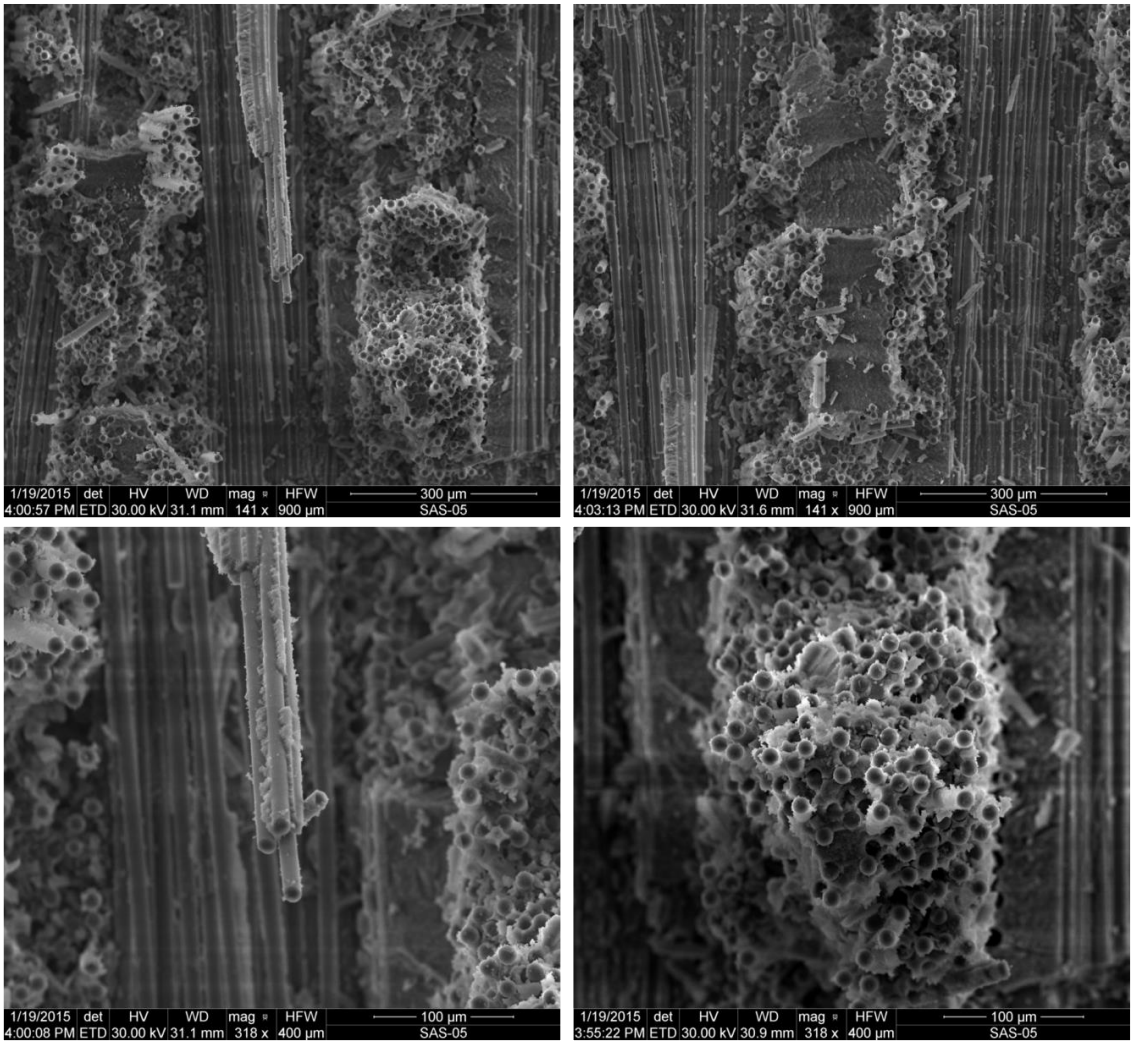

Figure 66 (continued): SEM micrographs of a fracture surface obtained in a tensile test of an N720/A specimen subjected to 10^5 cycles of prior tension-compression fatigue with σ_{max} = 70 MPa at 1200°C in steam.

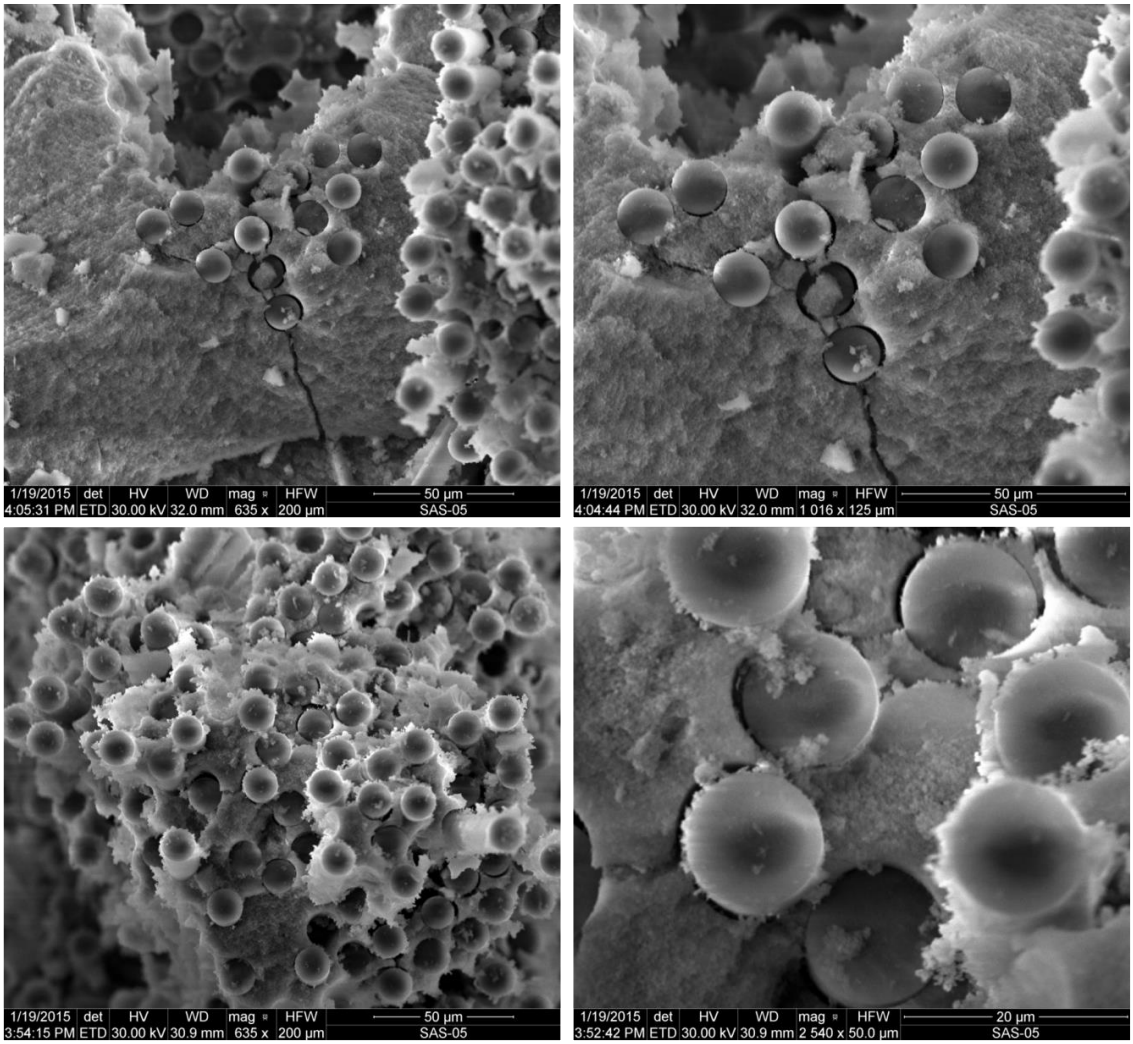

Figure 66 (continued): SEM micrographs of a fracture surface obtained in a tensile test of an N720/A specimen subjected to 10^5 cycles of prior tension-compression fatigue with σ_{max} = 70 MPa at 1200°C in steam.

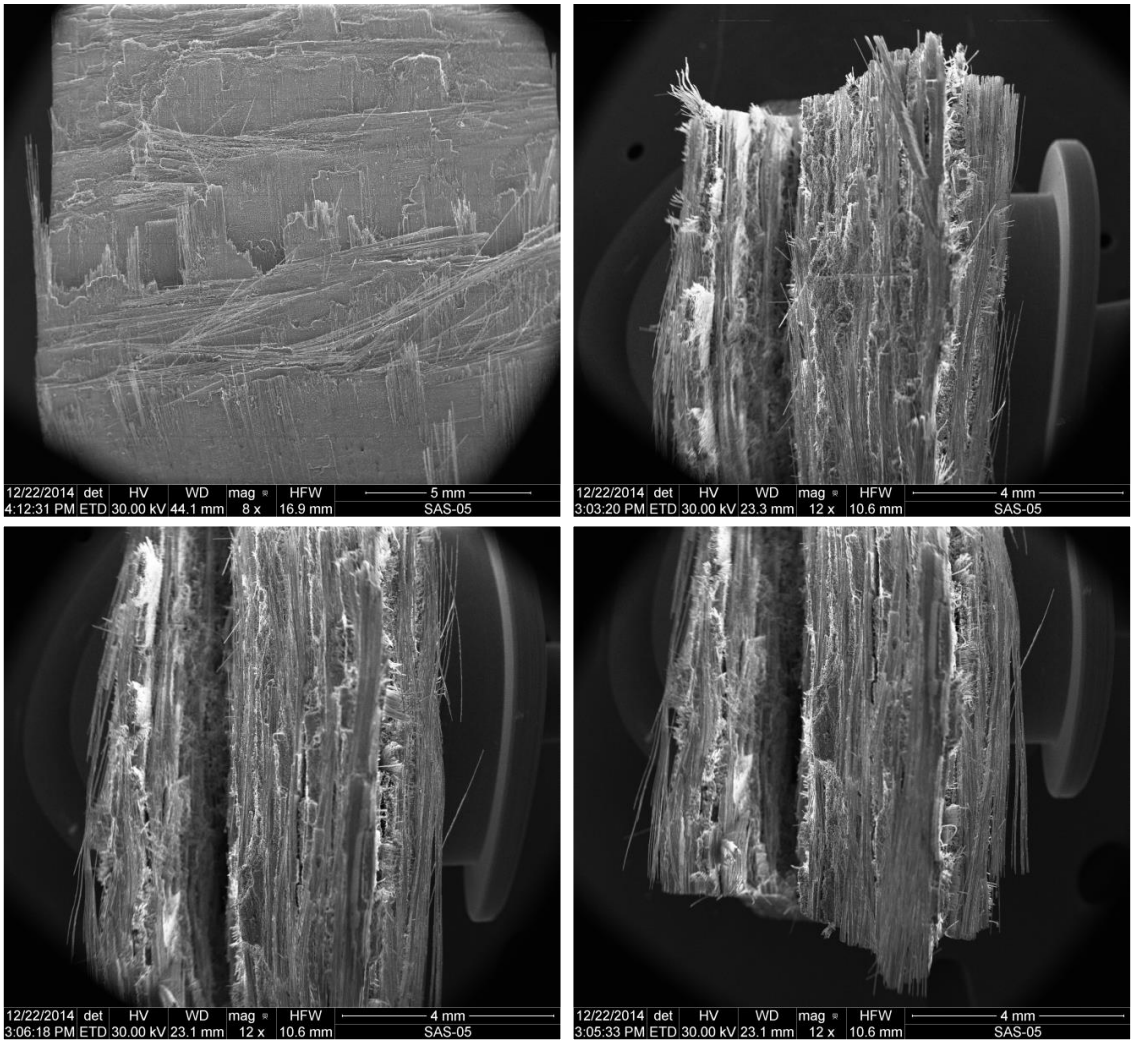

Figure 67: SEM micrographs of a fracture surface obtained in a tension-compression fatigue test performed at 1200°C in steam, σ_{max} = 75 MPa, N_f = 86,548 cycles.

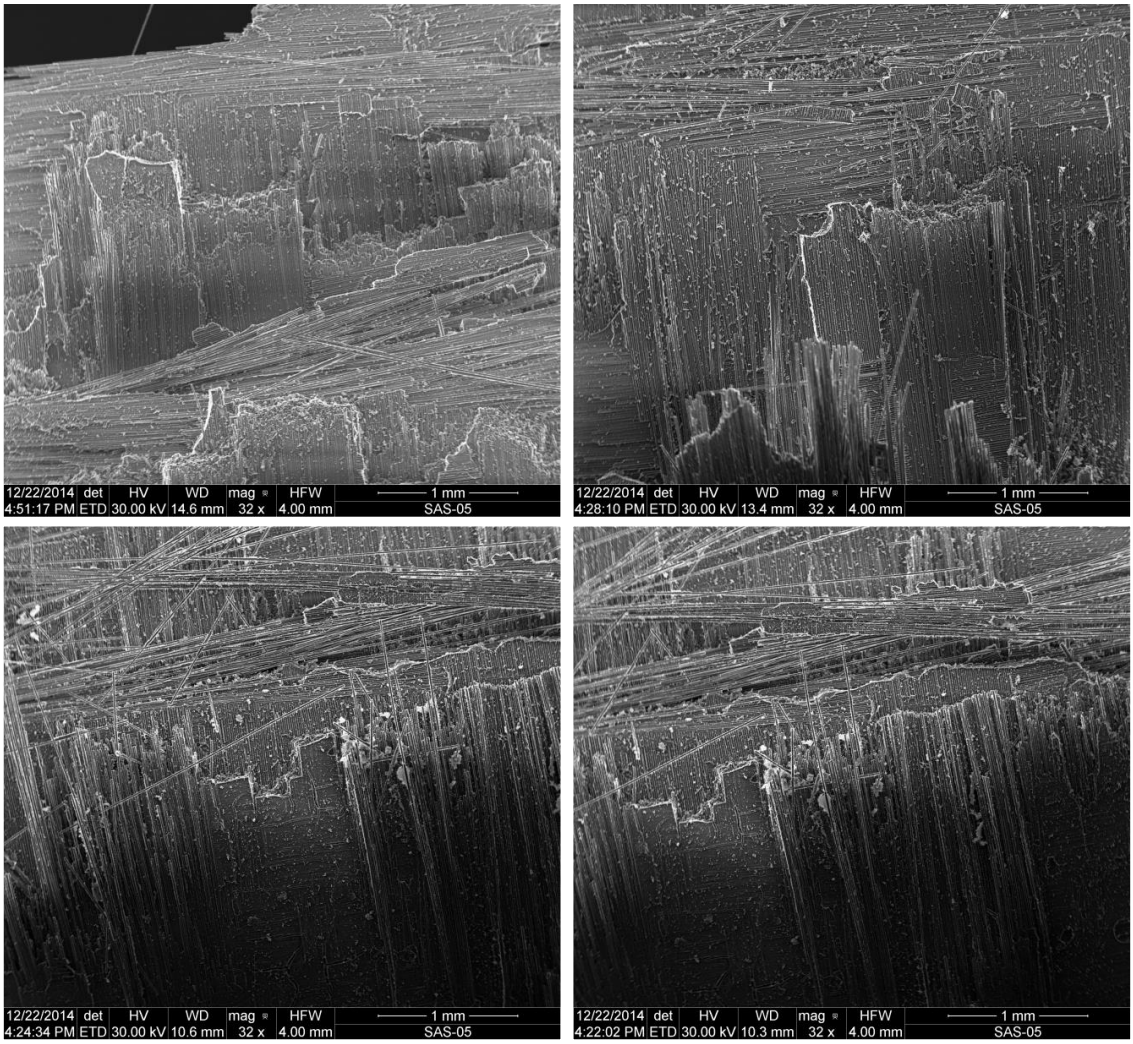

Figure 67: (continued): SEM micrographs of a fracture surface obtained in a tension-compression fatigue test performed at 1200°C in steam, σ_{max} = 75 MPa, N_f = 86,548 cycles.

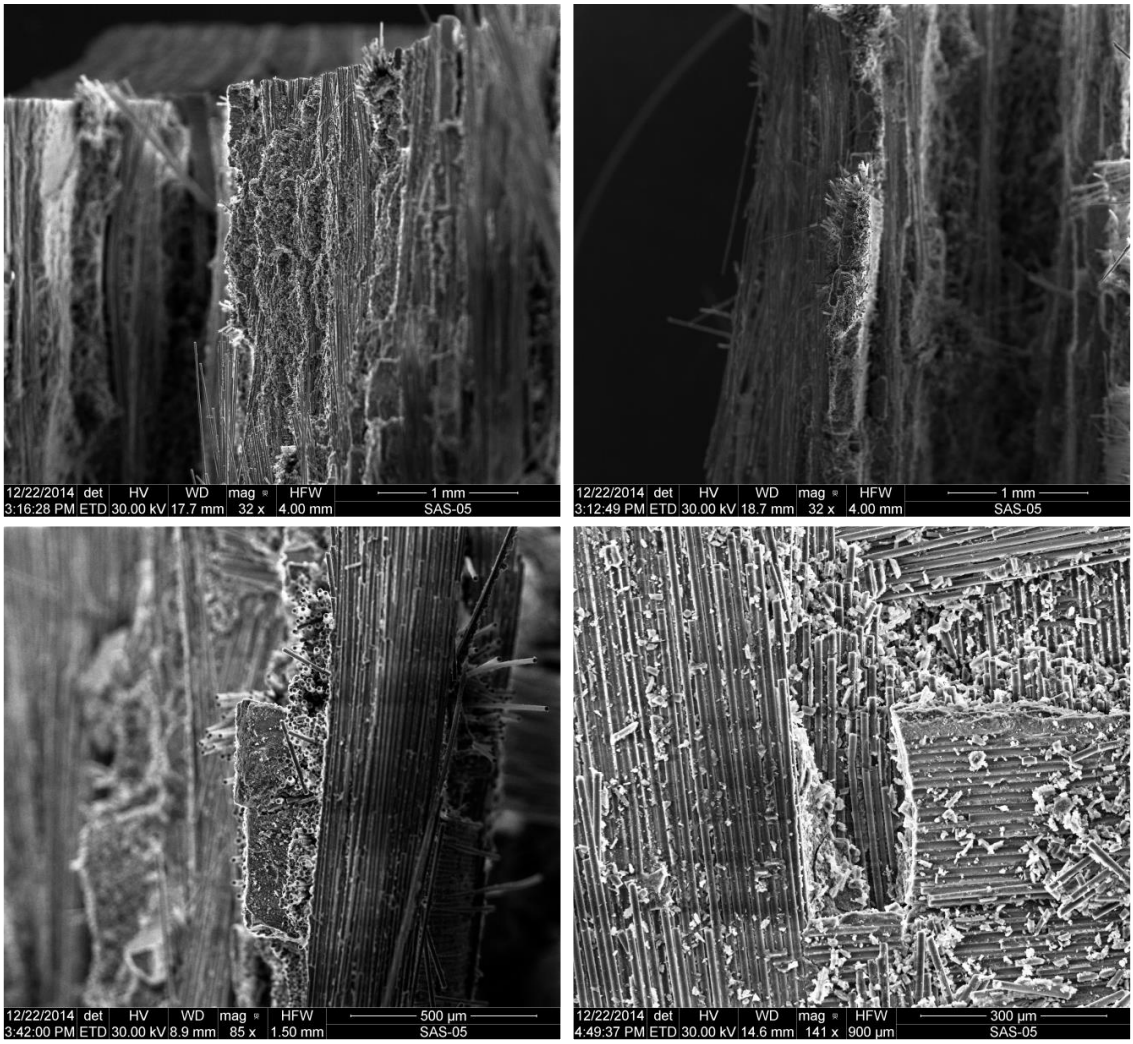

Figure 67 (continued): SEM micrographs of a fracture surface obtained in a tension-compression fatigue test performed at 1200°C in steam, σ_{max} = 75 MPa, N_f = 86,548 cycles.

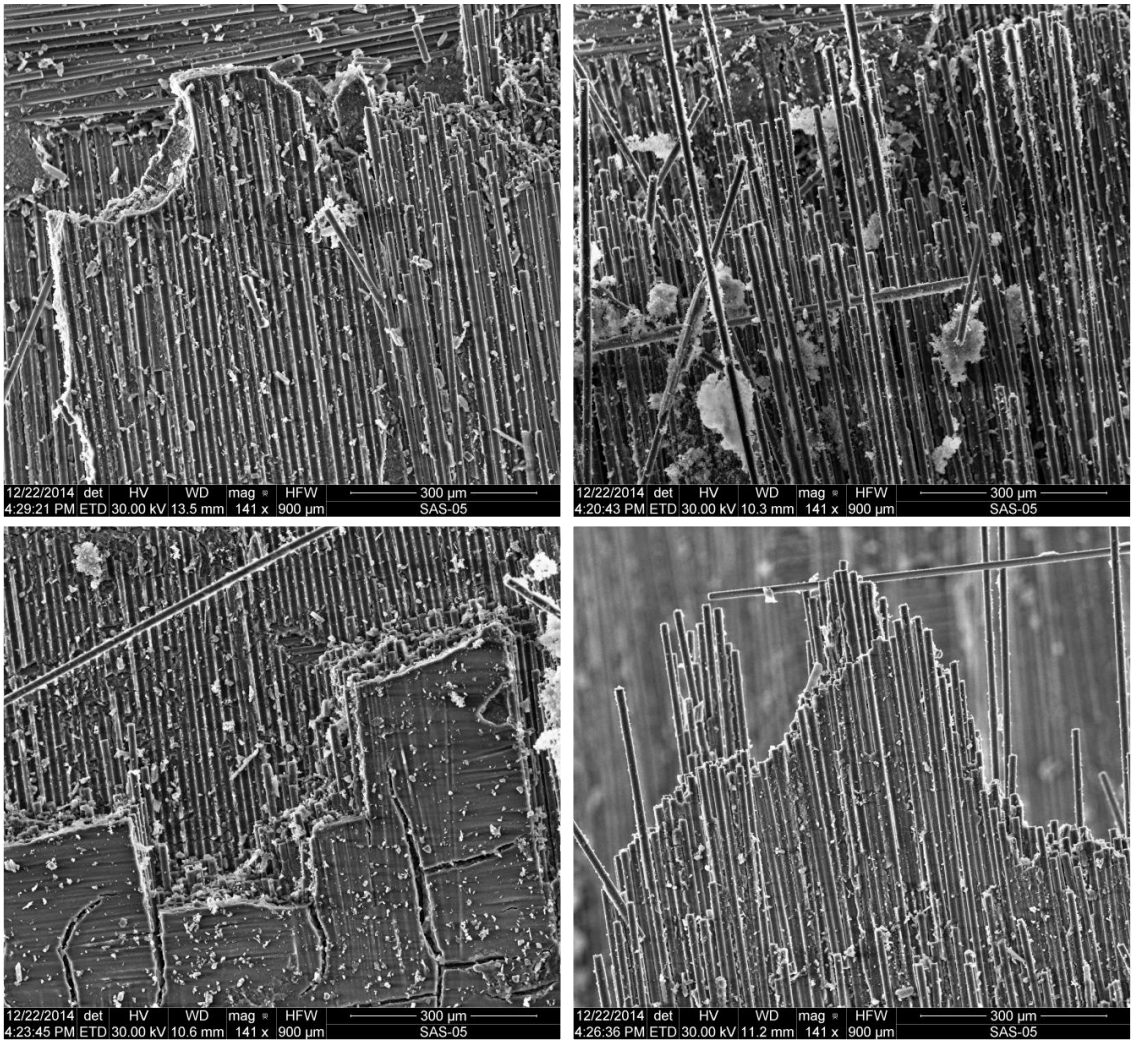

Figure 67: (continued): SEM micrographs of a fracture surface obtained in a tension-compression fatigue test performed at 1200°C in steam, σ_{max} = 75 MPa, N_f = 86,548 cycles.

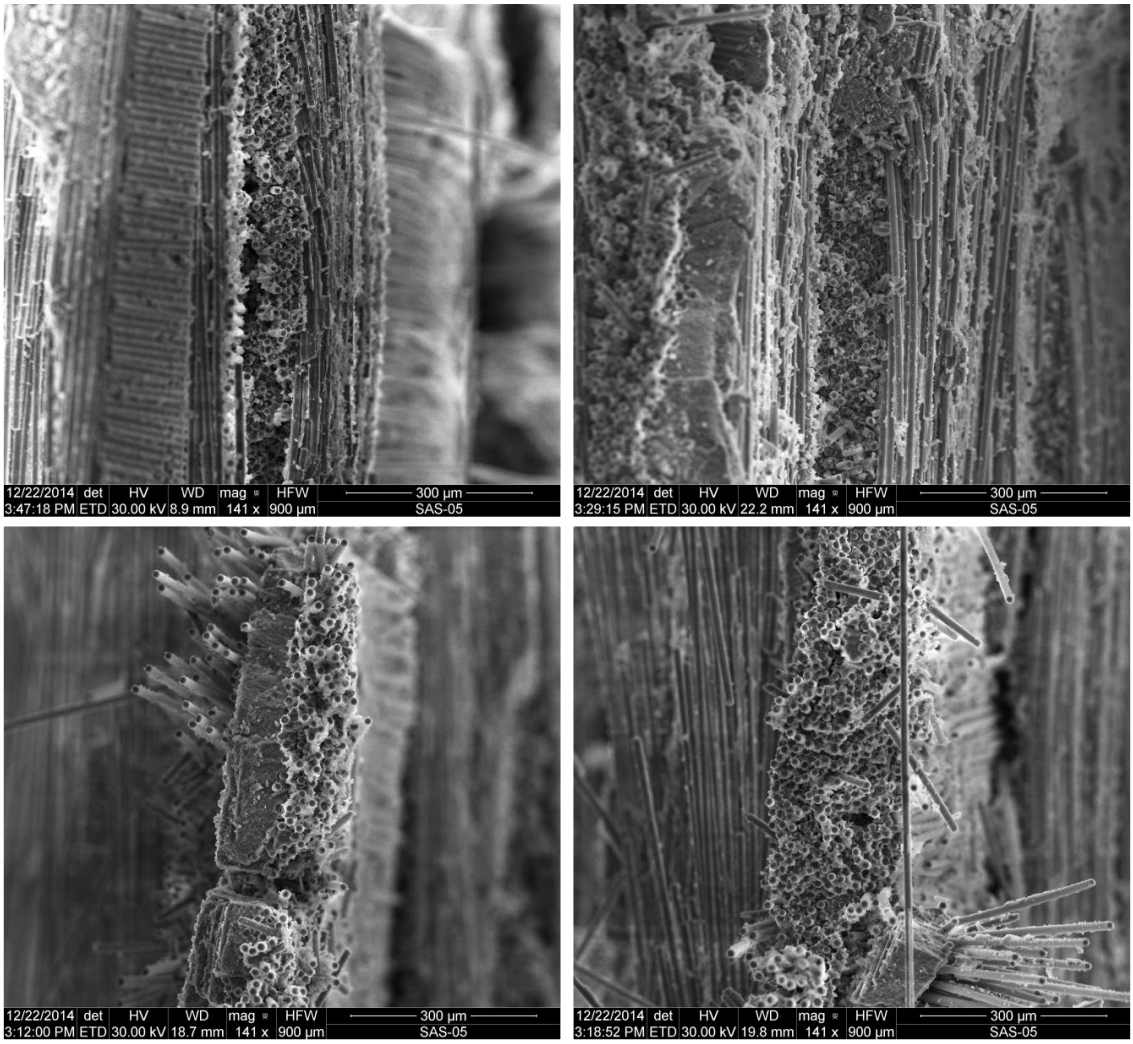

Figure 67: (continued): SEM micrographs of a fracture surface obtained in a tension-compression fatigue test performed at 1200°C in steam, σ_{max} = 75 MPa, N_f = 86,548 cycles.

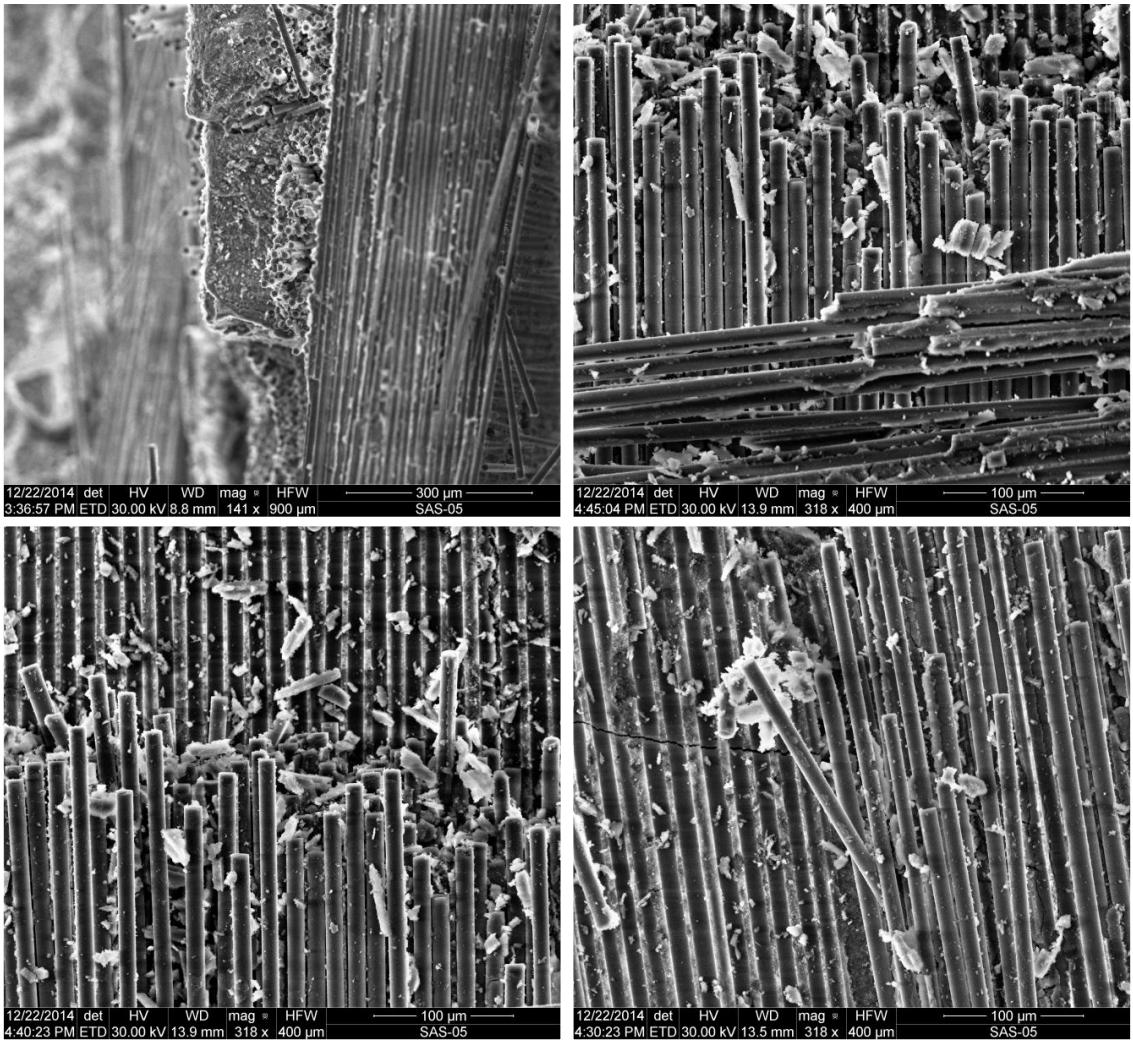

Figure 67: (continued): SEM micrographs of a fracture surface obtained in a tension-compression fatigue test performed at 1200°C in steam, σ_{max} = 75 MPa, N_f = 86,548 cycles.

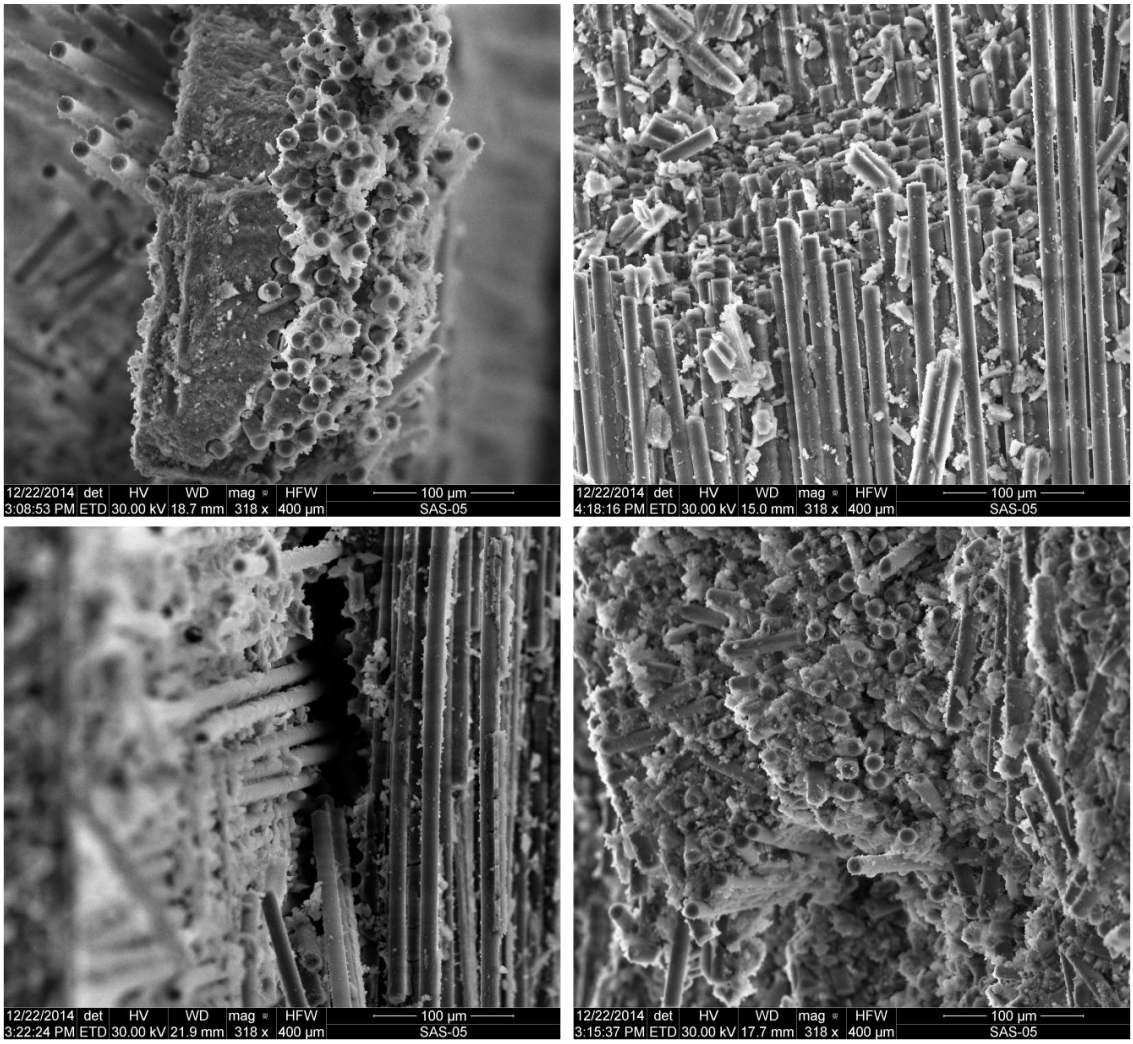

Figure 67: (continued): SEM micrographs of a fracture surface obtained in a tension-compression fatigue test performed at 1200°C in steam, σ_{max} = 75 MPa, N_f = 86,548 cycles.

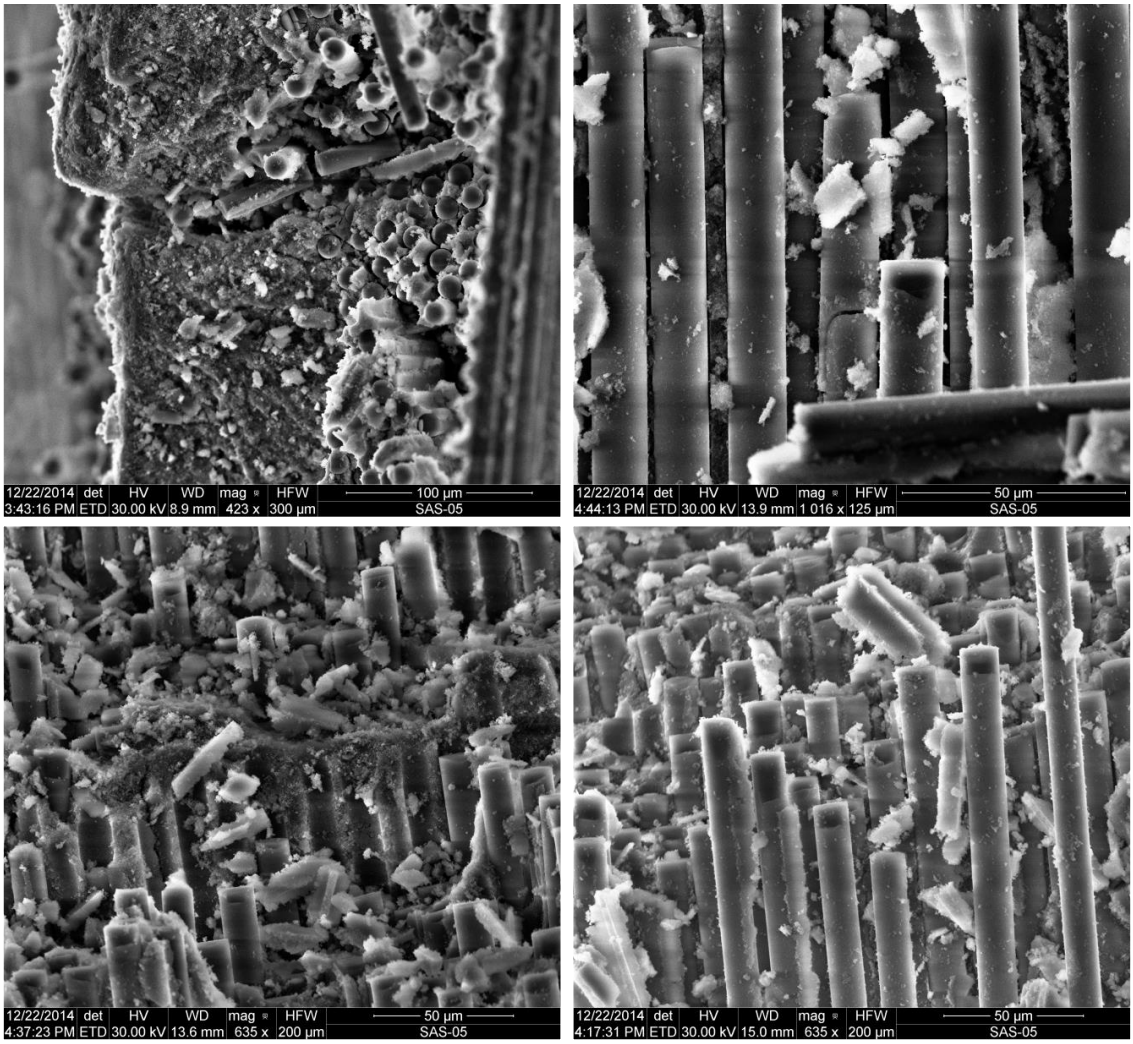

Figure 67: (continued): SEM micrographs of a fracture surface obtained in a tension-compression fatigue test performed at 1200°C in steam, σ_{max} = 75 MPa, N_f = 86,548 cycles.

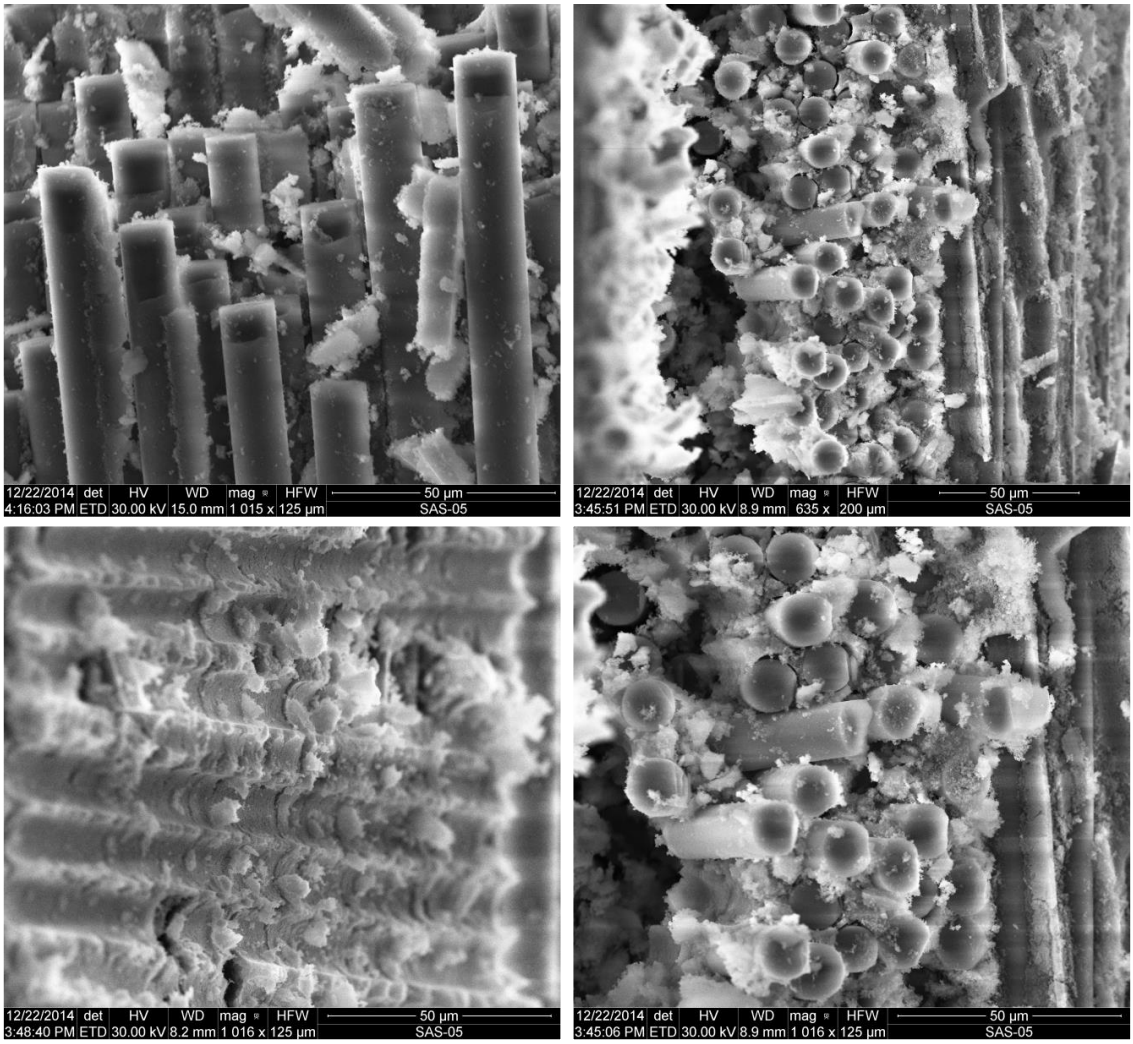

Figure 67: (continued): SEM micrographs of a fracture surface obtained in a tension-compression fatigue test performed at 1200°C in steam, σ_{max} = 75 MPa, N_f = 86,548 cycles.

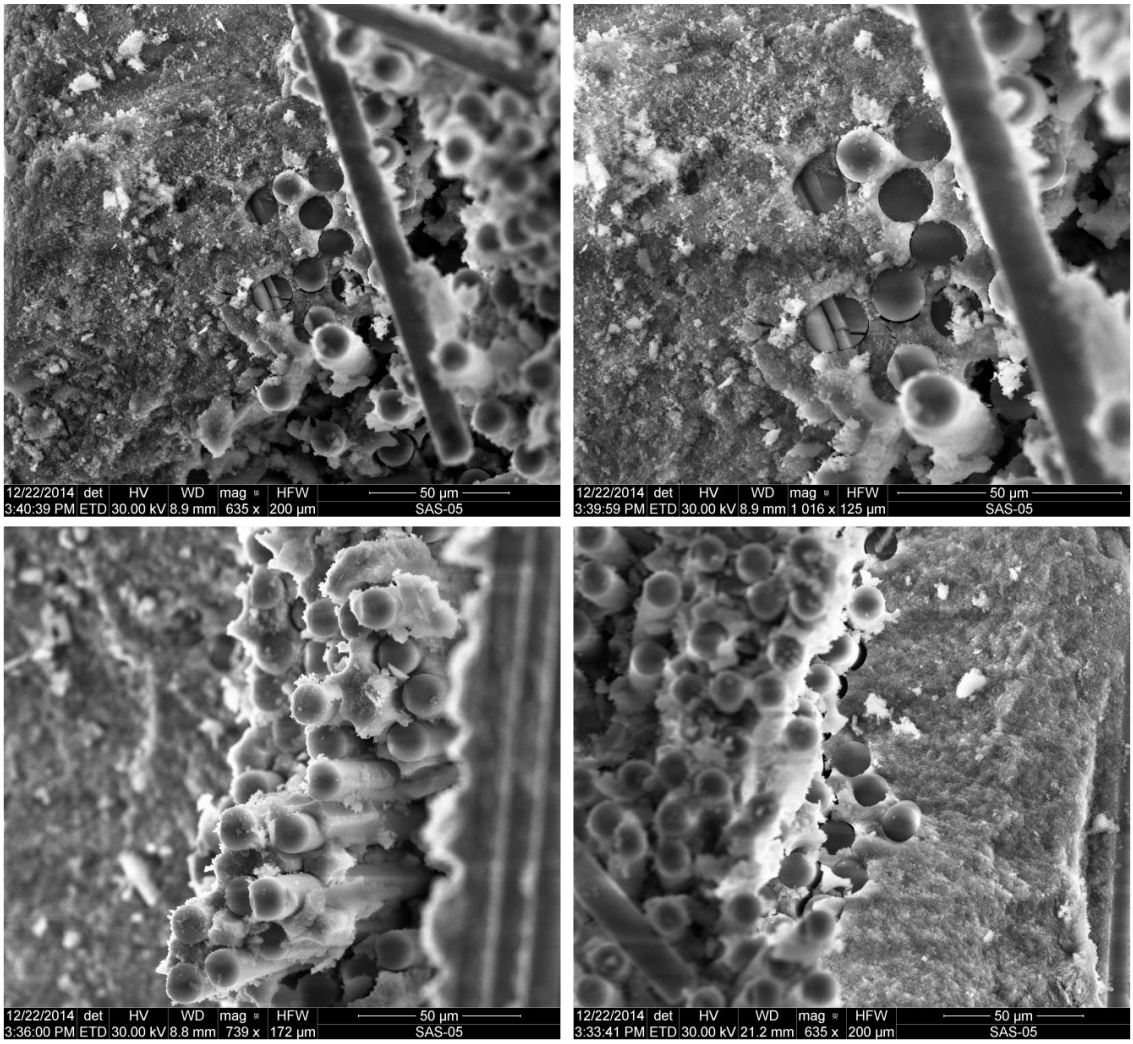

Figure 67: (continued): SEM micrographs of a fracture surface obtained in a tension-compression fatigue test performed at 1200°C in steam, σ_{max} = 75 MPa, N_f = 86,548 cycles.

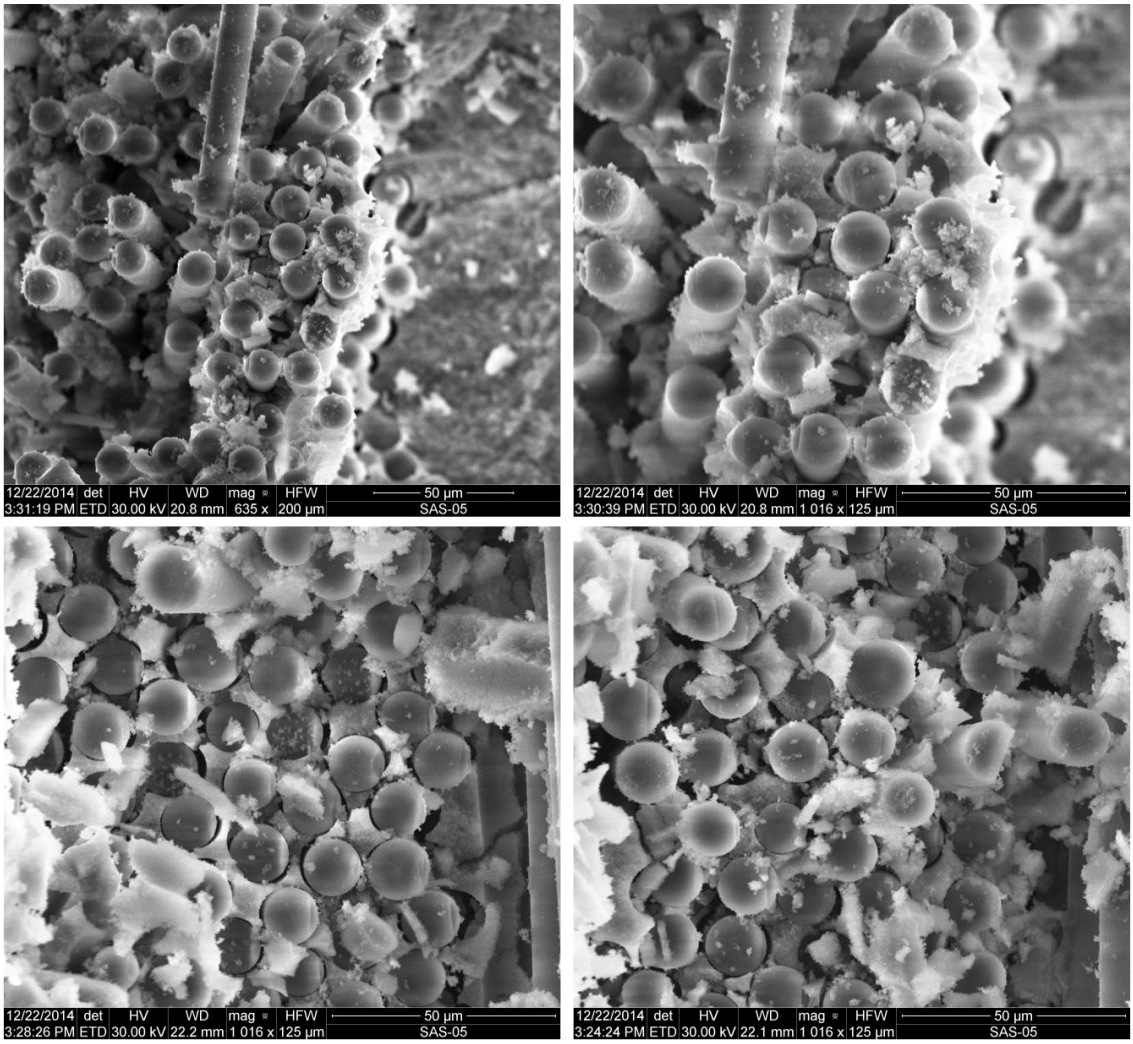

Figure 67: (continued): SEM micrographs of a fracture surface obtained in a tension-compression fatigue test performed at 1200°C in steam, σ_{max} = 75 MPa, N_f = 86,548 cycles.

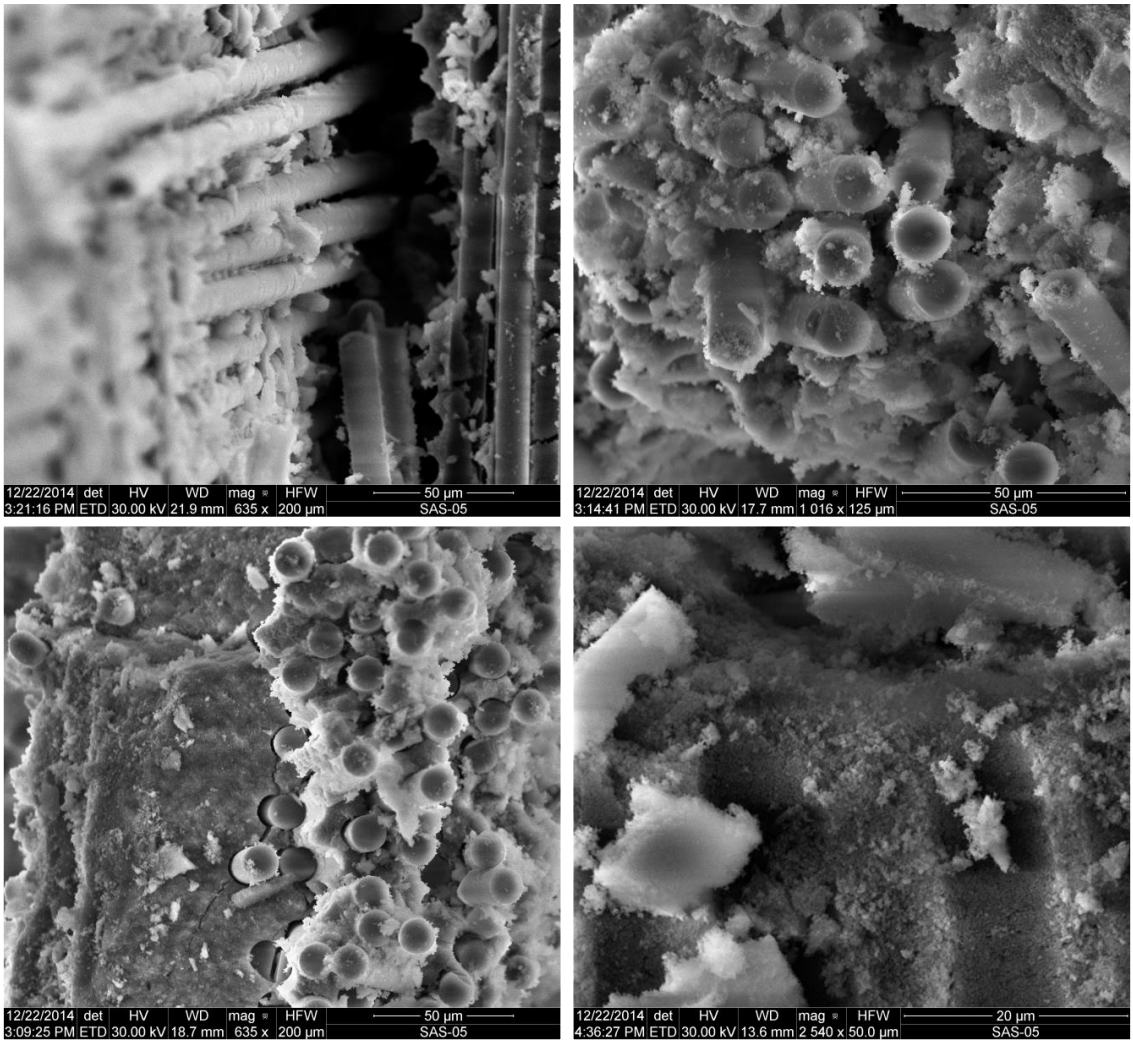

Figure 67: (continued): SEM micrographs of a fracture surface obtained in a tension-compression fatigue test performed at 1200°C in steam, σ_{max} = 75 MPa, N_f = 86,548 cycles.

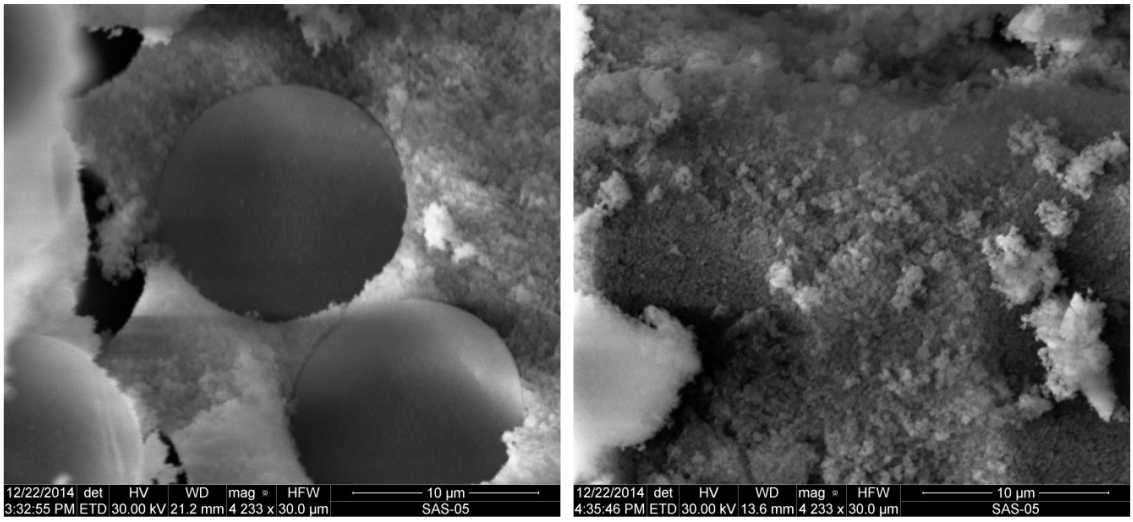

Figure 67: (continued): SEM micrographs of a fracture surface obtained in a tension-compression fatigue test performed at 1200°C in steam, σ_{max} = 75 MPa, N_f = 86,548 cycles.

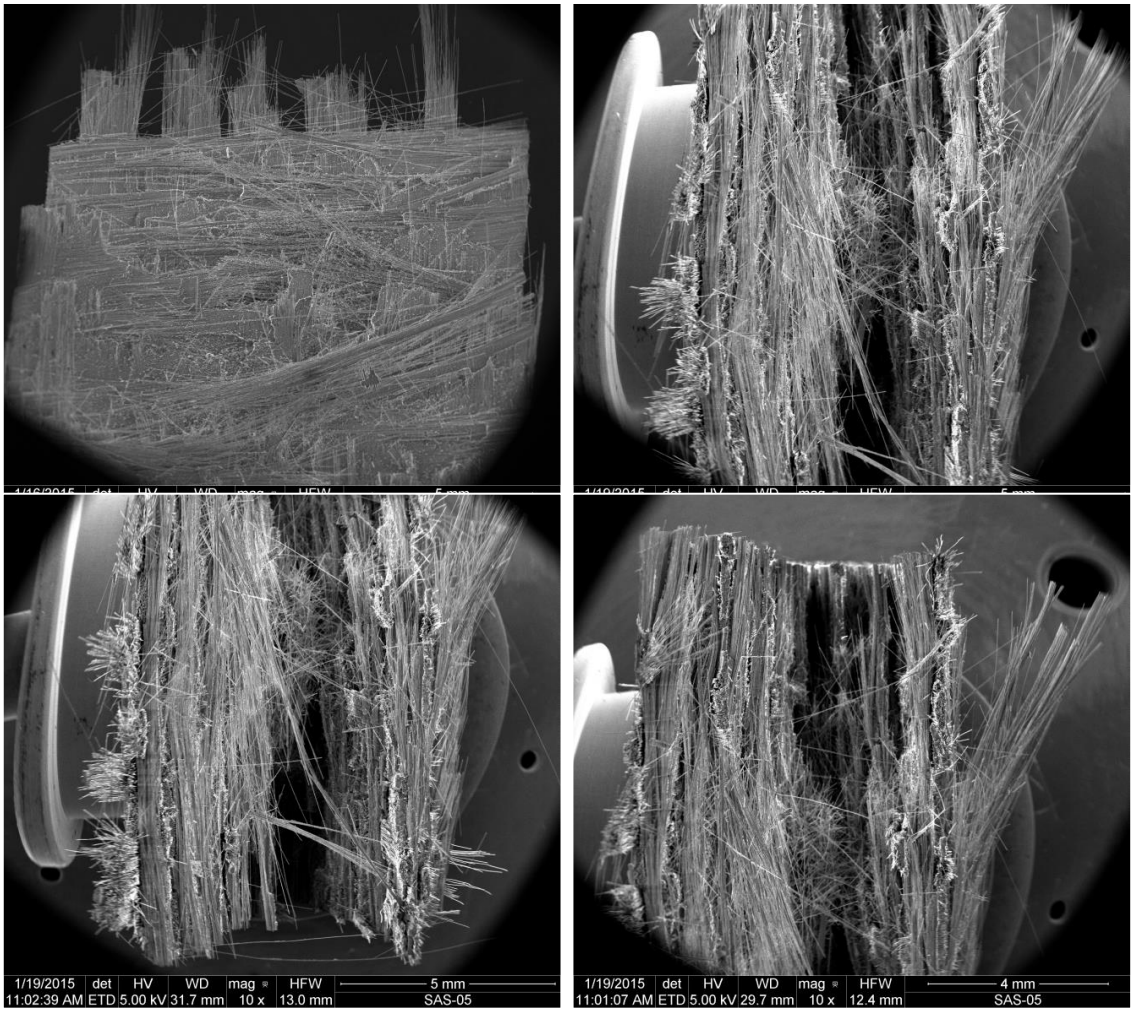

Figure 68: SEM micrographs of a fracture surface obtained in a tension-compression fatigue test performed at 1200°C in steam, σ_{max} = 100 MPa, N_f = 450 cycles.

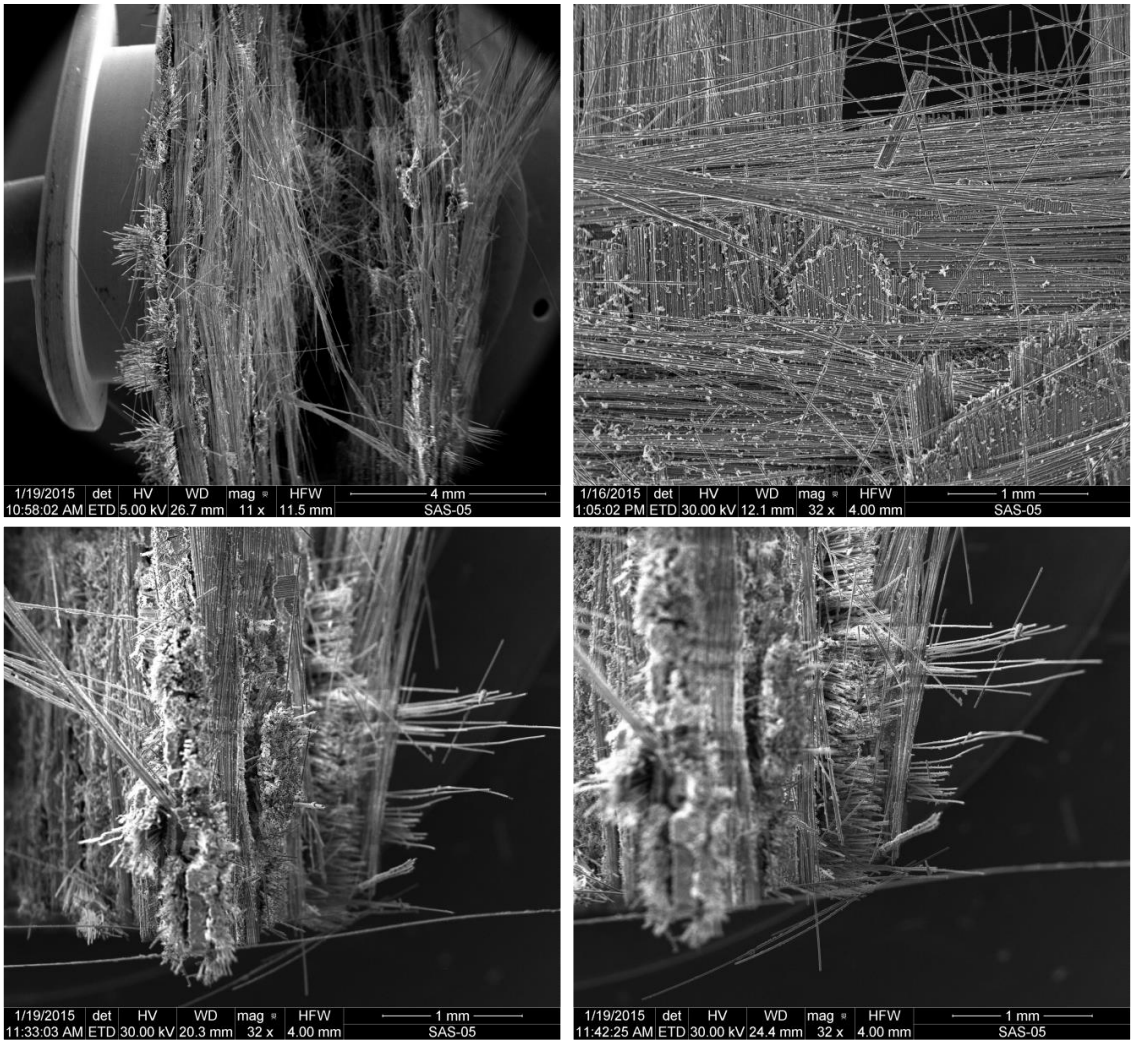

Figure 68 (continued): SEM micrographs of a fracture surface obtained in a tension-compression fatigue test performed at 1200°C in steam, σ_{max} = 100 MPa, N_f = 450 cycles.

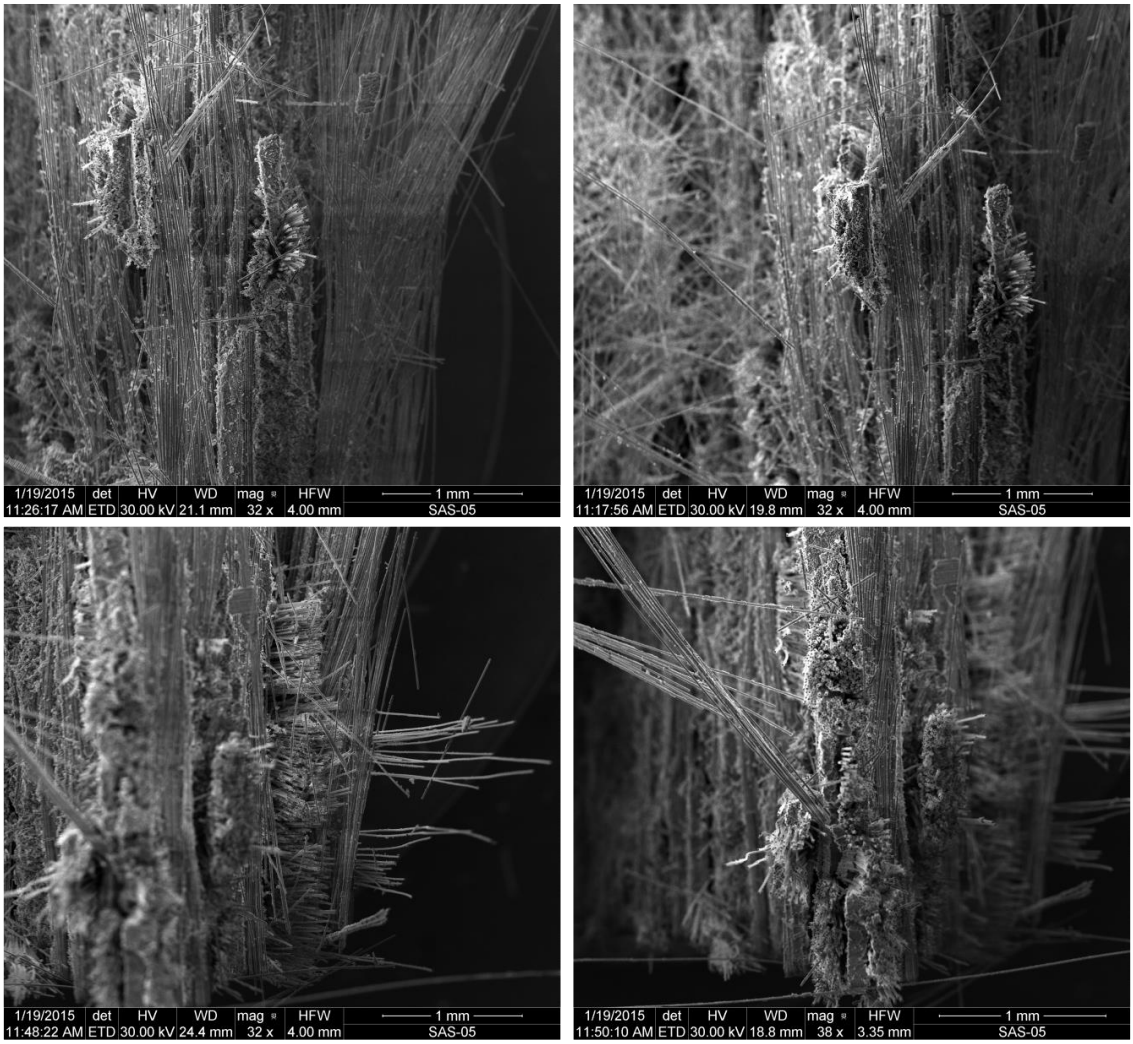

Figure 68 (continued): SEM micrographs of a fracture surface obtained in a tension-compression fatigue test performed at 1200°C in steam, σ_{max} = 100 MPa, N_f = 450 cycles.

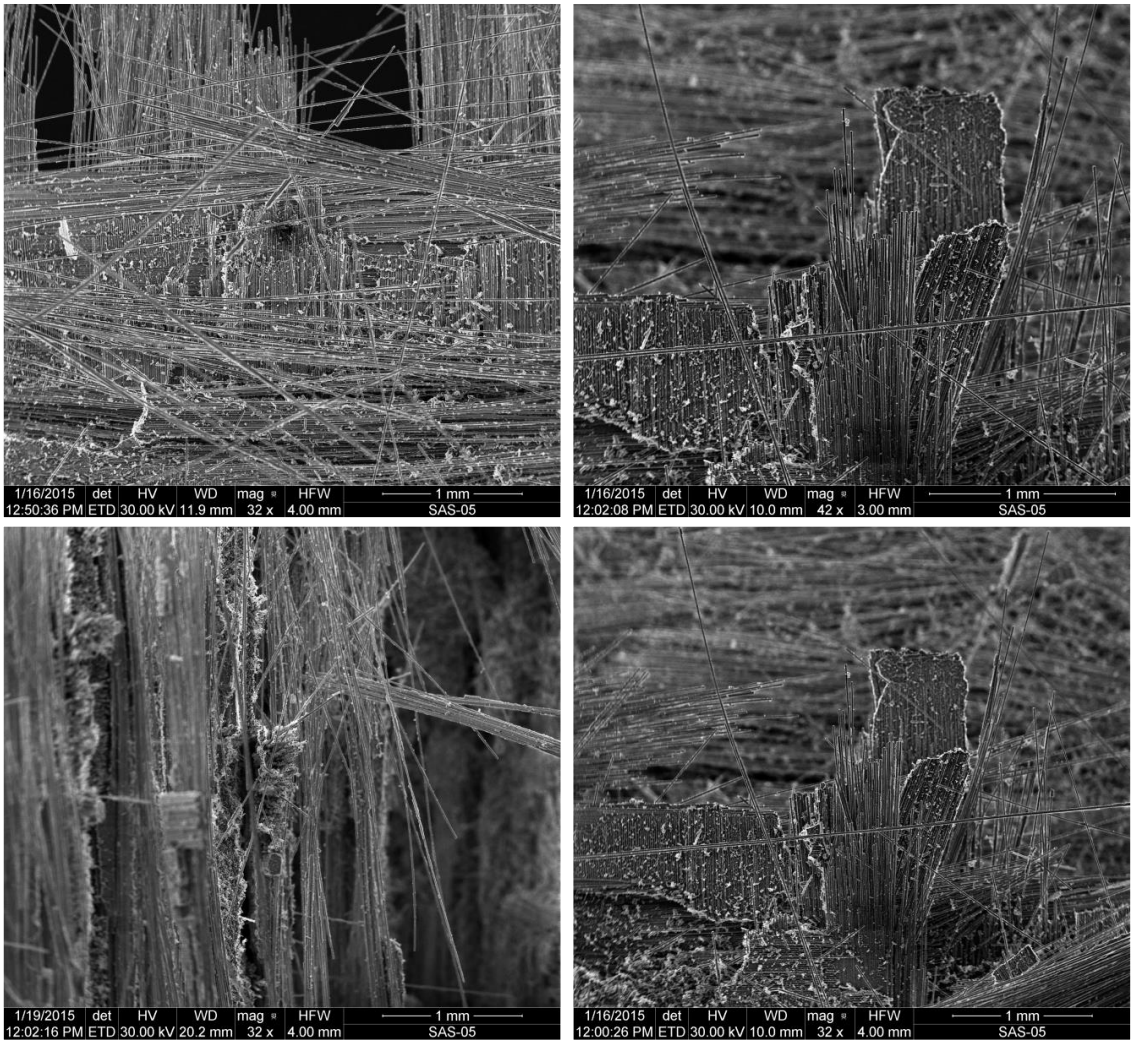

Figure 68 (continued): SEM micrographs of a fracture surface obtained in a tension-compression fatigue test performed at 1200°C in steam, σ_{max} = 100 MPa, N_f = 450 cycles.

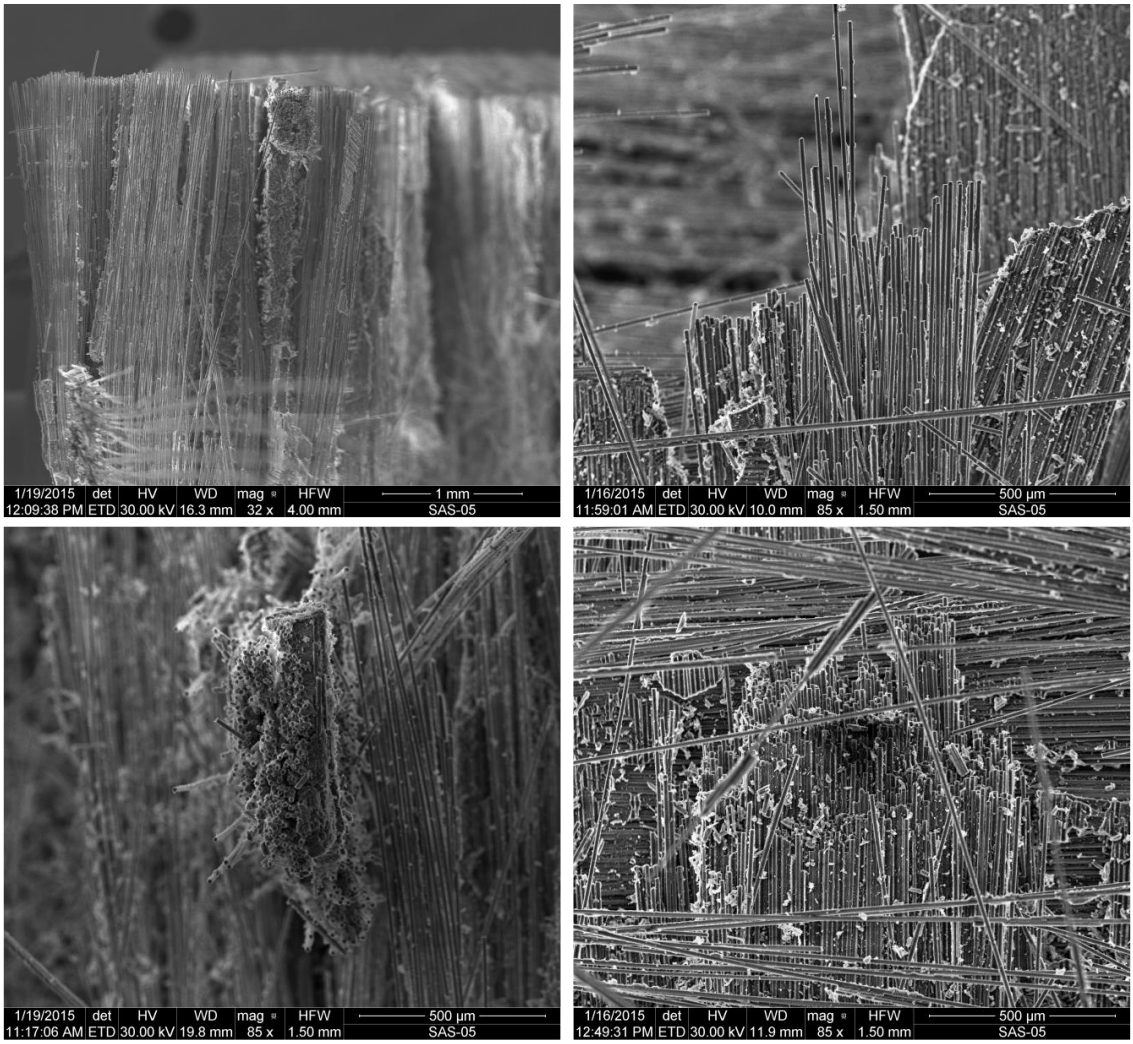

Figure 68 (continued): SEM micrographs of a fracture surface obtained in a tension-compression fatigue test performed at 1200°C in steam, σ_{max} = 100 MPa, N_f = 450 cycles.

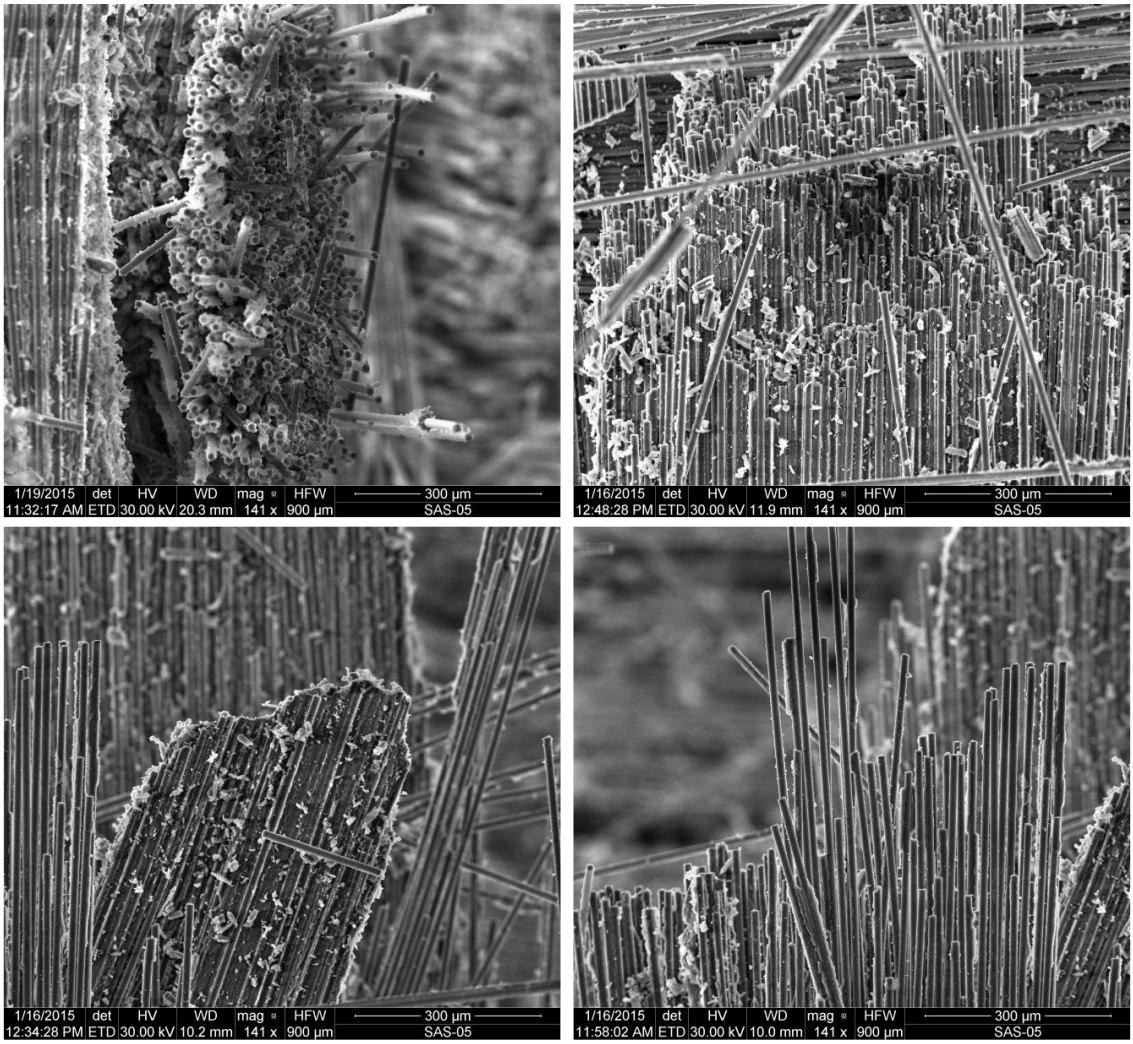

Figure 68 (continued): SEM micrographs of a fracture surface obtained in a tension-compression fatigue test performed at 1200°C in steam, σ_{max} = 100 MPa, N_f = 450 cycles.

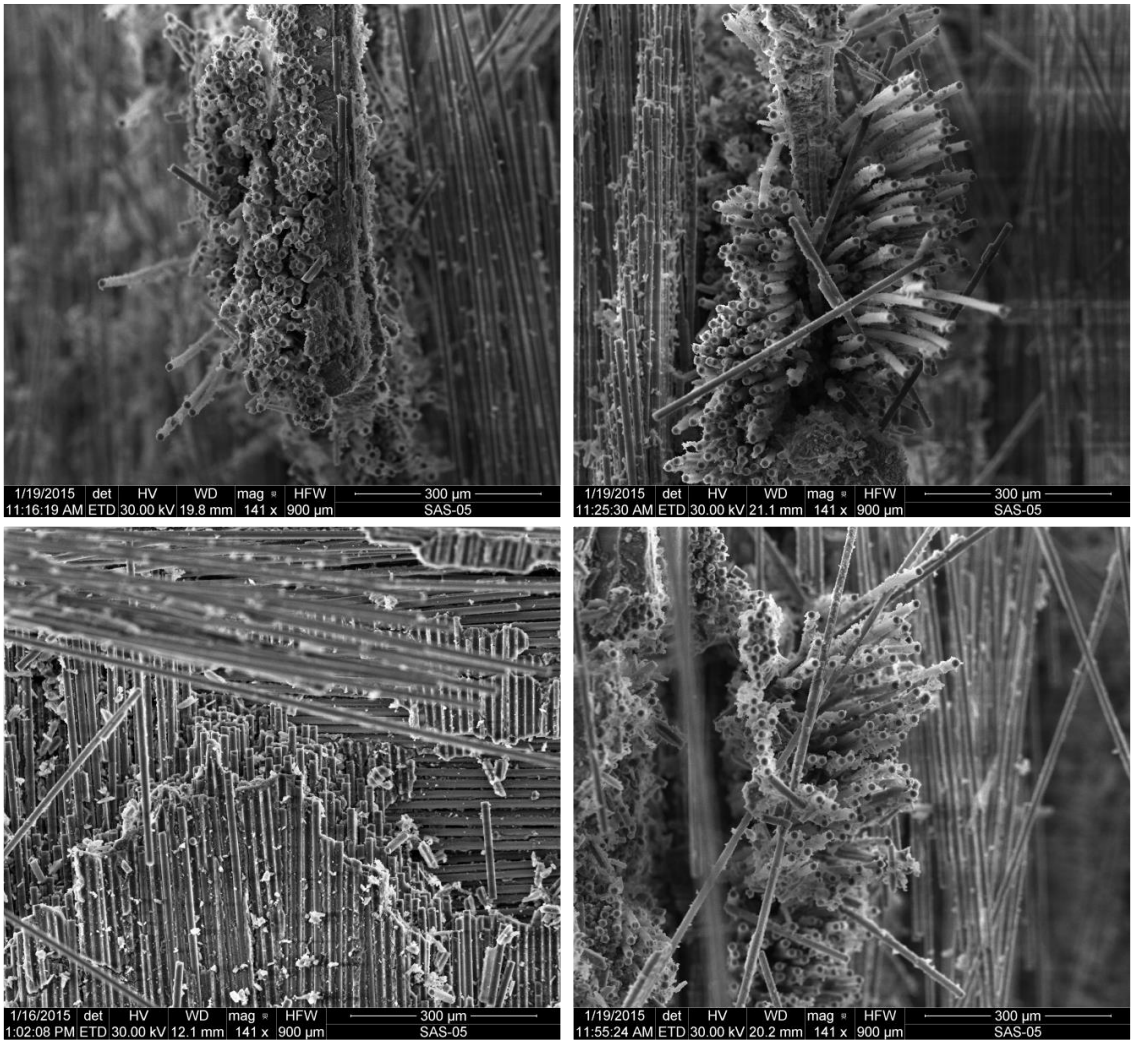

Figure 68 (continued): SEM micrographs of a fracture surface obtained in a tension-compression fatigue test performed at 1200°C in steam, σ_{max} = 100 MPa, N_f = 450 cycles.

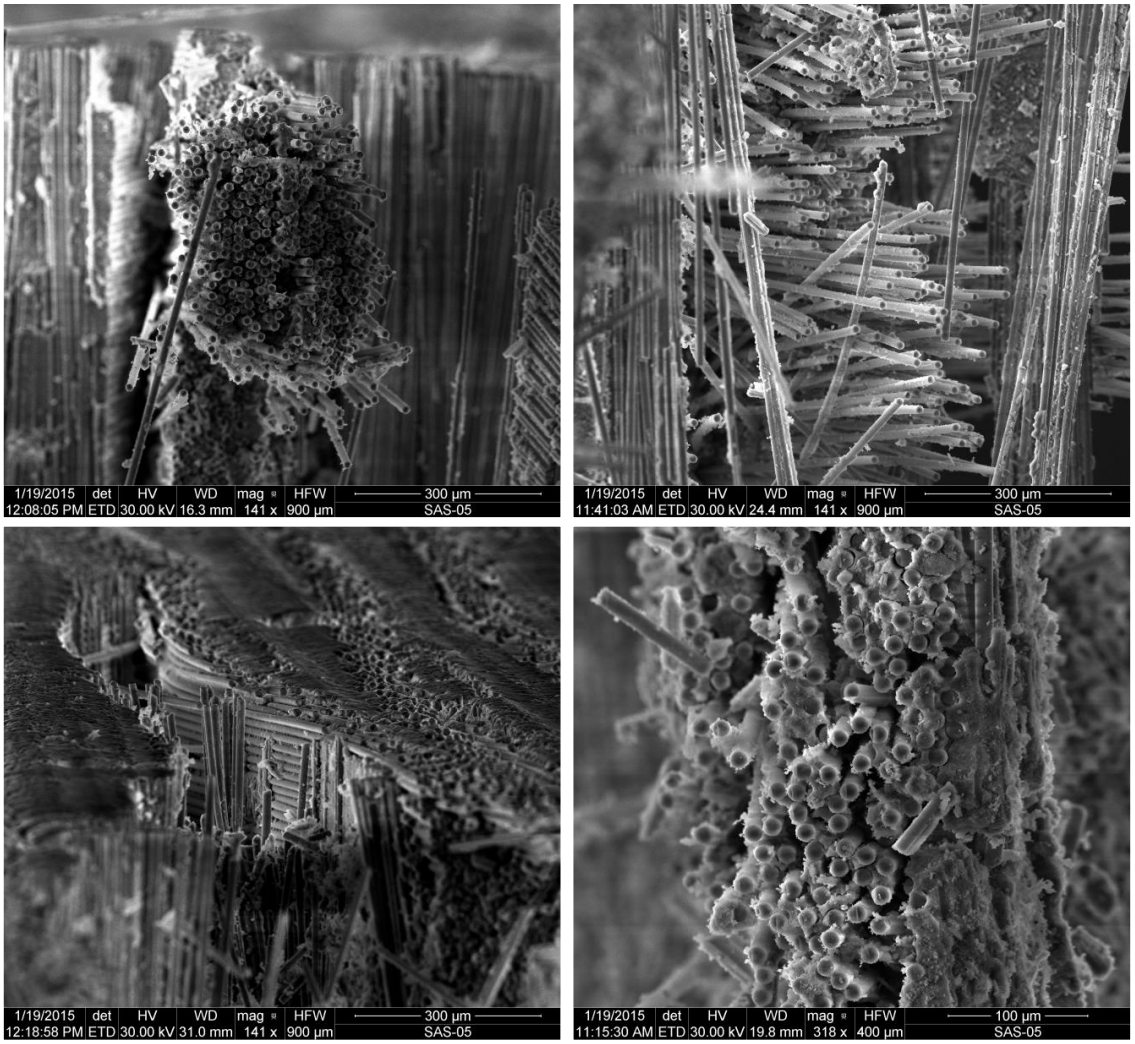

Figure 68 (continued): SEM micrographs of a fracture surface obtained in a tension-compression fatigue test performed at 1200°C in steam, σ_{max} = 100 MPa, N_f = 450 cycles.

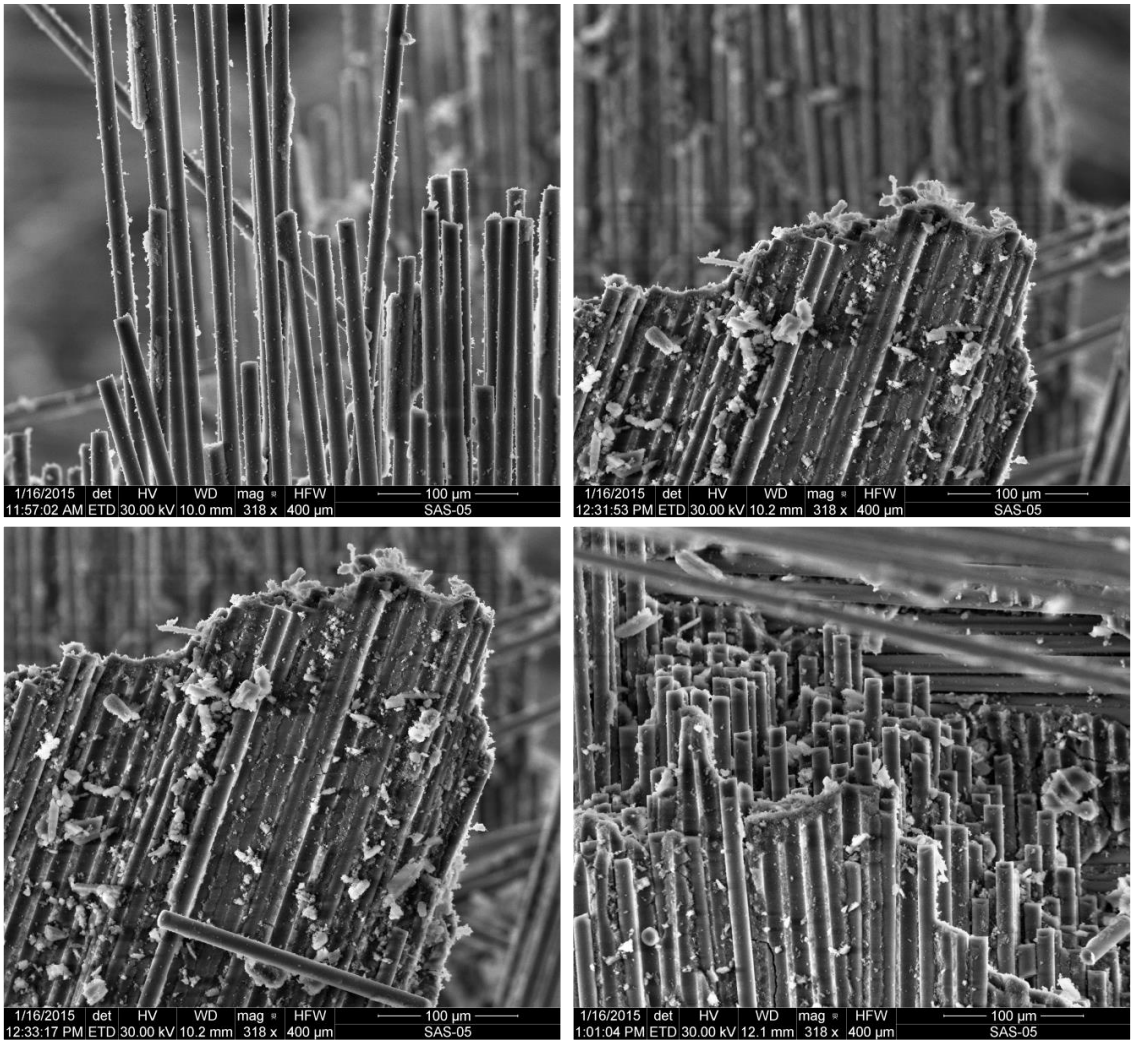

Figure 68 (continued): SEM micrographs of a fracture surface obtained in a tension-compression fatigue test performed at 1200°C in steam, σ_{max} = 100 MPa, N_f = 450 cycles.

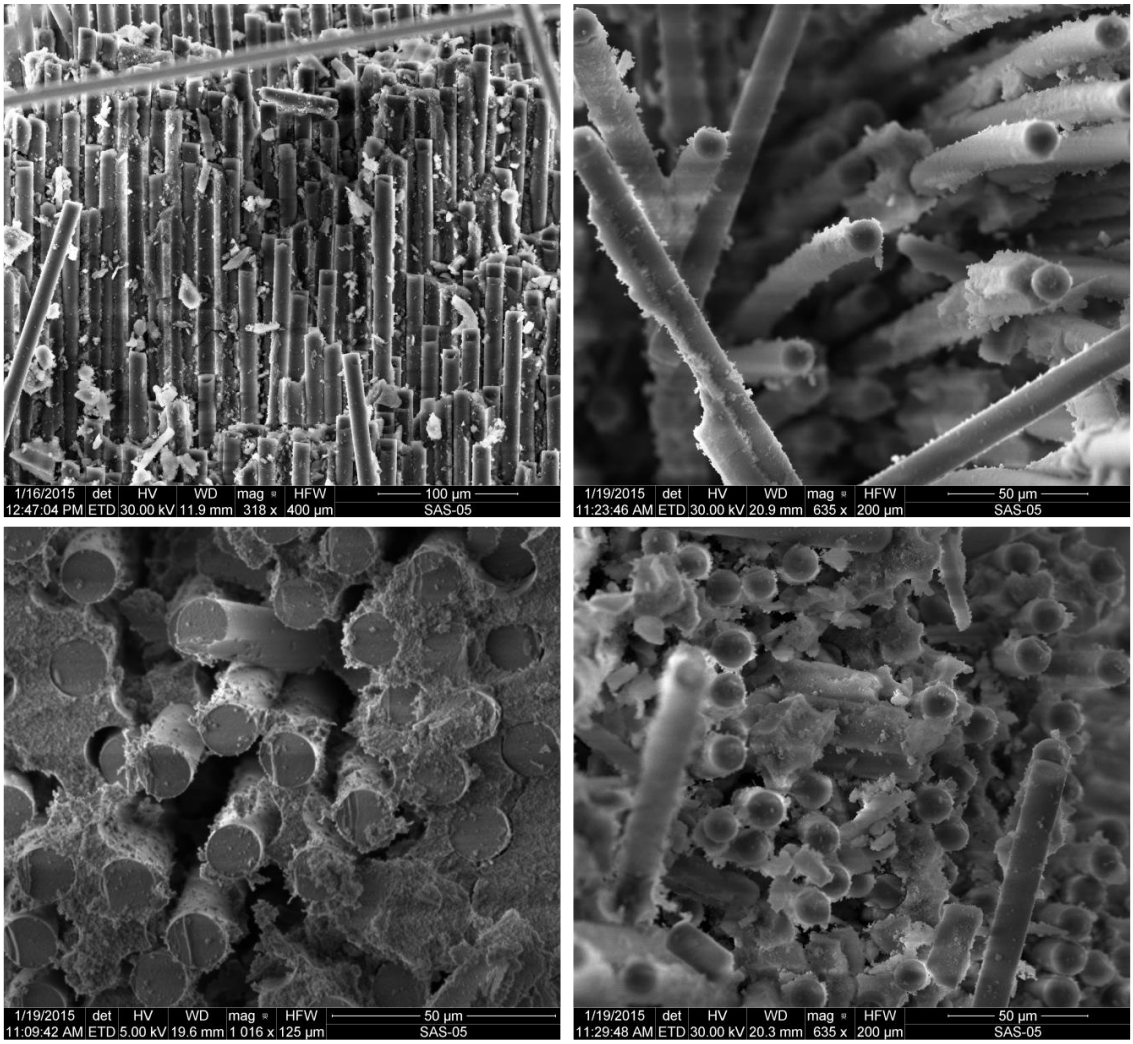

Figure 68 (continued): SEM micrographs of a fracture surface obtained in a tension-compression fatigue test performed at 1200°C in steam, σ_{max} = 100 MPa, N_f = 450 cycles.

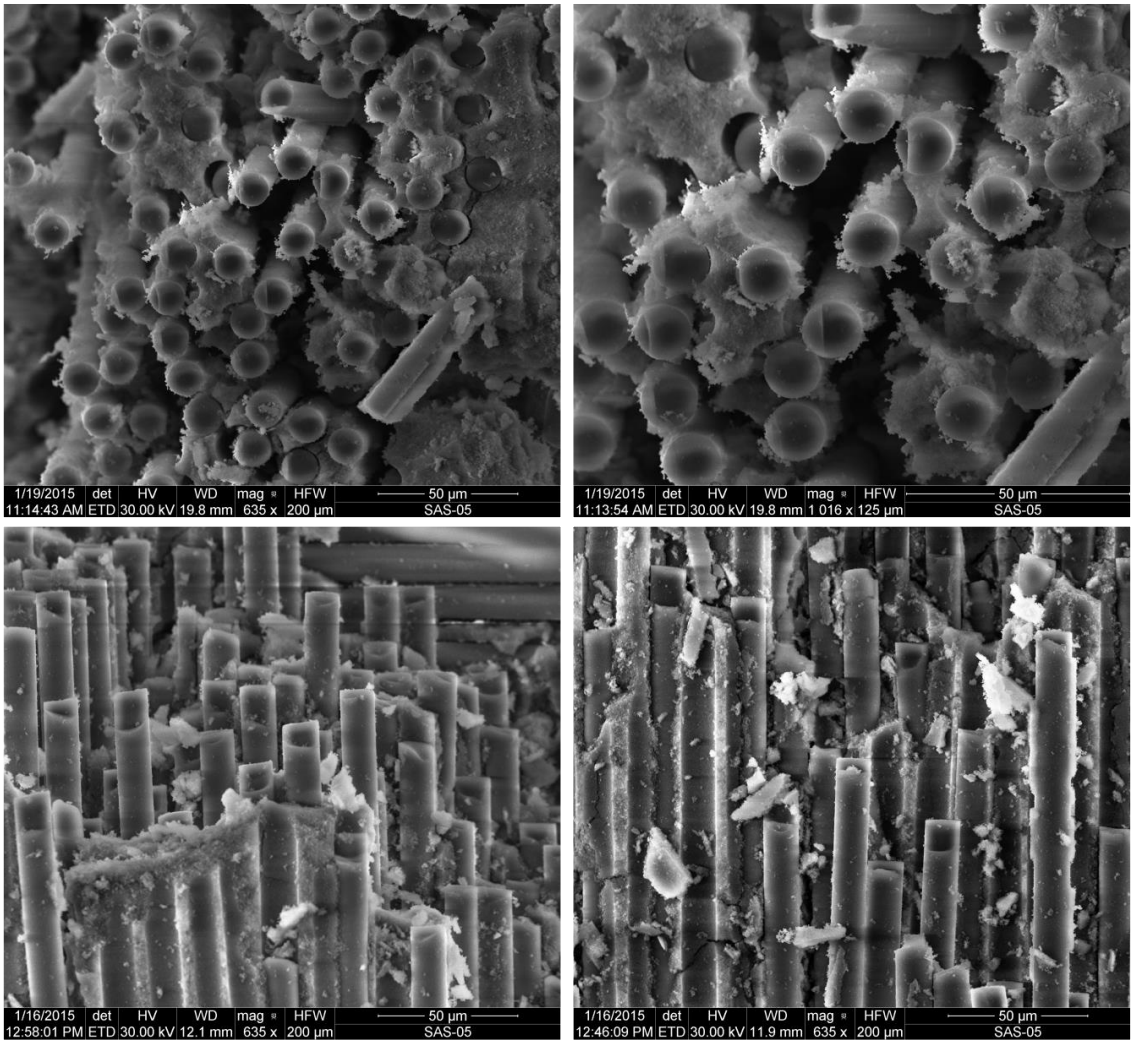

Figure 68 (continued): SEM micrographs of a fracture surface obtained in a tension-compression fatigue test performed at 1200°C in steam, σ_{max} = 100 MPa, N_f = 450 cycles.

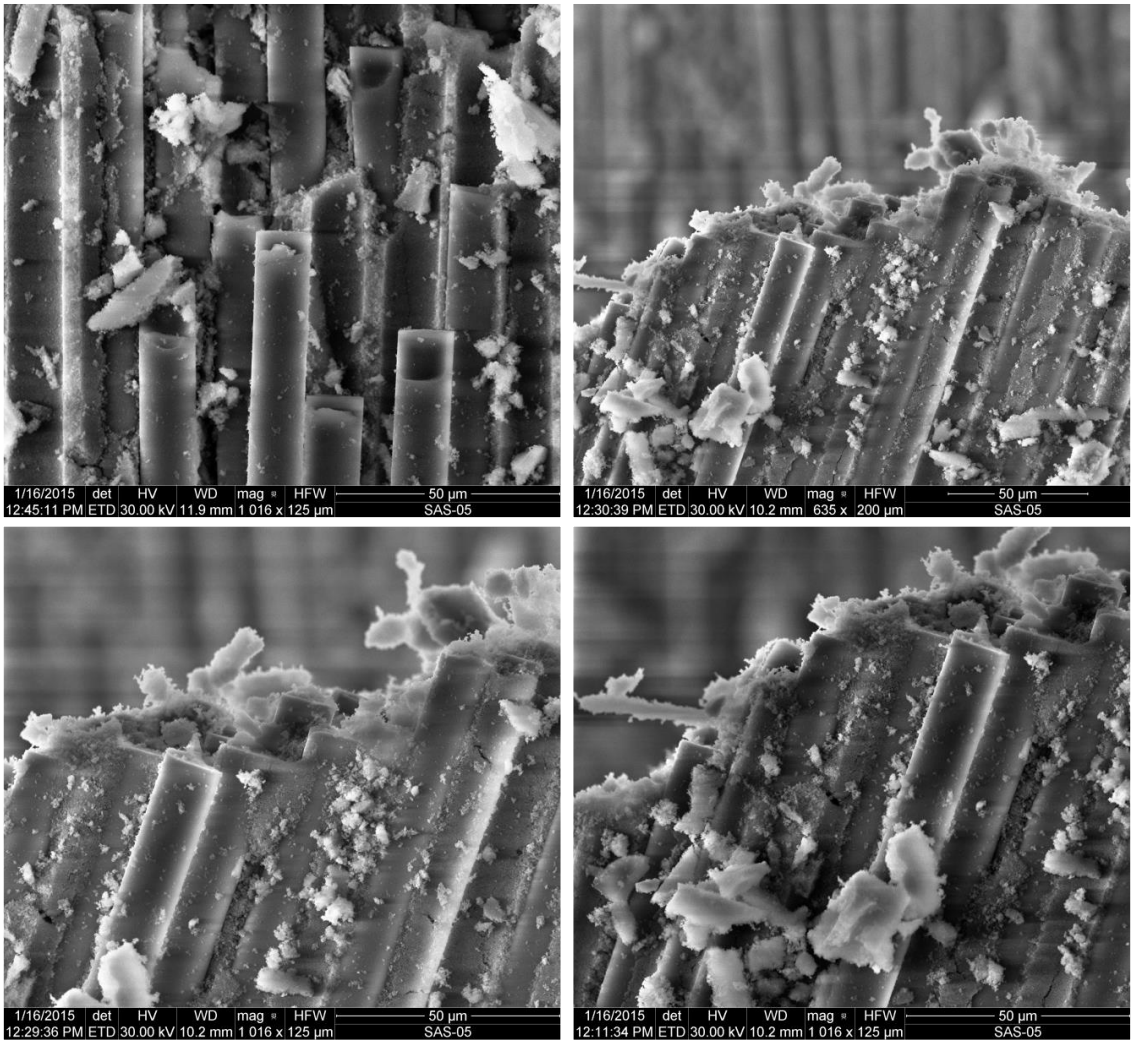

Figure 68 (continued): SEM micrographs of a fracture surface obtained in a tension-compression fatigue test performed at 1200°C in steam, σ_{max} = 100 MPa, N_f = 450 cycles.

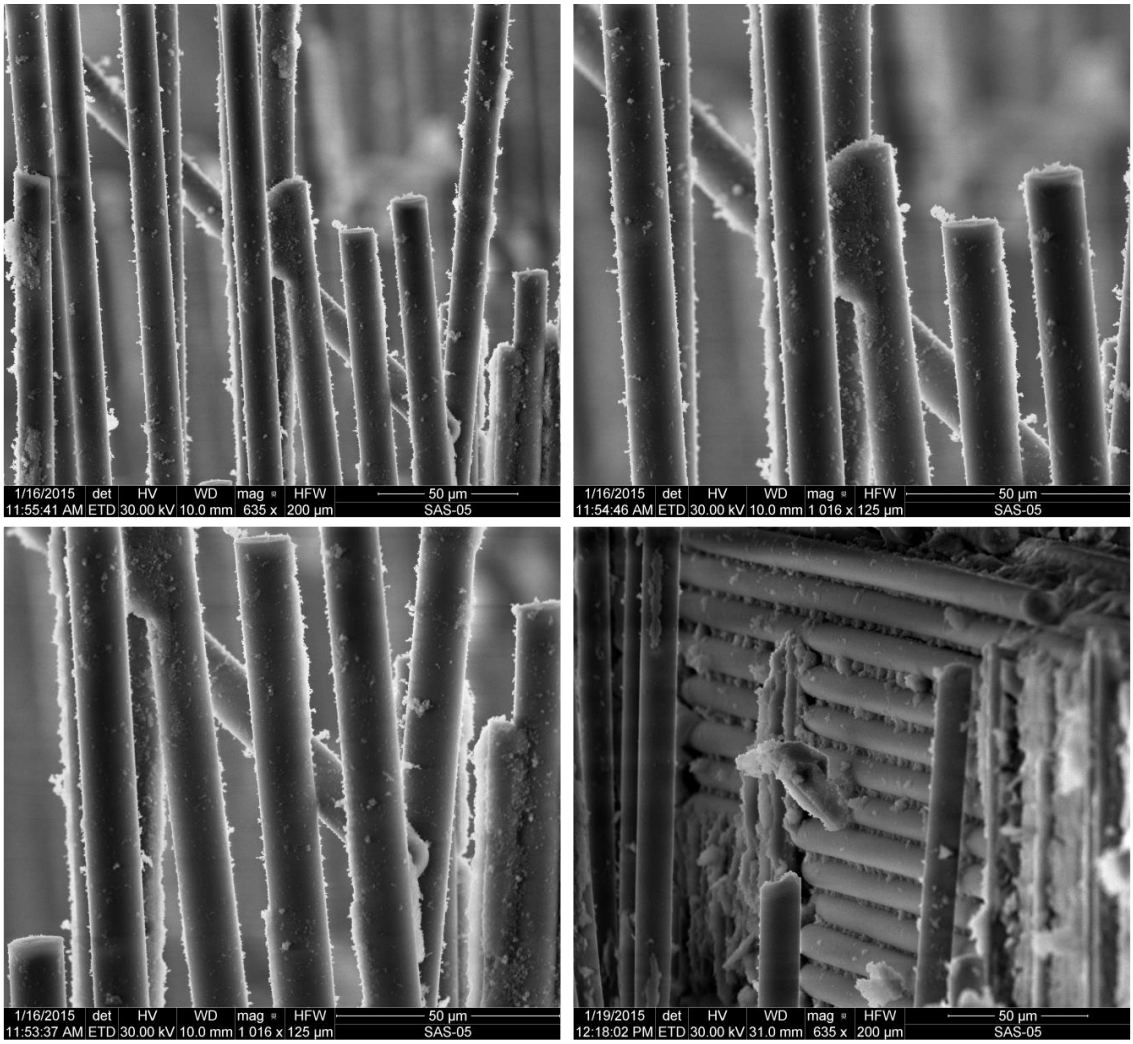

Figure 68 (continued): SEM micrographs of a fracture surface obtained in a tension-compression fatigue test performed at 1200°C in steam, σ_{max} = 100 MPa, N_f = 450 cycles.

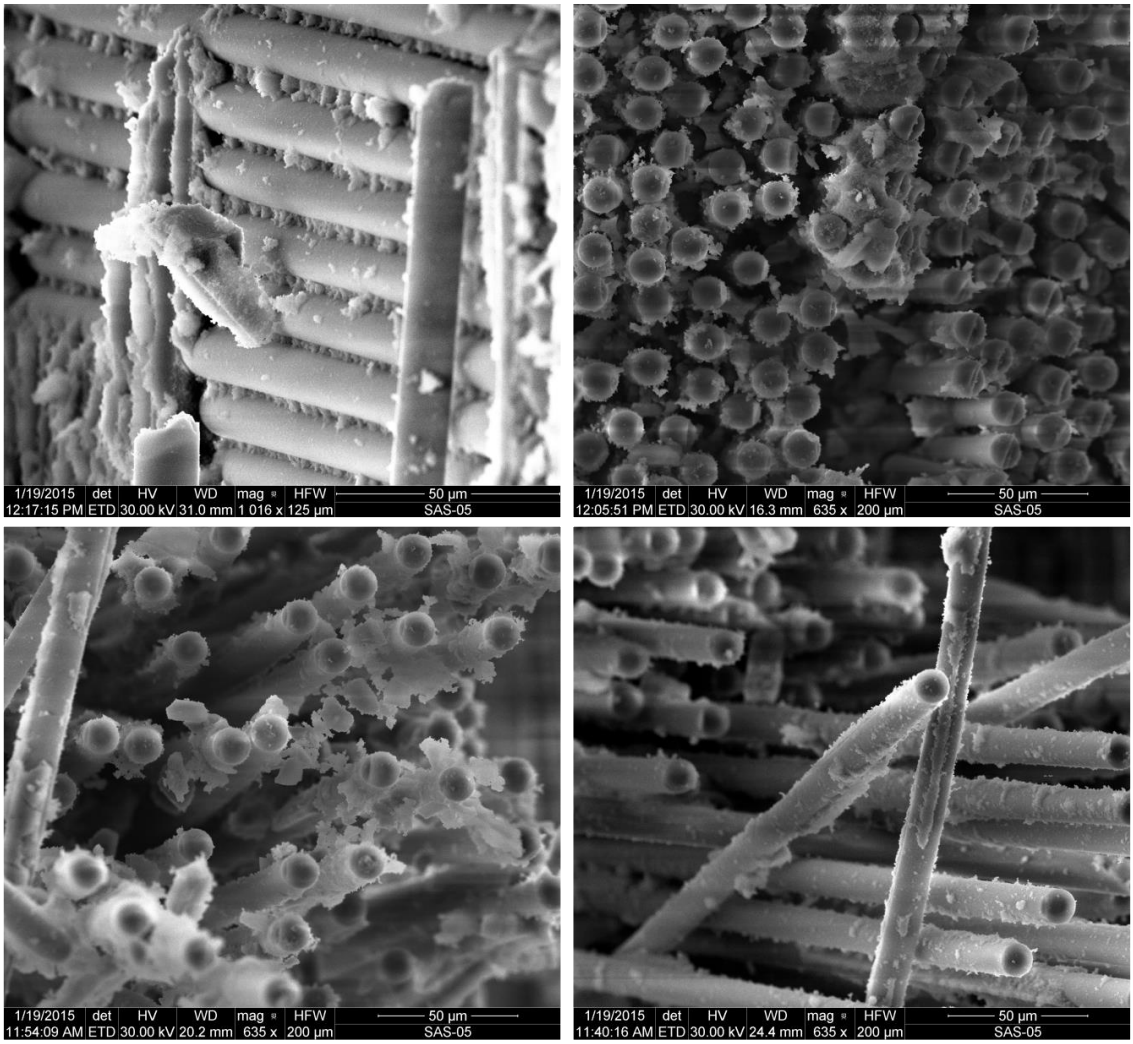

Figure 68 (continued): SEM micrographs of a fracture surface obtained in a tension-compression fatigue test performed at 1200°C in steam, σ_{max} = 100 MPa, N_f = 450 cycles.

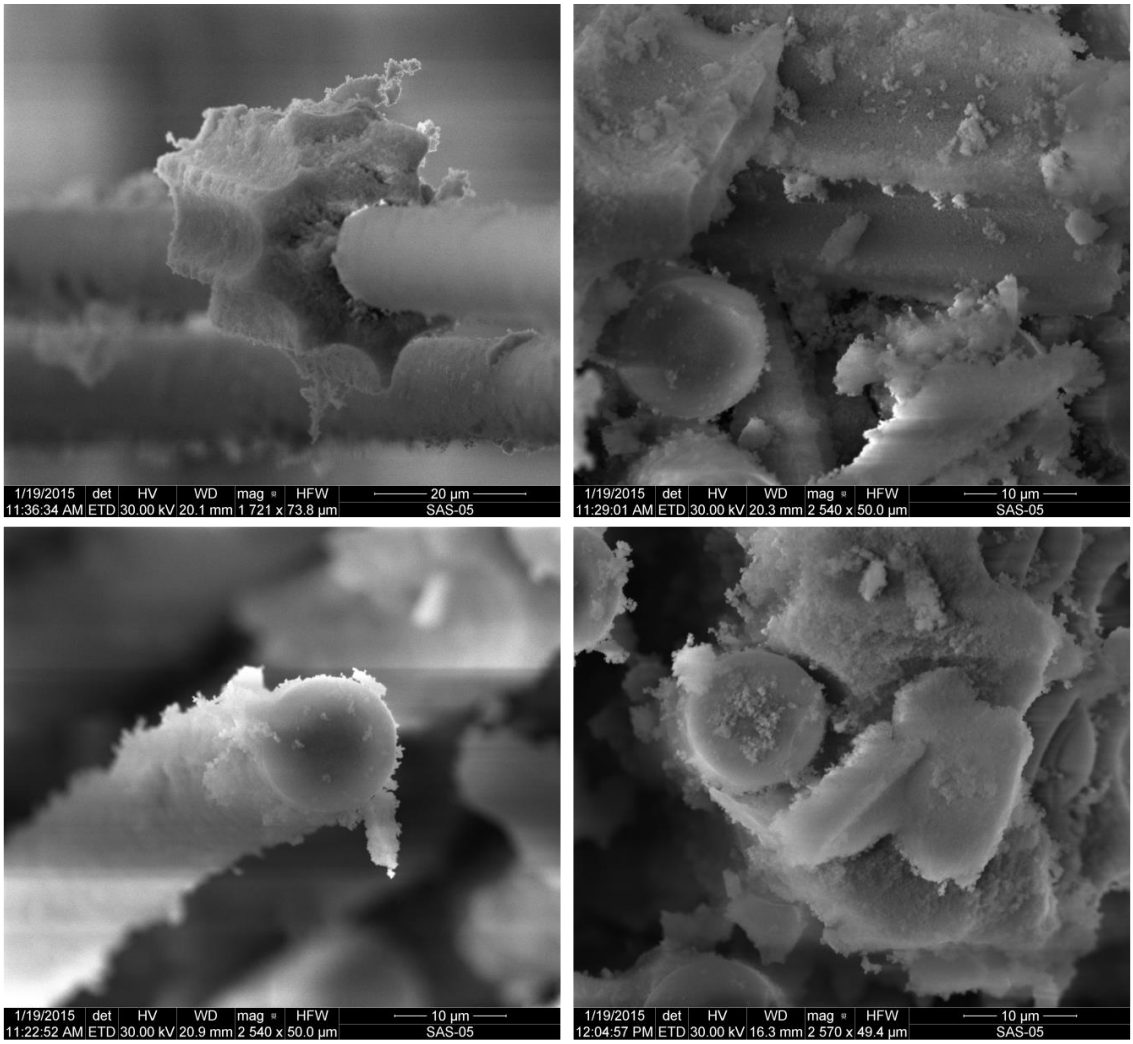

Figure 68 (continued): SEM micrographs of a fracture surface obtained in a tension-compression fatigue test performed at 1200°C in steam, σ_{max} = 100 MPa, N_f = 450 cycles.

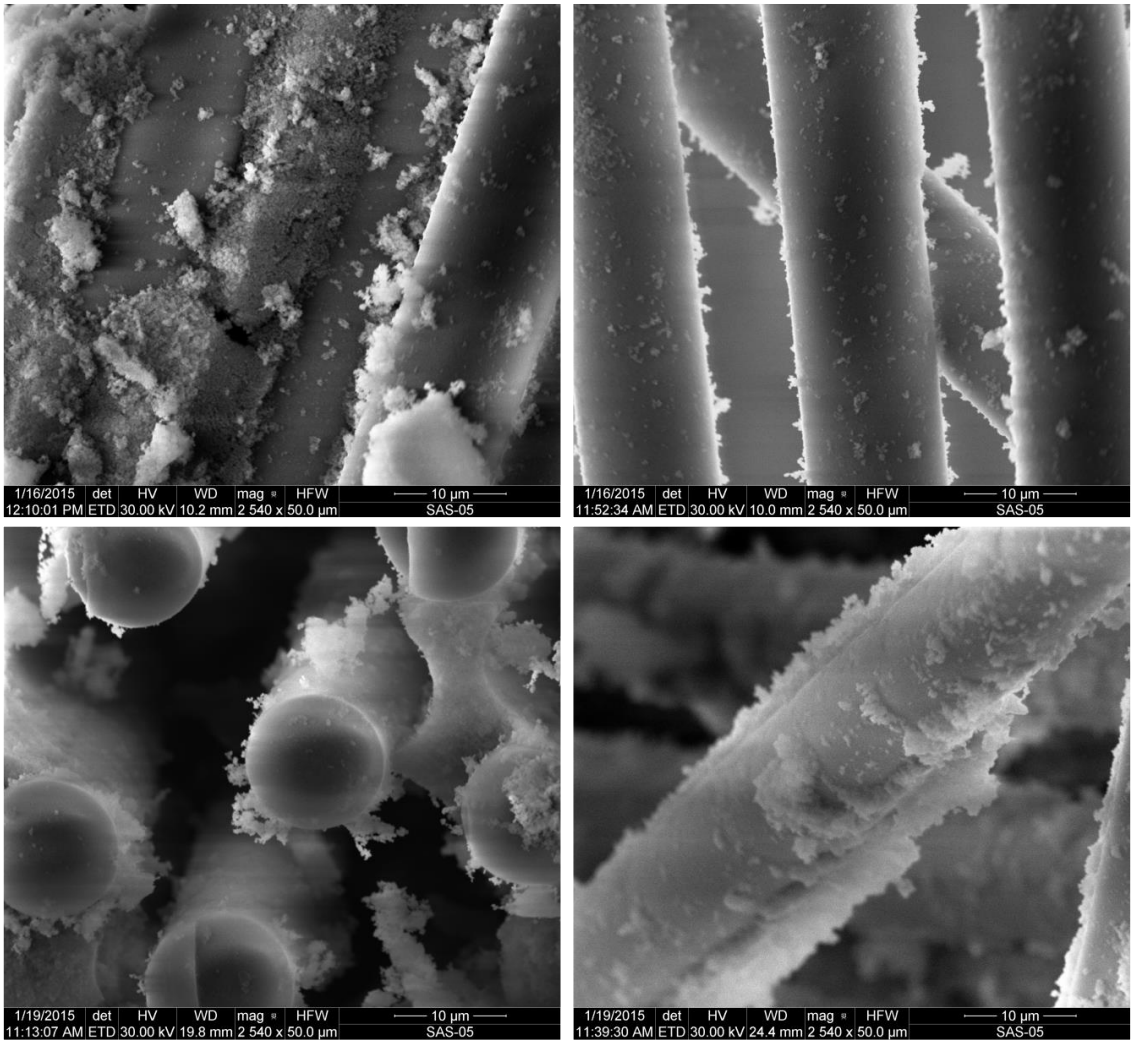

Figure 68 (continued): SEM micrographs of a fracture surface obtained in a tension-compression fatigue test performed at 1200°C in steam, σ_{max} = 100 MPa, N_f = 450 cycles.

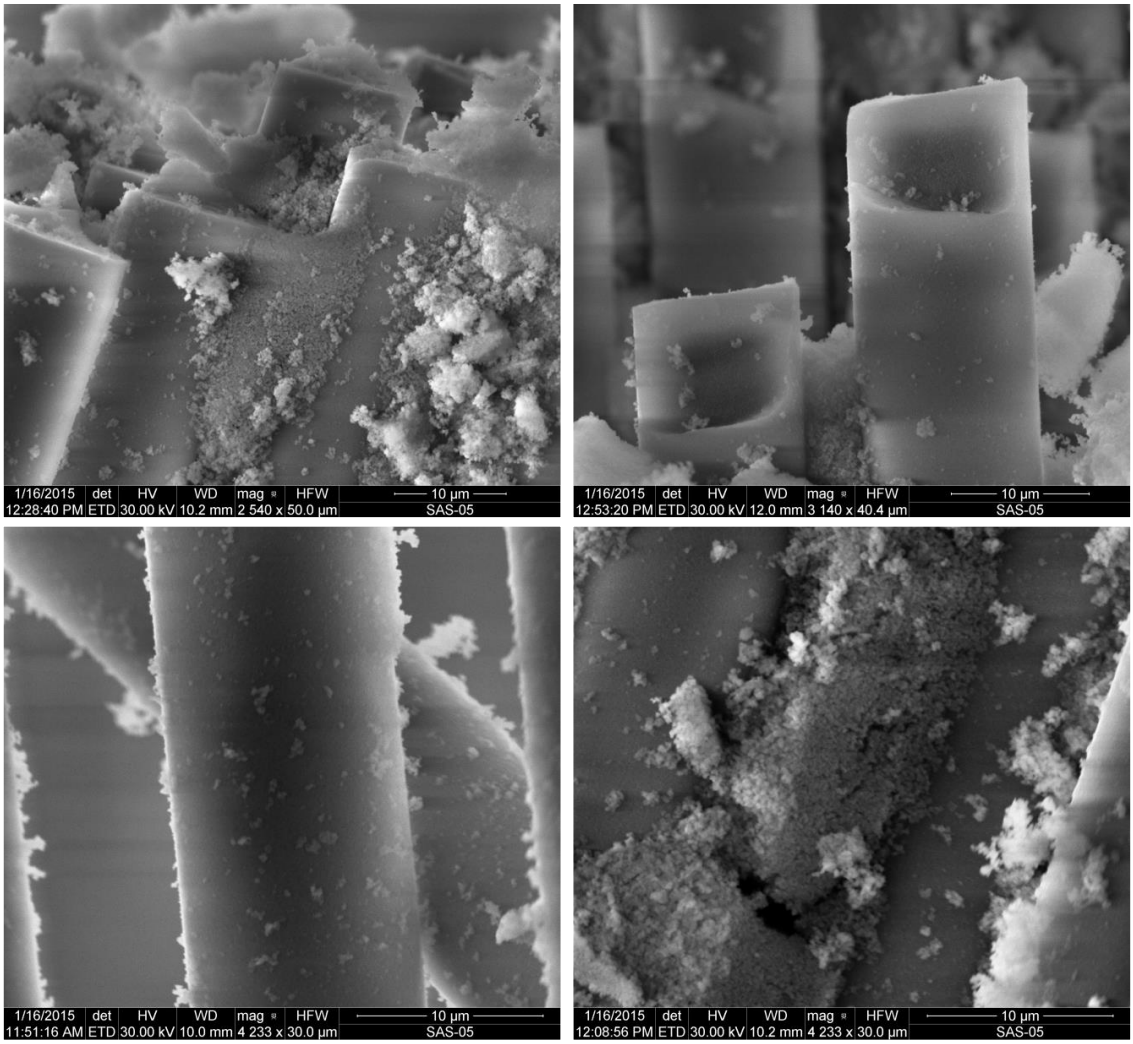

Figure 68 (continued): SEM micrographs of a fracture surface obtained in a tension-compression fatigue test performed at 1200°C in steam, σ_{max} = 100 MPa, N_f = 450 cycles.

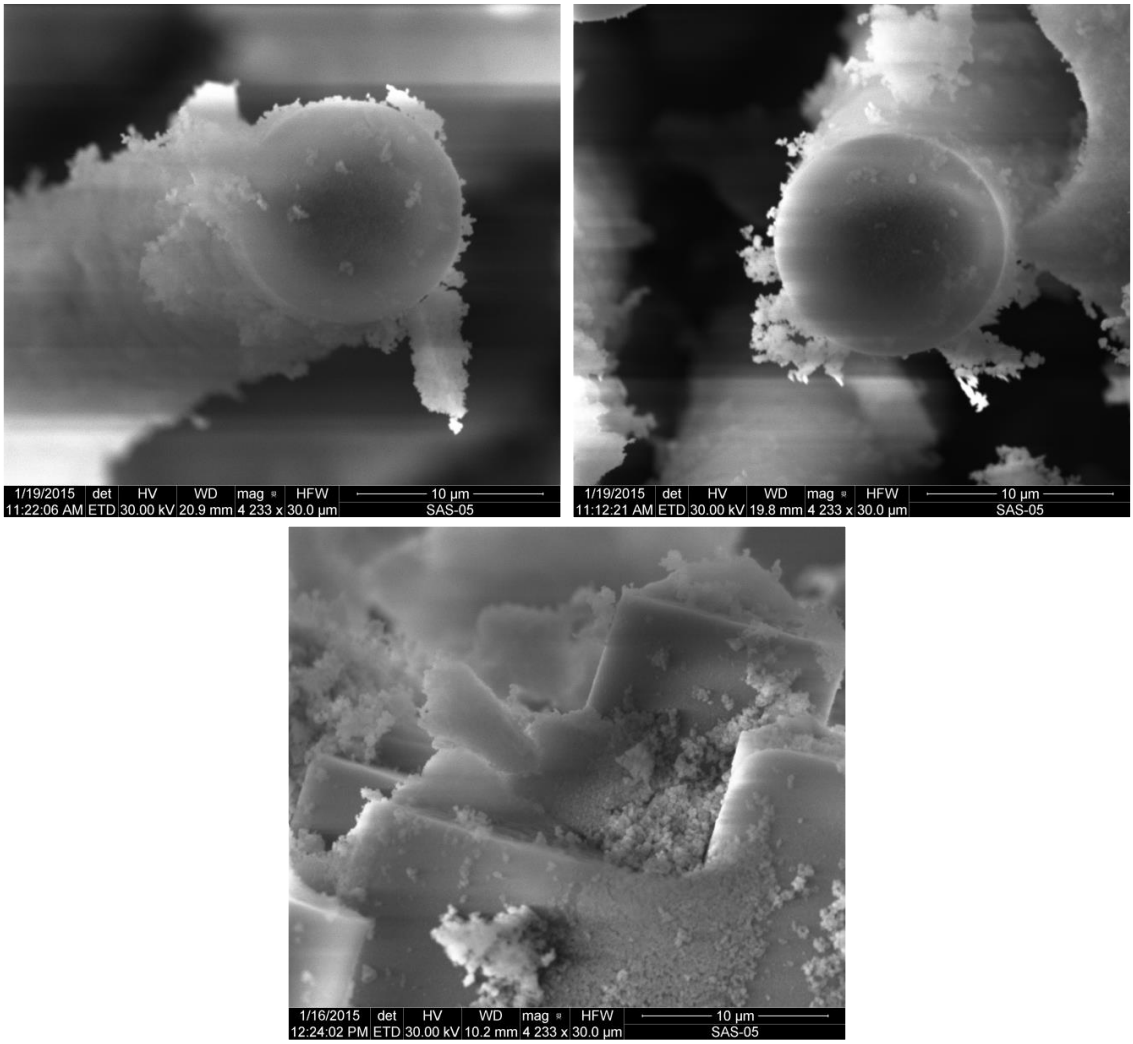

Figure 68 (continued): SEM micrographs of a fracture surface obtained in a tension-compression fatigue test performed at 1200°C in steam, σ_{max} = 100 MPa, N_f = 450 cycles.

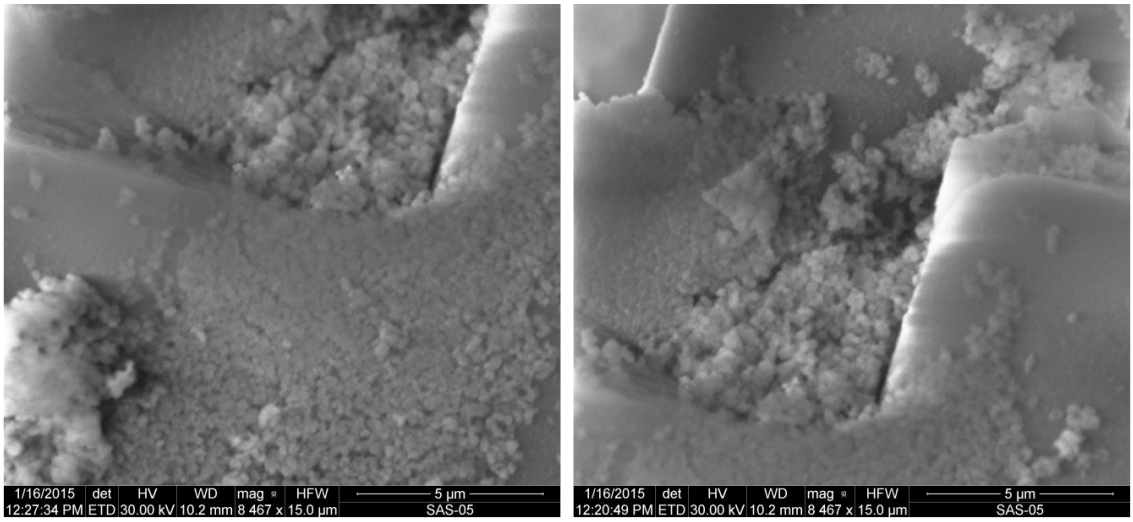

Figure 68 (continued): SEM micrographs of a fracture surface obtained in a tension-compression fatigue test performed at 1200°C in steam, σ_{max} = 100 MPa, N_f = 450 cycles.

Bibliography

[1] Cutler, John, “Understanding Aircraft Structures,” 2nd Edition, Blackwell Scientific Publications, Oxford, 1992.

[2] Megson, T.H.G., “Aircraft Structures for Engineering Students,” 5th Edition, Elsevier Ltd, Oxford, 2007.

[3] Daniel, Isaac M., Ishai, Ori., “Engineering Mechanics of Composite Materials,” Oxford University Press, New York, 2006.

[4] Ellyard, D., “Putting it Together – Science and Technology of Composite Materials,” Vol. 2013, 2000.

[5] Smith, F., “The Use of Composites in Aerospace Applications: Past, Present and Future Challenges,” 2013.

[6] Messick, D., “Luna Innovations’ ODiSI sensing platform provides greater insight into condition of composites,” 2012.

[7] Cookson, I., “Sector outperforms: 2008 M&A activity matches prior-year record,” *Aerospace Components*, No. February, 2009, pp. 1-5.

[8] Anonymous, “Composite Materials for Aircraft Industry,” Total Materia, 2004.

[9] Szweda, A., Butner, S., Ruffoni, J, Bacalski, “Development and Evaluation of Hybrid Oxide/Oxide Ceramic Matrix Composite Combustor Liners, *“Proceedings of GT2005 ASME Turbo Expo 2005: Power for Land, Sea and Air*, June 6-9, 2005, Reno-Tahoe Nevada, pp. 1-7.

[10] Anonymous, “Ceramic Matrix Composite (CMC) Technologies,” National Aeronautics and Space Administration, Glenn Research Center, PS–00921–1112–B103, www.nasa.gov.

[11] Cahn, R.W, Evans, A. G., McLean, M., “High-Temperature Structural Materials,” Chapman & Hall for the Royal Society, London; New York, 1996.

[12] Chawla, K. K., “Ceramic Matrix Composites,” Chapman and Hall, London; New York, 1993.

[13] Bansal, N. P., “Handbook of Ceramic Composites,” Kluwer Academic Publishers, Boston, 2005.

[14] Geiger, G., “Introduction to Ceramics,” American Ceramic Society, 2001.

[15] Schmidt, S., H. Knabe, H. Immich, R. Mestring, and A. Gessler. "Advanced Ceramic Matrix Composite Materials for Current and Future Propulsion Technology Applications." Acta Astronautica, 55, 2004: 409-420.

[16] Zok, Frank W. and Carlos G. Levi. “Mechanical Properties of Porous-Matrix Ceramic Composites,” Advanced Engineering Materials, 3[1-2]: 15-23 (2001)

[17] Wilson, D.M., Visser, L.R., “High performance oxide fibers for metal and ceramic composites,” *composites Part A: applied science and manufacturing,* Vol. 32, 2001, pp. 1143-1153.

[18] Ruggles-Wrenn, M., Radzicki, A.T., Baek, S.S., Keller, K.A., "Effect of loading rate on the monotonic tensile behavior and tensile strength of an oxide/oxide ceramic composite at 1200°C," *Materials Science & Engineering: A (Structural Materials: Properties, Microstructure and Processing),* Vol. 492, No. 1-2, 2008, pp. 88-94.

[19] Ruggles-Wrenn, M., Mall, S., Eber, C.A., Harlan, L.B., " Effects of steam environment on high-temperature mechanical behavior of Nextel^{TM}720/alumina (N720/A) continuous fiber ceramic composite," *composites Part A: applied science and manufacturing,* Vol. 37, 2006, pp. 2029-2040.

[20] Ruggles-Wrenn, M. B., Hetrick, G., Baek, S. S., “Effects of frequency and environment on fatigue behavior of an oxide–oxide ceramic composite at 1200 C,” *International Journal of Fatigue*, Vol. 30, No. 3, 2008, pp. 502-516.

[21] Mehrman, J. M., Ruggles-Wrenn, M. B., Baek, S. S. “Influence of hold times on the elevated-temperature fatigue behavior of an oxide–oxide ceramic composite in air and in steam environment,” *Composites Science and Technology*, Vol. 67, No. 7, 2007, pp. 1425-1438.

[22] Armani, C. J., Ruggles-Wrenn, M. B., Hay, R. S., & Fair, G. E., “Creep and microstructure of Nextel™ 720 fiber at elevated temperature in air and in steam,” *Acta Materialia*, Vol. 61, No. 16, 2013, pp. 6114-6124.

[23] Ruggles-Wrenn, M., and Genelin, C.L., "Creep of Nextel™720/alumina–mullite ceramic composite at 1200°C in air, argon, and steam," *Composites Science & Technology,* Vol. 69, No. 5, 2009, pp. 663-669.

[24] Ruggles-Wrenn, M., and Szymczak, N.R., "Effects of steam environment on compressive creep behavior of Nextel (TM) 720/Alumina ceramic composite at 1200 deg C," *Composites: Part A, Applied Science & Manufacturing,* Vol. 39, No. 12, 2008, pp. 1829-1837.

[25] Ruggles-Wrenn, M., and Kutsal, T., "Effects of steam environment on creep behavior of Nextel (TM) 720/alumina-mullite ceramic composite at elevated temperature," *Composites: Part A, Applied Science & Manufacturing,* Vol. 41, No. 12, 2010, pp. 1807-1816.

[26] Ruggles-Wrenn, M., Koutsoukos, P., and Baek, S., "Effects of environment on creep behavior of two oxide/oxide ceramic–matrix composites at 1200 °C," *Journal of Materials Science,* Vol. 43, No. 20, 2008, pp. 6734-6746.

[27] Ruggles-Wrenn, M., and Ozer, M., "Creep behavior of Nextel™720/alumina–mullite ceramic composite with ±45° fiber orientation at 1200°C," *Materials Science & Engineering: A,* Vol. 527, No. 20, 2010, pp. 5326-5334.

[28] Ruggles-Wrenn, M. B., & Whiting, B. A., "Cyclic creep and recovery behavior of Nextel™ 720/alumina ceramic composite at 1200° C," *Materials Science and Engineering: A*, Vol. 528, No. 3, 2011, pp. 1848-1856.

[29] Ruggles-Wrenn, M., and Braun, J.C., "Effects of steam environment on creep behavior of Nextel™720/alumina ceramic composite at elevated temperature," *Materials Science & Engineering: A,* Vol. 497, No. 1, 2008, pp. 101-110.

[30] Ruggles-Wrenn, M. B., & Pope, M. T., "Creep Behavior in Interlaminar Shear of a SiC/SiC Ceramic Composite with a Self-healing Matrix," *Applied Composite Materials*, Vol. 21, No. 1, 2013, pp. 1-13.

[31] Ruggles-Wrenn, M. B., & Sharma, V., "Effects of steam environment on fatigue behavior of two SiC/[SiC+ Si3N4] ceramic composites at 1300 C," *Applied Composite Materials*, Vol. 18, No. 5, 2011, pp. 385-396.

[32] Ruggles-Wrenn, M., Christensen, D.T., Chamberlain, A.L., "Effect of frequency and environment on fatigue behavior of a CVI SiC/SiC ceramic matrix composite at 1200C," *Composites Science and Technology,* Vol. 71, No. 2, 2011, pp. 190-196.

[33] Ruggles-Wrenn, M.B., and Jones, T.P., "Tension–compression fatigue of a SiC/SiC ceramic matrix composite at 1200 °C in air and in steam," *International Journal of Fatigue,* Vol. 47, No. 0, 2013, pp. 154-160.

[34] Wilson, D.M., Lieder, S.L., Lueneburg, D.C, "Microstructure and High Temperature Properties of Nextel 720 Fibers", *Ceramic Engineering and Science Proceedings*, 16(5):1005-1014 (1995).

[35] Wilson, D.M., "New High Temperature Oxide Fibers", St. Paul, MN: 3M Corporation, no date.

[36] J.M. Corum et al., Durability-Based Design Properties of Reference Crossply Carbon-Fiber Composite, ORNL/TM-200/322, Oak Ridge National Laboratory, Oak Ridge, Tenn., April 2001.

[37] Owen, MJ and Smith, T.R. “Plastics and Polymers.” Vol. 36, Feb. 1968: 33-44

[38] Mehrman, J.M. “Effect of Hold Times on Fatigue Behavior of Nextel™ 720/Alumina Ceramic Matrix Composite at 1200 °C in Air and in Steam Environment.” MS thesis, AFIT/GA/ENY/06-M23. School of Engineering and Management, Air Force Institute of Technology (AU), Wright-Patterson AFB, OH March 2006.

[39] Hetrick, Griffin. “Effects of Frequency and Environment on Fatigue Behavior of an Oxide-Oxide Ceramic Matrix Composite at 1200 °C.” MS thesis, AFIT/GA/ENY/06-J05. School of Engineering and Management, Air Force Institute of Technology (AU), Wright-Patterson AFB OH, June 2006.

[40] Eber, C.A. “Effect of Temperature and Steam Environment on Fatigue Behavior of an Oxide-Oxide Continuous Fiber Ceramic Composite.” MS thesis, AFIT/GA/ENY/05-M09. School of Engineering and Management, Air Force Institute of Technology (AU), Wright-Patterson AFB, OH March 2005.

[41] Harlan, L.B. “Creep-Rupture Behavior of an Oxide/Oxide Ceramic Matrix Composite at Elevated Temperatures in Air and Steam Environment.” MS thesis, AFIT/GA/ENY/05-M05. School of Engineering and Management, Air Force Institute of Technology (AU), Wright-Patterson AFB, OH, March 2005.

[42] Boyer, B.H. “Creep-Rupture and Fatigue Behavior of a Notched Oxide/Oxide Ceramic Matrix Composite at Elevated Temperature.” MS thesis, AFIT/GAE/ENY/08-J01. School of Engineering and Management, Air Force Institute of Technology (AU), Wright-Patterson AFB, OH March 2008.

[43] Anonymous, “Oxide Ceramic Matrix Composites,” COI Ceramics, Inc, http://www.coiceramics.com/oxidepg.html.

[44] Bansal, N. P., & Lamon, J. “Ceramic Matrix Composites: Materials, Modeling and Technology.” John Wiley & Sons, 2014.

[45] Szymczak, N.R. “Compressive Creep Behavior of Nextel 720/Alumina Ceramic Matrix Composite at 1200°C In Air and In Steam Environment.” MS thesis, AFIT/GAE/ENY/07-J20. School of Engineering and Management, Air Force Institute of Technology (AU), Wright-Patterson AFB, OH March 2007.

[46] Delapasse, Jacob. “Fatigue Behavior of an Advanced SiC/SiC Composite with an Oxidation Inhibited Matrix at 1200°C in Air and Steam.” MS Thesis, AFIT/GAE/ENY/06-J05. School of Engineering and Management, Air Force Institute of Technology (AU), Wright-Patterson Air Force Base, OH, March 2010.

[47] Tai WP, Watanabe T. High-Temperature Stability of Alumina in Argon and Argon/Water-Vapor Environments. J Am Cer Soc 1999; 82(1):245-48.

[48] Kronenberg AK, Castaing J, Mitchell TE, Kirby SH. Hydrogen Defects in α-Al_2O_3 and Water Weakening of Sapphire and Alumina Ceramics between 600 and 1000°C – I. Infrared Characterization of Defects. Acta Mater 2000; 48:1481-94.

[49] Korinek, L.M. and Castaing, J. “Slip and Twinning in Polycrystalline Alumina (α-Al_2O_3) Deformed under Hydrostatic Pressure between 600°C and 1000°C,” Journal of the American Ceramics Society, 4:566-573 (2003).

[50] Wannaparhun S, Seal S. “A combined spectroscopic and thermodynamic investigation of Nextel-720/Alumina ceramic matrix composite in air and water vapor at 1100 C.” J Am Ceram Soc 2003;86(9): 1628–30.

[51] Armani, C. J., Ruggles-Wrenn, M. B., Hay, R. S., & Fair, G. E. "Creep and microstructure of Nextel™ 720 fiber at elevated temperature in air and in steam." Acta Materialia 61.16 (2013): 6114-6124.

[52] Rosen BW. Mechanics of Composite Strengthening. Ch 3. In: Fiber Composite Gszczuk LB. Microbuckling Failure of Circular Fiber-Reinforced Composites. AIAA J 1975; 13:1311-18.

[53] Wang ASD. A Non-Linear Microbuckling Model Predicting the Compressive Strength of Unidirectional Composites. ASME Paper 78-WA/Aero 1, 1978.

[54] Hahn HT, Williams JG. Compressive Failure Mechanisms in Unidirectional Composites. In: Whitney JM editor, Composite Materials: Testing and Design (Seventh Conference), ASTM STP 893, American Society for Testing and Materials, 1986, 115-39.

[55] Arrowood R, Lankford J. Compressive Fracture Processes in an Alumina/Glass Composite. J Mat Sci 1987; 22:3737-47.

REPORT DOCUMENTATION PAGE

Form Approved
OMB No. 074-0188

1. REPORT DATE *(DD-MM-YYYY)*	**2. REPORT TYPE**	**3. DATES COVERED** *(From – To)*
26-03-2015	Master's Thesis	September 2013 – March 2015

TITLE AND SUBTITLE
Tension-Compression Fatigue of an Oxide/Oxide Ceramic Matrix Composite at Elevated Temperature in Air and Steam Environments

5a. CONTRACT NUMBER

5b. GRANT NUMBER

5c. PROGRAM ELEMENT NUMBER

6. AUTHOR(S)
Lanser, Richard L., Captain, USAF

5d. PROJECT NUMBER

5e. TASK NUMBER

5f. WORK UNIT NUMBER

7. PERFORMING ORGANIZATION NAMES(S) AND ADDRESS(S)
Air Force Institute of Technology
Graduate School of Engineering and Management (AFIT/EN)
2950 Hobson Way, Building 640
WPAFB OH 45433-7765

8. PERFORMING ORGANIZATION REPORT NUMBER
AFIT-ENY-MS-15-M-222

9. SPONSORING/MONITORING AGENCY NAME(S) AND ADDRESS(ES)
Air Force Research Laboratory
Larry Zawada
2230 10th Street
Wright-Patterson AFB, OH 45433
larry.zawada@us.af.mil

10. SPONSOR/MONITOR'S
AFRL/RXCC

11. SPONSOR/MONITOR'S REPORT NUMBER(S)

12. DISTRIBUTION/AVAILABILITY STATEMENT
DISTRUBTION STATEMENT A. APPROVED FOR PUBLIC RELEASE; DISTRIBUTION UNLIMITED.

13. SUPPLEMENTARY NOTES
This material is declared a work of the U.S. Government and is not subject to copyright protection in the United States.

14. ABSTRACT
Tension-compression fatigue behavior of an oxide-oxide ceramic matrix composite was investigated at 1200°C in air and steam. The composite is comprised of an alumina matrix reinforced with Nextel 720 fibers woven in an eight harness satin weave. The composite relies on a porous matrix for damage tolerance. Compression and tension tests to failure were conducted to characterize basic mechanical properties. Tension-compression fatigue tests were performed at 1 Hz frequency with a ratio of minimum to maximum stress of -1. Maximum stresses ranged from 60-120 MPa. Fatigue run-out (defined as 10^5 cycles) was achieved in air at 80 MPa and in steam at 70 MPa. Specimens subjected to 10^5 fatigue cycles in air retained 100% tensile strength. Steam reduced fatigue lives one order of magnitude and tensile strength 17-38%. Tension-compression fatigue lowered fatigue lives three orders of magnitude from published tension-tension fatigue lives. In air, tension-compression fatigue was shown to be more damaging than creep. The post-test composites microstructure was examined. Failure mechanisms were identified and fracture surface morphologies were characterized. The dominant failure mode under tension-compression fatigue was fiber micro-buckling. Shortened composite lives were associated with planar fractures and coordinated fiber failure due to increased fiber-matrix bonding and matrix densification.

15. SUBJECT TERMS
Ceramic Matrix Composites, Composite Materials, Ceramic Fibers, Ceramic Materials, Fiber Reinforced Composites, Alumina, Mullite, Oxides, Nextel™ 720 Fiber, Fully Reversed Fatigue, Tension-Compression Fatigue, N720/A

16. SECURITY CLASSIFICATION OF:			**17. LIMITATION OF ABSTRACT**	**18. NUMBER OF PAGES**	**19a. NAME OF RESPONSIBLE PERSON**
a. REPORT	**b. ABSTRACT**	**c. THIS PAGE**			Dr. Marina B. Ruggles-Wrenn, AFIT/ENY
U	**U**	**U**	**UU**	193	**19b. TELEPHONE NUMBER** *(Include area code)* 937-255-3636 x4641 marina.ruggles-wrenn@afit.edu

Standard Form 298 (Rev. 8-98)
Prescribed by ANSI Std. Z39-18